Phonon Polaritons in Polar Dielectric Heterostructures

Im Fachbereich Physik
der Freien Universität Berlin
eingereichte Dissertation

zur Erlangung des akademischen Grades des
Doktors der Naturwissenschaften (Dr. rer. nat.)

von

Nikolai Christian Paßler

Berlin, Mai 2020

Fritz-Haber-Institut
der Max-Planck-Gesellschaft

Erster Gutachter:
Prof. Dr. Martin Wolf
Fritz-Haber-Institut der Max-Planck-Gesellschaft, Berlin
Abteilung Physikalische Chemie

Zweiter Gutachter:
Prof. Dr. Paul Fumagalli
Freie Universität Berlin
Fachbereich Physik

Arbeitsgruppenleiter:
Dr. Alexander Paarmann
Fritz-Haber-Institut der Max-Planck-Gesellschaft, Berlin
Abteilung Physikalische Chemie

Tag der Disputation: 16. September 2020

Selbstständigkeitserklärung

Hiermit versichere ich, die vorliegende Dissertation eigenständig und ausschließlich unter Verwendung der angegebenen Quellen und Hilfsmittel angefertigt zu haben. Die vorliegende Arbeit ist in dieser oder anderer Form nicht als Prüfungsarbeit zur Begutachtung vorgelegt worden.

Berlin, 29. Mai 2020

Nikolai Christian Paßler

Contents

Publications Forming this Thesis

In the course of this doctoral thesis, various experimental and theoretical findings resulted in the publication of ten scientific articles in several journals including the Journal of the Optical Society of America (JOSA B), ACS Photonics, Nano Letters, ACS Nano, Physical Review B (PRB), Applied Physics Letters (APL), and Advanced Optical Materials (AOM). In the following table, the six (one of which including the associated erratum) of those articles that form this thesis are listed, and in chapter 4, the original publications are reprinted.

Table: List of publications forming this thesis with the author of this thesis (N.C.P.) as first author.

Title	Authors	Published	Journal	Page
Second Harmonic Generation from Critically Coupled Surface Phonon Polaritons [**I**]	N. C. Passler, I. Razdolski, S. Gewinner, W. Schöllkopf, M. Wolf and A. Paarmann	April 11, 2017	ACS Photonics	37
Generalized 4×4 matrix formalism for light propagation in anisotropic stratified media: study of surface phonon polaritons in polar dielectric heterostructures [**II**]	N. C. Passler and A. Paarmann	September 18, 2017	JOSA B	45
Generalized 4×4 matrix formalism for light propagation in anisotropic stratified media: study of surface phonon polaritons in polar dielectric heterostructures: erratum [**III**]	N. C. Passler and A. Paarmann	November 1, 2019	JOSA B	59
Strong Coupling of Epsilon-Near-Zero Phonon Polaritons in Polar Dielectric Heterostructures [**IV**]	N. C. Passler, C. R. Gubbin, T. G. Folland, I. Razdolski, D. S. Katzer, D. F. Storm, M. Wolf, S. De Liberato, J. D. Caldwell and A. Paarmann	June 12, 2018	Nano Letters	65
Second Harmonic Generation from Phononic Epsilon-Near-Zero Berreman Modes in Ultrathin Polar Crystal Films [**V**]	N. C. Passler, I. Razdolski, D. S. Katzer, D. F. Storm, J. D. Caldwell, M. Wolf and A. Paarmann	June 3, 2019	ACS Photonics	75
Surface Polariton-Like s-Polarized Waveguide Modes in Switchable Dielectric Thin Films on Polar Crystals [**VI**]	N. C. Passler, A. Heßler, M. Wuttig, T. Taubner and A. Paarmann	September 26, 2019	AOM	85
Layer-Resolved Absorption of Light in Arbitrarily Anisotropic Heterostructures [**VII**]	N. C. Passler, M. Jeannin and A. Paarmann	April 23, 2020	PRB	97

CHAPTER 1

Introduction

In the past decades, the scientific field of nanophotonics has emerged, aiming at understanding and harnessing the extraordinary properties of light and light-matter-interaction on the nanoscale. Restricted by the diffraction limit [1], conventional optical components like lenses or parabolic mirrors cannot focus light far below the wavelength. In nanophotonics, this limit is overcome by coupling light into subwavelength structures, enabling light confinement of more than 400 times smaller than the wavelength [2–4].

Squeezing light into nanoscale objects bears two intriguing advantages: Firstly, compared to the field amplitudes of a light wave propagating in free space, the local electric fields in a nanostructure are immensely enhanced, boosting the light-matter interaction considerably. These enhanced electric fields enable a variety of applications, such as improved solar cell efficiency [5], all-optical switching [6], or ultra-efficient sensing [7]. Secondly, subwavelength-confined light allows for miniaturization of optoelectronic devices, enabling advances such as on-chip, high-speed photodetectors [8] or ultra-fast miniature lasers [9] for all-optical integrated circuitry and communication.

For many years, the principle workhorse of nanophotonics has been the surface plasmon polariton (SPP), a surface excitation enabled by collective electron oscillations – a plasmon – supported in metallic materials at infrared (IR) up to visible wavelengths. Eminent milestones in the history of plasmonics employing the SPP have been the discovery of surface-enhanced raman scattering (SERS) [10] and plasmon-enhanced fluorescence [11], and the development of modern plasmonic devices such as single photon transistors [12] or nanolasers [13].

Only recently, other fundamental excitations than the SPP have started to attract broad attention in the nanophotonics community. A promising complementary candidate is the surface phonon polariton (SPhP), where the light is coupled to an optically active phonon mode in a polar crystal lattice instead of a plasmon in a metal. Owing to significantly longer lifetimes of optical phonons in single crystals compared to plasmons in metals, SPhPs provide an attractive low-loss alternative for nanophotonic applications at IR and THz frequencies [14].

Another advantage of SPhPs is the wealth of supporting materials, including most III-V semiconductor compounds, silicon carbide (SiC), several II-VI semiconductors, and various oxides such as magnesium oxide, molybdenum trioxide or gallium(III) trioxide, covering a broad frequency range in the IR. Furthermore, most of these materials feature optical anisotropy due to an anisotropic crystal structure, leading to non-trivial optical responses and novel nanophotonic phenomena. A prominent example are hyperbolic phonon polaritons [15], which have been demonstrated to enable subdiffraction imaging and hyperlensing [16].

On the other hand, SPhPs supported by a single material possess several limitations that hinder the application in nanophotonic technologies: The frequency window where the SPhP is accessible is small, the mode lacks active tunability, the spatial confinement and field enhancements are moderate, and only p-polarized light can be used for the excitation.

In this work, these limitations of SPhPs on bulk crystals are approached and overcome by the employment of layered heterostructures, built from various different materials. By investigating several exemplary systems, it is shown that the combination of SPhP-supporting crystals [**IV**, **V**], metals [**VII**], and other dielectric materials [**VI**] enables unique control over the properties of the excitable polariton modes. These findings demonstrate that layered heterostructures provide a versatile tool box for designing nanophotonic devices with user-defined optical responses and novel functionalities.

Experimentally, the investigation of phonon polaritons in layered heterostructures is realized in a home built prism coupling setup. The specific design of the setup allows for full control over the excitation conditions, enabling systematic experimental access to the phonon polariton properties. As an excitation source, the IR free electron laser (FEL) at the Fritz Haber Insitute (FHI) is employed. The machine is characterized by high-power, high-resolution radiation output, constituting the ideal source for non-linear optical methods such as second harmonic generation (SHG) spectroscopy [17].

By combining the prism coupling setup with the FEL, the non-linear optical response of phonon polaritons at IR frequencies can be probed. Establishing this concept, this work comprises the first observation of SHG from propagating SPhPs [**I**]. Subsequent studies demonstrate the SHG from strongly coupled SPhPs [**VIII**] and the Berreman mode [**V**], a phonon polariton excitable in thin films of deep sub-wavelength thickness. As is shown in these studies, the employment of SHG spectroscopy provides experimental access to the local electric field enhancement of the excited phonon polariton modes, being inaccessible by linear optical techniques.

Even though of central importance for scientific progress, experimental data can be elusive without a proper theoretical model. But in layered anisotropic media, the theoretical description of light-matter interaction is challenging, because most phonon polariton materials feature optical anisotropy. A known approach to this challenge is the 4×4 transfer matrix formalism. However, most previous publications on this subject consider only special cases, are numerically unstable, or lead to discontinuous solutions.

In this work, a numerically stable, generalized framework for the treatment of light-matter interaction in arbitrarily anisotropic layered heterostructures is developed [**II**, **VII**] that is implemented in an open-access computer program [18, 19].[1] As is demonstrated in the various studies of this work, the formalism allows for thorough simulations and analysis of phonon polaritons and their properties in layered media, enabling both corroborative calculations for experimental findings as well as predictive studies of yet unexplored nanophotonic structures.

This work is structured as follows: In chapter 2, the theoretical concepts are delineated, starting with the dielectric permittivity in section 2.1 as the fundamental quantity for the description of light-matter interaction. In section 2.2, phonon polaritons are introduced by deriving the dispersion relation of a bulk SPhP. Then, the concept of layered heterostructures is presented, providing an overview over the different phonon polariton modes arising in the investigated sample structures. Section 2.3 closes the theoretial concepts by explaining the process of SHG, and presenting a summary of the results obtained from the various SHG spectroscopy measurements.

[1] It is noted that the original formalism contains an error in the calculation of electric fields for the case of birefringence, that is, for anisotropic media with non-zero off-diagonal elements of the dielectric permittivity tensor in the lab frame. This error was corrected in an erratum [**III**], see page 59. None of the publications employing the formalism prior to the erratum are affected by the error, since birefringence does not occur in the systems investigated in these works.

Chapter 3 is dedicated to the experimental concepts. Section 3.1 discusses the most common methods for the excitation of phonon polaritons, and section 3.2 presents the implementation of the method employed in this work, the prism coupling in the Otto geometry. The chapter is completed by a description of the FHI FEL (section 3.3).

This work is a cumulative thesis. In chapter 4, the scientific articles that form this thesis are reprinted. Each publication is presented in a separate section, providing a short description of the content of the article, the context in the scope of this thesis, and the author contributions. A list of all publications originated in the course of this thesis can be found on page 117.

Chapter 5 discusses the perspectives of the techniques implemented in this work by outlining several possible pathways for future advances in the field of nanophotonics. Finally, chapter 6 concludes the presented work.

CHAPTER 2

Theoretical Concepts

In 1950, the Ukrainian physicist Tolpygo analyzed the interaction of dipole-carrying lattice vibrations with an electromagnetic field in the limit of long wavelengths [20], obtaining the first description of what later would be termed a *phonon polariton*. His analysis shows the splitting and bending of the light dispersion at frequencies of the lattice vibration, resulting in two distinct dispersion branches featuring an anti-crossing. These two bulk phonon polaritons (BPhPs) are the result of strong light-matter coupling, where the interaction between light and medium is so strong that a new, fully hybridized quasiparticle – the phonon polariton – is created, carrying the properties of both light and the lattice excitation.

In later years, different types of polaritons were discovered, depending on the dipole-carrying matter excitation that couples to the light. These types include exciton polaritons [21] and intersubband polaritons [22] resulting from electronic band transitions, SPPs [23] and SPhPs [14] arising from plasmon and phonon modes that propagate along an interface, and various other polariton types such as magnon polaritons [24] or Cooper pair polaritons [25].

Astonishingly, the optical response of any of the above mentioned polaritons can be fully described by the classical wave-interpretation of light given by Maxwell's equations [26], as long as the light intensity is large enough, that is, high above the single photon limit[1] [28]. Independent of the underlying quasiparticle that is coupling to the light, Maxwell's equations allow for a precise calculation of the electromagnetic fields emerging from the strong light-matter interaction, even in sub-wavelength structures of heterogeneous material compositions. Thus, owing to their universal validity and wide application variety, Maxwell's equations are up until today the standard framework for the semi-classical theoretical description of the interaction of light with matter.

Building on the description of light as electromagnetic wave in terms of the Maxwell's equations, this chapter starts with the concept of the dielectric permittivity for modeling optical resonances (section 2.1), discussing the Drude and the Lorentz model for the description of metallic and polar dielectric materials. In the following section 2.2, phonon polaritons in various heterostructures are discussed, providing an overview over the polariton modes that are investigated in the publications (chapter 4). Finally, section 2.3 focuses on the field enhancement associated with phonon polariton resonances and the resulting enhanced SHG, discussing the systems that were studied by means of SHG spectroscopy.

[1] Quantum optics effects [27] are not relevant for this work

2.1 The Dielectric Permittivity

The optical response of a material under the influence of an external electric field $\vec{E}$ is characterized by the polarization $\vec{P}$ generated in the material. When the external electric field reaches high intensities, $\vec{P}$ is a nonlinear, complicated function of $\vec{E}$, giving rise to nonlinear optical effects (see section 2.3 for more details). In many cases, however, a linear approximation is sufficient to describe the optical response, and the material's polarization $\vec{P}$ can be written as follows (in the dipole approximation) [26]:

$$\vec{P} = \epsilon_0(\bar{\varepsilon} - 1)\vec{E}, \tag{2.1.1}$$

where $\bar{\varepsilon}$ is the dielectric permittivity tensor, fully describing the optical response of a medium:

$$\bar{\varepsilon} = \begin{pmatrix} \varepsilon_{xx} & \varepsilon_{xy} & \varepsilon_{xz} \\ \varepsilon_{yx} & \varepsilon_{yy} & \varepsilon_{yz} \\ \varepsilon_{zx} & \varepsilon_{zy} & \varepsilon_{zz} \end{pmatrix}. \tag{2.1.2}$$

Hence, in principle, with the knowledge of the exact shape of $\bar{\varepsilon}$, any light-matter interaction of the medium can be predicted. In practice, however, the dielectric permittivity of a material cannot be determined for all optical frequencies in full detail. Instead, either experimental techniques such as ellipsometry are employed [29] in order to obtain the shape of the dielectric permittivity in a certain frequency range, or, a model is used that captures the dominant characteristics of the optical response of the material.

This work investigates the light-matter interaction of heterostructures made of various materials with very different optical responses, requiring both experimentally determined dielectric permittivity data (such as for the glass thallium bromo-iodide (KRS-5)), and theoretical models. The two models that are employed are the Drude model and the Lorentz model, which are presented in this section.

2.1.1 Drude Model

The Drude model is based on Drudes considerations about the movement of electrons in a metal published in 1900 [30]. In his classical approach, the electrons in a metal can move freely between the positively charged ions, forming an electron gas, and collisions with ions abruptly alter the velocity of the electrons. An external electric field accelerates the electrons, leading to an electric current. However, for increasing electric fields, the collision rate increases as well and thus the electrons feel an increasing resistance. The Drude model hence provides a physical explanation for Ohm's law [31].

Most certainly, the advances since 1900 of the quantum mechanical understanding of electrons in solid state physics have shown the limits of the Drude model. Specifically, in frequency ranges where other features are observable, such as electronic band transitions, the Drude model fails to predict the optical response. Many improvements of the basic Drude model have been proposed, achieving much more accurate descriptions [32–36]. Nonetheless, the basic model yields reasonable results for the overall trend of the optical response of a metallic material, which is why it is still broadly used for many applications.

In order to obtain the dielectric permittivity of a Drude metal, the equation of motion of a free electron is considered:

$$m\ddot{\vec{u}} + m\gamma\dot{\vec{u}} = q\vec{E}, \tag{2.1.3}$$

where m is the effective mass of the electron, $\vec{u}$ the position in space, γ the damping constant arising from the collisions with the ions, q the electron charge, and $\vec{E} = \vec{E}_0 e^{i\omega t}$ the incident electromagnetic field driving the electron motion with frequency ω. The solution of this differential equation is

$$\vec{u} = \frac{q\vec{E}}{m(-\omega^2 + i\omega\gamma)}. \tag{2.1.4}$$

For an ensemble of N electrons, the macroscopic polarization $\vec{P}$ amounts to

$$\vec{P} = Nq\vec{u} = \varepsilon_0\chi\vec{E} = \varepsilon_0(\varepsilon - 1)\vec{E}, \tag{2.1.5}$$

where in the second step the linear approximation of the polarization was assumed (Eq. 2.1.1), with χ being the electric susceptibility, and ε_0 the vacuum permittivity. Rearranging Equation 2.1.5 yields for the dielectric permittivity ε:

$$\varepsilon(\omega) = 1 - \frac{\omega_p^2}{\omega^2 - i\omega\gamma} \tag{2.1.6}$$

with the plasma frequency ω_p

$$\omega_p = \sqrt{\frac{Nq^2}{\varepsilon_0 m}}, \tag{2.1.7}$$

where N is given in units of inverse cubic centimeters, describing the free carrier concentration. At the plasma frequency, the real part of the dielectric permittivity crosses zero from negative to positive, representing the upper frequency limit of supported SPP modes, and marking the epsilon-near-zero (ENZ) frequency of metallic materials (see the publications reprinted in section 4.3 and 4.4 for further details on ENZ polaritons).

In general, the dielectric permittivity starts at a value $\mathrm{Re}\,(\varepsilon) > 1$ in the limit of zero frequency, and decreases for increasing frequency with each occurring resonance, such as phonon modes, plasmons and electronic transitions. At large enough frequencies, where there are no more optical resonances, $\mathrm{Re}\,(\varepsilon) = 1$, meaning that any material at large frequencies behaves equal to vacuum.

The Drude model describes the optical response of free electrons in a metallic material, and ω_p is the resonance frequency of the plasmon, that is, a collective, coherent oscillation of all electrons. For higher frequencies than the plasma frequency, however, any metal or semiconductor features more resonances, such as electronic transitions from core levels. These resonances lead to a quasi-static contribution to the dielectric permittivity at lower frequencies, i.e. in the range of the plasma frequency. In order to account for this contribution, the parameter ε_∞ is introduced, yielding the following dielectric permittivity of the Drude model:

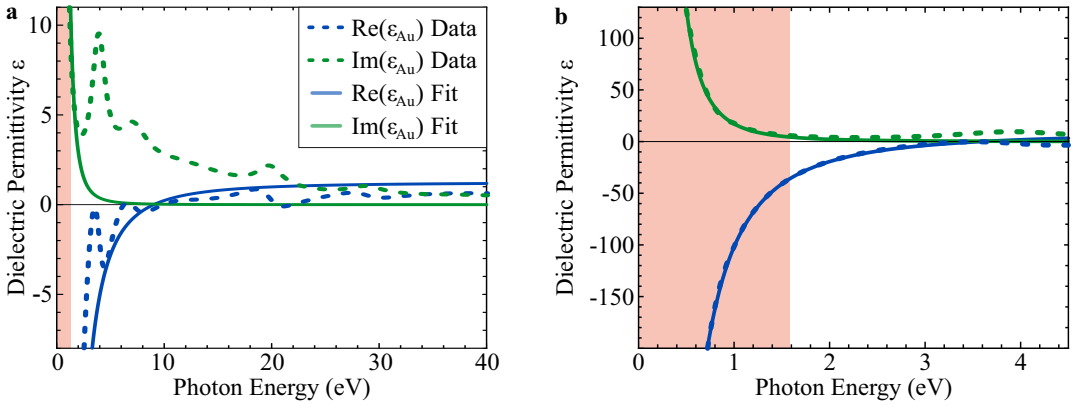

Figure 2.1.1: Drude model of the dielectric permittivity for gold. a The experimentally obtained dielectric permittivity of gold (Au) [37] is plotted as dashed lines, exhibiting various features in the shown frequency range. The Drude model fitted to the experimental data (solid lines) fails to reproduce most features, except for the IR frequency range (red shaded regions). **b** The same experimental data is fitted only in the IR, achieving good agreement. Thus, for nanophotonic studies in the IR, as they are performed in this thesis, the Drude model is a valid approximation for the optical response of Au.

$$\varepsilon(\omega) = \varepsilon_\infty \left(1 - \frac{\omega_p^2}{\omega^2 - i\omega\gamma}\right). \tag{2.1.8}$$

This model is adequate for all metallic materials, where the plasmon resonance dominates the optical response. This is, for example, the case for certain doped semiconductors [38], two-dimensional (2D) electron gases in quantum wells [39], or heavy-fermion metals [40]. In particular, in a recent publication (reprinted in section 4.6), the Drude model was successfully employed to describe the anisotropic optical response of a doped semiconductor multi-quantum well supporting intersuband polaritons [**VII**].

Other materials, such as Au or silver, on the other hand, feature various additional resonances in close proximity to the plasma frequency, and thus in this spectral range, the Drude model is not very accurate. In Fig. 2.1.1, the measured dielectric permittivity of Au is plotted as dashed lines, and the Drude model (Eq. 2.1.8) is fitted to the experimental data (solid lines). Clearly, the Drude model fails to describe the optical response in the mayor part of the plotted spectral range (Fig. 2.1.1a). However, the IR spectral range ($\lambda = 50\,\mu\text{m} - 780\,\text{nm}$, marked by a red shade in Fig. 2.1.1) is the frequency region where phonon polaritons, intersubband polaritons and semiconductor plasmon polaritons are located, and in this region, the Drude model achieves good agreement with the experimental data (Fig. 2.1.1b). Therefore, in the IR, where most investigations in this thesis are performed, the Drude model is an applicable and practical approximation even for Au.

2.1.2 Lorentz Model

After Drude had developed his model of free electrons, the Dutch physicist Lorentz extended the Drude model in order to describe electrons bound to an atom by adding a restorative force term. The corresponding equation of motion of the electrons in a harmonic potential driven by an external electric field is:

$$m\ddot{\vec{u}} + m\gamma\dot{\vec{u}} + m\omega_0^2\vec{u} = q\vec{E}, \tag{2.1.9}$$

where ω_0 is the resonance frequency of the particle in the harmonic potential. Analogous to the Drude model, the solution of this equation is

$$\vec{u} = \frac{q\vec{E}}{m\left(\omega_0^2 - \omega^2 + i\omega\gamma\right)}, \tag{2.1.10}$$

and the dielectric permittivity can be formulated as

$$\varepsilon(\omega) = \varepsilon_\infty + \frac{Nq^2}{\epsilon_0 m}\frac{1}{\omega_0^2 - \omega^2 + i\omega\gamma}. \tag{2.1.11}$$

Even though originally conceived for bound electrons, the Lorentz model can be applied to any charged particle in a harmonic potential, and thus also allows to describe the optical response of lattice atoms in a crystal. A crystal with $N_{u.c.}$ atoms in the primitive unit cell has 3 acoustic and $3N_{u.c.} - 3$ optical modes. For the long-wavelength limit, that is, at the Brillouin zone center, in optical phonons, the atoms describe an out of phase movement with specific periodicity. In the case of polar crystals, where at least two atoms with different partial charge are present, the optical phonons create a time-varying dipole, which can couple to light.

Depending on the vibration direction with respect to the propagation direction, a distinction is made between longitudinal optical (LO) and transverse optical (TO) modes. In polar crystals such as SiC, aluminium nitride (AlN) or gallium nitride (GaN), a gap between the two resonance frequencies ω_{TO} and ω_{LO} can be found at the zone center, which does not exist in non-polar crystals. This lifting of the degeneracy between the optical branches arises due to the macroscopic polarization of the LO mode, leading to a higher LO frequency than the TO frequency [41]. The region between both frequencies is called the reststrahlen (*German for residual rays*) band.

However, due to the orthogonality between propagation direction and polarization of light, only the TO mode is IR active, while the LO mode (propagation direction and polarization are parallel) cannot be excited. Thus, in polar crystals, the resonance frequency in Eq. 2.1.9 and 2.1.11 is the frequency of the TO phonon, $\omega_0 = \omega_{\mathrm{TO}}$.

Solving Eq. 2.1.11 at ω_{LO}, where $\varepsilon(\omega_{\mathrm{LO}}) = 0$ [42], yields for the dielectric permittivity of a polar crystal:

$$\varepsilon(\omega) = \varepsilon_\infty \frac{\omega^2 - \omega_{\mathrm{LO}}^2 - i\gamma\omega}{\omega^2 - \omega_{\mathrm{TO}}^2 - i\gamma\omega}. \tag{2.1.12}$$

This model is used to describe the optical response of all polar crystals investigated in this thesis. In Fig. 2.1.2, the principle dielectric permittivities of SiC, AlN, and GaN are plotted, which are the three

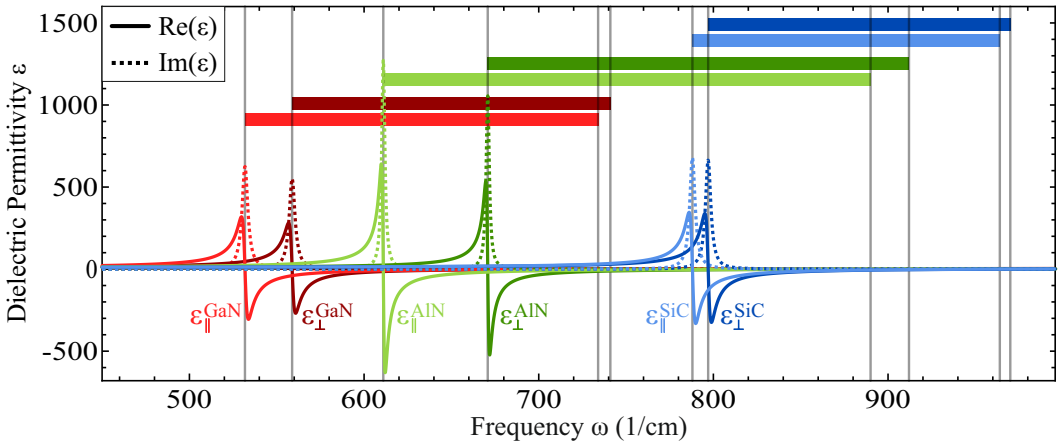

Figure 2.1.2: Lorentz model of the dielectric permittivity for 6H-SiC, AlN, and GaN. The material parameters are given in table 2.1.1. All three materials are uniaxial crystals, featuring different ordinary ($\perp$) and extraordinary ($\parallel$) principle dielectric permittivities. The reststrahlen bands, where the real part of ε is negative, are highlighted with horizontal color bars, delimited by the respective TO and LO frequencies ω_{TO} and ω_{LO}.

polar crystals that are most predominantly employed. At the TO frequency, the resonance in each material is apparent as a peak in the imaginary part of ε (dashed lines). The real part (solid lines), on the other hand, is negative in the reststrahlen band (marked by horizontal bars in Fig. 2.1.2), crossing zero at both the TO and LO frequency.

For anisotropic materials, the principle dielectric permittivities $\bar{\varepsilon}_{ii}$ differ (Eq. 2.1.2) and thus, each $\bar{\varepsilon}_{ii}$ is defined by Eq. 2.1.12 with a unique set of material parameters. 6H-SiC, AlN, and GaN are uniaxial crystals, featuring one extraordinary crystal axis ($\parallel$) along which the dielectric permittivity is different than along the two ordinary axes ($\perp$). Crystals where the extraordinary axis is orthogonal to the surface plane are called c-cut. In Fig. 2.1.2, the respective ordinary and extraordinary permittivities ($\varepsilon_{\parallel}$ and $\varepsilon_{\perp}$) of all three crystals are shown. A summary of the material parameters is given in table 2.1.1.

Table 2.1.1: Material parameters of uniaxial 6H-SiC, AlN, and GaN. Parameters employed to model the dielectric permittivity of 6H-SiC, AlN, and GaN in all publications that were written in the course of this thesis (reprinted in chapter 4).

Parameter	6H-SiC [43]	AlN [44]	GaN [44]
$\omega_{\mathrm{TO}}^{\parallel}$	788 cm^{-1}	611 cm^{-1}	531.8 cm^{-1}
$\omega_{\mathrm{TO}}^{\perp}$	797 cm^{-1}	670.8 cm^{-1}	558.8 cm^{-1}
$\omega_{\mathrm{LO}}^{\parallel}$	964 cm^{-1}	890 cm^{-1}*	734 cm^{-1}
$\omega_{\mathrm{LO}}^{\perp}$	970 cm^{-1}	912 cm^{-1}	741 cm^{-1}
γ	3.75 cm^{-1}	2.2 cm^{-1}	4 cm^{-1}
$\varepsilon_{\infty}^{\parallel}$	6.78	5.35	$\varepsilon_{\infty}^{\parallel}$= 4.35
$\varepsilon_{\infty}^{\perp}$	6.56	5.35	$\varepsilon_{\infty}^{\perp}$= 4.16

*Note that in contrast to the here reported literature value, fitting of experimental data has yielded a value of 900 cm^{-1}, which is used throughout the thesis and in all publications.

Some materials, such as doped semiconductors, feature both free electrons and IR-active phonons. In that case, the optical response can be described by a combined Drude-Lorentz model with the dielectric permittivity taking the form

$$\varepsilon(\omega) = \varepsilon_\infty \left(1 - \frac{\omega_p^2}{\omega^2 - i\omega\gamma_e} + \frac{\omega^2 - \omega_{\mathrm{LO}}^2 - i\gamma_p\omega}{\omega^2 - \omega_{\mathrm{TO}}^2 - i\gamma_p\omega}\right), \tag{2.1.13}$$

where γ_e and γ_p are the electron and the phonon damping, respectively.

Analogous to metals supporting SPPs below the plasma frequency, polar crystals support SPhPs modes in the reststrahlen band, where Re (ε) is negative. The following section discusses phonon polaritons in polar crystals, describing the different types of polariton modes that arise in dielectric heterostructures, as investigated in the scientific articles published in the course of this thesis (reprinted in chapter 4).

2.2 Phonon Polaritons

Phonon polaritons are excitations that arise under light-matter interaction with phonons in the strong-coupling limit, yielding hybridized modes with both phononic and electromagnetic characteristics. The simplest phonon polariton is the bulk phonon polariton (BPhP), which emerges when light travels through a bulk polar crystal at frequencies in proximity to the ω_{TO} resonance frequency. As originally observed by Tolpygo [20], around the reststrahlen band, the light dispersion splits up into two branches, featuring an avoided crossing (see Fig. 2.2.1, blue lines). The dispersion relation of the BPhP is obtained by plugging the permittivity of a polar crystal (Eq. 2.1.11) into the light dispersion of a plane wave [26]:

$$k_{\mathrm{BPhP}} = \frac{\omega}{c}\varepsilon = \frac{\omega}{c}\varepsilon_\infty \frac{\omega^2 - \omega_{\mathrm{LO}}^2 - i\gamma\omega}{\omega^2 - \omega_{\mathrm{TO}}^2 - i\gamma\omega}. \tag{2.2.1}$$

Besides the solution of plane waves traveling through a bulk material, at interfaces of materials with different dielectric permittivity, Maxwell's equations yield the solution of a surface wave, the so called *surface polariton*. Here, the matter excitation that couples to the light is a surface electric dipole wave with resonance frequency ω_{S}, where the associated electric field strength decays exponentially with increasing distance to the interface [45].

Depending on the charged particles that form the surface electric dipole wave, different types of surface polaritons arise, such as the surface plasmon polariton (SPP) for free electrons, or the surface phonon polariton (SPhP) for lattice ions. In the following, without loss of generality for other types of surface polaritons, the dispersion of a SPhP will be derived. The second part of this section discusses polaritons in layered systems of more than one interface and material, summarizing the polaritonic modes investigated in this thesis, such as thin-film modes, the Berreman mode, volume-confined hyperbolic polaritons, and polariton-like waveguide modes.

2.2.1 Dispersion Relation of a Surface Phonon Polariton

The simplest system supporting a surface phonon polariton is a single interface of an isotropic polar crystal adjacent to a dielectric material of constant positive dielectric permittivity. The interface between the polar crystal (material P) and the adjacent dielectric (material D), described by the dielectric permittivities ε_P and ε_D, is defined to be the x-y-plane at $z = 0$, where the polar crystal extends into $z < 0$, and the dielectric material into the opposite half-space ($z > 0$).

The surface wave satisfying Maxwell's equations is chosen to propagate along the x-direction, with its electric fields pointing in the x-z-plane (transverse magnetic), yielding the following explicit form:

$$\vec{E} = \vec{E}_0^{\mathrm{D,P}}\, e^{i\left(\omega t - k_x x \pm k_z^{\mathrm{D,P}} z\right)}, \tag{2.2.2}$$

where the superscripts D and P stand for the dielectric ($z > 0$) and the polar crystal ($z < 0$), and the $\pm$ sign is to be read such that the top sign corresponds to the $z > 0$ half-space, and the bottom sign to $z < 0$. The in-plane momentum k_x is conserved at the interface, which is why it is defined material-independently. Plugging this surface wave into the three-dimensional wave equation $\Delta\vec{E} = \frac{\varepsilon^{\mathrm{D,P}}}{c^2}\ddot{\vec{E}}$

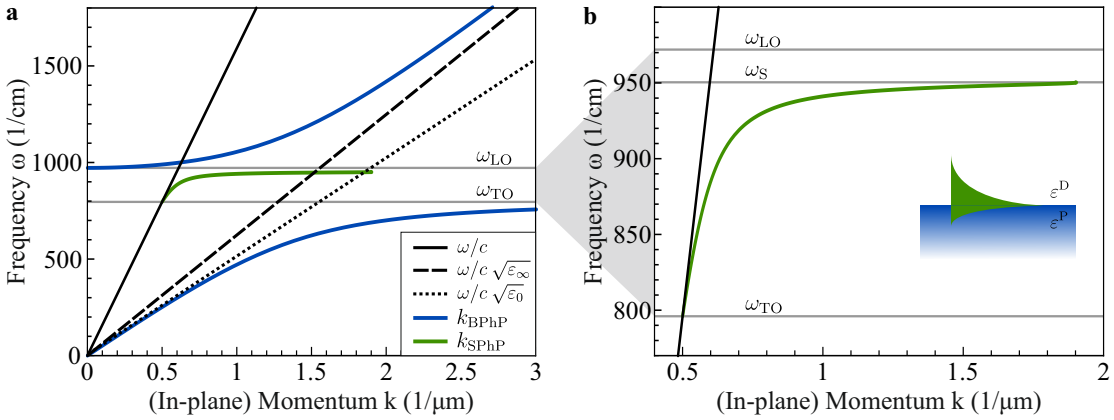

Figure 2.2.1: Dispersion relations of BPhPs and SPhPs Light traveling in a material of constant epsilon features a linear dispersion, such as the light line in vacuum (black solid line). The dashed and dotted black lines represent the limits for large and small frequencies, respectively, of the dispersion of light in a polar crystal (blue line). At frequencies in proximity to the reststrahlen band, the BPhP arises, featuring an avoided crossing. Inside the reststrahlen band, the SPhP is supported at the surface of the polar crystal, ranging from ω_{TO} up to the cut-off frequency ω_S (shown in b). The modes are exemplified for a SiC crystal. Note that the BPhP has a momentum that points along the propagation direction through the bulk crystal, and hence the absolute value is plotted, while the SPhP is plotted along its in-plane momentum, because it only propagates along the crystal surface. The inset in b sketches the exponentially decaying electric field of a SPhP propagating along the surface of a polar crystal of dielectric permittivity ε^P adjacent to a dielectric material with permittivity ε^D.

leads to an expression for the out-of-plane momentum k_z:

$$k_z^{D,P} = \sqrt{\frac{\omega^2}{c^2}\varepsilon^{D,P} - k_x^2}. \tag{2.2.3}$$

In order to get an actual surface wave, however, the $\vec{E}$-field should vanish with increasing distance to $z = 0$. This is only achieved for complex $k_z^{D,P}$, because then the z part in the exponent of Eq. 2.2.2 becomes real and leads to an exponential decay in both z directions:

$$\vec{E} = \vec{E}_0^{D,P}\, e^{i(\omega t - k_x x)}\, e^{\mp \kappa^{D,P} z}, \tag{2.2.4}$$

where

$$\kappa^{D,P} \equiv i k_z^{D,P} \tag{2.2.5}$$

is required to be real and positive.

From Maxwell's equations, the following equation for a p-polarized plane wave can be derived [42]:

$$\frac{\partial^2 E_x}{\partial z^2} + \frac{\omega^2}{c^2}\varepsilon E_x - \frac{\partial^2 E_z}{\partial x \partial z} = 0. \tag{2.2.6}$$

When Eq. 2.2.4 is plugged into this equation, the following relation between the field components is obtained:

$$E_{0z}^{D,P} = \mp i \frac{k_x}{\kappa^{D,P}} E_{0x}^{D,P}, \tag{2.2.7}$$

and applying Maxwell's boundary conditions for the displacement $\vec{D}$ ($\varepsilon^{\mathrm{D}} E^{\mathrm{D}}_{0z} = \varepsilon^{\mathrm{P}} E^{\mathrm{P}}_{0z}$) and the electric field $\vec{E}$ ($E^{\mathrm{D}}_{0x} = E^{\mathrm{P}}_{0x}$) yields:

$$\frac{\kappa^{\mathrm{D}}}{\varepsilon^{\mathrm{D}}} = -\frac{\kappa^{\mathrm{P}}}{\varepsilon^{\mathrm{P}}}. \tag{2.2.8}$$

κ^{D}, κ^{P} and ε^{D} are positive by definition. This leads to the condition that in order to support a SPhP, ε^{P} has to be negative. A polar crystal fulfills this requirement in the reststrahlen band between ω_{TO} and ω_{LO}. However, it can be shown that the exact condition reads $\varepsilon^{\mathrm{P}} < -\varepsilon^{\mathrm{D}}$ [42], which leads to a reduced upper frequency limit $\omega_{\mathrm{S}} < \omega_{\mathrm{LO}}$. Substituting $\kappa^{\mathrm{D,P}}$ (Eq. 2.2.5) into equation 2.2.8 finally gives the dispersion relation for a SPhP:

$$k_x = k_{\mathrm{SPhP}} = \frac{\omega}{c}\sqrt{\frac{\varepsilon^{\mathrm{D}}\varepsilon^{\mathrm{P}}}{\varepsilon^{\mathrm{D}} + \varepsilon^{\mathrm{P}}}}. \tag{2.2.9}$$

Note that the derivation is independent on the supporting material. Therefore, Eq. 2.2.9 is not only valid for SPhPs, but holds for any type of surface polariton, for example the SPP supported on metals or doped semiconductors. In Fig. 2.2.1, the SPhP dispersion is plotted together with the dispersion relation for bulk phonon polaritons.

2.2.2 Phonon Polariton Modes in Layered Heterostructures

Recent advances in the field of nanophotonics have shown that SPhPs offer great potential for technological applications, such as super-resolution imaging [16, 46, 47], highly efficient sensing [48], or enhanced nonlinear-optical conversion efficiency [49–51].

A single SPhP supported by the surface of a bulk polar crystal as derived in the previous section, however, possesses several limitations that hinder the application in nanophotonic technologies:

(i) SPhPs are only supported in the small frequency window of the reststrahlen band of the supporting polar crystal,

(ii) the dispersion relation is fixed by the material parameters, and thus the SPhP lacks active tunability,

(iii) the spatial confinement in lateral direction is only moderate, because SPhPs are accessible at wavelengths in the micrometer range, and the evanescent penetration depth scales with the wavelength,

(iv) the electric field enhancement of a SPhP only reaches moderate values of up to 10 [**I**], which is relatively low compared to the field enhancements achieved in some plasmonic nanostructures [52–54], and

(v) SPhPs are only excitable by p-polarized light, limiting the versatility of polariton-based nanophotonics.

In the course of this thesis, all these limitations of SPhPs on bulk crystals have been approached and treated. The key tool to overcome these restrictions has been the employment of layered heterostructures, built from various different polar crystals, metals, and dielectric materials. This section provides an overview over the investigated layered systems (visualized in Fig. 2.2.2), the arising polariton modes, and their advantageous properties, referencing the published article where the respective system is discussed in detail.

Additionally to the experimental studies, in this thesis a theoretical framework has been developed that allows to calculate the optical response of a multilayer structure of arbitrarily anisotropic materials, including the layer-resolved absorption, transmittance, and electric field distribution. This framework has been used for all simulations of the investigated samples, and is described in detail in two published articles [**II**, **VII**] (reprinted on pages 45 and 97). For the simulations in this section, the same framework is employed.

Thin-Film Polaritons One approach to modify the bulk SPhP (sketched in Fig. 2.2.2a) is to reduce the film thickness d of the sample. For thicknesses in the range of the penetration depth of the bulk SPhP (for polar crystals such as SiC and AlN, this is the case for $d \lesssim 1\,\mu\mathrm{m}$ [**V**]), an interaction between the two interfaces arises, resulting in two *thin-film polaritons (TFPs)* (sketched in Fig. 2.2.2b). In terms of the dispersion, the single bulk SPhP dispersion (gray line in Fig. 2.2.2c for AlN) splits up into the symmetric and antisymmetric TFP branch (green lines), where the splitting increases for decreasing film thickness. Thus, the film thickness acts as a tuning parameter for modifying the polariton dispersion.

The dispersion of polaritons in a three-layer system can be determined by numerical evaluation of the following equation [55–57]:

$$1 + \frac{\varepsilon_1 k_{z3}}{\varepsilon_3 k_{z1}} = i \tan\left(k_{z2} d\right) \left(\frac{\varepsilon_2 k_{z3}}{\varepsilon_3 k_{z2}} + \frac{\varepsilon_1 k_{z2}}{\varepsilon_2 k_{z1}} \right), \tag{2.2.10}$$

where the indexes 1-3 refer to the three layers, and the out-of-plane momenta k_z are given by Eq. 2.2.3. The dispersions shown in Fig. 2.2.2c,e have been calculated using Eq. 2.2.10.

ENZ Polaritons In the limit of ultra-thin films ($d < \lambda/100$, with λ being the free-space wavelength) [57], the symmetric TFP dispersion is pushed completely against the LO phonon frequency, where the dielectric permittivity crosses zero (Fig. 2.2.2c). Therefore, this TFP is called an *epsilon-near-zero (ENZ) polariton*, featuring intriguing properties such as ultra-long wavelengths and immense field enhancements compared to the bulk SPhP (see the publication reprinted on page 65 [**IV**] for further details on ENZ polaritons).

Berreman Modes Most phonon polaritons have in-plane momenta larger than light in vacuum (black line in Fig. 2.2.2c), resulting in an evanescent mode that is guided at the interface without radiating into the far-field. An exception is the *Berreman mode*, which arises in ultra-thin films on the left side of the light line, and therefore can be probed via free-space excitation. Similar to the symmetric TFP, the dispersion of the Berreman mode in a polar crystal (red lines in Fig. 2.2.2c) lies in close proximity to the LO phonon frequency, and thus features ENZ characteristics such as an

immense out-of-plane field enhancement (see the publication reprinted on page 75 [**V**] for further details on Berreman modes).

Strongly Coupled Polaritons Polaritons are by definition modes arising due to the strong coupling of light with matter. Interestingly, polaritons can again couple strongly with other polaritons, forming new hybrid polaritons with shared characteristics of the uncoupled modes.

A system where such a strong coupling can be observed is an ultra-thin AlN film on a SiC substrate, as sketched in Fig. 2.2.2d, where the modes that couple are the SiC substrate SPhP (blue dispersion line in Fig. 2.2.2e) and the ENZ TFP of the AlN film (green dispersion line). Together, these modes form two new hybridized *strongly coupled polaritons* with an avoided crossing of the two dispersion branches (red lines), combining the properties of the uncoupled modes (see the publication reprinted on page 65 [**IV**] for further details on strongly coupled polaritons in layered heterostructures).

Notably, as an alternative to layered heterostructures, three-dimensional (3D) nanostructures can also support strongly coupled polaritons. This has been demonstrated for SiC nanopillars on a SiC substrate, where the phonon polariton resonances localized in the nanopillars strongly couple to the SPhPs propagating on the substrate (see publication [**VIII**] for further details).

Actively Tunable, Refractive Index-Shifted Polaritons The SPhP dispersion depends on the dielectric permittivity of the supporting crystal ε^{P} and of the adjacent medium ε^{D} (or, equivalently, the refractive index $n = \sqrt{\varepsilon}$). Changing ε^{D} influences the SPhP, resulting in a frequency shift of the dispersion that can be exploited for sensing applications [48, 58–60].

A system that features *refractive index-shifted (n-shifted) polaritons* is depicted in Fig. 2.2.2f, where a thin $Ge_3Sb_2Te_6$ (GST) film is placed on a SiC substrate. In Fig. 2.2.2g, the dispersion of the bare SiC SPhP (blue solid line) and the n-shifted SPhPs (purple and red solid lines) are plotted. GST is a phase-change material (PCM) which can be switched reversibly between its crystalline (c-GST) and amorphous (a-GST) phase, and due to the refractive index contrast between the two phases, two different n-shifted SPhPs are supported. By electrically or optically switching the GST phase, the n-shifted SPhP dispersion can be *actively tuned*. (see the publication reprinted on page 85 [**VI**] for further details on actively tunable, n-shifted polaritons).

Polariton-Like Waveguide Modes In thin films of high refractive index embedded in media of lower n, standing waves are supported that cannot freely propagate in the adjacent media due to the refractive index contrast, forming so-called *waveguide modes (WMs)*. These modes can be either p- or s-polarized, and their dispersion is usually very steep compared to SPhPs. A thin GST film supports WMs, and when placed on a SiC substrate, the dispersion of the s-polarized WM is pushed upwards into the SiC reststrahlen band, resulting in a comparable dispersion as the SPhP (dashed lines in Fig. 2.2.2g). The dispersion of WMs is given by the following equation (specified for the GST/SiC heterostructure) [61]:

$$\frac{\omega}{c}\sqrt{\varepsilon_{\mathrm{GST}} - \hat{k}^2}\, d_{\mathrm{GST}} - \Phi_{\mathrm{SiC/GST}} - \Phi_{\mathrm{GST/air}} = m\pi, \tag{2.2.11}$$

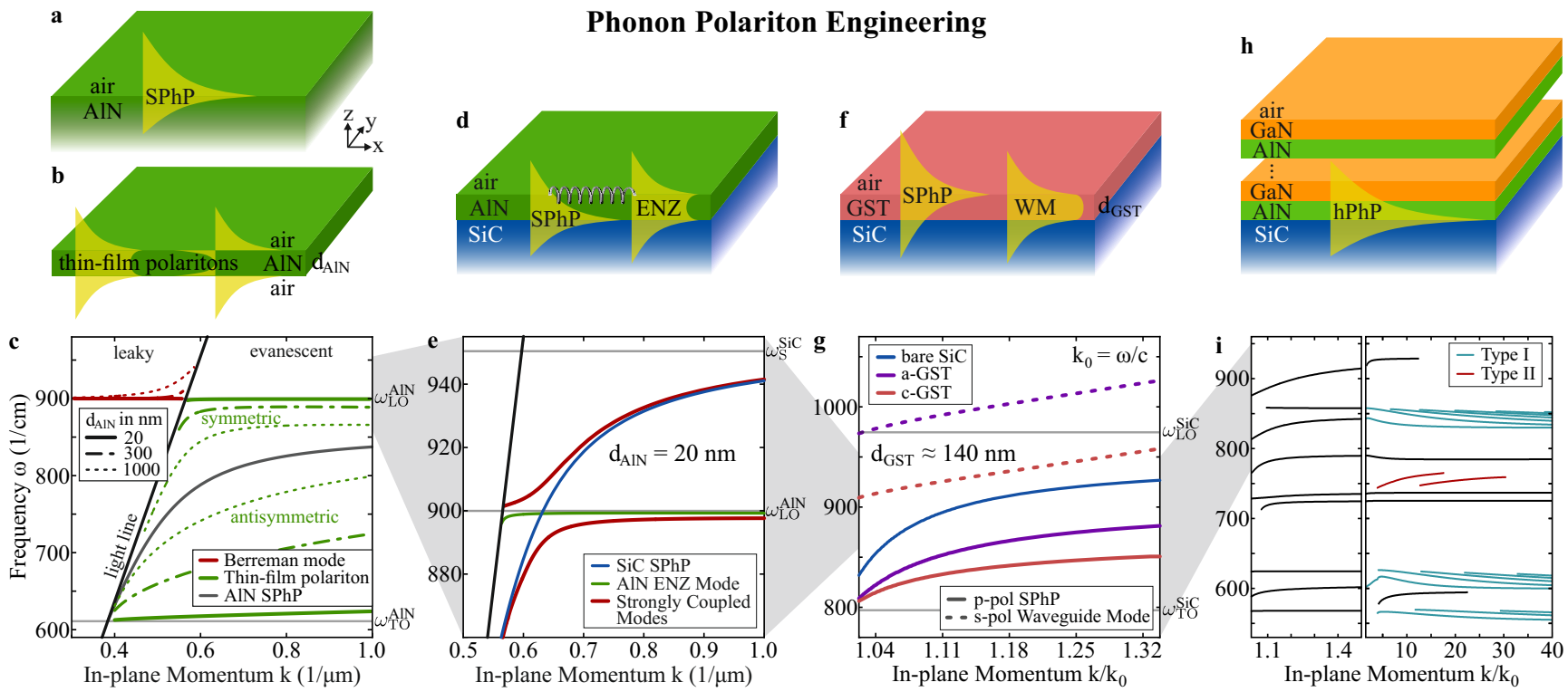

Figure 2.2.2: Phonon polariton engineering using polar dielectric heterostructures. **a** Sketch of a SPhP propagating on an AlN bulk crystal. The electric field strength is illustrated in yellow, evanescently decaying in z-direction into both media. **b** In a thin AlN film, two thin-film polaritons (TFPs) with symmetric and antisymmetric electric field distribution are supported. **c** Dispersion lines of leaky and evanescent phonon polaritons in bulk and thin-film AlN. On the right side of the light line, the bulk AlN SPhP (gray line) and the two TFPs disperse, whereas on the left side of the light line, the leaky Berreman mode arises. Both Berreman mode and the symmetric ultra-thin film polariton are epsilon-near-zero (ENZ) modes, dispersing in close proximity to $\omega_{\mathrm{LO}}^{\mathrm{AlN}}$. **d** Sketch of an AlN/SiC heterostructure, where the bulk SiC SPhP strongly couples to the ENZ TFP of the AlN thin film. **e** Dispersion of the strongly coupled polariton modes (red lines) featuring an avoided crossing. **f** Sketch of a heterostructure comprising a thin film of the reversibly switchable phase-change material GST on a SiC substrate. The system simultaneously supports p-polarized SPhPs and s-polarized waveguide modes (WMs), both being actively tunable by switching of the GST phase. **g** Dispersion lines of the SPhP (solid lines) and the WM (dashed lines) for amorphous (purple lines) and crystalline (red lines) GST. **h** Sketch of a crystalline hybrid (XH) comprising a polar dielectric superlattice of atomically thin AlN and GaN films on a SiC substrate, supporting volume-confined hyperbolic phonon polaritons (hPhPs) of type I and type II. **i** Dispersion lines of the phonon polariton modes arising in the XH. At large in-plane momenta, the typical mode progression of volume-confined hPhPs is observed (turquoise and red lines). Note that the dispersion lines in subfigures c and e were calculated using Eq. 2.2.10, yielding a momentum axis with absolute values. The dispersion lines in subfigures g and i, on the other hand, were obtained by transfer-matrix simulations (for details see the publication reprinted on page 45 [**II**]), and here, the momentum axis is plotted in relative values. The light line in subfigures g and i is a vertical line located at $k/k_0 = 1$.

where $\Phi_{\text{SiC/GST}}$ and $\Phi_{\text{GST/air}}$ are the phase differences upon reflection at the substrate/film (SiC/GST) and the film/incident medium (GST/air) interfaces, $\hat{k} \equiv k/k_0 = n_{\text{air}} \sin\theta$ is the in-plane momentum (with $k_0 = \omega/c$), and d_{GST} is the GST film thickness.

Strikingly, in the GST/SiC heterostructure, the distinctive properties of the polar crystal substrate modify the WM such that its spatial confinement and electric fields are enhanced, resulting in an s-polarized WM with polariton-like characteristics. Simultaneously supporting p-polarized SPhPs and s-polarized WMs, the GST/SiC system provides a versatile platform for actively tunable, omnipolarized nanophotonic applications (see the publication reprinted on page 85 [**VI**] for further details on polariton-like WMs).

Volume-Confined Hyperbolic Polaritons A hyperbolic material is a material that features frequency regions where one (type II) or two (type I) principle dielectric permittivities have a negative real part, while along the other axes, $\text{Re}\,(\varepsilon) > 0$. In those regions, hyperbolic phonon polaritons (hPhPs) can be observed [15]. Some materials are hyperbolic by nature, such as hexagonal boron nitride (hBN) or quartz (SiO_2), but alternatively, a hyperbolic material can be synthesized by periodically stacking thin layers of different media [62–64]. In Fig. 2.2.2h, such an artificial hyperbolic material is sketched, where multiple atomically thin layers of AlN and GaN thin films form a $\sim 650\,\text{nm}$ thick superlattice, also called crystalline hybrid (XH) [65].

In thin films of hyperbolic materials, such as the sketched XH, standing waves with discrete resonances are supported, giving rise to *volume-confined hPhPs* [16, 66, 67]. In Fig. 2.2.2i, the dispersion of all polaritons supported by the XH system is shown, featuring a rich variety of modes in the broad frequency range of $550 - 950\ \text{cm}^{-1}$. For large in-plane momenta, the volume-confined hPhPs of type I (turquoise lines) and type II (red lines) can be observed, featuring their characteristic higher-order mode progression [68] (see publication [**IX**] for further details on hPhPs).

In summary, in only four different material systems comprising different polar dielectric material slabs, a large variety of polariton modes arises, covering TFPs [**V**], Berreman modes [**V**], ENZ polaritons [**IV**], strong coupling [**IV**], refractive index-shifting [**VI**], WMs [**VI**] and volume-confined hPhPs [**IX**]. By studying these systems it is demonstrated that tailoring the material system allows to overcome the limitations of a bulk SPhP for nanophotonic applications: phonon polaritons can be actively tuned, their frequency window broadened, their spatial confinement and electric fields dramatically enhanced, and the polarization bottleneck of SPhPs circumvented by employing s-polarized, polariton-like WMs.

This thesis provides a broad overview over phonon polariton modes arising in layered heterostructures. In principle, the same physics can be observed in systems of 3D structure, as is exemplified for subdiffractional nanostructures in publication [**VIII**]. However, 3D structures entail a significantly higher level of complexity, rendering the unambiguous assignment and prediction of polariton modes a formidable task. By focusing on well-defined systems consisting of layered media, this thesis provides a thorough and robust benchmark of the physics of phonon polaritons in anisotropic heterostructures.

2.3 Polariton-Enhanced Nonlinear Optical Response

When light is compressed into sub-wavelength length scales, the local electric field can be immensely enhanced compared to a freely propagating wave. Such a field enhancement naturally occurs for polaritons, and can reach immense values when the modes experience additional spatial confinement in nanoscale structures, as it is the case for TFPs or volume-confined hPhPs. These field enhancements can be experimentally probed by measuring the nonlinear optical response.

In this thesis, second harmonic generation (SHG), a second-order nonlinear optical effect, is employed for the experimental investigation of the field enhancements of various phonon polaritons in layered heterostructures. Therefore, in the first part, this section provides a brief introduction to SHG. In the second part, the calculated field enhancement of the studied phonon polaritons and the resulting experimental SHG yield is discussed. The theoretical calculations of the optical field enhancements were performed employing the 4×4 transfer matrix formalism developed in the course of this thesis (for details see the publication reprinted on page 45 [**II**]).

2.3.1 Second Harmonic Generation (SHG)

The optical response of a material, that is, the created polarization $\vec{P}$ under an external electric field $\vec{E}$, is approximately linear, as long as the incident intensity is weak enough (Eq. 2.1.1). For stronger incident fields, however, every material exhibits a nonlinear response, which is the driving principle of nonlinear optics. The electric polarization $\vec{P}$ is then a complicated function of $\vec{E}$, and cannot be written down analytically any more. This is the origin of many nonlinear optical effects like SHG, sum frequency generation, difference frequency generation, or electro-optical rectification – all of them second-order effects – and many others of higher order.

In the special case of plane waves and in the electric dipole approximation, the electric polarization $\vec{P}$ can be expanded in a power series of $\vec{E}$ [69]:

$$\begin{aligned}\vec{P}(\omega) = &\chi^{(1)}(\omega) \cdot \vec{E}(\omega) \\ &+ \chi^{(2)}(\omega_3 = \pm\omega_1 \pm \omega_2) : \vec{E}(\omega_1)\vec{E}(\omega_2) \\ &+ \dots ,\end{aligned} \tag{2.3.1}$$

where $\chi = 1 - \varepsilon$ is the electric susceptibility, describing the optical response of a material under the influence of an external electric field $\vec{E}$. The nth coefficient $\chi^{(n)}$ of χ is a tensor of rank $(n+1)$ and, in principle, allows to describe any nonlinear optical response of the material of any nth order. In practice, however, exact solutions of χ are not feasible even for the most simple systems, which makes nonlinear optics a timely, thriving field of research.

In a very simple picture, the effect of SHG can be understood in terms of an energy diagram as a three-level process, which is depicted in Fig. 2.3.1a. Two incident photons at energy $\hbar\omega_{\text{FEL}}$ from the incident light source, in this work a FEL, are needed in order to excite a system from the ground state $|0\rangle$ to the state $|2\rangle$, through the intermediate state $|1\rangle$, which lies at half the energy difference between $|0\rangle$ and $|2\rangle$. The energy from $|2\rangle$ is then emitted as a photon at double frequency $\omega_{\text{SHG}} = 2\omega_{\text{FEL}}$, constituting the SHG signal. The measured SHG intensity I_{SHG} is, most generally, given by

$$I_{\text{SHG}} \propto |\chi^{(2)}(2\omega = \omega + \omega)\vec{E}(\omega)^2|^2, \tag{2.3.2}$$

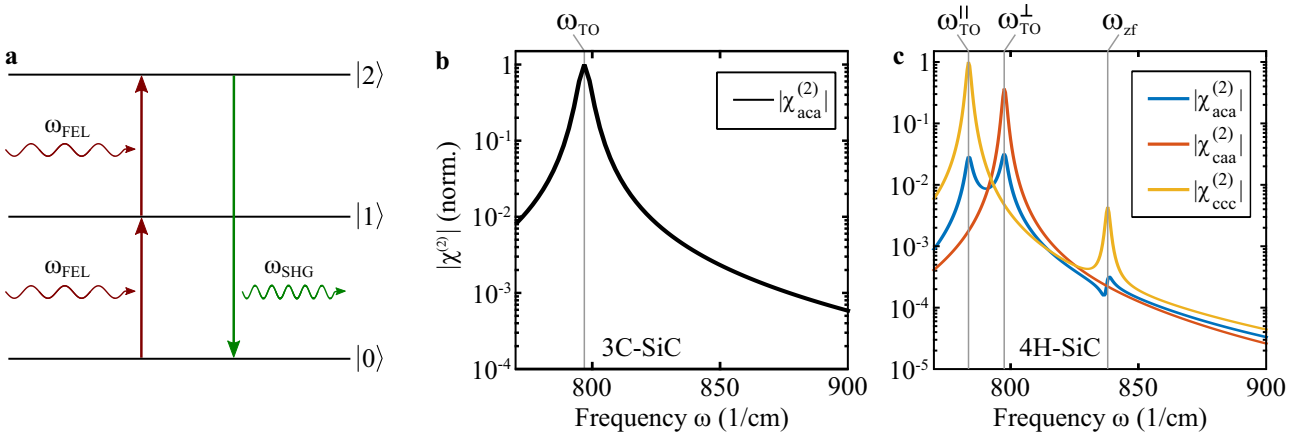

Figure 2.3.1: Second harmonic generation and the second-order susceptibility of SiC. a Energy diagram with three states, visualizing the process of SHG, where two incident photons at same frequency ω_{FEL} are converted into the SH photon with double frequency ω_{SHG}. Within the electric dipole approximation, this process occurs only in materials with broken inversion symmetry. In general, $|1\rangle$ and $|2\rangle$ can be virtual energy levels. If the material exhibits a resonance at incident frequency, however, these states are real, and the process is called resonant SHG. **b** and **c** Dispersion of the non-zero $\chi^{(2)}$ elements in 3C-SiC and 4H-SiC, respectively. Additional to the resonances at the TO phonon frequencies, 4H-SiC features a resonance at the zone-folded (zf) phonon frequency, arising due to the supperlattice along the extraordinary crystal axis [70, 71]. $\chi^{(2)}$ dispersions are adapted from Ref. [70]

where $\chi^{(2)}$ is the second-order susceptibility tensor, which has in total 27 coefficients, and $\vec{E}^2$ is a symmetric tensor. Therefore, the resulting SHG signal can exhibit enhancements of two types: (i) originating from a $\chi^{(2)}$ resonance, and (ii) from a resonance in the local fields at the sample site. For the case of polar crystals, the $\chi^{(2)}$ dispersion only exhibits features at the IR-active phonon resonances such as the TO phonon (as an example, Fig. 2.3.1b and c show the relevant $\chi^{(2)}$ elements of 3C-SiC and 4H-SiC, respectively). On the other hand, phonon polaritons feature strong local field enhancements and therefore contribute significantly to the second harmonic (SH) signal via the $\vec{E}^2$ term, enabling polariton-enhanced SHG. In the following section, the field enhancement of the phonon polariton modes studied in this work is discussed in detail.

Regarding the SHG signal from the bulk, the $\chi^{(2)}$ coefficients depend on the crystal symmetry, and for the case of centrosymmetric materials (in the electric dipole approximation), they vanish completely (Tables for the non-vanishing coefficients can be found in several text books [69, 72]). At the surface of a crystal, inversion symmetry is broken. Hence, even though a material does not exhibit SHG from the bulk, it will produce a surface SHG signal, which can be employed as a very surface-sensitive probing method [73–75]. In a material with broken inversion symmetry, on the other hand, the surface signal is usually negligible [74], which is the case for all samples investigated in this work.

When the incident frequency ω_{FEL} coincides with a resonance in the probed material, resonant SHG can be observed [17, 73], accounting for a strong enhancement. While resonant enhancement of SHG from the bulk in non-centrosymmetric materials [17, 76, 77] as well as surface SHG from inversion symmetric media [73, 78, 79] has been studied intensively, the process of resonant SHG arising from phonon polaritons is mostly unexplored and a major component of this thesis. Notably, in that regard, also sum frequency generation (SFG) spectroscopy and microscopy has recently emerged as a complementary tool [80].

Here, by investigating the SH response of bulk SPhPs (reprinted on page 4.1 [**I**]), strongly coupled phonon polaritons [**VIII**], and Berreman modes (reprinted on page 4.4 [**V**]), this thesis provides thorough experimental evidence of the nonlinear optical response of phonon polaritons in polar dielectric heterostructures. In the following section, the field enhancements of the phonon polaritons responsible for the observed SH signals are discussed.

2.3.2 Field Enhancement of Phonon Polaritons Probed with SHG

The strong confinement of light as it occurs for phonon polaritons in nanoscale structures leads to enhanced light-matter interaction, enabling nanophotonic applications such as highly efficient sensing [7, 81], all-optical switching [6, 82], and low-loss frequency conversion [83, 84]. Here, SHG spectroscopy [17] is employed as experimental method to probe the field enhancement of phonon polaritons, while the transfer matrix formalism (see page 45 [**II**]) is employed as theoretical tool for calculating the field enhancement in layered media responsible for the SHG yield. In the following, the field enhancement and the obtained SH yield of three systems are discussed, comprising a bare SiC crystal, a thin-film AlN/SiC heterostructure, and SiC nanopillars on a SiC substrate.

SiC SPhP The SHG yield of evanescent SPhPs can be probed in the so-called Otto geometry (for details see chapter 3). In Fig. 2.3.2a, the experimental SHG spectrum from a SPhP propagating on a bare SiC crystal obtained in the Otto geometry is shown. The spectrum features a strong, sharp peak at the SPhP resonance frequency (~ 910 cm^{-1}) that originates in the field enhancement associated with the SPhP.

Fig. 2.3.2b plots the calculated electric field distribution of the SiC SPhP as a function of z-position, that is, along the direction normal to the surface, and the incident frequency ω. Here, the in-plane component of the electric field $\vec{E}_x$ is shown, clearly featuring a peak at the SPhP resonance frequency, localized at the air/SiC interface. These enhanced electric fields give rise to the observed peak in the SHG spectrum. The out-of-plane component $\vec{E}_z$ (not shown here) features a similar enhancement in air [**I**], while inside SiC, $\vec{E}_z$ is slightly suppressed [56] (for more details on the SHG from the SiC SPhP see the publication reprinted on page 37 [**I**]).

AlN/SiC Berreman Mode As has been discussed in section 2.2.2, a AlN/SiC heterostructure supports a leaky Berreman mode dispersing at in-plane momenta smaller than light in vacuum, and strongly coupled phonon polaritons arise on the evanescent side of the light line. In Fig. 2.3.2c, an SHG spectrum of the AlN/SiC system is shown, which was obtained under free-space excitation in order to probe the leaky Berreman mode. The SHG spectrum features a pronounced peak at the Berreman mode resonance frequency (~ 900 cm^{-1}), arising from the field enhancement associated with the Berreman mode. As is shown in Fig. 2.3.2d, the out-of-plane electric field features an extreme spatial confinement localized in the thin AlN film and reaching immense enhancement values of > 40. Interestingly, the in-plane fields $\vec{E}_x$ (not shown here) are featureless at the Berreman resonance frequency [**V**]. Hence, the out-of-plane fields are the sole origin of the enhanced SH signal, observable as a peak in the SHG spectrum.

Note that the SHG peak of the Berreman mode lies in the wing of the SH signal at the SiC LO phonon frequency [70]. The two SH signals interfere constructively and destructively depending on the frequency, resulting in the asymmetric peak shape of the Berreman mode SHG (for more details

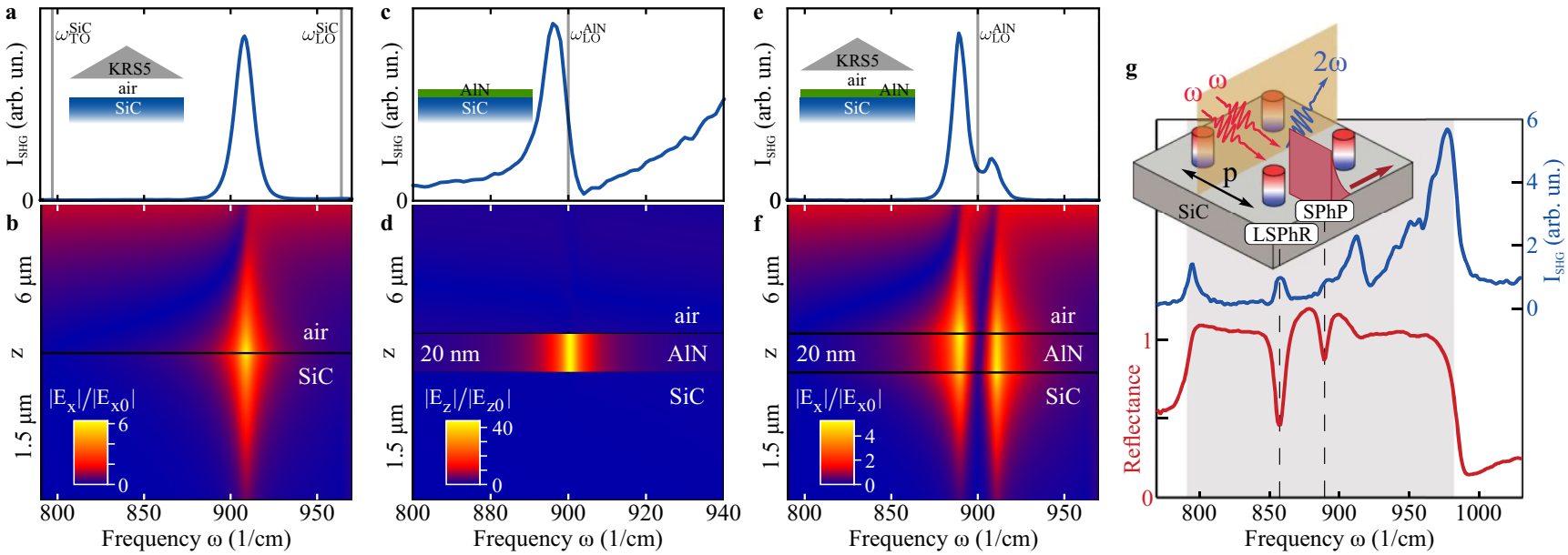

Figure 2.3.2: Field enhancement of phonon polaritons probed with SHG spectroscopy. **a** SHG spectrum of the reststrahlen band of bare SiC measured in the Otto geometry (see section 3.2 for details) at an incident angle of $\theta \approx 30\,^{\circ}$, featuring a resonance peak at the frequency of the SPhP [**I**]. **b** In-plane electric field distribution along the z-direction of the SiC SPhP at the air/SiC interface. At the SPhP resonance frequency, the local electric field is enhanced, reaching a maximum value of ~ 6 at the interface. This field enhancement is the origin of the measured peak in the SHG spectrum. **c** SHG spectrum under free-space excitation of an AlN/SiC heterostructure at $\theta \approx 60\,^{\circ}$, featuring a resonance peak at the frequency of the Berreman mode [**V**]. **d** Out-of-plane electric field distribution of the Berreman mode in the multilayer system. At the Berreman resonance frequency in close proximity to $\omega_{\mathrm{LO}}^{\mathrm{AlN}}$, the local electric field features an immense enhancement of up to ~ 40, strongly localized in the AlN thin film. This field enhancement gives rise to the enhanced SHG signal shown in c. **e** SHG spectrum of the same AlN/SiC heterostructure as in c, measured in the Otto geometry at $\theta \approx 29\,^{\circ}$. In the Otto geometry, the evanescently bound, strongly coupled phonon polaritons can be excited [**IV**], yielding two resonance peaks in proximity to $\omega_{\mathrm{LO}}^{\mathrm{AlN}}$ [42]. **f** In-plane electric field distribution of the strongly coupled phonon polaritons, featuring two peaks in the field enhancement at the resonance frequencies of the two modes bound to the AlN layer, originating the measured SHG peaks. **g** Reflectance and SHG spectrum of SiC nanopillars on a SiC substrate. The localized surface phonon resonance (LSPhR) of the nanopillars couples to the propagating SPhP, yielding two resonance dips in the reflectance, and two peaks in the SHG spectrum [**VIII**]. In both strongly coupled systems, the SHG yield of the two coupled modes is subject to a phase modulation induced by the background contribution of the SiC substrate. Figure adapted from publication [**VIII**].

on the field enhancement and SH yield of the Berreman mode see the publication reprinted on page 75 [**V**]).

AlN/SiC Strongly Coupled Phonon Polaritons When probing the AlN/SiC heterostructure in the Otto geometry, the strongly coupled phonon polaritons discussed in section 2.2.2 can be excited. An SHG spectrum obtained for this configuration is shown in Fig. 2.3.2e, where two resonance peaks arise at the frequencies of the coupled modes. The origin of the different peak heights is still under investigation. As for the two previous systems, the origin of this enhanced SHG signal is the field enhancement associated with the phonon polariton modes.

Fig. 2.3.2f shows the calculated in-plane electric field distribution of the two strongly coupled phonon polaritons in the AlN/SiC heterostructure, featuring two resonances that are of similar shape as the field distribution of the bare SiC SPhP (Fig. 2.3.2b). The field distributions (both $\vec{E}_x$ and $\vec{E}_z$ [**IV**]) of the two modes are of similar amplitude and shape, indicating full hybridization of the substrate SPhP and the ENZ mode at strong coupling conditions. For more details on the field enhancement of strongly coupled phonon polaritons see the publication reprinted on page 65 [**IV**].

SiC Nanopillar Localized Phonon Polariton Resonances Periodic nanostructures of polar crystals with 3D confinement, such as nanopillars as sketched in Fig. 2.3.2g, support localized surface phonon resonances (LSPhRs), which are tunable in frequency by the nanopillar diameter D and the periodicity p [3, 85, 86]. In the case of SiC nanopillars on a SiC substrate, a so-called monopole mode is supported, where the entire pillar is charged with one polarity, while the substrate carries the counter-charge. In a nanopillar configuration of large periodicity compared to D, as it is illustrated in Fig. 2.3.2g ($D \approx 1\,\mu\text{m}$, $p = 5 - 7\,\mu\text{m}$), the substrate supports a propagating SPhP that can couple strongly to the monopole mode [87].

In Fig. 2.3.2g, one exemplary reflectance spectrum (red line) of the investigated nanopillar system is shown, exhibiting two pronounced dips in the reststrahlen band at the resonance frequencies of the LSPhR (the nanopillar monopole mode) and the propagating SPhP, marked by dashed lines. The field enhancement of both modes lead to a resonant SH yield, resulting in peaks in the SHG spectrum (blue line). For further details on the nanopillar modes, see Ref. [3, 85, 86]. Publication [**VIII**] discusses the SHG from the strongly coupled LSPhR and SPhP modes in detail.

Within this thesis, SHG is demonstrated to be a powerful experimental tool for probing the enhanced local electric fields of phonon polaritons, ranging from single-crystal SPhPs over Berreman modes to strongly coupled polaritons. Notably, the devised method provides the only direct experimental access to the field enhancement of phonon polaritons in the IR. Furthermore, the developed 4×4 transfer matrix formalism (see page 45) is shown to be a key theoretical tool for calculating the field enhancement of phonon polaritons in layered heterostructures of anisotropic materials. Thus, the investigations summarized in this section demonstrate the high level of insight into the local electric fields of phonon polaritons that is gained by the presented experimental and theoretical methods.

CHAPTER 3

Experimental Approaches

Phonon polaritons are, except for the leaky Berreman mode, evanescent modes that cannot radiate into the far-field, and vice versa cannot be accessed by incident plane waves in a free-space excitation scheme. This aspect of being non-radiative renders phonon polaritons excellent excitations for nanophotonic applications that aim at harvesting, localizing and guiding light in sub-wavelength nanostructures. On the other hand, the study of non-radiative modes also requires special excitation schemes, such as grating coupling, prism coupling, or scattering-type scanning near-field optical microscopy (s-SNOM).

The first section of this chapter describes the most common experimental methods for the excitation of phonon polaritons. In this work, the Otto geometry for prism coupling has been implemented, and the details of the setup are provided in section 3.2. Finally, in section 3.3 the FEL at the FHI in Berlin is characterized, which was employed as a high intensity, mid-infrared (MIR) light source for all spectroscopy measurements performed in the course of this thesis.

3.1 Excitation of Phonon Polaritons

The reason for the non-radiative nature of phonon polaritons is their momentum-mismatch with plane waves propagating in vacuum. In order to be excitable, the dispersion must feature a crossing point with the dispersion of the incident light, but evanescent phonon polaritons disperse only on the right hand side of the light line, see Fig. 2.2.1. The additional in-plane momentum required for the excitation of phonon polaritons can be provided by evanescent waves or nanostructures, such as for the evanescent wave generated under total internal reflection, or the light scattered off a sharp tip. In the following, four common excitation schemes are discussed and compared.

Grating Coupling One way to couple to surface polaritons is to cut a periodic line grating into the sample surface, as has been demonstrated for SPPs propagating on flat metallic surfaces [88, 89] and on metal tips [90, 91], and for SPhPs on a SiO_2 crystal [92]. Alternatively, the grating can be evaporated onto the sample, as has recently been shown for gold gratings on hyperbolic metamaterials [63, 64]. By this means, the induced polarization in the sample receives a total momentum composed of the incoming in-plane momentum and an additional grating momentum, and thus can cross the polariton dispersion. In Fig. 3.1.1a, the excitation of a surface polariton with a grating on a flat sample is sketched. The periodicity p of the grating defines the provided momentum q_{grating}, leading to the following total momentum k_x^g [93]:

$$k_x^g = q_x + q_{\text{grating}} = \frac{\omega}{c}\sin\theta + n\frac{2\pi}{p}, \tag{3.1.1}$$

where q_x is the in-plane momentum of the incident light in air and $n \in \mathbb{Z}$ is the grating order. For the excitation of a surface polariton, the dispersion given by Eq. 3.1.1 has to cross the polariton dispersion, fulfilling the equation

$$k_{\text{surface polariton}} = k_x. \tag{3.1.2}$$

In Fig. 3.1.1b, the SPhP dispersion on a bare SiC crystal (green line) is plotted together with the dispersion given by Eq. 3.1.1 (red lines) for various incident angles θ and the grating orders $n = 1$ and -1. For $n = -1$, the total momentum k_x is negative, meaning that a SPhP is excited that propagates in the reverse in-plane direction of the incoming light.

In a reflectance measurement, the excitation of a SPhP leads to a resonance dip in the reststrahlen band, where otherwise the reflectance is 1 due to the negative real part of the dielectric permittivity. By measuring the reflectance spectra and extracting the SPhP resonance frequencies for various incident angles θ, the SPhP dispersion can be reconstructed.

Gratings allow for the excitation of surface polaritons in a free-space experiment, where the sample can be directly illuminated without the need of additional equipment. On the other hand, (i) the fabrication of gratings requires precise lithographic methods that have to be employed for each investigated sample, (ii) the 3D structure of a grating provides numerous scattering sites that perturb the propagation of the surface polariton and modify its dispersion, and (iii) a precise theoretical description is difficult to achieve for samples with high surface roughness. Therefore, while gratings provide a straight-forward way to probe surface polaritons on a proof-of-principle basis, they are of limited use for a detailed, theory-supported investigation of polaritonic systems.

Prism Coupling in the Kretschmann Geometry Another way to couple to surface polaritons is to provide the lacking in-plane momentum by employing a prism made of a material with high refractive index. The total in-plane momentum is then given by

$$k_x^p = q_x\sqrt{\varepsilon^{\text{P}}} = \frac{\omega}{c}\sin\theta\sqrt{\varepsilon^{\text{P}}}, \tag{3.1.3}$$

where ε^{P} is the dielectric permittivity of the prism.

In a prism coupling excitation scheme, the surface polariton has to be excited at a sample surface adjacent to air or another material with a dielectric permittivity smaller than ε^{P}. In the so-called Kretschmann geometry [94], this is achieved by placing a thin film of the polariton-active medium onto the prism, and the surface polariton is excited at the opposite sample surface adjacent to air (sketched in Fig. 3.1.1c). Furthermore, the incident angle θ has to be larger than the critical angle of total internal reflection of the prism material, in order to generate an evanescent wave that leaks into the sample and is capable of coupling to the surface polariton.

The Kretschmann geometry is mainly employed for the investigation of SPPs, where thin metal films are evaporated onto the prism [94–98], whereas SPhPs are typically studied by different methods.

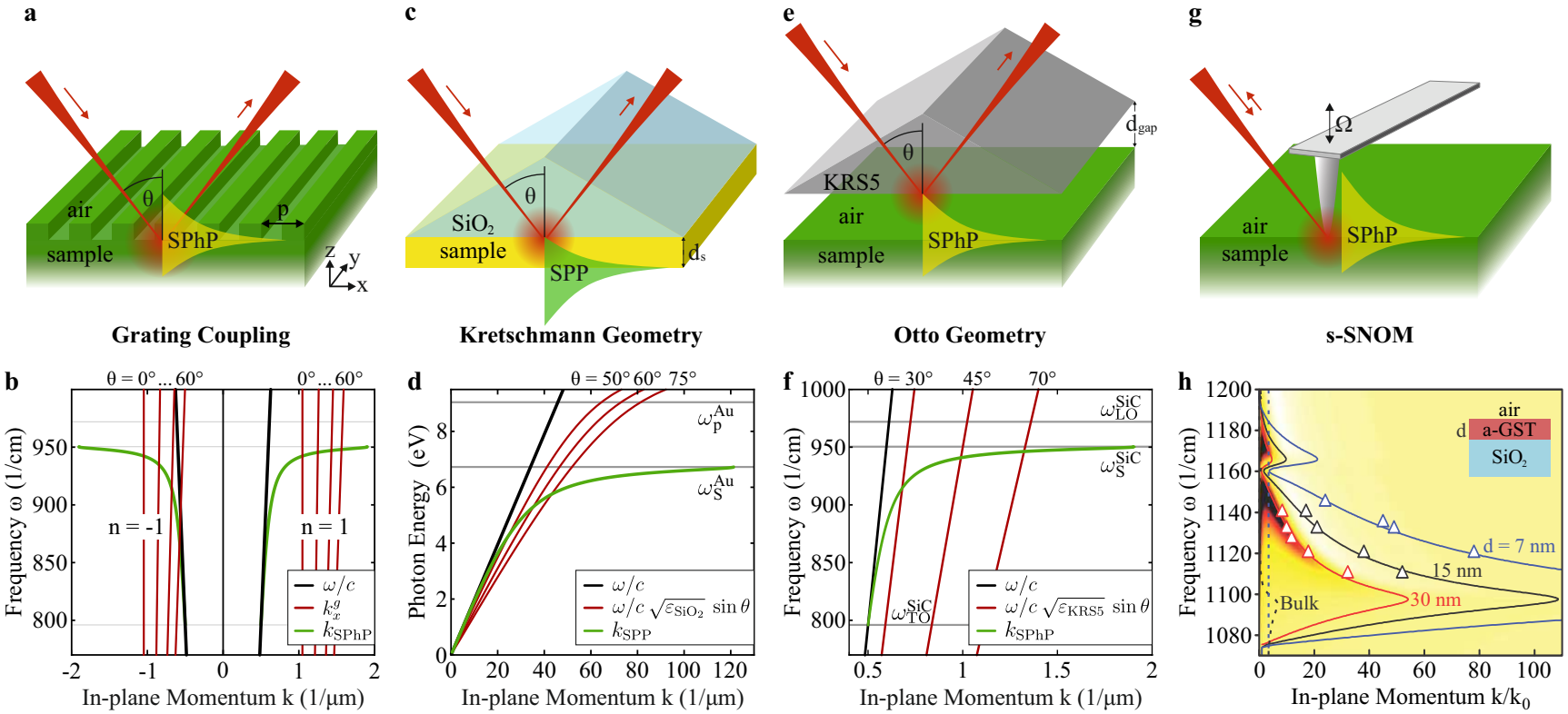

Figure 3.1.1: Experimental methods for the excitation of surface polaritons. **a** Sketch of a grating edged into the sample surface, allowing to couple to surface polaritons via free-space radiation. **b** Dispersion of a SiC SPhP (green lines) either launched in the same in-plane direction ($k > 0$) as the incoming beam or counter-propagating ($k < 0$), and the dispersion of the grating light line k_x^g, see Eq. 3.1.1 (red lines), for various incident angles θ and the grating orders $n = 1$ and -1. Excitation of the SPhP occurs at the crossing points of k_x^g and k_{SPhP}. **c** Sketch of prism coupling in the Kretschmann geometry, where the surface polariton is launched at the bottom side of the sample film (yellow). **d** Dispersion of a Au SPP (green line) and the prism light lines k_x^p, see Eq. 3.1.3 (red lines), for various incident angles. **e** Illustration of the Otto geometry, implementing a coupling prism parallel to the sample leaving a variable air gap of size d_{gap}. SPhPs are launched by evanescent waves leaking across the air gap. **f** Dispersion of a SiC SPhP (green line) and prism light lines for a KRS-5 prism. **g** Sketch of the operation principle of s-SNOM. The incoming light is scattered off the oscillating tip of an atomic force microscope (AFM), thereby launching surface polaritons on the sample surface. **h** Exemplary dispersion graph with experimental data (triangles) obtained by s-SNOM (figure adapted from Ref. [4]). Compared to the other excitation methods, s-SNOM allows to excite surface polaritons at large in-plane momenta.

In Fig. 3.1.1d, the dispersion of a SPP on Au (green line) is plotted together with the in-plane light dispersion (Eq. 3.1.3) in a SiO_2 prism for three different incident angles. Analogous to the grating coupling, varying θ allows to reconstruct the polariton dispersion, however only up to a limit ($\theta = 90\,^\circ$) defined by the refractive index of the prism material.

Compared to the grating coupling, the Kretschmann geometry stands out by its structural robustness and simplicity. Furthermore, the excitation of surface polaritons in the Kretschmann geometry is well-defined and can be easily treated theoretically by means of a transfer matrix formalism. On the other hand, each sample and even each thickness of the same sample requires a new prism, which is probably the reason why SPhPs are typically not studied in the Kretschmann geometry, because suitable prism materials in the IR are quite expensive (for example KRS-5 or diamond).

Prism Coupling in the Otto Geometry In 1968, three years before Kretschmann originated his coupling configuration, Otto proposed a prism coupling method to surface polaritons where a small gap of size d_{gap} is opened between prism and sample [23]. The Otto geometry is illustrated in Fig. 3.1.1e and is implemented in this work (see section 3.2 for details on the setup).

The total in-plane momentum k_x in the Otto geometry is the same as for the Kretschmann geometry, see Eq. 3.1.1, and the condition for excitation is given by Eq. 3.1.2. The dispersion of a bulk SiC SPhP and the light dispersion in a KRS-5 prism is plotted in Fig. 3.1.1f. As for grating coupling and the Kretschmann geometry, the incident angle θ serves as a tuning parameter for reconstruction of the SPhP dispersion, and it has to be larger than the critical angle of total internal reflection of the prism material ($\sim 25\,^\circ$ for KRS-5 in the IR).

As for the Kretschmann geometry, a surface polariton in the Otto geometry is a three-layer mode, sensing the presence of the coupling prism. This leads to a strong dependence of the excitation efficiency on d_{gap}. For large distances, the exponentially decaying evanescent wave under total internal reflection cannot excite the surface polariton effectively. For smaller d_{gap}, the evanescent wave and the surface polariton overlap such that optimal coupling conditions are reached. At this critical distance d_{crit}, the reflectance reaches its minimum and will be even zero for resonant wave vector matching, meaning that the incoming light is fully absorbed by the surface polariton. By further reducing the gap size, the radiative loss of the surface polariton into the prism increases, and the coupling efficiency decreases (see the publication reprinted on page 37 [**I**] for further details on the critical coupling behavior).

Compared to grating coupling and the Kretschmann geometry, the Otto geometry only requires a single coupling prism, which can be utilized to study any bulk sample or layered heterostructure of arbitrary thickness. Furthermore, a unique experimental advantage of the Otto configuration is the adjustability of the gap size d_{gap}. However, the precise control of the gap size is challenging. Specifically for SPPs, the gap sizes lie in the nanometer range, whereas SPhPs are accessible for micrometer gap sizes.

The setup developed in this work (see section 3.2) is one of the first[1] experimental realizations of the Otto geometry that allows for reproducible sub-micrometer control over the gap with direct, non-invasive read-out of the gap size. As is demonstrated in the publications originated during the course of this thesis, this unique setup[2] enables the possibility to investigate the critical coupling

[1] to the best of my knowledge

[2] In correspondence, *PIKE Technologies* has recently started the development of a comercialized Otto geometry setup

behavior of SPhPs [I], study several modes of different coupling conditions in the same sample [IV, VI], and reconstruct the SPhP dispersion at critical coupling conditions at all frequencies [I, IV, X], being inaccessible by other coupling methods.

Compared to grating coupling and the Kretschmann geometry, the Otto geometry proves to be a versatile, reproducible, and robust tool for the investigation of SPhPs in the IR. However, the momentum range that can be probed is limited by the refractive index of the prism material, rendering the Otto geometry only suitable for modes that propagate in proximity to the light line in vacuum. As is demonstrated in this work, the low-momentum region possesses a rich variety of polariton modes featuring numerous intriguing phenomena. Nonetheless, some modes disperse at larger in-plane momenta, and therefore are unreachable with the Otto geometry. These modes, such as volume-confined hPhPs in hyperbolic thin films, can be studied employing s-SNOM, as is discussed in the following.

Scattering-type Near-Field Optical Microscopy A sub-wavelength small object scatters an incoming plane wave into waves covering a continuum of in-plane momenta, allowing to couple to surface polaritons that disperse at momenta far off the light line in air. scattering-type scanning near-field optical microscopy (s-SNOM) employs the tip of an AFM as a scattering object (sketched in Fig. 3.1.1g), and by bringing the tip close to the sample surface, high-momentum surface polaritons are launched in the sample. The tip oscillates at frequency Ω, and by locking to the higher-harmonics of the back-reflected light, the scattered contributions off the tip can be extracted [99–101].

In order to obtain information about the launched SPhPs, the tip is scanned across an edge or spot on the sample, where the SPhPs are reflected. The back-reflected wave interferes with the launched wave, forming a standing wave with a measurable intensity modulation, which allows to retrieve the wavelength and propagation length of the excited SPhP. This technique has been demonstrated for various systems, including bare SiC [102, 103], hPhPs in hBN [16], and SPhPs in SiO_2 modulated by a thin-film PCM [4]. The dispersion of the latter system is shown in Fig. 3.1.1h, where the triangles indicate the experimental data obtained with s-SNOM, yielding in-plane momenta of up to $k/k_0 = 80$.

s-SNOM is a powerful technique to study the local fields of surface polaritons in nanoscale structures. A complementary approach is the photothermal-induced resonance (PTIR) technique, where the absorption of short laser pulses by the sample are detected with an AFM [104, 105]. Enabled by the sharp tip of the AFM, the spatial resolution of s-SNOM and PTIR far exceeds other coupling methods, and the local properties of polaritons can be mapped out by scanning the sample surface. On the other hand, due to the need of a back-reflector on the sample surface and the presence of the tip as scattering object, theoretical modeling of the experimental data is cumbersome.

In conclusion, s-SNOM provides information about the high-momentum modes on the nanoscale, whereas the Otto geometry is better suited for the investigation of low-momentum surface polaritons in macroscopically smooth layered heterostructures. Compared to grating coupling and the Kretschmann geometry, the Otto geometry is more versatile, and provides deeper insight into the surface polariton properties by controlling the gap size. This work implements the Otto geometry, focusing on phonon polaritons in layered polar dielectric heterostructures and their characteristics in the low-momentum range. The experimental setup is presented in the following section.

3.2 The Otto Geometry Setup

As discussed in the previous section, the Otto geometry enables thorough investigations of SPhPs in layered heterostructures due to the tunability of in-plane momentum and excitation efficiency via incidence angle and gap size, respectively. The experimental implementation together with the spectroscopic setup is illustrated in Fig. 3.2.1. The collimated incident FEL beam is focussed by an off-axis mirror ($f = 646\,\mathrm{mm}$) onto the prism. After passing through the Otto geometry, where the beam is totally reflected at the prism backside, the light is separated by a dichroic beam splitter (longwave pass at $\lambda = 7\,\mu\mathrm{m}$) for measuring the reflectance and the generated SHG signal separately. In order to ensure reproducibility and accuracy of the detection for varying incident angles, the pick-up mirror that directs the beam onto the beam splitter is mounted on a motorized translation and rotation stage.

The Otto geometry comprises the sample and the prism with a small gap in between. In Fig. 3.2.2, the constructed Otto geometry system is shown in a real image. The gap size can be adjusted by means of three *Newport* motorized actuators with a minimum incremental motion of $0.1\,\mu\mathrm{m}$, which are arranged in a triangular shape. This assembly is attached to a two-axis mirror mount, allowing the horizontal and vertical matching of the incident and reflected beam. Finally, this is mounted on a rotation stage for measuring at different incident angles θ, and on a x-y-z translation stage for fine adjustment, i.e. altogether being a 9-axis system.

The triangular prism used in this work is made of KRS-5, with a basis size of $1' \times 1'$ and side angles of $30\,^\circ$. Due to the high refractive index of KRS-5 (in the IR, $n_{\text{KRS-5}} \approx 2.4$), a rotation of the entire Otto geometry translates into a much smaller change of the incident angle θ inside the prism. Geometric beam propagation calculations allow to convert the incident angle θ inside the prism into the external incidence angle with respect to the prism side surface and vice versa. The prism geometry was chosen such that for an incident wavelength of $\lambda = 11\,\mu\mathrm{m}$, the incident angle θ can be tuned in a range from still below the critical angle of total internal reflection ($\sim 25\,^\circ$ for KRS-5) up to a maximally possible angle of $\theta \approx 50\,^\circ$, allowing to map the polariton dispersion from the light line up to a maximum momentum.

As sketched in Fig. 3.2.1 in green, a reflective fiber collimator directs the light of a *Thorlabs* tungsten NIR source onto the ground-off top of the KRS-5 prism, and collects the signal reflected at the prism back side and the sample surface. The reflected light is guided through a bifurcated fiber bundle and analyzed in an *Ocean Optics* NIR spectrometer. Interference between the reflected light from the prism back side and the sample leads to a modulation in the white-light spectrum, and Fourier transformation of the spectrum allows to determine the gap size d_{gap}. Note that exclusively the small gap size between prism and sample is probed, because owing to the incoherence of the white-light, the setup is not sensible to larger interface distances such as the prism front and backside.

Prior to the SPhP excitation measurements, the modulation contrast of the white-light spectrum enables to optimize the parallelism between prism and sample. After establishing parallelism, d_{gap} is monitored continuously and simultaneously to the SPhP experiments. The d_{gap} range that can be read out by the white-light interferometry setup lies between $\sim 100\,\mathrm{nm}$ and $\sim 60\,\mu\mathrm{m}$. Roughness of the sample and the prism backside further restricts the lower limit, leading to typical minimum gap sizes of approximately $1\,\mu\mathrm{m}$. The resulting accessible d_{gap} range is perfectly suited for the excitation of SPhPs, since the typical critical gap sizes of optimal coupling conditions of phonon polaritons

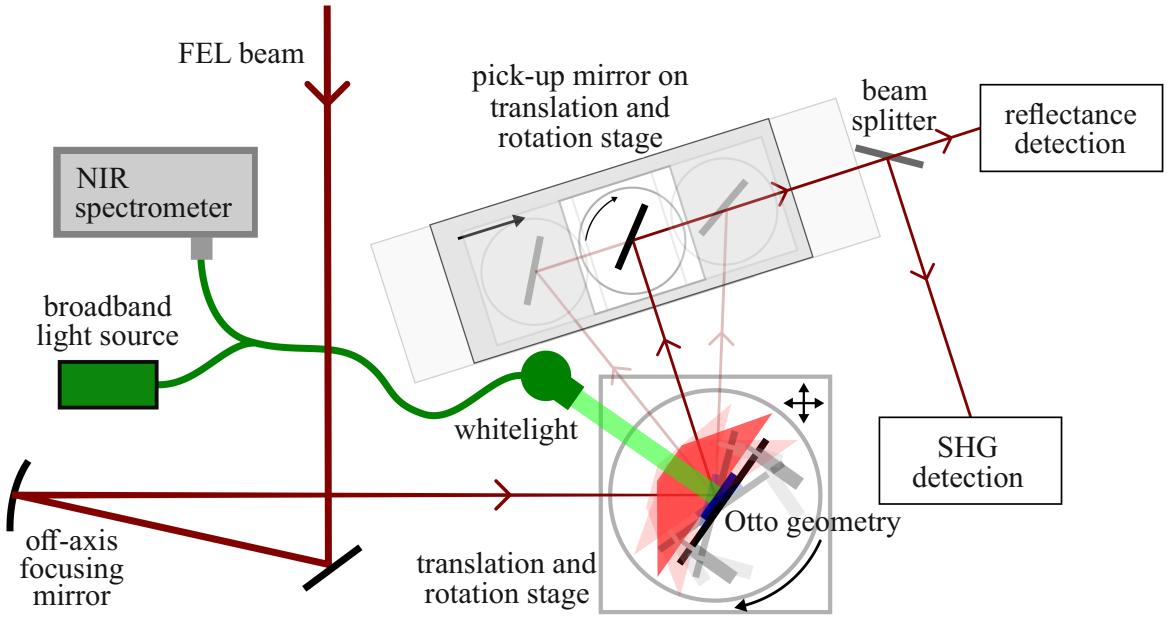

Figure 3.2.1: Setup for reflectance and SHG measurements employing the Otto geometry. Different incident angles θ can be measured by rotating the Otto assembly and moving and rotating the pick-up mirror to the position, where the detection beam path is met again. Motorized actuators allow the adjustment of the gap size between prism and sample. The prism top is ground off in order to couple in a collimated white-light beam. The reflected white-light signal carrying interferometric information is analyzed in a near-infrared (NIR) spectrometer, allowing to determine the gap size.

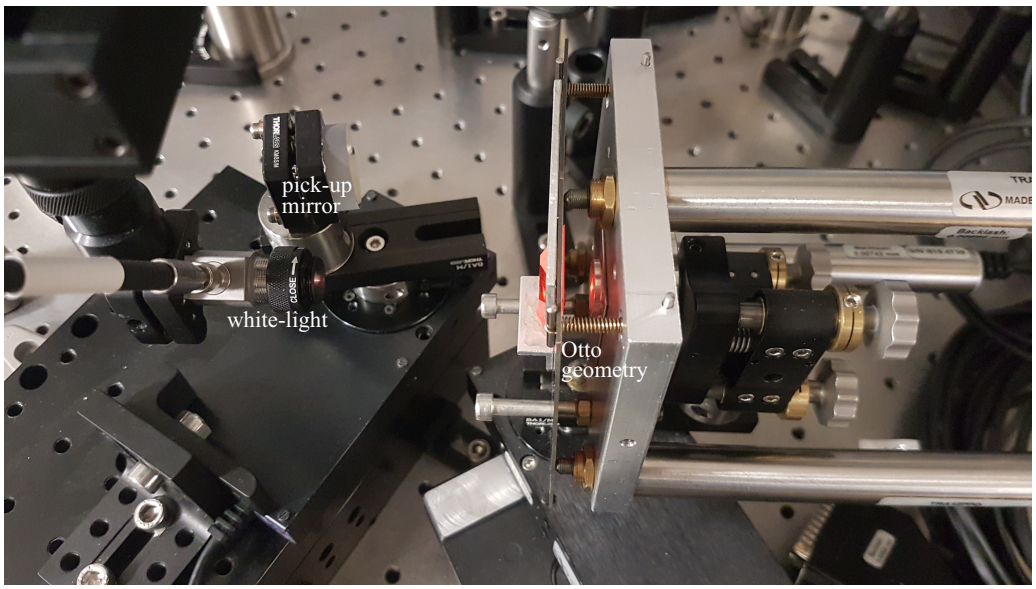

Figure 3.2.2: Home-made and designed 9-axis Otto geometry construction with mounted KRS-5 prism. Three motorized actuators allow to control the gap size on the sub-micrometer scale. Note that in the image, no sample is mounted and the gap is opened maximally for illustration purposes. From the left, the fiber-coupled white-light beam is directed onto the ground-off prism top.

lie in the range of $\sim 1 - 20\,\mu\mathrm{m}$. For further details on the white-light interferometry setup, see publication [**X**].

In summary, the constructed Otto geometry setup enables thorough experimental studies of phonon polaritons in any flat sample, allowing to determine the linear and nonlinear optical response of the polariton modes, analyze their critical coupling conditions by controlling the gap size, and map out the polariton dispersion by scanning the wavelength and incident angle. This renders the here developed Otto geometry setup a highly versatile and flexible experimental tool for the investigation of phonon polaritons in layered heterostructures, as is demonstrated in the publications reprinted in chapter 4.

3.3 The FHI Free Electron Laser

The FHI FEL is a MIR oscillator FEL which has been installed in 2011 on the campus of the Fritz Haber Insitute (FHI) and started operating in 2013 [106]. The machine generates spectrally sharp, frequency-tunable, high-intensity laser output in the MIR, constituting the ideal excitation source for the investigation of phonon polaritons by means of reflectance and SHG spectroscopy. In the following, the FHI FEL is briefly described.

The setup is illustrated in Fig. 3.3.1. After generation in a thermionic gridded electron gun, two linear accelerators (linacs) speed up the electrons to energies in the range of $15\,\mathrm{MeV}$ to $50\,\mathrm{MeV}$. While the first linac operates at a nominal electron energy of $20\,\mathrm{MeV}$, the second can be tuned to boost or lessen the electron energy in the mentioned range. The electron gun generates pulsed electron bunches of about $200\,\mathrm{pC}$ at a repetition rate of $1\,\mathrm{GHz}$. Before entering the linacs, these electron micro pulses pass through a $1\,\mathrm{GHz}$ buncher, which reduces the micro pulse length to $1\,\mathrm{ps}$ to $5\,\mathrm{ps}$. Each bunch can then be effectively accelerated in the linacs, which create a macro pulse structure of pulse lengths of $1\,\mu\mathrm{s}$ to $15\,\mu\mathrm{s}$ with a repetition rate of $10\,\mathrm{Hz}$. In table 3.3.1, the most important properties of the accelerator system are listed.

Table 3.3.1: Specifications of the electron accelerator of the FHI FEL [106].

Parameter	*Value*
Electron energy	15-50 MeV
Bunch charge	200 pC
Micro pulse length	1-5 ps
Micro pulse repetition rate	1 GHz
Macro pulse length	1-15 µs
Macro pulse repetition rate	10 Hz

After guidance through a $90\,^\circ$ curve by means of isochronous bends, the electron beam enters the MIR wedged-pole undulator which has a total length of $2\,\mathrm{m}$ and is composed of 50 periods with a period length of $\lambda_u = 40\,\mathrm{mm}$. The tunable undulator gap has a nominal minimum size of $16.5\,\mathrm{mm}$ and features the generation of radiation in the range of $3\,\mu\mathrm{m}$ to $50\,\mu\mathrm{m}$. Up to date, the MIR undulator is the only operating FEL arm. The construction of the longer, far-IR undulator depicted in Fig. 3.3.1 is currently in preparation and will be initiated in the near future. This second undulator is designed to cover the wavelength range of $10\,\mu\mathrm{m}$ to $150\,\mu\mathrm{m}$ and will be synchronized with the MIR undulator, allowing for two-color experiments in the IR.

The undulator is enclosed by two gold-plated copper mirrors, forming the laser cavity of $L_0 = 5.4\,\mathrm{m}$ length. Both mirrors are of concave spherical shape, with radii of curvature of $2.65\,\mathrm{m}$ and $3.51\,\mathrm{m}$ of the end mirror and the outcoupling mirror, respectively. Since hole outcoupling is employed, five mirrors with different hole diameters (0.75, 1, 1.5, 2.5, and $3.5\,\mathrm{mm}$) are available in order to optimize the lasing performance at all wavelengths. The end mirror is mounted on top of a precision translation stage, which can be used for a wavelength dependent cavity length tuning [106]. This adjusts the cavity length to a value of $L_0 - \Delta\lambda$, where $\Delta\lambda = q\lambda$ is the wavelength synchronized cavity detuning. In practice, the factor q is usually set to $0 < q < 5$. By this means, the accessible wavelength range at a specific electron energy, that is, in a single wavelength scan, can be significantly increased.

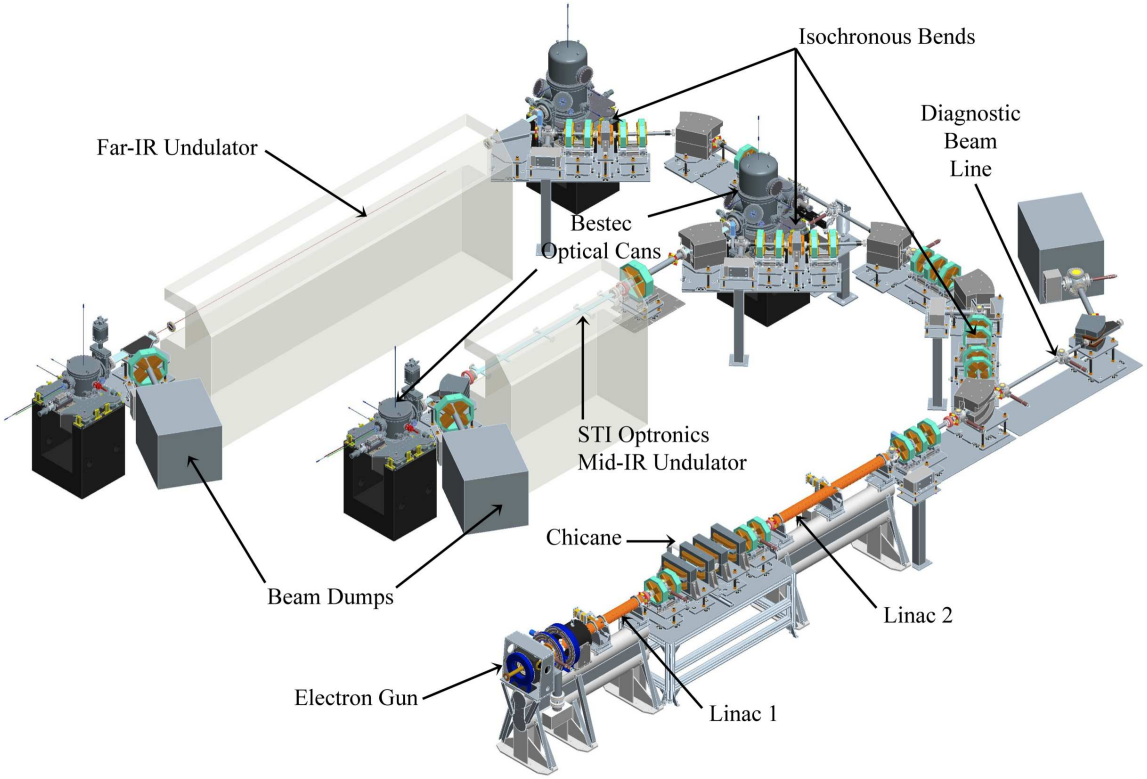

Figure 3.3.1: Sketch of the FHI FEL showing the electron acceleration segment and the two FEL systems with different undulator length. In two linear accelerators Linac 1 and Linac 2, the electrons are speeded up to energies up to $50\,\mathrm{MeV}$, and then are conducted into one of the FEL cavities, where the IR laser pulses are generated. The picture is taken from Ref. [106].

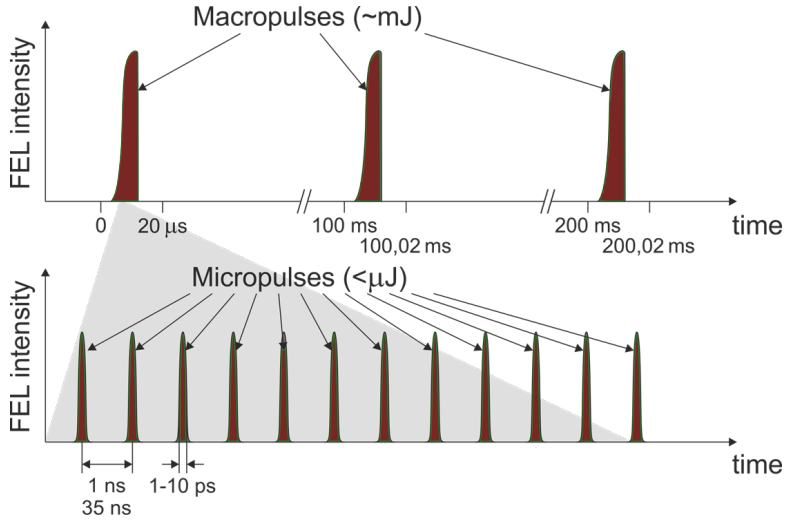

Figure 3.3.2: Pulse structure of the FEL. Each macro pulse (with $\sim 100\,\mathrm{ms}$ time spacing) exhibits a bunch of micro pulses, separated by $1\,\mathrm{ns}$ with a duration of $1 - 10\,\mathrm{ps}$.

Furthermore and more importantly, the emission bandwidth decreases with increasing q, which enables a practical method of enhancing the spectral resolution. In table 3.3.2, the most important properties of the MIR FEL are listed.

Table 3.3.2: Specifications of the MIR FEL [106].

Parameter	*Value*
Undulator length	$2\,\mathrm{m}$
period length λ_u	$40\,\mathrm{mm}$
number of periods	50
Cavity length L_0	$5.4\,\mathrm{m}$

The pulse structure of the FEL output radiation is dominated by the input electron pulse structure, exhibiting macro pulses at $\sim$10 Hz repetition rate, each consisting of a bunch of micro pulses at 1 GHz repetition rate. The resulting intensity distribution is sketched in Fig. 3.3.2.

In summary, the FEL provides laser radiation of high coherence, small spectral band width and tunable IR wavelength, enabling spectroscopic measurements of phonon polaritons with high spectral resolution and well-defined excitation conditions. Furthermore, the high power of the FHI FEL enables the possibility of employing SHG spectroscopy, rendering the machine a unique tool for studying the linear and non-linear optical response of phonon polaritons in the IR.

CHAPTER 4

Publications

In this chapter, the six scientific articles forming this thesis are reprinted. The erratum of one publication is also included. A list of these publications can be found on page vii, and a list of all publications originated during the course of this thesis can be found on page 117.

4.1 Second Harmonic Generation from Critically Coupled Surface Phonon Polaritons

Nikolai Christian Passler, Ilya Razdolski, Sandy Gewinner, Wieland Schöllkopf, Martin Wolf, and Alexander Paarmann

This publication (Passler *et al.*, ACS Photonics 2017, **4**, 1048-1053 [**I**]) reports on the first SHG from critically coupled SPhPs on SiC excited in the Otto-type prism coupling geometry. The supporting information is reprinted in appendix A.1.

This is the first paper that emerged from the Otto geometry implementation constructed in the course of the thesis (section 3.2). Employing the full mechanical control over the prism-sample distance, this publication explores the dependence of the excitation conditions and the optical field enhancement of SPhPs on the size of the air gap between prism and sample. The work establishes the Otto geometry as a tool for the investigation of surface polaritons in layered media at infrared wavelengths, paving the way for the other publications reporting on experiments that where conducted during this thesis. Furthermore, the FEL is employed for the first time for performing SHG spectroscopy on prism-coupled SPhPs.

Author contributions

A.P. originated the concept and devised the SHG method and the Otto-configuration experiments. The manuscript was written by **N.C.P.** and A.P., with all authors assisting in the proof-reading and preparation for final submission. **N.C.P.** constructed the Otto-configuration setup. The SHG measurements were performed by **N.C.P.**, I.R., and A.P., and the results were analyzed by **N.C.P.** and A.P. S.G. and W.S. operated the FEL. Computations of the linear and non-linear optical response were completed by A.P. and **N.C.P.** The experimental design and project management were provided by M.W. and A.P.

go to list of publications

ACS Photonics

Letter

pubs.acs.org/journal/apchd5

Second-Harmonic Generation from Critically Coupled Surface Phonon Polaritons

Nikolai Christian Passler, Ilya Razdolski, Sandy Gewinner, Wieland Schöllkopf, Martin Wolf, and Alexander Paarmann*

Fritz-Haber-Institut der Max-Planck-Gesellschaft, Faradayweg 4-6, 14195 Berlin, Germany

Supporting Information

ABSTRACT: Mid-infrared nanophotonics can be realized using subdiffractional light localization and field enhancement with surface phonon polaritons in polar dielectric materials. We experimentally demonstrate second-harmonic generation due to the optical field enhancement from critically coupled surface phonon polaritons at the 6H-SiC−air interface, employing an infrared free-electron laser for intense, tunable, and narrowband mid-infrared excitation. Critical coupling to the surface polaritons is achieved using a prism in the Otto geometry with adjustable width of the air gap, providing a contact-free access to the polariton dispersion with full control over the excitation conditions. The calculated reflectivity and second-harmonic spectra reproduce the complete experimental data set with high accuracy, allowing for a quantification of the optical field enhancement. We also reveal the mechanism for low out-coupling efficiency of the second-harmonic light in the Otto geometry. Perspectives on surface phonon polariton-based nonlinear sensing and nonlinear waveguide coupling are discussed.

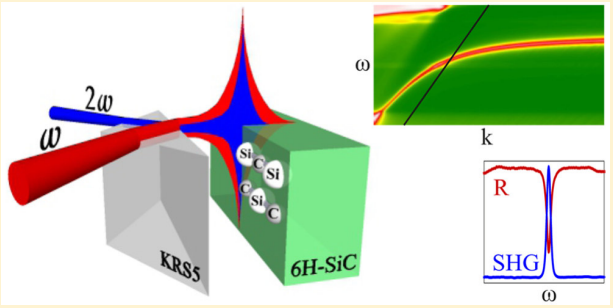

KEYWORDS: *surface phonon polariton, Otto geometry, nonlinear optics, silicon carbide, nanophononics, infrared free-electron laser*

Surface polaritons are the key building block of nanophotonics since these excitations allow for extreme light localization accompanied by significant enhancement of the local optical fields. A large body of research has focused on surface plasmon polaritons (SPPs) at noble metal surfaces,[1] which has led to a number of applications ranging from optical near-field microscopy to nonlinear plasmonic nanosensors.[2−7] Recently, an alternative approach was introduced employing surface phonon polaritons (SPhPs), which can be excited in the mid-infrared (mid-IR) at the surface of polar dielectrics.[8−10] In these materials, optical phonon resonances in the dielectric response result in a negative permittivity in the Reststrahl range between the transverse optical (TO) and longitudinal optical (LO) phonon frequencies and, in consequence, the existence of a highly dispersive surface polariton.[11] Notably, the much reduced optical losses of SPhPs as compared to SPPs have been argued to potentially solve the loss problem that was identified as the key limitation for widespread implementation of plasmonic devices.[12,13] Recent pioneering experiments have employed SPhPs for optical switching,[14] as well as subdiffractional light confinement[15−17] and strongly enhanced nonlinear response in subwavelength nanostructures.[18]

A systematic study of the linear and nonlinear-optical response of surface polaritons is enabled by prism coupling either in Kretschmann−Raether[19] or Otto[20] configuration. In both cases, the high refractive index of the prism operated in a regime of total internal reflection provides the large momenta required to excite the surface waves.[19] While mostly employed for studies of SPPs,[21−25] a few works also investigated SPhPs with prism coupling in the mid-IR.[8,10,26,27] Specifically in the Otto configuration, the surface polariton is excited across an air gap of adjustable width, providing contact-free access to the surface mode with extrinsic tunability of the excitation efficiency, which can lead to critical coupling conditions.[10] Strong optical field enhancement at critical coupling was predicted but could not be experimentally confirmed using linear optical techniques. Instead, nonlinear-optical approaches such as second-harmonic generation (SHG) are highly sensitive to the localized electromagnetic fields.[18,22,25,28−30]

In this Letter, we experimentally demonstrate the first SHG from critically coupled SPhPs, allowing us to accurately determine the associated optical field enhancement. We employ the Otto geometry for prism coupling to SPhPs at the 6H-SiC−air interface across a variable air gap and detect reflectivity and SHG output spectroscopically at various positions in the SPhP dispersion, using an infrared free-electron laser (FEL) for tunable narrowband excitation. By varying the air gap width between the prism and the sample, we demonstrate critical coupling behavior of the SPhP excitation efficiency. The calculated linear and nonlinear response reproduces the full data set of reflectivity and SHG spectra with high accuracy. We

Received: February 7, 2017
Published: April 11, 2017

DOI: 10.1021/acsphotonics.7b00118
ACS Photonics 2017, 4, 1048−1053

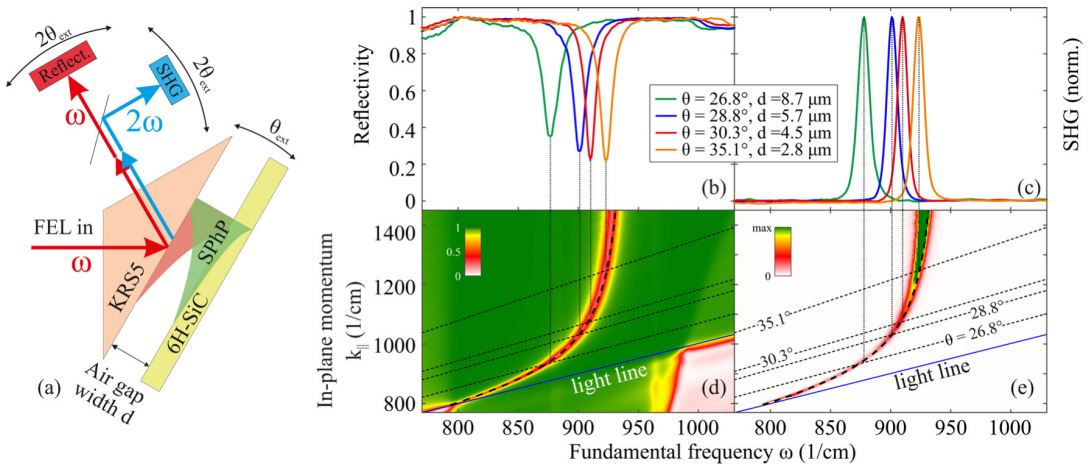

Figure 1. (a) Schematic of the experimental setup (not to scale) for Otto-type prism coupling to propagating SPhPs. Tuning the FEL frequency ω, air gap width d, and excitation-detection angle θ_{ext}–$2\theta_{ext}$ allows for full control over the SPhP excitation conditions. We measure both SHG intensity and reflectivity of the fundamental beam simultaneously using a dichroic beam splitter. For illustration, we also schematically show the evanescent fields leaking into the air gap from the prism side (red shaded) and SPhP (green shaded) at critical coupling conditions. Experimental reflectivity (b) and SHG (c) spectra taken for multiple incidence angles, each near the respective critical coupling gap width (see legend), leading to the most efficient SPhP excitation. Calculated reflectivity (d) and SHG (e) maps evaluated at critical coupling conditions show how the signals follow the SPhP dispersion (thick dashed lines): for each given incidence angle θ, the in-plane momentum of the fundamental light (sloped dashed lines) intersects with the SPhP dispersion at the respective spectral positions of the SPhP resonances in the reflectivity and SHG (vertical dotted lines).

extract the optical field enhancement, analyze the out-coupling of the SHG intensity in the Otto geometry, and discuss several potential applications of the nonlinear response from SPhPs.

RESULTS AND DISCUSSION

Excitation of propagating SPhPs and detection of their reflectivity and SHG response is realized experimentally as schematically shown in Figure 1a. We implement the Otto arrangement[8,10,20] by placing a triangular prism (KRS5, $n_{prism} \approx 2.4$, Korth) operated in the regime of total internal reflection onto a motorized mount in front of the sample, allowing for continuous tuning of the air gap width d. Rotation of the prism–sample assembly by angle $\Delta\theta_{ext} \approx n_{prism}\Delta\theta$ changes the in-plane momentum $k_{\parallel} = \frac{\omega}{c} n_{prism} \sin\theta$ of the incoming wave, allowing to excite SPhPs at different points along the dispersion.[8] Here, θ is the incidence angle inside the prism of refractive index n_{prism}, and ω is the frequency of the incoming mid-IR beam. We use an infrared FEL[31] as tunable, narrow band p-polarized excitation source, and the reflected fundamental and SHG beams are detected after a dichroic beam splitter. As a sample, we use a semi-insulating 6H-SiC c-cut single crystal; see the Supporting Information for further details on the experiment.

Notably, the efficiency of coupling the incoming light to the SPhPs in this geometry sensitively depends on the air gap width d.[10] The decay length L of the evanescent waves into the air gap for both the totally reflected incoming light and the SPhP strongly varies with the in-plane momentum $k_{\parallel}$:[19]

$$L = \frac{\lambda}{2\pi\sqrt{k_{\parallel}^2 c^2/\omega^2 - 1}} \quad (1)$$

where λ is the wavelength and c the speed of light in a vacuum. For small gaps $d \ll L$ with large overlap of the two evanescent waves, the strong radiative coupling of the SPhP back into the prism is a significant loss channel and prevents efficient excitation, while for large gaps $d \gg L$ the small overlap between the two evanescent waves inhibits an efficient energy transfer. There is, however, a critical coupling gap width d_{crit} where the radiative and intrinsic losses of the SPhP exactly balance each other, and critical coupling to SPhPs is achieved.[10] This is illustrated with the red- and green-shaded areas in Figure 1a for prism-side and SPhP waves, respectively. Since $k_{\parallel}$ strongly varies along the SPhP dispersion, both L and the critical gap width d_{crit} also vary from less than 1 μm for large momenta to tens of μm at small momenta when approaching the light line.

In consequence, the Otto arrangement allows for a high-precision, direct measurement of the full surface polariton dispersion if the critical coupling conditions are adapted appropriately. This mapping of the SPhP dispersion is demonstrated in Figure 1b and c, where we show experimental reflectivity and SHG spectra, respectively, at four different incidence angles, each taken near the respective d_{crit}. Under these conditions, a reflectivity dip of ~80% indicates efficient excitation of the SPhP. The spectral position of the dip follows the SPhP dispersion (see Figure 1d) as the incidence angle is changed. At the same time, the field enhancement associated with the efficiently excited SPhP results in significant increase of the SHG yield, as evidenced by the single, narrow peak in each of the SHG spectra (c).

For comparison, we show calculated reflectivity and SHG maps at critical coupling conditions in Figure 1d and e, respectively, plotted as a function of fundamental frequency ω and in-plane momentum $k_{\parallel}$. The reflectivity is calculated using the transfer matrix approach[32−34] (see Supporting Information for details), while the SHG intensity is computed using

$$I(2\omega) \propto |(T_b \vec{E}_{SiC}(2\omega))(\chi^{(2)}(-2\omega;\, \omega,\, \omega)\vec{E}_{SiC}^{\,2}(\omega)/\Delta k)|^2 \quad (2)$$

Here, $\vec{E}_{SiC}(\omega)$ is the local optical field on the SiC side of the SiC–air interface, which we obtain from the transfer matrix approach, and $\chi^{(2)}$ is the nonlinear susceptibility of 6H-SiC,[30] while Δk accounts for the wave vector mismatch for SHG in reflection.[30,35] Additionally, we explicitly account for the field

DOI: 10.1021/acsphotonics.7b00118
ACS Photonics 2017, 4, 1048−1053

coupling of the nonlinear polarization by projecting it onto $T_b\vec{E}_{SiC}(2\omega)$, with $\vec{E}_{SiC}(2\omega)$ being the local field of the respective mode at 2ω and $2k_{||}$ propagating from SiC back into the prism and T_b the transmission coefficient back to the prism. See the Supporting Information for details on the SHG calculations.

To demonstrate the critical behavior of the response, we acquired reflectivity spectra for multiple values of the air gap width d for selected incidence angles, exemplified for $\theta = 28.8°$ and $\theta = 35.1°$ in Figure 2a and b, respectively. At the smallest gap (black lines), a shallow broad dip in the reflectivity at $\omega \approx 900$ cm^{-1} reports on excitation of highly lossy SPhPs with pronounced radiative coupling. As d is increased, the reflectivity dip increases in amplitude and narrows while simultaneously blue-shifting. A maximum dip depth of ~80% (blue lines) indicates that the critical coupling conditions are reached. For even larger gaps (orange lines), the amplitude of the dip drops again, while the narrowing and blue-shifting of the resonance converge, approaching the intrinsic line width and frequency of the uncoupled surface polariton, cf. Figure 1d. The qualitative behavior is identical between the two incidence angles shown here. However, the respective air gaps are clearly different; see legends in Figure 1a and b, where d essentially scales with the evanescent length L in eq 1. The calculated reflectivity perfectly reproduces the experimental data, including subtle features due to the 6H-SiC crystal anisotropy, such as reflectivity dips at the zone-folded weak modes at ~885 cm^{-1} and the axial LO phonon at 964 cm^{-1}.[30,36,37]

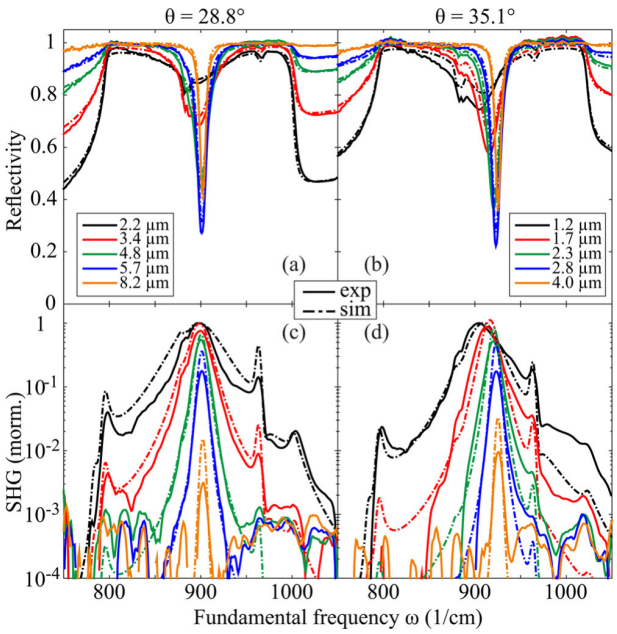

Figure 2. Experimental (solid lines) and calculated (dot-dashed lines) reflectivity (a, b) and SHG (c, d) spectra of the 6H-SiC−air interface in the Otto geometry, shown for selected air gap widths d (see legends) and incidence angles $\theta = 28.8°$ (a, c) and $\theta = 35.1°$ (b, d). The SHG spectra were normalized to the maximum at the smallest gap width. Note the logarithmic scale in (c) and (d).

The simultaneously acquired SHG spectra are shown in Figure 2c,d. At small gaps, the data exhibit some additional spectral features;[30,35] however, a pronounced SPhP resonance can be clearly distinguished (note the logarithmic scale), with SPhP peak positions and line widths qualitatively following those observed in the reflectivity as d is increased. However, the amplitude behavior is clearly different for the SHG; we observe a steady decrease of the SHG amplitude at the SPhP resonance with increasing d. The calculated SHG spectra also shown in Figure 2c,d (dash-dotted lines) not only reproduce all the features in the spectra with high accuracy, but also predict the steady decrease of the SPhP resonance amplitude of the SHG with increasing width d of the air gap. This is very surprising, since the maximum field enhancement and, in consequence, most efficient nonlinear signal generation are expected at critical coupling.[10,19]

We summarize the SPhP resonance behavior for the full experimental data set in Figure 3. Lorentzian fits of the SPhP resonance in the experimental (symbols) and theoretical (lines) reflectivity (a, c, e) and SHG (b, d, f) spectra yield the amplitude (a, b), Q-factor (c, d), and position (e, f) of the reflectivity dip and SHG peak, respectively. The high experimentally achieved Q-factors, i.e., the ratios between center frequency and line width, mark the high quality of the SPhP resonance. Notably, the SHG resonances are intrinsically narrower as compared to the reflectivity dips due to the second-order nature of the interaction, leading to the consistently higher Q-factors. Remarkable agreement between experiment and theory is observed throughout the full data set. We note here that these calculations use a single set of parameters globally extracted from the full reflectivity data set. Hereby we explicitly include angular beam divergence and finite spectral width of the light source, being the main experimental limitations for achieving full SPhP resonance amplitude near

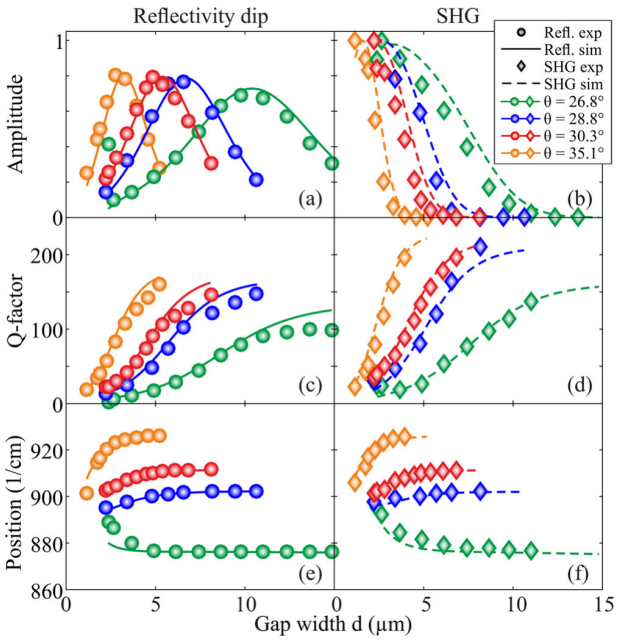

Figure 3. Air gap width d-dependence of the SPhP resonance amplitude (a, b), Q-factor (c, d), and spectral position (e, f) at four different incidence angles, as extracted from the experimental (symbols) and calculated (lines) reflectivity (a, c, e) and SHG (b, d, f) spectra. Critical coupling is achieved at the respective maximum of the reflectivity dip amplitude in (a). The Q-factors increase and the spectral positions shift as d is increased, converging toward the values of the weakly coupled, intrinsic surface polariton resonance, more rapidly with increasing θ and $k_{||}$, i.e., further away from the light line.

DOI: 10.1021/acsphotonics.7b00118
ACS Photonics 2017, 4, 1048−1053

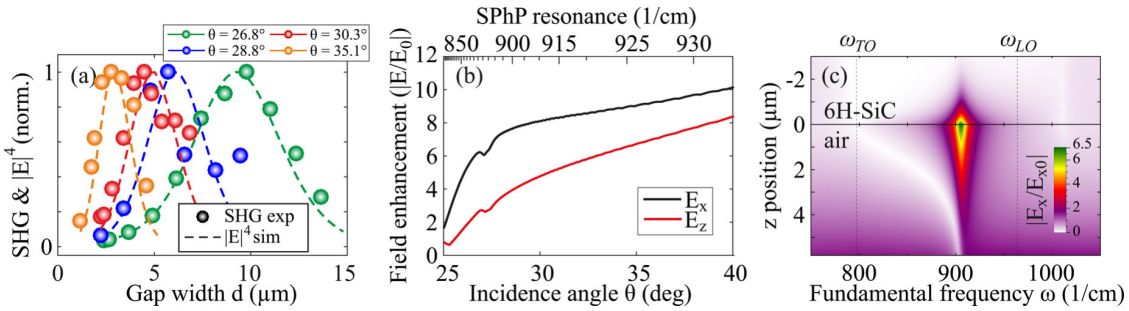

Figure 4. (a) The SHG signals corrected for out-coupling losses (symbols) perfectly follow the fourth power of the calculated local optical fields (lines). (b) SPhP optical field enhancement $|E/E_0|$ with E_0, the incoming field magnitude, evaluated at the critical coupling gap for in-plane E_x (black) and out-of-plane E_z (red) field components as a function of internal incidence angle (bottom) and corresponding SPhP resonance position (top). (c) Example of the spatio-spectral distribution of in-plane field enhancement, shown at critical coupling for $\theta = 28.8°$ with $d = 5.8$ μm. All electric fields are evaluated on the SiC side of the SiC−air interface.

to and far away from the light line, respectively; see the Supporting Information for details. We emphasize that only the reflectivity data were used for the global fitting, while the SHG spectra were simply calculated using nonlinear susceptibility extracted in previous experiments.[30]

The direct comparison of the SPhP resonance amplitudes of the reflectivity dip and the SHG peak (see Figure 3a and b, respectively) for the different incidence angles suggests a correlation between the critical coupling gap marking the strongest modulation of the reflectivity and the apparent decay length of the SHG amplitude. Indeed, if rescaled for the respective critical coupling gap width d_{crit}, the curves for different incidence angles are almost identical; see Figure S3 in the Supporting Information. To understand these observations, we need to consider two mechanisms determining the detectable SHG signal in the far field: (i) efficiency of SHG due to the local field enhancement provided by the SPhPs and (ii) the out-coupling of that nonlinear signal across the air gap into the prism and into the far field. In the case of low losses, the local field enhancement associated with surface polariton excitations is typically expected to follow the magnitude of the reflectivity dip;[10,19] that is, the maximum enhancement should be achieved at the critical coupling condition.

It is, however, important to realize that the SHG is generated with large in-plane momentum $k_{||,SHG} = 2\ k_{SPhP} > k_{0,SHG}$, where $k_{0,SHG}$ is the wavenumber of the SHG light propagating in air. This corresponds to the condition of total internal reflection for the SHG at the SiC−air interface, and only an evanescent wave is expected to leak into the air gap. Evaluating eq 1 for this wave reveals exactly half the evanescent length for the SHG as compared to the fundamental radiation on both sides of the air gap, resulting in an extremely poor overlap and largely suppressed far-field coupling of the SHG at critical coupling conditions. In our SHG calculations, this effect is explicitly accounted for by the gap width d-dependence of $T_b\vec{E}_{SiC}(2\omega)$ in eq 2, whose amplitude rapidly decays with d. In fact, we find that at critical coupling only ∼0.1% of the generated nonlinear signal is harvested into the far-field intensity.

Therefore, we can recover the second-harmonic intensity generated in SiC by correcting the experimental signals for the out-coupling efficiency $|T_b\ \vec{E}_{SiC}(2\omega)|^2$, as shown in Figure 4a. As expected from the last factor in eq 2, these signals now follow the fourth power of the resonantly enhanced fundamental optical fields $|E_{SiC}(\omega)|$, which are also plotted there. With this information, we can confidently extract the magnitude of the field enhancement in SiC at critical coupling, which is plotted in Figure 4b along the SPhP dispersion. We plot both in-plane and out-of-plane fields, E_x and E_z, respectively, since due to the symmetry of the $\chi^{(2)}$ tensor, both components contribute significantly to the SHG output.[30] Notably, the small dip in these curves at $\theta \approx 27.5°$ marks the resonant interaction of the SPhP with the zone-folded phonon modes in 6H-SiC.[18] For illustration, we also show an example of the spatio-spectral distribution of field enhancement along the normal-to-surface direction z in Figure 4c.

The excellent agreement between the experimental and calculated SHG response corroborates our observation of the extremely efficient nonlinear-optical conversion inside the SiC crystal, in particular in comparison to SPPs. From our data, we estimate an exceptional nonlinear conversion efficiency exceeding $\sim 10^{-6}$, which is a result of (i) the large field enhancement due to the high Q-factor of the SPhP resonance, (ii) the broken inversion symmetry as well as proximity to an ionic resonance of the nonlinear susceptibility[30,38] in the SPhP host, and (iii) the large effective volume of SHG generation as compared for instance to subdiffractional nanostructures.[18]

The broken inversion symmetry and the ionic resonance (ii) are unique fingerprints of SPhP materials as opposed to noble metals used in plasmonics.[1] Hereby, the enhancement of $\chi^{(2)}$ close to the ionic resonance at the TO frequency,[30,38] i.e., in the spectral range where the SPhP can be excited, is a generic feature for all polar dielectrics. Our approach is applicable to all non-centrosymmetric, polar dielectrics, such as α-quartz, ZnO, AlN, InP, GaAs, and ZnTe, to name a few, known to exhibit large nonlinear coefficients, as well as artificially designed hybrid materials[39] with yet unknown SPhP dispersion relations. Additionally, the strong dispersion of SPhPs provides spectral tunability of the field enhancement resonance with extraordinarily high Q-factors.

The combination of these features suggests several appealing scenarios for future applications of nonlinear nanophononics.[18] Previous linear sensing schemes[27,40] could be extended into the nonlinear domain with larger contrasts and higher Q-factors. Taking advantage of the large resonant, high-Q nonlinear signals from the broken-inversion SPhP host, these approaches could straightforwardly be implemented using narrow-bandwidth quantum-cascade lasers. Similarly, our approach could be extended to four-wave mixing experiments,[21,41] sensitive to either the SPhP host or a liquid phase analyte in the gap (cf. Figure 4c for the relevant length scales of field enhancement inside the gap). This could, for instance, lead to a drastic

DOI: 10.1021/acsphotonics.7b00118
ACS Photonics 2017, 4, 1048−1053

resonant enhancement of time-resolved vibrational spectroscopy signals from molecules in solution.[42]

Overall, the Otto geometry provides an ideal platform for studying the linear and nonlinear response from surface polaritons. As compared to the Kretschmann geometry, it allows extrinsically controlling the SPhP coupling efficiency due to the adjustable air gap width and is a contact-free approach that does not require samples to be deposited onto the prism, making it much more versatile. Additionally, we also note that SPhP materials are typically largely transparent above the Reststrahl frequency range. Together with the generation of nonlinear signal under conditions of total internal reflection, this suggests that the Otto geometry could be used for high-contrast nonlinear waveguide coupling,[43] which would also solve the problem of low out-coupling efficiency in reflective SHG detection and allow harvesting the full magnitude of the nonlinear signals.

CONCLUSION

In conclusion, we demonstrated the first SHG from critically coupled SPhPs, enabling high-precision measurements of the associated optical field enhancement, here shown for 6H-SiC as a model system. We use the critical coupling behavior of the Otto geometry to maximize the SPhP excitation efficiency. Despite poor far-field coupling of the SHG signals, which is shown to be a generic feature of the Otto arrangement, the large bulk nonlinearity of the crystal facilitates exceptional nonlinear-optical conversion from SPhPs, owing to the broken inversion symmetry of the host material and the high quality of the SPhP resonance. Being applicable to a wide range of polar dielectrics supporting SPhPs, our approach could be employed to extract the unknown polariton dispersion and field enhancement in artificially designed SPhP hybrids and opens the path to several new and appealing applications of nonlinear nanophononics.

ASSOCIATED CONTENT

Supporting Information

The Supporting Information is available free of charge on the ACS Publications website at DOI: 10.1021/acsphotonics.7b00118.

Details on the experimental procedure, practical implementation of the Otto geometry and the free-electron laser (S1), details on the transfer matrix calculations (S2), description of the fitting procedure (S3), normalization of the SPhP coupling efficiency data for different incidence angles to the respective critical gap width (S4), and details of the second-harmonic calculations (S5) (PDF)

AUTHOR INFORMATION

Corresponding Author

*E-mail: alexander.paarmann@fhi-berlin.mpg.de.

ORCID

Alexander Paarmann: 0000-0002-8271-2284

Notes

The authors declare no competing financial interest.

ACKNOWLEDGMENTS

The authors thank K. Horn (FHI Berlin) for providing the SiC sample.

REFERENCES

(1) Maier, S. A. *Plasmonics: Fundamentals and Applications*; Springer: US, 2007; pp 1−223.
(2) Sonntag, M. D.; Pozzi, E. A.; Jiang, N.; Hersam, M. C.; Van Duyne, R. P. Recent Advances in Tip-Enhanced Raman Spectroscopy. *J. Phys. Chem. Lett.* **2014**, *5*, 3125−3130.
(3) Müller, M.; Kravtsov, V.; Paarmann, A.; Raschke, M. B.; Ernstorfer, R. Nanofocused Plasmon-Driven Sub-10 fs Electron Point Source. *ACS Photonics* **2016**, *3*, 611−619.
(4) Anker, J. N.; Hall, W. P.; Lyandres, O.; Shah, N. C.; Zhao, J.; Van Duyne, R. P. Biosensing with plasmonic nanosensors. *Nat. Mater.* **2008**, *7*, 442−453.
(5) Kabashin, A. V.; Evans, P.; Pastkovsky, S.; Hendren, W.; Wurtz, G. a.; Atkinson, R.; Pollard, R.; Podolskiy, V. a.; Zayats, a. V. Plasmonic nanorod metamaterials for biosensing. *Nat. Mater.* **2009**, *8*, 867−871.
(6) Martín-Becerra, D.; Armelles, G.; González, M. U.; García-Martín, A. Plasmonic and magnetoplasmonic interferometry for sensing. *New J. Phys.* **2013**, *15*, 085021.
(7) Mesch, M.; Metzger, B.; Hentschel, M.; Giessen, H. Nonlinear Plasmonic Sensing. *Nano Lett.* **2016**, *16*, 3155−3159.
(8) Falge, H. J.; Otto, A. Dispersion of Phonon-Like Surface Polaritons on α-Quartz Observed by Attenuated Total Reflection. *Phys. Status Solidi B* **1973**, *56*, 523−534.
(9) Huber, A. J.; Ocelic, N.; Kazantsev, D.; Hillenbrand, R. Near-field imaging of mid-infrared surface phonon polariton propagation. *Appl. Phys. Lett.* **2005**, *87*, 081103.
(10) Neuner, B.; Korobkin, D.; Fietz, C.; Carole, D.; Ferro, G.; Shvets, G. Critically coupled surface phonon-polariton excitation in silicon carbide. *Opt. Lett.* **2009**, *34*, 2667−9.
(11) Adachi, S. *Optical Properties of Crystalline and Amorphous Semiconductors: Materials and Fundamental Principles*; Springer US: Boston, MA, 1999; pp 33−61.
(12) Khurgin, J. B. How to deal with the loss in plasmonics and metamaterials. *Nat. Nanotechnol.* **2015**, *10*, 2−6.
(13) Caldwell, J. D.; Lindsay, L.; Giannini, V.; Vurgaftman, I.; Reinecke, T. L.; Maier, S. A.; Glembocki, O. J. Low-loss, infrared and terahertz nanophotonics using surface phonon polaritons. *Nanophotonics* **2015**, *4*, 1−26.
(14) Li, P.; Yang, X.; Maß, T. W. W.; Hanss, J.; Lewin, M.; Michel, A.-K. U.; Wuttig, M.; Taubner, T. Reversible optical switching of highly confined phonon-polaritons with an ultrathin phase-change material. *Nat. Mater.* **2016**, *15*, 870−875.
(15) Wang, T.; Li, P.; Hauer, B.; Chigrin, D. N.; Taubner, T. Optical Properties of Single Infrared Resonant Circular Microcavities for Surface Phonon Polaritons. *Nano Lett.* **2013**, *13*, 5051−5055.
(16) Caldwell, J. D.; Glembocki, O. J.; Francescato, Y.; Sharac, N.; Giannini, V.; Bezares, F. J.; Long, J. P.; Owrutsky, J. C.; Vurgaftman, I.; Tischler, J. G.; Wheeler, V. D.; Bassim, N. D.; Shirey, L. M.; Kasica, R.; Maier, S. A. Low-Loss, Extreme Subdiffraction Photon Confinement via Silicon Carbide Localized Surface Phonon Polariton Resonators. *Nano Lett.* **2013**, *13*, 3690−3697.
(17) Gubbin, C. R.; Martini, F.; Politi, A.; Maier, S. A.; De Liberato, S. Strong and Coherent Coupling between Localized and Propagating Phonon Polaritons. *Phys. Rev. Lett.* **2016**, *116*, 246402.
(18) Razdolski, I.; Chen, Y.; Giles, A. J.; Gewinner, S.; Schöllkopf, W.; Hong, M.; Wolf, M.; Giannini, V.; Caldwell, J. D.; Maier, S. A.; Paarmann, A. Resonant Enhancement of Second-Harmonic Generation in the Mid-Infrared Using Localized Surface Phonon Polaritons in Subdiffractional Nanostructures. *Nano Lett.* **2016**, *16*, 6954−6959.
(19) Raether, H. *Surface Plasmons on Smooth and Rough Surfaces and on Gratings*; Springer, 1988.
(20) Otto, A. Excitation of nonradiative surface plasma waves in silver by the method of frustrated total reflection. *Z. Phys. A: Hadrons Nucl.* **1968**, *216*, 398−410.
(21) Palomba, S.; Novotny, L. Nonlinear Excitation of Surface Plasmon Polaritons by Four-Wave Mixing. *Phys. Rev. Lett.* **2008**, *101*, 056802.

(22) Grosse, N. B.; Heckmann, J.; Woggon, U. Nonlinear Plasmon-Photon Interaction Resolved by k-Space Spectroscopy. *Phys. Rev. Lett.* **2012**, *108*, 136802.
(23) Temnov, V. V. Ultrafast acousto-magneto-plasmonics. *Nat. Photonics* **2012**, *6*, 728−736.
(24) Foley, J. J., IV; Harutyunyan, H.; Rosenmann, D.; Divan, R.; Wiederrecht, G. P.; Gray, S. K. When are Surface Plasmon Polaritons Excited in the Kretschmann-Raether Configuration? *Sci. Rep.* **2015**, *5*, 9929.
(25) Razdolski, I.; Makarov, D.; Schmidt, O. G.; Kirilyuk, A.; Rasing, T.; Temnov, V. V. Nonlinear Surface Magnetoplasmonics in Kretschmann Multilayers. *ACS Photonics* **2016**, *3*, 179−183.
(26) Okada, T.; Nagai, M.; Tanaka, K. Resonant phase jump with enhanced electric field caused by surface phonon polariton in terahertz region. *Opt. Express* **2008**, *16*, 5633.
(27) Zheng, G.; Xu, L.; Zou, X.; Liu, Y. Excitation of surface phonon polariton modes in gold gratings with silicon carbide substrate and their potential sensing applications. *Appl. Surf. Sci.* **2017**, *396*, 711−716.
(28) Quail, J. C.; Rako, J. G.; Simon, H. J.; Deck, R. T. Optical Second-Harmonic Generation with Long-Range Surface Plasmons. *Phys. Rev. Lett.* **1983**, *50*, 1987−1989.
(29) Kauranen, M.; Zayats, A. V. Nonlinear plasmonics. *Nat. Photonics* **2012**, *6*, 737−748.
(30) Paarmann, A.; Razdolski, I.; Gewinner, S.; Schöllkopf, W.; Wolf, M. Effects of crystal anisotropy on optical phonon resonances in midinfrared second harmonic response of SiC. *Phys. Rev. B: Condens. Matter Mater. Phys.* **2016**, *94*, 134312.
(31) Schöllkopf, W.; Gewinner, S.; Junkes, H.; Paarmann, A.; von Helden, G.; Bluem, H.; Todd, A. M. M. The new IR and THz FEL facility at the Fritz Haber Institute in Berlin. *Proc. SPIE* **2015**, *9512*, 95121L.
(32) Berreman, D. W. Optics in Stratified and Anisotropic Media: 4 × 4-Matrix Formulation. *J. Opt. Soc. Am.* **1972**, *62*, 502.
(33) Yeh, P. Electromagnetic propagation in birefringent layered media. *J. Opt. Soc. Am.* **1979**, *69*, 742.
(34) Xu, W.; Wood, L. T.; Golding, T. D. Optical degeneracies in anisotropic layered media: Treatment of singularities in a 4 × 4 matrix formalism. *Phys. Rev. B: Condens. Matter Mater. Phys.* **2000**, *61*, 1740−1743.
(35) Paarmann, A.; Razdolski, I.; Melnikov, A.; Gewinner, S.; Schöllkopf, W.; Wolf, M. Second harmonic generation spectroscopy in the Reststrahl band of SiC using an infrared free-electron laser. *Appl. Phys. Lett.* **2015**, *107*, 081101.
(36) Engelbrecht, F.; Helbig, R. Effect of crystal anisotropy on the infrared reflectivity of 6H-SiC. *Phys. Rev. B: Condens. Matter Mater. Phys.* **1993**, *48*, 15698−15707.
(37) Bluet, J.; Chourou, K.; Anikin, M.; Madar, R. Weak phonon modes observation using infrared reflectivity for 4H, 6H and 15R polytypes. *Mater. Sci. Eng., B* **1999**, *61*−*62*, 212−216.
(38) Mayer, A.; Keilmann, F. Far-infrared nonlinear optics. I. $\chi^{(2)}$ near ionic resonance. *Phys. Rev. B: Condens. Matter Mater. Phys.* **1986**, *33*, 6954−6961.
(39) Caldwell, J. D.; Vurgaftman, I.; Tischler, J. G.; Glembocki, O. J.; Owrutsky, J. C.; Reinecke, T. L. Atomic-scale photonic hybrids for mid-infrared and terahertz nanophotonics. *Nat. Nanotechnol.* **2016**, *11*, 9−15.
(40) Neuner, B.; Korobkin, D.; Fietz, C.; Carole, D.; Ferro, G.; Shvets, G. Midinfrared Index Sensing of pL-Scale Analytes Based on Surface Phonon Polaritons in Silicon Carbide †. *J. Phys. Chem. C* **2010**, *114*, 7489−7491.
(41) De Leon, I.; Shi, Z.; Liapis, A. C.; Boyd, R. W. Measurement of the complex nonlinear optical response of a surface plasmon-polariton. *Opt. Lett.* **2014**, *39*, 2274.
(42) Hamm, P.; Zurek, M.; Mantele, W.; Meyer, M.; Scheer, H.; Zinth, W. Femtosecond infrared spectroscopy of reaction centers from Rhodobacter sphaeroides between 1000 and 1800 cm^{-1}. *Proc. Natl. Acad. Sci. U. S. A.* **1995**, *92*, 1826−1830.
(43) Zheng, G.; Chen, Y.; Bu, L.; Xu, L.; Su, W. Waveguide-coupled surface phonon resonance sensors with super-resolution in the mid-infrared region. *Opt. Lett.* **2016**, *41*, 1582.

DOI: 10.1021/acsphotonics.7b00118
ACS Photonics 2017, 4, 1048−1053

4.2 Generalized 4 × 4 matrix formalism for light propagation in anisotropic stratified media: study of surface phonon polaritons in polar dielectric heterostructures

Nikolai Christian Passler and Alexander Paarmann

This publication (Passler and Paarmann, JOSA B 2017, **34**, 2128-2139 [**II**]) presents a theoretical framework for the calculation of light-matter interaction in arbitrarily anisotropic multilayer systems. Compared to previous work [107–111], the here developed formalism is numerically stable, free from discontinuities, and handles media with any isotropic or anisotropic permittivity tensor. An online version of the computer code programmed in Matlab [18] and Python [112] has been published as open source.

Most of the experimental studies conducted during this thesis investigate stratified sample systems with anisotropic materials. For all of them, the algorithm developed in this publication has been employed for predicting, analyzing and simulating the optical response of the sample, as well as fitting the experimental spectra with exceptional accuracy.

The broad applicability and user friendliness of the formalism resulted in frequent use by many research groups, which eventually led to the discovery of an error in the calculation of the electric field distributions for birefringence, that is, for media with non-zero off-diagonal elements of the dielectric permittivity tensor in the lab frame. The correction of the error was published in an erratum in 2019 [**III**], which is reprinted on page 59. All publications prior to this erratum investigate isotropic or anisotropic media with diagonal permittivity tensor, and thus are not affected by the error in the original formalism.

Author contributions

N.C.P. and A.P. originated the concept. The manuscript was written by **N.C.P.** and A.P. **N.C.P.** devised the fundamental framework of the formalism, and **N.C.P.** and A.P. developed the final algorithm. Computations of the example systems were completed by A.P. and **N.C.P.** The project management was provided by A.P.

go to list of publications

Research Article | Journal of the Optical Society of America B 1

Generalized 4×4 Matrix Formalism for Light Propagation in Anisotropic Stratified Media: Study of Surface Phonon Polaritons in Polar Dielectric Heterostructures

NIKOLAI CHRISTIAN PASSLER[1,*] AND ALEXANDER PAARMANN[1]

[1] Fritz-Haber-Institut der Max-Planck-Gesellschaft, Faradayweg 4-6,14195 Berlin, Germany
[*] Corresponding author: passler@fhi-berlin.mpg.de

Compiled August 23, 2017

We present a generalized 4×4 matrix formalism for the description of light propagation in birefringent stratified media. In contrast to previous work, our algorithm is capable of treating arbitrarily anisotropic or isotropic, absorbing or non-absorbing materials and is free of discontinous solutions. We calculate the reflection and transmission coefficients and derive equations for the electric field distribution for any number of layers. The algorithm is easily comprehensible and can be straight forwardly implemented in a computer program. To demonstrate the capabilities of the approach, we calculate the reflectivities, electric field distributions, and dispersion curves for surface phonon polaritons excited in the Otto geometry for selected model systems, where we observe several distinct phenomena ranging from critical coupling to mode splitting, and surface phonon polaritons in hyperbolic media.

OCIS codes:

http://dx.doi.org/10.1364/ao.XX.XXXXXX

1. INTRODUCTION

Light-matter interaction in complex hybrid nanostructures has become a central problem of modern nanophotonics [1]. Specifically thin films, periodic layered media or other stratified systems have proven to exhibit extensive functionality, for instance in anti-reflection coatings [2, 3], transistors [4, 5], thin-film photovoltaics [6, 7], or sensing [8–10]. However, the angle of incidence-dependent calculation of light propagation in a general multilayer structure rapidly becomes cumbersome, especially if optical anisotropy and absorption are taken into account. In order to solve this problem, many authors have presented 4×4 matrix approaches [11–17] based on Maxwell's equations. However, many of these methods consider only special cases of the dielectric tensor [11, 14, 15, 17] or lead to discontinuous solutions [13, 16].

These problems become particularly critical in the mid- and far-infrared Reststrahlen spectral region of polar dielectrics [18], where surface phonon polaritons (SPhPs) can be excited [19–22]. Here, the highly dispersive and often strongly anisotropic behavior of the dielectric function precludes the use of formalisms that are restricted to special cases. However, it is exactly in these materials and atomic-scale heterostructures thereof [23–26], that SPhPs have very recently been demonstrated to enable many novel phenomena such as hyperbolic superlensing [27, 28] and negative refraction [29, 30]. For instance, hexagonal boron nitride as one of the key components of van der Waals heterostructures [31], displays many interesting nanophotonic properties due to its naturally hyperbolic character [23, 28, 30, 32, 33]. Therefore, a most general, robust, and easily implementable numerical formalism to analyze the optical response in arbitrarily anisotropic multilayer heterostructures is highly desirable.

In this work, we present a comprehensible 4×4 matrix formalism, which can be straight-forwardly implemented in a computer program [34]. Our algorithm combines several previous approaches [11–15] in such a way that numerical instabilities and discontinuous solutions are prevented, to enable a robust treatment of light incident on any number of arbitrarily anisotropic or isotropic, absorbing or non-absorbing layers. In addition to reflection and transmission coefficients, we also calculate the full electric field distributions throughout the heterostructure, which is particularly useful for analysis of polariton modes and their associated local field enhancements. To demonstrate the capabilities of our algorithm, we present simulation results for several model systems where SPhPs can be excited using prism coupling in the Otto geometry [20]: 6H-SiC, GaN/SiC, SiC/GaN/SiC, and α-quartz, covering a number of phenomena such as critical coupling to SPhPs [21, 22], index-sensing

Passler, N.C., Paarmann, A.,
Generalized 4x4 matrix formalism for light propagation in anisotropic stratified media: study of surface phonon polaritons in polar dielectric heterostructures.
Journal of the Optical Society of America B 2017, 34, 10, 2128-2139. https://doi.org/10.1364/JOSAB.34.002128

[35], mode-splitting [36], wave-guiding [37], and polaritons in hyperbolic media [29, 32].

2. THEORY

A. Matrix Formalism

The incident medium is assumed to be non-absorptive and isotropic, and the magnetic permeability μ is taken as a scalar. The coordinate system is defined such that the multilayer surfaces are parallel to the x-y-plane and the z-direction is orthogonal to the surface, pointing from the incident medium towards the substrate and being zero at the first interface between incident medium and layer $i = 1$. The layers are indexed from $i = 1$ to $i = N$, whereas the incident medium is $i = 0$ and the substrate $i = N + 1$. Each layer has an individual thickness d_i, and the thickness of the complete multilayer system is $D = \sum_{i=1}^{N} d_i$. Furthermore, each medium i is characterized by an individual dielectric tensor $\bar{\varepsilon}_i$. The incident beam is chosen to propagate in the x-z-plane with a wave vector $\vec{k}_i$ in layer i:

$$\vec{k}_i = \frac{\omega}{c}(\xi, 0, q_i), \tag{1}$$

where $\xi = \sqrt{\varepsilon_{inc}}\,\sin(\theta)$ is the x-component of $\vec{k}_i$ which is conserved throughout the complete multilayer system, ε_{inc} is the isotropic dielectric constant of the incident medium, θ is the incident angle, and q_i is the dimensionless z-component of the wave vector in layer i.

For a given diagonal dielectric tensor $\bar{\varepsilon}$ with principle dielectric constants ε_x, ε_y, and ε_z, the following transformation allows to rotate the crystal orientation into the lab frame:

$$\bar{\varepsilon}' = \Omega\,\bar{\varepsilon}\,\Omega^{-1} = \Omega \begin{pmatrix} \varepsilon_x & 0 & 0 \\ 0 & \varepsilon_y & 0 \\ 0 & 0 & \varepsilon_z \end{pmatrix} \Omega^{-1}, \tag{2}$$

with the coordinate rotation matrix Ω given by the Euler angles ϑ, φ, and ψ (see e.g. Eq. 2 in [15]). Furthermore, optical activity or the response to a static magnetic field can be incorporated into $\bar{\varepsilon}$ [38], which then becomes non-diagonal, but this will not be discussed here.

A.1. Eigenmodes in Medium i

In general, each layer will have exactly four eigenmodes, i.e. four possible solutions for the propagation of an electromagnetic wave. They differ in polarization and propagation direction and have four different z-components of the wave vector, q_{ij}, with $j = 1, 2, 3, 4$. In order to obtain these four solutions, we follow the approach by Berreman [11], where the layer index i is omitted for brevity.

First, the Maxwell equations are written in a 6×6-matrix form, where the time derivative has already been performed, assuming monochromatic waves at frequency ω:

$$\mathbf{RG} \equiv \begin{pmatrix} 0 & 0 & 0 & 0 & -\frac{\partial}{\partial z} & \frac{\partial}{\partial y} \\ 0 & 0 & 0 & \frac{\partial}{\partial z} & 0 & -\frac{\partial}{\partial x} \\ 0 & 0 & 0 & -\frac{\partial}{\partial y} & \frac{\partial}{\partial x} & 0 \\ 0 & \frac{\partial}{\partial z} & -\frac{\partial}{\partial y} & 0 & 0 & 0 \\ -\frac{\partial}{\partial z} & 0 & \frac{\partial}{\partial x} & 0 & 0 & 0 \\ \frac{\partial}{\partial y} & -\frac{\partial}{\partial x} & 0 & 0 & 0 & 0 \end{pmatrix} \begin{pmatrix} E_x \\ E_y \\ E_z \\ H_x \\ H_y \\ H_z \end{pmatrix} = -i\omega \begin{pmatrix} D_x \\ D_y \\ D_z \\ B_x \\ B_y \\ B_z \end{pmatrix} \equiv -i\omega\mathbf{C}. \tag{3}$$

If only linear effects are considered, a relation between $\mathbf{G}$ and $\mathbf{C}$ can be formulated as follows[1]

$$\mathbf{C} = \mathbf{MG} \equiv \begin{pmatrix} \bar{\varepsilon} & \bar{\rho}_1 \\ \bar{\rho}_2 & \bar{\mu} \end{pmatrix} \mathbf{G}, \tag{4}$$

where $\bar{\mu}$ is the permeability tensor, and $\bar{\rho}_1$ and $\bar{\rho}_2$ are optical rotation tensors.

By combining Eq. 3 and 4, the following spatial wave equation is obtained, where $\mathbf{g}$ is the spatial part of $\mathbf{G} = \mathbf{g}e^{-i\omega t}$:

$$\mathbf{Rg} = -i\omega\mathbf{Mg}. \tag{5}$$

As shown explicitly by Berreman, the normal field projections $g_3 = E_z$ and $g_6 = H_z$ can be solved in terms of the other four parameters, and thus be eliminated. In short, this yields

$$\frac{\partial}{\partial z}\Psi = i\frac{\omega}{c}\mathbf{\Delta}\Psi, \tag{6}$$

where

$$\Psi = \begin{pmatrix} E_x \\ H_y \\ E_y \\ -H_x \end{pmatrix} \tag{7}$$

is the reordered dimensionless field vector. $\mathbf{\Delta}$ is exactly defined

[1] Please note the difference to the original work by Berremann, who instead reports $\mathbf{G} = \mathbf{MC}$ in Eq. (3) of Ref. [11].

in terms of **M** as follows:

$$\begin{aligned}
\Delta_{11} &= M_{51} + (M_{53}+\xi)a_{31} + M_{56}a_{61}\\
\Delta_{12} &= M_{55} + (M_{53}+\xi)a_{35} + M_{56}a_{65}\\
\Delta_{13} &= M_{52} + (M_{53}+\xi)a_{32} + M_{56}a_{62}\\
\Delta_{14} &= -M_{54} - (M_{53}+\xi)a_{34} - M_{56}a_{64}\\
\Delta_{21} &= M_{11} + M_{13}a_{31} + M_{16}a_{61}\\
\Delta_{22} &= M_{15} + M_{13}a_{35} + M_{16}a_{65}\\
\Delta_{23} &= M_{12} + M_{13}a_{32} + M_{16}a_{62}\\
\Delta_{24} &= -M_{14} - M_{13}a_{34} - M_{16}a_{64}\\
\Delta_{31} &= -M_{41} - M_{43}a_{31} - M_{46}a_{61}\\
\Delta_{32} &= -M_{45} - M_{43}a_{35} - M_{46}a_{65}\\
\Delta_{33} &= -M_{42} - M_{43}a_{32} - M_{46}a_{62}\\
\Delta_{34} &= M_{44} + M_{43}a_{34} + M_{46}a_{64}\\
\Delta_{41} &= M_{21} + M_{23}a_{31} + (M_{26}-\xi)a_{61}\\
\Delta_{42} &= M_{25} + M_{23}a_{35} + (M_{26}-\xi)a_{65}\\
\Delta_{43} &= M_{22} + M_{23}a_{32} + (M_{26}-\xi)a_{62}\\
\Delta_{44} &= -M_{24} - M_{23}a_{34} - (M_{26}-\xi)a_{64},
\end{aligned} \tag{8}$$

where the elements of a_{mn} are given by

$$a_{3n} = \begin{pmatrix} (M_{61}M_{36} - M_{31}M_{66})/b \\ ((M_{62}-\xi)M_{36} - M_{32}M_{66})/b \\ 0 \\ (M_{64}M_{36} - M_{34}M_{66})/b \\ (M_{65}M_{36} - (M_{35}+\xi)M_{66})/b \\ 0 \end{pmatrix} \tag{9}$$

$$a_{6n} = \begin{pmatrix} (M_{63}M_{31} - M_{33}M_{61})/b \\ (M_{63}M_{32} - M_{33}(M_{62}-\xi))/b \\ 0 \\ (M_{63}M_{34} - M_{33}M_{64})/b \\ (M_{63}(M_{35}+\xi) - M_{33}M_{65})/b \\ 0 \end{pmatrix},$$

and b is defined by

$$b = M_{33}M_{66} - M_{36}M_{63}. \tag{10}$$

Note that $\mathbf{\Delta}$ and a_{mn}, in contrast to the formulas given by Berreman, do not contain the factor $\frac{c}{\omega}$ before each ξ, which is because ξ is chosen to be dimensionless here.

The **M**-matrix of the corresponding material is assumed to be z-independent, i.e. we only consider homogeneous layers (a numerical solution if **M** depends on z has been given by Berreman [11]). In the z-independent case, the four eigenvalues q_{ij} of $\Delta(i)$, indexed with j for each layer i, represent the z-components of the wave vectors of the four eigenmodes Ψ_{ij} in the material:

$$q_{ij}\mathbf{\Delta}(i) = \Psi_{ij}\mathbf{\Delta}(i). \tag{11}$$

A.2. Sorting of the Eigenmodes

At this point, the four solutions have to be ordered in an unambiguous manner in order to avoid unstable solutions and discontinuities. The approach presented here is based on the work of Li *et al.* [12]. First of all, the modes have to be separated into forward propagating (transmitted) and backward propagating (reflected) waves, which is done as follows:

$$\begin{aligned}
q_{ij} \text{ is real:} \quad & q_{ij} \geq 0 \longrightarrow \text{transmitted}\\
& q_{ij} < 0 \longrightarrow \text{reflected}\\
q_{ij} \text{ is complex:} \quad & Im(q_{ij}) \geq 0 \longrightarrow \text{transmitted}\\
& Im(q_{ij}) < 0 \longrightarrow \text{reflected},
\end{aligned} \tag{12}$$

because real wave vectors point in the propagation direction, and complex wave vectors describe an exponentially damped wave. The transmitting waves will be labeled q_{i1} and q_{i2}, the reflected waves q_{i3} and q_{i4}. Each pair, however, also has to be sorted in order to ensure solutions without discontinuities. For this, the eigenvectors Ψ_{ij} of Eq. 11 of each layer are analyzed by [12]

$$C(q_{ij}) = \frac{|\Psi_{ij1}|^2}{|\Psi_{ij1}|^2 + |\Psi_{ij3}|^2}, \tag{13}$$

allowing to finally sort the four eigenvalues as follows:

$$C(q_{i1}) > C(q_{i2}) \quad \text{and} \quad C(q_{i3}) > C(q_{i4}). \tag{14}$$

This means for the four solutions, that q_{i1} and q_{i3} describe p-polarized, and q_{i2} and q_{i4} s-polarized waves, transmitted and reflected, respectively.

In the case of birefringence, i.e., for at least one principle axis of a anisotropic dielectric tensor neither in the $x-y$ plane nor along the y-axis, the assignment of modes being either s- and p-polarized fails, resulting in ambiguous sorting of the four eigenmodes, and in consequence, potentially discontinuous solutions. In these cases, the Poynting vector S_{ij} need to be analyzed in Eq. 13 instead of the electric field:

$$C(q_{ij}) = \frac{|S_{ijx}|^2}{|S_{ijx}|^2 + |S_{ijy}|^2}, \tag{15}$$

with

$$S_{ij} = \begin{pmatrix} S_{ijx} \\ S_{ijy} \\ S_{ijz} \end{pmatrix} = \vec{E}_{ij} \times \vec{H}_{ij} = \begin{pmatrix} E_{ijy}H_{ijz} - E_{ijz}H_{ijy} \\ E_{ijz}H_{ijx} - E_{ijx}H_{ijz} \\ E_{ijx}H_{ijy} - E_{ijy}H_{ijx} \end{pmatrix}, \tag{16}$$

where with Eq. 7, $E_{ijx} = \Psi_{ij1}$, $E_{ijy} = \psi_{ij3}$, $H_{ijx} = -\psi_{ij4}$,$H_{ijy} = \psi_{ij2}$, and [11]

$$E_{ijz} = a_{31}(i)E_{ijx} + a_{32}(i)E_{ijy} + a_{34}(i)H_{ijx} + a_{35}(i)H_{ijy} \tag{17}$$

$$H_{ijz} = a_{61}(i)E_{ijx} + a_{62}(i)E_{ijy} + a_{64}(i)H_{ijx} + a_{65}(i)H_{ijy}. \tag{18}$$

A.3. Transfer Matrix with Treatment of Singularities

In previous works [11, 14, 15], the authors assume fully anisotropic dielectric tensors, and their formalisms suffer from singularities for several special cases, i.e. if the material is isotropic, or even if the dielectric tensor has only diagonal components. These cases have in common that the four solutions of Eq. 11 become degenerate. To resolve this issue, we here follow the solution presented by Xu *et al.* [13]. We note, however, that the authors only considered non-optical active media

with isotropic magnetic permeability, such that in the following we also set $\bar{\mu} = \mu\,\bar{1}$ and $\bar{\rho}_1 = \bar{\rho}_2 = \bar{0}$, with $\bar{1}$ and $\bar{0}$ the unity matrix and the matrix consisting just of zeros, respectively. More general solutions to avoid singularities also without these restrictions are beyond the scope of this work.

To set up the transfer matrix according to Xu *et al.* [13] using the appropriately sorted q_{ij}, we now write the electric field vectors $\vec{\gamma}_{ij}$ of the four eigenmodes in each layer i as follows:

$$\vec{\gamma}_{ij} = \begin{pmatrix} \gamma_{ij1} \\ \gamma_{ij2} \\ \gamma_{ij3} \end{pmatrix}. \tag{19}$$

The values of γ_{ijk}, being free of singularities, are then given by the following formulas [13]:

$$\begin{aligned}
&\gamma_{i11} = \gamma_{i22} = \gamma_{i42} = -\gamma_{i31} = 1,\\
&\gamma_{i12} = \begin{cases} 0, & q_{i1} = q_{i2} \\ \frac{\mu_i\varepsilon_{i23}(\mu_i\varepsilon_{i31}+\xi q_{i1}) - \mu_i\varepsilon_{i21}(\mu_i\varepsilon_{i33}-\xi^2)}{(\mu_i\varepsilon_{i33}-\xi^2)(\mu_i\varepsilon_{i22}-\xi^2-q_{i1}^2) - \mu_i^2\varepsilon_{i23}\varepsilon_{i32}}, & q_{i1} \neq q_{i2} \end{cases}\\
&\gamma_{i13} = \begin{cases} -\frac{\mu_i\varepsilon_{i31}+\xi q_{i1}}{\mu_i\varepsilon_{i33}-\xi^2}, & q_{i1} = q_{i2} \\ -\frac{\mu_i\varepsilon_{i31}+\xi q_{i1}}{\mu_i\varepsilon_{i33}-\xi^2} - \frac{\mu_i\varepsilon_{i32}}{\mu_i\varepsilon_{i33}-\xi^2}\gamma_{i12}, & q_{i1} \neq q_{i2} \end{cases}\\
&\gamma_{i21} = \begin{cases} 0, & q_{i1} = q_{i2} \\ \frac{\mu_i\varepsilon_{i32}(\mu_i\varepsilon_{i13}+\xi q_{i2}) - \mu_i\varepsilon_{i12}(\mu_i\varepsilon_{i33}-\xi^2)}{(\mu_i\varepsilon_{i33}-\xi^2)(\mu_i\varepsilon_{i11}-q_{i2}^2) - (\mu_i\varepsilon_{i13}+\xi q_{i2})(\mu_i\varepsilon_{i31}+\xi q_{i2})}, & q_{i1} \neq q_{i2} \end{cases}\\
&\gamma_{i23} = \begin{cases} -\frac{\mu_i\varepsilon_{i32}}{\mu_i\varepsilon_{i33}-\xi^2}, & q_{i1} = q_{i2} \\ -\frac{\mu_i\varepsilon_{i31}+\xi q_{i2}}{\mu_i\varepsilon_{i33}-\xi^2}\gamma_{i21} - \frac{\mu_i\varepsilon_{i32}}{\mu_i\varepsilon_{i33}-\xi^2}, & q_{i1} \neq q_{i2} \end{cases}\\
&\gamma_{i32} = \begin{cases} 0, & q_{i3} = q_{i4} \\ \frac{\mu_i\varepsilon_{i21}(\mu_i\varepsilon_{i33}+\xi^2) - \mu_i\varepsilon_{i23}(\mu_i\varepsilon_{i31}+\xi q_{i3})}{(\mu_i\varepsilon_{i33}-\xi^2)(\mu_i\varepsilon_{i22}-\xi^2-q_{i3}^2) - \mu_i^2\varepsilon_{i23}\varepsilon_{i32}}, & q_{i3} \neq q_{i4} \end{cases}\\
&\gamma_{i33} = \begin{cases} \frac{\mu_i\varepsilon_{i31}+\xi q_{i3}}{\mu_i\varepsilon_{i33}-\xi^2}, & q_{i3} = q_{i4} \\ \frac{\mu_i\varepsilon_{i31}+\xi q_{i3}}{\mu_i\varepsilon_{i33}-\xi^2} + \frac{\mu_i\varepsilon_{i32}}{\mu_i\varepsilon_{i33}-\xi^2}\gamma_{i32}, & q_{i3} \neq q_{i4} \end{cases}\\
&\gamma_{i41} = \begin{cases} 0, & q_{i3} = q_{i4} \\ \frac{\mu_i\varepsilon_{i32}(\mu_i\varepsilon_{i13}+\xi q_{i4}) - \mu_i\varepsilon_{i12}(\mu_i\varepsilon_{i33}-\xi^2)}{(\mu_i\varepsilon_{i33}-\xi^2)(\mu_i\varepsilon_{i11}-q_{i4}^2) - (\mu_i\varepsilon_{i13}+\xi q_{i4})(\mu_i\varepsilon_{i31}+\xi q_{i4})}, & q_{i3} \neq q_{i4} \end{cases}\\
&\gamma_{i43} = \begin{cases} -\frac{\mu_i\varepsilon_{i32}}{\mu_i\varepsilon_{i33}-\xi^2}, & q_{i3} = q_{i4} \\ -\frac{\mu_i\varepsilon_{i31}+\xi q_{i4}}{\mu_i\varepsilon_{i33}-\xi^2}\gamma_{i41} - \frac{\mu_i\varepsilon_{i32}}{\mu_i\varepsilon_{i33}-\xi^2}, & q_{i3} \neq q_{i4}. \end{cases}
\end{aligned} \tag{20}$$

These solutions are finite and continuous for isotropic and anisotropic media, and therefore can be used to formulate a generalized, stable transfer matrix.

For this purpose, the boundary conditions for electric and magnetic fields are applied in order to connect the fields of two adjacent layers $i-1$ and i. Formulated for all four modes simultaneously, the boundary conditions in matrix form become:

$$\mathbf{A}_{i-1}\vec{E}_{i-1} = \mathbf{A}_i\vec{E}_i, \tag{21}$$

where $\mathbf{A}_i$ is calculated in terms of γ_{ijk} by [13]

$$\mathbf{A}_i = \begin{pmatrix} \gamma_{i11} & \gamma_{i21} & \gamma_{i31} & \gamma_{i41} \\ \gamma_{i12} & \gamma_{i22} & \gamma_{i32} & \gamma_{i42} \\ \frac{q_{i1}\gamma_{i11}-\xi\gamma_{i13}}{\mu_i} & \frac{q_{i2}\gamma_{i21}-\xi\gamma_{i23}}{\mu_i} & \frac{q_{i3}\gamma_{i31}-\xi\gamma_{i33}}{\mu_i} & \frac{q_{i4}\gamma_{i41}-\xi\gamma_{i43}}{\mu_i} \\ \frac{1}{\mu_i}q_{i1}\gamma_{i12} & \frac{1}{\mu_i}q_{i2}\gamma_{i22} & \frac{1}{\mu_i}q_{i3}\gamma_{i32} & \frac{1}{\mu_i}q_{i4}\gamma_{i42} \end{pmatrix}, \tag{22}$$

and $\vec{E}_i$ is the dimensionless 4-component electric field vector of the solution, i.e., representing the field for the full multilayer system. Conveniently, $\vec{E}_i$ is defined as [13]:

$$\vec{E} \equiv \begin{pmatrix} E^p_{\text{trans}} \\ E^s_{\text{trans}} \\ E^p_{\text{refl}} \\ E^s_{\text{refl}} \end{pmatrix} \tag{23}$$

where $E^{p(s)}_{\text{trans}}$ and $E^{p(s)}_{\text{refl}}$ are the in-plane field amplitudes of the transmitted and reflected mode, p-polarized and s-polarized, respectively.

By multiplying $\mathbf{A}_i^{-1}$ on both sides of eq. 21, the following relation is obtained, where the interface matrix $\mathbf{L}_i$ is defined implicitly:

$$\vec{E}_{i-1} = \mathbf{A}_{i-1}^{-1}\mathbf{A}_i\vec{E}_i \equiv \mathbf{L}_i\vec{E}_i. \tag{24}$$

By inspection of eq. 22 it becomes clear that the columns of matrix $\mathbf{A}_i$ resemble the four eigenmodes Ψ_{ij} of the respective layer, however, with the order of the elements being E_x, E_y, H_x, and H_y. Therefore, the matrix operation $\mathbf{A}_i\vec{E}_i$ essentially represents the projection of the solution field vector onto the eigenmodes of the layer, while $\mathbf{A}_{i-1}^{-1}\mathbf{A}_i$ projects the eigenmodes in layer i onto the ones of layer $i-1$. The different order of the column vector elements as compared to eq. 7 must be accounted for, which will be done conveniently after formulating the transfer matrix of the complete multilayer system.

In order to do so, first the propagation matrix $\mathbf{P}_i$, as it was called by Yeh [15], has to be defined. For the sign convention chosen here, it is given by

$$\mathbf{P}_i = \begin{pmatrix} e^{-i\frac{\omega}{c}q_{i1}d_i} & 0 & 0 & 0 \\ 0 & e^{-i\frac{\omega}{c}q_{i2}d_i} & 0 & 0 \\ 0 & 0 & e^{-i\frac{\omega}{c}q_{i3}d_i} & 0 \\ 0 & 0 & 0 & e^{-i\frac{\omega}{c}q_{i4}d_i} \end{pmatrix}. \tag{25}$$

With this, the transfer matrix $\mathbf{T}_i$ of a single layer i, which is composed of parts from the enclosing interface matrices and the propagation matrix, is defined as:

$$\mathbf{T}_i = \mathbf{A}_i\mathbf{P}_i\mathbf{A}_i^{-1}, \tag{26}$$

and the transfer matrix $\mathbf{T}_{\text{tot}}$ of all N layers is then obtained by evaluating

$$\mathbf{T}_{\text{tot}} = \prod_{i=1}^{N}\mathbf{T}_i. \tag{27}$$

However, $\mathbf{T}_{\text{tot}}$ on its own is not sufficient to calculate the reflectivity or transmittance of the multilayer system, since for the first and the last interface, i.e. the interfaces with the incident

medium $i = 0$ and the substrate $i = N + 1$, only half of the interface matrices $\mathbf{L}_1$ and $\mathbf{L}_{N+1}$ are included. The full transfer matrix $\mathbf{\Gamma}_N$ is obtained as follows, where different notations are shown in order to clarify the equivalence of the various approaches found in the literature [11, 13–15]:

$$\begin{aligned}\mathbf{\Gamma}_N &= \mathbf{A}_0^{-1}\mathbf{T}_{\text{tot}}\mathbf{A}_{N+1}\\ &= \mathbf{A}_0^{-1}\mathbf{T}_1\mathbf{T}_2...\mathbf{T}_N\mathbf{A}_{N+1}\\ &= \mathbf{A}_0^{-1}\mathbf{A}_1\mathbf{P}_1\mathbf{A}_1^{-1}\mathbf{A}_2\mathbf{P}_2\mathbf{A}_2^{-1}...\mathbf{A}_N\mathbf{P}_N\mathbf{A}_N^{-1}\mathbf{A}_{N+1}\\ &= \mathbf{L}_1\mathbf{P}_1\mathbf{L}_2\mathbf{P}_2...\mathbf{L}_N\mathbf{P}_N\mathbf{L}_{N+1}.\end{aligned} \tag{28}$$

The first line is perfectly suited for the implementation in a computer program, and furthermore allows to directly see how the transfer matrix of a single interface ($N = 0$) is calculated, i.e. $\mathbf{\Gamma}_0 = \mathbf{A}_0^{-1}\mathbf{A}_1$. The last line, on the other hand, illustrates how systematic the matrix approach solves the propagation of electromagnetic waves in a multilayer medium, simply stringing together interface matrices $\mathbf{L}_i$ and propagation matrices $\mathbf{P}_i$, for each interface and layer, respectively.

From the full transfer matrix $\mathbf{\Gamma}_N$, reflection and transmission coefficients for both s- and p-polarized incident, reflected, and transmitted waves can be calculated, as it has been shown by Yeh [15], using:

$$\vec{E}_0^- = \mathbf{\Gamma}_N\vec{E}_{N+1}^+, \tag{29}$$

where $\vec{E}_{i-1}^-$ and $\vec{E}_i^+$ denote the fields on both sides of the interface between layer i and $i-1$, respectively, see Fig. 1 (a). However, before writing down the equations, the matrix $\mathbf{\Gamma}_N$ has to be transformed such that the order of the field components corresponds to the chosen order of Yeh:

$$\vec{E}^* = \begin{pmatrix} E^p_{\text{trans}} \\ E^p_{\text{refl}} \\ E^s_{\text{trans}} \\ E^s_{\text{refl}} \end{pmatrix}, \tag{30}$$

in contrast to the sorting shown in Eq. 23, which the transfer matrix $\mathbf{\Gamma}_N$ is built from. Therefore, the transformation

$$\mathbf{\Gamma}_N^* = \Lambda_{1324}^{-1}\mathbf{\Gamma}_N\Lambda_{1324}, \tag{31}$$

where Λ_{1324} is given by

$$\Lambda_{1324} = \begin{pmatrix} 1 & 0 & 0 & 0 \\ 0 & 0 & 1 & 0 \\ 0 & 1 & 0 & 0 \\ 0 & 0 & 0 & 1 \end{pmatrix}, \tag{32}$$

yields the transfer matrix $\mathbf{\Gamma}_N^*$ that is compatible with the Yeh formalism [15].

B. Reflectivity and Transmittance

Employing the transformed transfer matrix of the complete multilayer system $\mathbf{\Gamma}_N^*$, the reflection and transmission coefficients for s- and p-polarized light, i.e. r_{ss}, r_{pp}, t_{ss}, and t_{pp}, and the mode coupling reflection and transmission coefficients r_{sp}, r_{ps}, t_{sp}, and t_{ps} can be calculated, where the subscripts refer to incoming and outgoing polarization, respectively. The coefficients are given in terms of the matrix elements of $\mathbf{\Gamma}_N^*$ as follows [15]:

$$r_{pp} = \frac{\Gamma^*_{21}\Gamma^*_{33} - \Gamma^*_{23}\Gamma^*_{31}}{\Gamma^*_{11}\Gamma^*_{33} - \Gamma^*_{13}\Gamma^*_{31}} \qquad t_{pp} = \frac{\Gamma^*_{33}}{\Gamma^*_{11}\Gamma^*_{33} - \Gamma^*_{13}\Gamma^*_{31}} \tag{33}$$

$$r_{ss} = \frac{\Gamma^*_{11}\Gamma^*_{43} - \Gamma^*_{41}\Gamma^*_{13}}{\Gamma^*_{11}\Gamma^*_{33} - \Gamma^*_{13}\Gamma^*_{31}} \qquad t_{ss} = \frac{-\Gamma^*_{11}}{\Gamma^*_{11}\Gamma^*_{33} - \Gamma^*_{13}\Gamma^*_{31}} \tag{34}$$

$$r_{ps} = \frac{\Gamma^*_{41}\Gamma^*_{33} - \Gamma^*_{43}\Gamma^*_{31}}{\Gamma^*_{11}\Gamma^*_{33} - \Gamma^*_{13}\Gamma^*_{31}} \qquad t_{ps} = \frac{\Gamma^*_{31}}{\Gamma^*_{11}\Gamma^*_{33} - \Gamma^*_{13}\Gamma^*_{31}} \tag{35}$$

$$r_{sp} = \frac{\Gamma^*_{11}\Gamma^*_{23} - \Gamma^*_{21}\Gamma^*_{13}}{\Gamma^*_{11}\Gamma^*_{33} - \Gamma^*_{13}\Gamma^*_{31}} \qquad t_{sp} = \frac{\Gamma^*_{13}}{\Gamma^*_{11}\Gamma^*_{33} - \Gamma^*_{13}\Gamma^*_{31}}, \tag{36}$$

and the reflectivity R and intensity enhancement T for a certain polarization are obtained by calculating the absolute square of the corresponding coefficient, i.e. $R_{kl} = |r_{kl}|^2$ and $T_{kl} = |t_{kl}|^2$ with $k, l = s, p$. Please note that the total transmission of the multilayer stack is distinct from T, where additionally energy conservation needs to be accounted for. In the case of an absorptive substrate, the transmission coefficients represent the magnitude of the in-plane component of the $\vec{E}$-field vector in the substrate at the interface with layer N. This particular fact will be clarified in the following, where we calculate the electric field distribution in the multilayer system employing the presented transfer-matrix formalism.

C. Electric Field Distribution

Using the interface and propagation matrices $\mathbf{L}_i$ and $\mathbf{P}_i$, respectively, an electric field vector can be projected to any point in the multilayer system. As a starting point, the transmission coefficients are utilized to formulate the in-plane components of the electric field $\vec{E}_{N+1}^+$ in the substrate at the interface with layer N, see Fig. 1 (a):

$$\vec{E}_{N+1}^+ = \begin{pmatrix} E^p_{\text{trans}} \\ E^s_{\text{trans}} \\ E^p_{\text{refl}} \\ E^s_{\text{refl}} \end{pmatrix} = \begin{pmatrix} t_{pp} + t_{sp} \\ t_{ss} + t_{ps} \\ 0 \\ 0 \end{pmatrix}, \tag{37}$$

where the reflected components are set to zero, since no light source is assumed to be on the substrate side of the multilayer system. Please note that we here conveniently go back to the field sorting according to eq. 23, allowing to directly reuse any interface and propagation matrices that were calculated along the way to the full transfer matrix $\mathbf{\Gamma}_N$. As it is shown in Fig. 1 (a), the electric field vectors on both sides of an interface are connected by the interface matrix $\vec{E}_{i-1}^- = \mathbf{L}_i\vec{E}_i^+$. Furthermore, the propagation through layer i is given by the propagation matrix $\mathbf{P}_i$, which can be evaluated z-dependently:

$$\begin{aligned}\vec{E}_i(z) &= \mathbf{P}_i(z)\vec{E}_i^-\\ &= \begin{pmatrix} e^{-i\frac{\omega}{c}q_{i1}z} & 0 & 0 & 0 \\ 0 & e^{-i\frac{\omega}{c}q_{i2}z} & 0 & 0 \\ 0 & 0 & e^{-i\frac{\omega}{c}q_{i3}z} & 0 \\ 0 & 0 & 0 & e^{-i\frac{\omega}{c}q_{i4}z} \end{pmatrix}\vec{E}_i^-,\end{aligned} \tag{38}$$

with $0 < z < d_i$ being the relative z-position in layer i. As it is indicated by the black arrows in Fig. 1, starting from $\vec{E}_{N+1}^+$, interface matrices $\mathbf{L}_i$ and propagation matrices $\mathbf{P}_i$ are used to

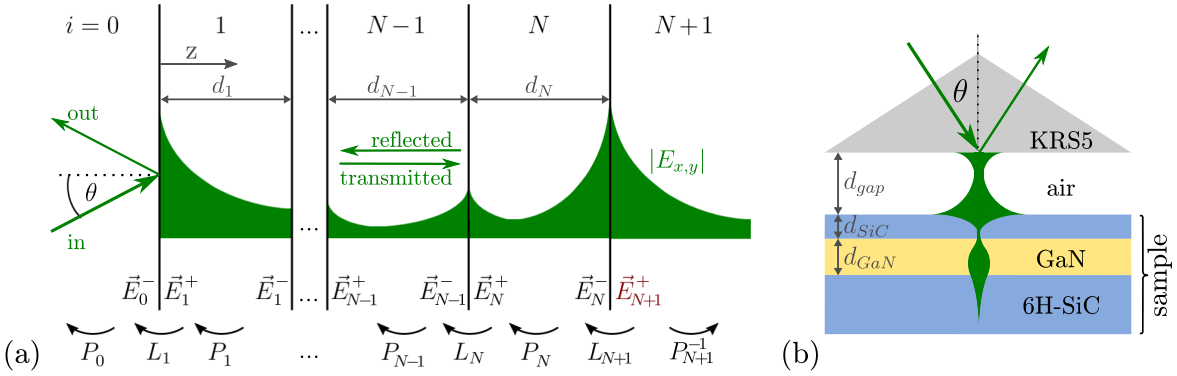

Fig. 1. (a) By means of the transfer-matrix formalism, the $\vec{E}$-field distribution can be calculated at any point in the multilayer system. Starting from $\vec{E}^{+}_{N+1}$, subsequent multiplication of the interface matrices $\mathbf{L}_i$ and propagation matrices $\mathbf{P}_i$ allows to propagate the wave back to the incident medium, and into the substrate. For the case of evanescent waves, the $\vec{E}$-field is exemplary sketched in green. (b) In the Otto geometry (not to scale), a highly refractive prism provides the necessary in-plane momentum for resonant coupling to SPhPs, propagating along the interfaces of the multilayer system. Here, the SiC / GaN / SiC heterostructure is sketched, discussed in Sec. 3C.

subsequently propagate the wave towards the incident medium. In the reverse direction, the inverse propagation matrix $\mathbf{P}^{-1}_{N+1}$ allows to calculate the $\vec{E}$-fields in the substrate.

By this means, the four in-plane components E^{p}_{trans}, E^{s}_{trans}, E^{p}_{refl}, and E^{s}_{refl} are obtained as a function of z. Within each layer, there are only two possible shapes of the absolute amplitude of these components: they either describe a (damped) sinusoidal propagating wave, or an exponentially decaying evanescent wave. In order to get the complete field present in the multilayer system, the forward (transmitted) and backward (reflected) components for each polarization have to be added up. This summation of the components is performed as follows:

$$E_x = E^{p}_{\text{trans}} - E^{p}_{\text{refl}} \tag{39}$$

$$E_y = E^{s}_{\text{trans}} + E^{s}_{\text{refl}} \tag{40}$$

$$E_z = \left(-\frac{\xi\varepsilon_x}{q_{i1}\varepsilon_z}E^{p}_{\text{trans}}\right) - \left(-\frac{\xi\varepsilon_x}{q_{i3}\varepsilon_z}E^{p}_{\text{refl}}\right), \tag{41}$$

where the negative signs for E_x and E_z account for the phase flip during reflection. The out-of-plane component E_z has been calculated employing Maxwell's Eq. $\nabla \times \vec{H} = \varepsilon\frac{d\vec{E}}{dt}$ for E^{p}_{trans} and E^{p}_{refl} individually. The corresponding out-of-plane wave vector components q_z are given by the layer-dependent solutions $j = 1$ and $j = 3$, i.e. $q^{p}_{\text{trans}} = q_{i1}$ and $q^{p}_{\text{refl}} = q_{i3}$, as defined in Eqs. 12 and 14. Note that Eq. 41 is only valid for a dielectric tensor that is diagonal in the lab frame.

In the case of evanescent waves, the $\vec{E}$ field components typically have peaks at the interfaces and valleys inside the layers, which is sketched in Fig. 1 (a) in green. Such evanescent waves can occur for strong absorption in the medium or, alternatively, if the incident angle θ is larger than the critical angle of total internal reflection from the incidence medium to medium $i = 1$, implying that the refractive indices fulfill $n_0 > n_1$. This is the case for resonant excitation of SPhPs in the Otto geometry [20–22], being analyzed in section 3.

D. Distinction to Previous Algorithms

In the last decades, many authors have provided different 4×4 matrix approaches for the calculation of light propagation in anisotropic stratified media, but either they focus on special cases, thus lacking full generality, or the calculation, when implemented in a computer program, leads to numerical instabilities. For instance, the Berreman and Yeh formalisms [11, 15] as well as the generalized approach by Lin-Chung and Teitler [14] assume solely fully anisotropic tensors, and hence lead to singularities if the material is isotropic or even if the three main dielectric components coincide with the laboratory coordinate system. A solution to these singularities is given by Xu [13], who, on the other hand, provides an unstable solution for solving the eigensystem of electric field modes of the multilayer system. Neither of these approaches delivers a robust strategy for uniquely assigning the different modes in each layer, as given by Li *et al.* [12]. Here, by combining the different approaches, a numerically stable formalism is achieved, which is capable of handling isotropic or anisotropic, as well as absorbing or non-absorbing materials for each layer including the substrate.

Specifically, we calculate the four eigenmodes of each layer as derived by Berreman [11], which are correctly sorted into forward and backward, s- and p-polarized rays using the approach of Li *et al.* [12]. The four eigenvalues q_{ij} are used to obtain interface matrices free from discontinuities as shown by Xu *et al.* [13]. Following the generalized approach of Lin-Chung *et al.* [14], we then compose the complete transfer matrix correctly, and finally specify the transformation necessary for the calculation of reflection and transmission coefficients based on the work of Yeh [15]. In addition, we specifically illustrate how to calculate the electric field distribution throughout the full heterostructure. The formalism presented here is tailored for the robust calculation of light propagation in any isotropic or anisotropic stratified medium. Its generalized form is mandatory for the simulations involving highly dispersive and strongly anisotropic dielectric permittivities, as it is the case for SPhPs in polar dielectric heterostructures, being discussed in the following section.

3. SIMULATIONS

In general, the transfer-matrix formalism presented in the previous section can be employed for any wavelength and any number of layers, each described by an arbitrary dielectric ten-

sor. In the following, we focus on SPhPs in polar crystals in the mid-infrared spectral region. These surface modes exist due to negative dielectric permittivity in the Reststrahlen band between the transverse optical (TO) and longitudinal optical (LO) frequencies [20]. All cases discussed in the following are also implemented in the Matlab example code [34].

Specifically, we employ our formalism for the simulation of SPhP resonances in four different model systems: bare 6H-silicon carbide (SiC) in Sec. A, a thin layer of gallium nitride (GaN) on top of 6H-SiC in Sec. B, an additional thin SiC layer on top of GaN/SiC in Sec. C, as sketched in Fig. 1 (b), and α-quartz in Sec. D. We chose these model heterostructures built from anisotropic, polar dielectrics in order to briefly demonstrate the variety of SPhP modes than can exist in such stratified systems, as a starting point for future detailed studies of the SPhPs in these and similar structures.

All materials considered here are uniaxial, and for Sections A, B, and C, the crystal axes are chosen to be normal to the sample surface, i.e. $\bar{\varepsilon} = \Big((\varepsilon_\perp, 0, 0), (0, \varepsilon_\perp, 0), (0, 0, \varepsilon_\parallel)\Big)$ with the ordinary and extraordinary dielectric functions, $\varepsilon_\perp$ and $\varepsilon_\parallel$, respectively, taken from literature [39, 40]. In Sec. D, we simulate the dispersion of SPhPs for different crystal orientations of α-quartz [41], being a natural hyperbolic material [29] in the frequency range of $350 - 600\ \mathrm{cm}^{-1}$. For all schemes, the SPhPs are excited in the Otto geometry [20, 21] using KRS5 as a highly refractive coupling medium ($n \approx 2.4$). Using p-polarized light at incidence angles above the critical angle of total internal reflection ($\theta_{\mathrm{crit}} \approx 25°$), the large in-plane momentum of the evanescent wave in the air gap allows to couple to the SPhP modes in the multilayer structure [22].

A. Surface Phonon Polariton in 6H-SiC

In a bare SiC sample, a single SPhP mode propagating along the air-SiC interface is known to be accessible at frequencies inside the Reststrahlen region between $\omega_{TO,\perp} = 797\ \mathrm{cm}^{-1}$ and $\omega_{LO,\perp} = 968\ \mathrm{cm}^{-1}$ [21, 22]. In the Otto geometry [42], the air gap width d_{gap} is a critical coupling parameter in terms of excitation efficiency, while the incidence angle θ allows to select the excitation frequency along the SPhP dispersion [22]. Employing the transfer-matrix formalism, the reflectivity of such a system can be evaluated by means of Eq. 33 as a function of incidence frequency ω, incidence angle θ, and gap width d_{gap}.

Four exemplary reflectivity spectra are shown in Fig. 2 (a) at an incident angle of $\theta = 30°$. The simulations feature the Reststrahlen band with high reflectivity between TO and LO frequencies, as well as the SPhP resonance at $\sim 910\ \mathrm{cm}^{-1}$. The amplitude and width of the SPhP dip strongly depend on the air gap width, demonstrating the critical coupling behavior [22]. Furthermore, an anisotropy dip at the axial LO frequency [39], and the two weak modes arising due to zone-folding along the c-axis in 6H-SiC [43] are reproduced.

In Fig. 2 (b), the absolute $\vec{E}_x$-field amplitude is shown as a function of frequency and z-position at $\theta = 30°$ and the corresponding critical gap of $d_{\mathrm{gap}} = 5.5\,\mu\mathrm{m}$. The 6H-SiC substrate extends into the $z > 5.5\,\mu\mathrm{m}$ half-space, while the prism lies at $z < 0$, which is not shown in this plot. At the SPhP resonance frequency, a strong $\vec{E}_x$-field enhancement localized at the air-SiC interface is observed. As illustrated in a previous work [22], the field enhancement at the interface can be extracted to calculate the enhancement of second harmonic yield at the SPhP resonance in such a configuration. In order to determine the non-linear sources in a more complex structure, the $\vec{E}$-field distribution inside the multilayer system is a key tool.

In Fig. 2 (c), an axis-transformed reflectivity map is shown, exhibiting the SPhP dispersion at wave vectors exceeding the light line (solid blue line). The map is built by evaluating the reflectivity as a function of light frequency ω and incidence angle θ, at the critical coupling gap width d_{crit} for each θ [22], which is plotted in the inset. For θ smaller than the angle of total internal reflection in the prism, the reflectivity is evaluated for $d_{\mathrm{gap}} = 0$. The numerical simulations perfectly agree with the theoretically calculated single-interface dispersion curve at the air-SiC interface (dashed-dotted blue line) [44]. Following this procedure, our matrix formalism can be employed to predict polariton modes in more complicated structures and analyze their dispersion, as illustrated in the following examples.

B. GaN / 6H-SiC

In the second system we consider, a 2 µm thick film of hexagonal gallium nitride (GaN) is added on top of 6H-SiC, as shown in Fig. 3. Note that the Reststrahlen band of GaN lies at lower frequencies between $\omega_{TO,\perp} = 560\ \mathrm{cm}^{-1}$ and $\omega_{LO,\perp} = 742\ \mathrm{cm}^{-1}$ [40] and does not overlap with the SiC Reststrahlen region. In the reflectivity spectra in Fig. 3 (a), three strong resonances can be observed at (i) $\sim 680\ \mathrm{cm}^{-1}$, (ii) $\sim 810\ \mathrm{cm}^{-1}$, and (iii) $\sim 1000\ \mathrm{cm}^{-1}$. All resonances exhibit the SPhP-characteristic critical coupling behavior [21, 22], although each with a distinct critical gap width. Mode (i) appears clearly in the GaN Reststrahlen band. Mode (ii) is as a red-shifted SiC SPhP, the magnitude of red-shifting increasing with increasing GaN layer thickness (not shown), which can be interpreted as index-shifting of the SiC SPhP by the GaN layer [35]. Mode (iii) surprisingly emerges at the upper edge of the SiC high-reflectivity band at $\sim 1000\ \mathrm{cm}^{-1}$, i.e., outside the spectral region supporting SPhPs, and likely corresponds to a waveguiding mode at small positive $\varepsilon_{\mathrm{SiC}}$ and large $\varepsilon_{\mathrm{GaN}}$ at this frequency.

The origin of the modes can be further analyzed by means of the $\vec{E}_x$-field distribution, which is calculated for $d_{\mathrm{gap}} = 3.5\,\mu\mathrm{m}$ and shown in Fig. 3 (b). Resonance (i) is localized at the air-GaN interface and is spectrally broad, since for $d_{\mathrm{gap}} = 3.5\,\mu\mathrm{m}$, the excitation is over-coupled with large radiative losses back into the prism [22]. Due to the negative permittivity of the GaN Reststrahlen band, the underlying SiC substrate has no considerable influence on this air-GaN SPhP. For mode (ii), on the other hand, the GaN layer is transparent and the SiC substrate exhibits negative permittivity. This polariton mode has its peak intensity at the air-GaN interface, but extends down into SiC. Mode (iii), on the other hand, has field enhancement peaks at both the air-GaN and the GaN-SiC interface and exhibits a phase flip inside the GaN layer, suggesting the first-order waveguiding nature of the mode.

In the dispersion plot in Fig. 3 (c), the three polariton branches can be observed on the right-hand side of the light line. As a blue dashed line, the theoretical air-GaN SPhP dispersion is shown [44], coinciding with the lowest-frequency resonance identified as a GaN SPhP. The small deviation of the dispersion from the simulations at large wavenumbers arises due to calculating the map using the critical gap width of SiC (see inset in Fig. 2 (c)), which is somewhat larger for GaN. The theoretical air-SiC SPhP dispersion is shown again (blue dot-dashed line) in order to demonstrate the large index-red-shift of the polariton mode (ii) due to the GaN layer. In contrast to the typical converging shape of the SPhP dispersion, mode (iii) exhibits an almost linear behavior, following the position of the θ-dependent upper edge of

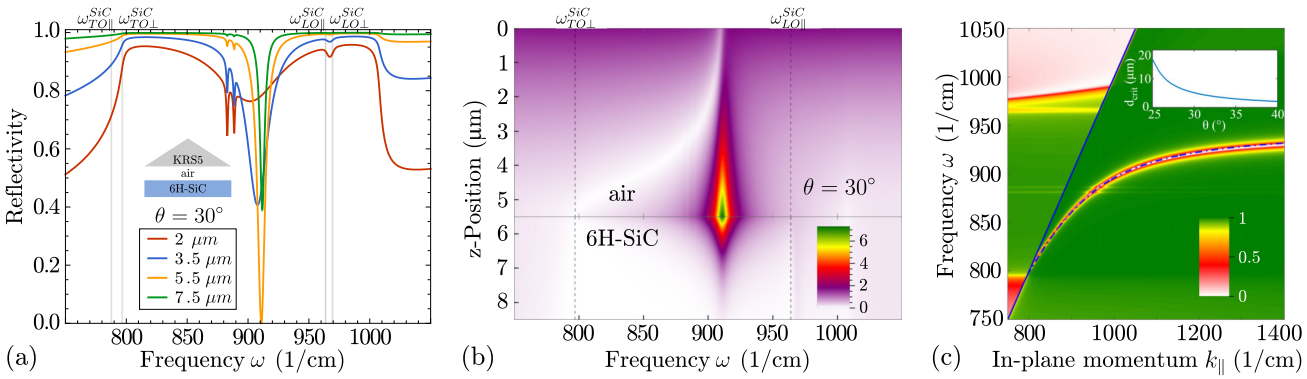

Fig. 2. Simulations of a single SPhP resonance in 6H-SiC excited in the Otto geometry. (a) Reflectivity spectra in the Reststrahlen region at 30° incident angle for four different gap widths, illustrating the critical coupling behavior of the SPhP resonance at $\sim 910\ \mathrm{cm}^{-1}$. (b) E_x-field enhancement at the air-SiC interface as a function of excitation frequency and z-position. The simulation reveals the spatial localization of the field enhancement of the SPhP and allows to predict the non-linear yield, see text. (c) Simulated reflectivity map showing the SPhP dispersion in the three-layer Otto configuration together with the theoretical two-layer dispersion (dashed-dotted blue line), both being in excellent agreement.

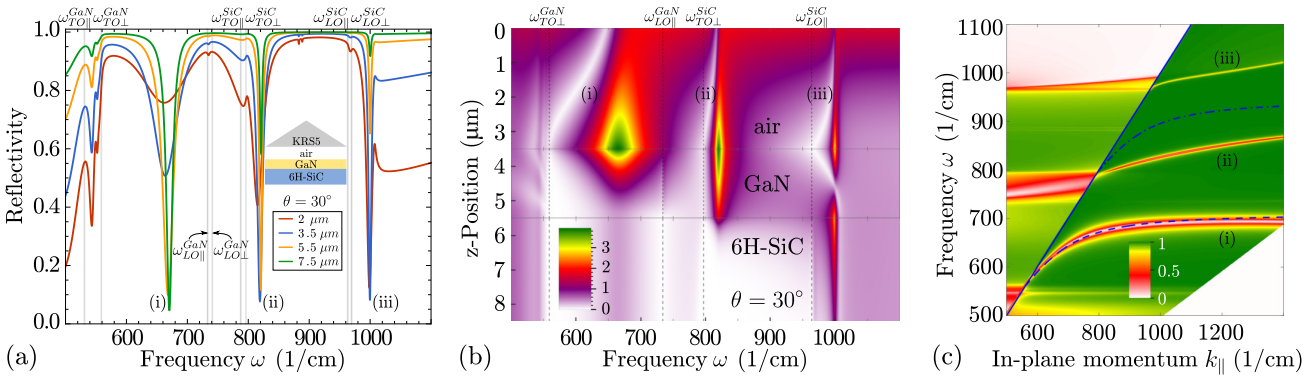

Fig. 3. Simulations of resonances in 2 µm GaN on 6H-SiC excited in the Otto geometry. (a) Reflectivity spectra in the Reststrahlen regions of both media at $\theta = 30°$ for four different gap widths, illustrating the appearance of three modes. (b) Absolute $\vec{E}_x$-field amplitude in the air-GaN-SiC system as a function of excitation frequency and z-position. The simulation reveals the spatial localization of each mode: (i) the GaN SPhP mode at $\sim 680\ \mathrm{cm}^{-1}$ is localized at the air-GaN interface, (ii) the index-shifted SiC-SPhP-like mode at $\sim 820\ \mathrm{cm}^{-1}$ extends into the SiC substrate, and (iii) the waveguide-like mode at $\sim 1000\ \mathrm{cm}^{-1}$ peaks at both interfaces, featuring a phase flip inside the GaN layer. (c) Simulated dispersions in the four-layer Otto configuration together with the theoretical two-layer SPhP dispersions of SiC (dashed-dotted blue line) and GaN (dashed blue line). The GaN SPhP dispersion is in excellent agreement with the simulations, indicating no significant modification by the SiC substrate. The SiC SPhP dispersion, on the other hand, is strongly index-shifted to lower frequencies by the presence of the GaN layer.

the high-reflectivity band [22]. In particular the unusual dispersion of the modes (ii) and (iii) is very interesting, and certainly deserves further systematic study.

C. 6H-SiC / GaN / 6H-SiC

On top of the previous system, we here consider an additional 700 nm thick 6H-SiC layer, as sketched in Fig. 1 (b). In Fig. 4 (a), the reflectivity spectra of such a system are shown at $\theta = 30°$, again for the same four different values of d_{gap}. As can be inferred from the critical coupling behavior accompanied by almost-zero reflectivity, the multilayer structure now supports at least five different modes, each with an individual critical gap width.

Analogous to mode (iii) in Sec. B, a mode (v) appears at $\sim$ 1000 cm^{-1}, but here additionally a similar mode (ii) is observed at the upper GaN Reststrahlen edge at $\sim$ 750 cm^{-1}. By inspection of the $\vec{E}$-field distribution in Fig. 4 (b), this similar nature of modes (ii) and (v) can be identified, both having field maxima at the interfaces of the GaN and SiC film, respectively, while exhibiting a phase flip inside the respective layer. Interestingly, mode (v), which spectrally appears at the upper SiC Reststrahlen edge, is spatially localized at the interfaces of the GaN layer, while mode (ii) occuring at $\sim$ 750 cm^{-1}, i.e. at the upper GaN Reststrahlen edge, is spatially localized at the SiC film interfaces. In consequence, the appearance of both modes can be attributed to a waveguide configuration with refractive indices $n_1/n_2/n_3$, where $n_2 > n_1, n_3$. Additionally, the GaN SPhP (i) is now strongly modified by the SiC top layer, exhibiting a pronounced red-shift as compared to bare GaN.

The strongest field enhancement at the chosen gap of $d_{\text{gap}} = 3.5\,\mu$m, however, arises from the two resonances around 900 cm^{-1} in Fig. 4 (b). These modes (iii) and (iv) are localized at the air-SiC interface, but extend further into the system with a second maximum inside the GaN layer. The field distribution in the SiC top layer suggests assignment to symmetric (iii) and asymmetric (iv) thin-film modes [45], with the asymmetric mode (iv) exhibiting a phase flip. However, the second enhancement inside the GaN layer points towards a GaN waveguided mode coupled to these SiC thin film modes. Further systematic studies are required to clarify the exact nature of these modes.

As for the previous systems, in Fig. 4 (c), the dispersion relations are shown. Clearly, the GaN SPhP, mode (i), is strongly index-shifted by the SiC overlayer owing to the large refractive index of SiC below its Reststrahlen band [39], as compared to the calculated SPhP on bare GaN (blue, dashed line). In fact, it is shifted so strongly that it is almost pushed out of the Reststrahlen band of GaN. Slightly thicker SiC films ($>$ 850 nm) result in complete quenching of the resonance (not shown). Despite their apparent similarity, modes (ii) and (v) show qualitatively different dispersions, converging for mode (ii) and diverging for mode (v). Possibly, this can be due to the adjacent lower SiC Reststrahlen edge for mode (ii), functioning as a hard upper limit for the dispersion. Finally, the dispersions of modes (iii) and (iv) enclose the single-interface SiC SPhP (blue, dash-dotted line), which is approached by the symmetric mode close to the light line, and by the asymmetric mode for large in-plane momenta. Note that due to the particular multilayer structure, the dispersions are clearly very different from the thin-film modes supported by a free-standing film [45].

The dispersion map shown in Fig. 4 (c) illustrates the rich polariton structure that emerges even for relatively simple multilayer systems. A full analysis of these modes clearly goes beyond the scope of this work, but we here show that our algorithm provides a complete toolset for further studies.

D. Surface Phonon Polaritons in Hyperbolic α-Quartz

The previous examples dealt with materials exhibiting a relatively small anisotropy, where the axial-planar phonon frequency difference is smaller than the TO-LO splitting. There is a number of materials having a large anisotropy instead. For example, h-BN exhibits very large optical phonon anisotropy such that the planar (ordinary) and axial (extraordinary) Reststrahlen bands do not overlap anymore [23, 28, 30, 32, 33]. Similarly, several oxides like α-quartz or sapphire exhibit different numbers of axial and planar infrared-active phonon modes [41, 46]. Both scenarios can lead to infrared spectral regions where the material exhibits a hyperbolic dispersion of its dielectric response, meaning that the real part of its dielectric tensor has both positive and negative principle components [32, 33]. In the spectral regions where only one element is negative, the hyperbolic material is of type I, while for two negative components, it is of type II [32].

As an alternative natural hyperbolic material [29], we here simulate the polariton dispersions in α-quartz in the region of 350 − 600 cm^{-1}. A systematic description of all crystal orientation-dependent SPhP modes was presented by Falge and Otto [20], whose two-layer dispersion formulas are employed for comparison with our transfer-matrix simulations. In Fig. 5 (a), (b), (c) we show reflectivity maps in the Otto geometry for three crystal orientations with the c-axis parallel to x, y (both in-plane), and z (out-of-plane), respectively. The blue dashed lines, representing the two-layer dispersions from Ref. [20], are in excellent agreement with the simulated dispersion curves obtained from the transfer-matrix formalism. In Fig. 5 (d) and (e), the real part of the dielectric function along the ordinary axes ($\varepsilon_{a,b}$) and along the extraordinary c-axis (ε_c), respectively, are shown. In yellow and green, the regions are marked where α-quartz is type I (HPI) and type II (HPII) hyperbolic, respectively.

For $c \parallel y$, the two appearing SPhPs originate from the ordinary dielectric components $\varepsilon_{a,b}$ only because of their intrinsic p-polarized nature, and hence are called "ordinary" SPhPs [20]. In the case of an a-cut crystal ($c \parallel x$), on the other hand, one normal SPhP ($\varepsilon_x, \varepsilon_z < 0$) at $\approx$ 500 cm^{-1} and two modes in the HPI regions exist. This situation is reversed in a c-cut crystal ($c \parallel z$), where two modes appear in the HPII regions. The upper mode, however, reaches up into the normal SPhP region around 500 cm^{-1}, thereby changing its character along the dispersion. Note that we here only observe modes for the in-plane dielectric component ε_x being negative, while the out-of-plane component can be negative (normal) or positiv (hyperbolic).

In contrast to hBN, α-quartz can be fabricated with any crystal orientation, therefore enabling the possibility of custom-designed polariton resonances. However, its intrinsic hyperbolic nature and the character of the appearing SPhP modes have not yet been investigated in detail. As we have shown, the presented transfer-matrix formalism proves to be an excellent tool for the analysis of the linear response of highly anisotropic materials such as α-quartz, allowing for quantitative predictions for polariton modes.

E. Discussion

We have presented examples of anisotropic multilayer structures made from polar dielectrics reaching into sub-wavelength dimensions, as well as phonon polariton resonances in hyperbolic materials. Combining these two can lead to effective material properties with yet unexplored functionality and tunability.

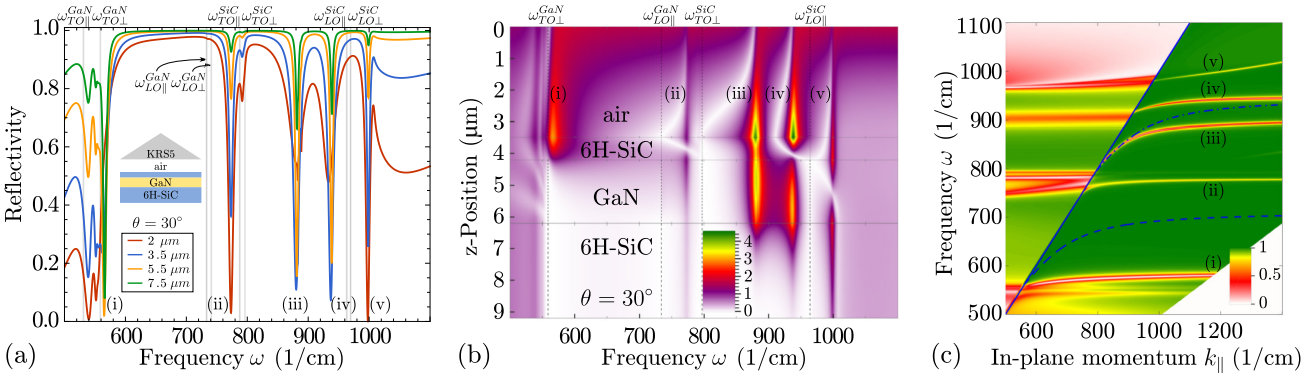

Fig. 4. Simulations of resonances in 700 nm 6H-SiC / 2 µm GaN on 6H-SiC excited in the Otto geometry. (a) Reflectivity spectra in the Reststrahlen region at 30° incident angle for four different gap widths, showing the appearance of five different modes, labeled (i)-(v). (b) Absolute $\vec{E}_x$-field amplitude in the air-SiC-GaN-SiC system as a function of excitation frequency and z-position. The simulation reveals the spatial localization of each mode. The SiC SPhP appears to split into two branches (iii) and (iv) at $\sim$ 900 cm^{-1}, exhibiting symmetric and anti-symmetric field distributions in the SiC top film, coupled to a waveguiding mode in the GaN film. (c) Simulated dispersions in the five-layer Otto configuration together with the theoretical two-layer SPhP dispersions of SiC (dashed-dotted blue line) and GaN (dashed blue line). In contrast to the previous examples, all mode branches differ strongly from the respective single-interface SPhP dispersions.

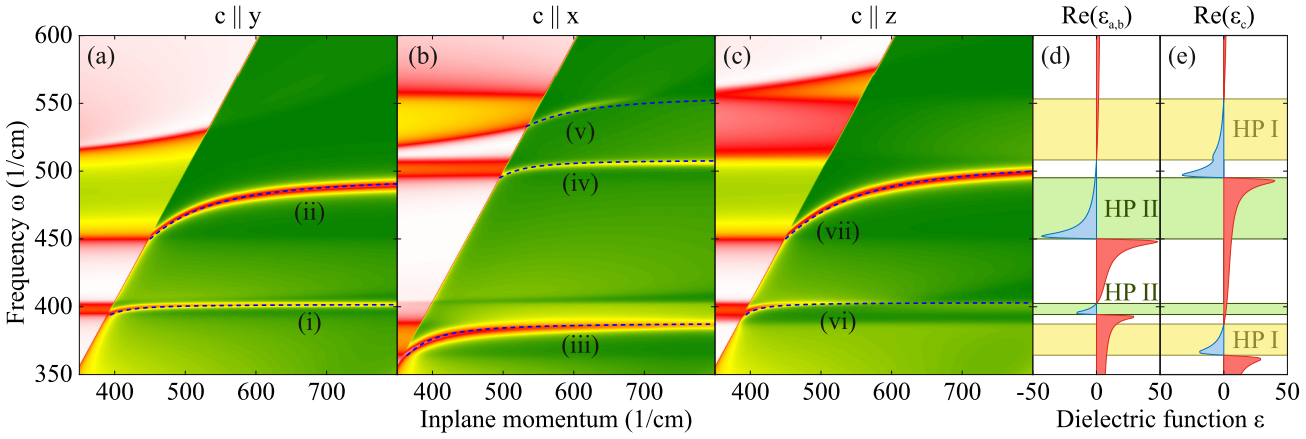

Fig. 5. Simulations of SPhP dispersions in hyperbolic α-quartz excited in the Otto geometry. (a), (b), and (c) show critical-gap reflectivity maps for the crystal orientations with $c \parallel y$, $c \parallel x$, and $c \parallel z$, respectively. The critical gap has been estimated by taking $2d_{\text{crit}}$ from SiC, accounting for the increased penetration depth of evanescent waves at half the wavelength [22]. Nonetheless, the modes exhibit different critical coupling conditions due to different damping constants. As blue dashed lines, the two-layer SPhP dispersions[20] are shown, being in excellent agreement with the simulations. In (d) and (e), the real part of the ordinary ($\varepsilon_{a,b}$) and extraordinary (ε_c) dielectric components are shown, plotted in red and blue for the positive and negative regions, respectively, for better visibility. In yellow and green we highlight the regions where α-quartz is hyperbolic of type I and II, respectively, allowing for direct identification of the modes observed in (a-c).

As the layer thicknesses d are further reduced, extreme optical confinement $\lambda/d > 1000$ may be achieved which is typically inaccessible in plasmonics due to the much shorter wavelengths employed [47]. In the ultimate regime of atomic-scale heterostructures [25, 26], one can additionally expect the optical properties to deviate from calculations using bulk parameters of the constituent materials due to microscopic modification of the material properties [25]. As we have shown, the formalism presented here is perfectly suited to simulate the optical response of such systems and could therefore be very useful in future studies of ultrathin-film dielectric heterostructures.

Additionally, our formalism can be straight-forwardly extended into the nonlinear regime with arbitrary distribution of nonlinear optical sources. Notably, nonlinear-optical effects such as second harmonic generation (SHG) or sum-frequency generation are known to be extremely sensitive to the layer arrangements and thicknesses in thin-film heterostructures [17, 48, 49]. For SPhPs, only a few proof-of-concept nonlinear experiments have been performed [22, 50], demonstrating that the sub-diffractional light localization can lead to drastic enhancement of the SHG yield. It is then obvious that thin-film heterostructures of polar dielectrics would allow tuning of the mid-infrared nonlinear properties with yet unexplored level of control and enhancement. The algorithm presented here provides the complete electric field distributions in such structures, enabling predictive studies of the nonlinear-optical response.

4. CONCLUSION

We have presented a generalized 4×4 matrix formalism allowing to calculate the linear optical response of arbitrarily anistropic or isotropic, absorbing or non-absorbing multilayer structures. The algorithm is comprehensible, robust, free of discontinuous solutions, and can easily be implemented in a computer program [34]. The robustness of the algorithm is achieved by combining previous formalisms such that discontinuities and poles are completely avoided in the different steps of the algorithm. We give the equations for reflection and transmission coefficients, as well as for the full electric field distribution throughout the heterostructure. As a test ground, we applied the algorithm to simulations of SPhPs excited in the Otto geometry for selected anisotropic multilayer samples, where we observed critical coupling behavior, index shifting, mode splitting, waveguiding, as well as phonon polaritons in hyperbolic materials. Our algorithm holds high promise for predicting SPhP modes in ultrathin films, hyperbolic structures, and atomic-scale heterostructures, as well as their nonlinear-optical response.

5. ACKNOWLEDGMENTS

We thank I. Razdolski (FHI Berlin) for careful reading of the manuscript, and M. Wolf (FHI Berlin) for supporting this work.

REFERENCES

1. S. A. Maier, *Plasmonics: Fundamentals and applications* (Springer US, 2007).
2. J. Hiller, J. D. Mendelsohn, and M. F. Rubner, "Reversibly erasable nanoporous anti-reflection coatings from polyelectrolyte multilayers," Nature Materials **1**, 59–63 (2002).
3. J.-Q. Xi, M. F. Schubert, J. Kim, E. F. Schubert, M. Chen, S.-Y. Lin, W. Lie, and J. A. Smart, "Optical thin-filmmaterials with low refractive index for broadband elimination of Fresnel reflection," Nature Photonics **1**, 176 (2007).
4. K. Nomura, "Thin-Film Transistor Fabricated in Single-Crystalline Transparent Oxide Semiconductor," Science **300**, 1269–1272 (2003).
5. R. A. Street, "Thin-Film Transistors," Advanced Materials **21**, 2007–2022 (2009).
6. K. L. Chopra, P. D. Paulson, and V. Dutta, "Thin-film solar cells: an overview," Progress in Photovoltaics: Research and Applications **12**, 69–92 (2004).
7. B. Shin, O. Gunawan, Y. Zhu, N. A. Bojarczuk, S. J. Chey, and S. Guha, "Thin film solar cell with 8.4% power conversion efficiency using an earth-abundant Cu 2 ZnSnS 4 absorber," Progress in Photovoltaics: Research and Applications **21**, 72–76 (2013).
8. N. Patel, P. Patel, and V. Vaishnav, "Indium tin oxide (ITO) thin film gas sensor for detection of methanol at room temperature," Sensors and Actuators B: Chemical **96**, 180–189 (2003).
9. K. S. Yoo, S. H. Park, and J. H. Kang, "Nano-grained thin-film indium tin oxide gas sensors for H2 detection," Sensors and Actuators B: Chemical **108**, 159–164 (2005).
10. H. Gong, J. Hu, J. Wang, C. Ong, and F. Zhu, "Nano-crystalline Cu-doped ZnO thin film gas sensor for CO," Sensors and Actuators B: Chemical **115**, 247–251 (2006).
11. D. W. Berreman, "Optics in Stratified and Anisotropic Media: 4x4-Matrix Formulation," Journal of the Optical Society of America **62**, 502 (1972).
12. Z.-M. Li, B. T. Sullivan, and R. R. Parsons, "Use of the 4x4 matrix method in the optics of multilayer magnetooptic recording media," Applied Optics **27**, 1334 (1988).
13. W. Xu, L. T. Wood, and T. D. Golding, "Optical degeneracies in anisotropic layered media: Treatment of singularities in a 4x4 matrix formalism," Physical Review B **61**, 1740–1743 (2000).
14. P. J. Lin-Chung and S. Teitler, "4x4 Matrix formalisms for optics in stratified anisotropic media," Journal of the Optical Society of America A **1**, 703 (1984).
15. P. Yeh, "Electromagnetic propagation in birefringent layered media," Journal of the Optical Society of America **69**, 742 (1979).
16. S. Zhang and F. Wyrowski, "Simulations of general electromagnetic fields propagation through optically anisotropic media," in "Proc. SPIE," , vol. 9630 D. G. Smith, F. Wyrowski, and A. Erdmann, eds. (2015), vol. 9630, p. 96300A.
17. D. B. O'Brien and A. M. Massari, "Modeling multilayer thin film interference effects in interface-specific coherent nonlinear optical spectroscopies," Journal of the Optical Society of America B **30**, 1503 (2013).
18. S. Adachi, "The Reststrahlen Region," in "Optical Properties of Crystalline and Amorphous Semiconductors: Materials and Fundamental Principles," (Springer US, Boston, MA, 1999), pp. 33–61.
19. A. J. Huber, N. Ocelic, D. Kazantsev, and R. Hillenbrand, "Near-field imaging of mid-infrared surface phonon polariton propagation," Applied Physics Letters **87**, 081103 (2005).
20. H. J. Falge and A. Otto, "Dispersion of Phonon-Like Surface Polaritons on α-Quartz Observed by Attenuated Total Reflection," Physica Status Solidi (B) **56**, 523–534 (1973).
21. B. Neuner, D. Korobkin, C. Fietz, D. Carole, G. Ferro, and G. Shvets, "Critically coupled surface phonon-polariton excitation in silicon carbide." Optics letters **34**, 2667–9 (2009).
22. N. C. Passler, I. Razdolski, S. Gewinner, W. Schöllkopf, M. Wolf, and A. Paarmann, "Second-Harmonic Generation from Critically Coupled Surface Phonon Polaritons," ACS Photonics **4**, 1048–1053 (2017).
23. S. Dai, Z. Fei, Q. Ma, A. S. Rodin, M. Wagner, A. S. McLeod, M. K. Liu, W. Gannett, W. Regan, K. Watanabe, T. Taniguchi, M. Thiemens, G. Dominguez, A. H. C. Neto, A. Zettl, F. Keilmann, P. Jarillo-Herrero, M. M. Fogler, and D. N. Basov, "Tunable Phonon Polaritons in Atomically Thin van der Waals Crystals of Boron Nitride," Science **343**, 1125–1129 (2014).
24. J. D. Caldwell and K. S. Novoselov, "Van der Waals heterostructures: Mid-infrared nanophotonics," Nature Materials **14**, 364–366 (2015).
25. J. D. Caldwell, I. Vurgaftman, J. G. Tischler, O. J. Glembocki, J. C. Owrutsky, and T. L. Reinecke, "Atomic-scale photonic hybrids for mid-infrared and terahertz nanophotonics," Nature Nanotechnology **11**, 9–15 (2016).
26. A. Woessner, M. B. Lundeberg, Y. Gao, A. Principi, P. Alonso-González,

M. Carrega, K. Watanabe, T. Taniguchi, G. Vignale, M. Polini, J. Hone, R. Hillenbrand, and F. H. L. Koppens, "Highly confined low-loss plasmons in graphene–boron nitride heterostructures," Nature Materials **14**, 421–425 (2014).

27. T. Taubner, D. Korobkin, Y. Urzhumov, G. Shvets, and R. Hillenbrand, "Near-field microscopy through a SiC superlens." Science (New York, N.Y.) **313**, 1595 (2006).
28. P. Li, M. Lewin, A. V. Kretinin, J. D. Caldwell, K. S. Novoselov, T. Taniguchi, K. Watanabe, F. Gaussmann, and T. Taubner, "Hyperbolic phonon-polaritons in boron nitride for near-field optical imaging and focusing," Nature Communications **6**, 7507 (2015).
29. R. Rodrigues da Silva, R. Macêdo da Silva, T. Dumelow, J. A. P. da Costa, S. B. Honorato, and A. P. Ayala, "Using Phonon Resonances as a Route to All-Angle Negative Refraction in the Far-Infrared Region: The Case of Crystal Quartz," Physical Review Letters **105**, 163903 (2010).
30. E. Yoxall, M. Schnell, A. Y. Nikitin, O. Txoperena, A. Woessner, M. B. Lundeberg, F. Casanova, L. E. Hueso, F. H. L. Koppens, and R. Hillenbrand, "Direct observation of ultraslow hyperbolic polariton propagation with negative phase velocity," Nature Photonics **9**, 674–678 (2015).
31. A. K. Geim and I. V. Grigorieva, "Van der Waals heterostructures," Nature **499**, 419–425 (2013).
32. J. D. Caldwell, A. V. Kretinin, Y. Chen, V. Giannini, M. M. Fogler, Y. Francescato, C. T. Ellis, J. G. Tischler, C. R. Woods, A. J. Giles, M. Hong, K. Watanabe, T. Taniguchi, S. a. Maier, and K. S. Novoselov, "Sub-diffractional volume-confined polaritons in the natural hyperbolic material hexagonal boron nitride." Nature communications **5**, 5221 (2014).
33. Z. Jacob, "Nanophotonics: Hyperbolic phonon–polaritons," Nature Materials **13**, 1081–1083 (2014).
34. N. C. Passler and A. Paarmann, "Generalized 4x4 Matrix algorithm for light propagation in anisotropic stratified media (Matlab files)," https://doi.org/10.5281/zenodo.847015 (2017).
35. B. Neuner, D. Korobkin, C. Fietz, D. Carole, G. Ferro, and G. Shvets, "Midinfrared Index Sensing of pL-Scale Analytes Based on Surface Phonon Polaritons in Silicon Carbide," The Journal of Physical Chemistry C **114**, 7489–7491 (2010).
36. N. Novikova, V. Yakovlev, E. Vinogradov, S. Ng, Z. Hassan, and H. A. Hassan, "Substrate surface polariton splitting due to thin zinc oxide and aluminum nitride films presence," Applied Surface Science **267**, 93–96 (2013).
37. G. Zheng, Y. Chen, L. Bu, L. Xu, and W. Su, "Waveguide-coupled surface phonon resonance sensors with super-resolution in the mid-infrared region," Optics Letters **41**, 1582 (2016).
38. A. Yariv and P. Yeh, *Optical Waves in Crystals: Propagation and Control of Laser Radiation* (1984).
39. A. Paarmann, I. Razdolski, S. Gewinner, W. Schöllkopf, and M. Wolf, "Effects of crystal anisotropy on optical phonon resonances in midinfrared second harmonic response of SiC," Physical Review B **94**, 134312 (2016).
40. A. Kasic, M. Schubert, S. Einfeldt, D. Hommel, and T. E. Tiwald, "Free-carrier and phonon properties of n- and p-type hexagonal GaN films measured by infrared ellipsometry," Physical Review B - Condensed Matter and Materials Physics **62**, 7365–7377 (2000).
41. F. Gervais and B. Piriou, "Temperature dependence of transverse and longitudinal optic modes in the α and β phases of quartz," Physical Review B **11**, 3944–3950 (1975).
42. A. Otto, "Excitation of nonradiative surface plasma waves in silver by the method of frustrated total reflection," Zeitschrift für Physik **216**, 398–410 (1968).
43. J. Bluet, K. Chourou, M. Anikin, and R. Madar, "Weak phonon modes observation using infrared reflectivity for 4H, 6H and 15R polytypes," Materials Science and Engineering: B **61-62**, 212–216 (1999).
44. H. Raether, *Surface Plasmons on Smooth and Rough Surfaces and on Gratings* (Springer, 1988).
45. P. Berini, "Long-range surface plasmon polaritons," Advances in Optics and Photonics **1**, 484 (2009).
46. F Gervais and B Piriou, "Anharmonicity in several-polar-mode crystals: adjusting phonon self-energy of LO and TO modes in Al 2 O 3 and TiO 2 to fit infrared reflectivity," Journal of Physics C: Solid State Physics **7**, 2374 (1974).
47. S. Campione, I. Brener, and F. Marquier, "Theory of epsilon-near-zero modes in ultrathin films," Physical Review B **91**, 121408 (2015).
48. I. Razdolski, D. Makarov, O. G. Schmidt, A. Kirilyuk, T. Rasing, and V. V. Temnov, "Nonlinear Surface Magnetoplasmonics in Kretschmann Multilayers," ACS Photonics **3**, 179–183 (2016).
49. S. Palomba and L. Novotny, "Nonlinear Excitation of Surface Plasmon Polaritons by Four-Wave Mixing," Physical Review Letters **101**, 056802 (2008).
50. I. Razdolski, Y. Chen, A. J. Giles, S. Gewinner, W. Schöllkopf, M. Hong, M. Wolf, V. Giannini, J. D. Caldwell, S. A. Maier, and A. Paarmann, "Resonant Enhancement of Second-Harmonic Generation in the Mid-Infrared Using Localized Surface Phonon Polaritons in Subdiffractional Nanostructures," Nano Letters **16**, 6954–6959 (2016).

4.2.1 Generalized 4 × 4 matrix formalism for light propagation in anisotropic stratified media: study of surface phonon polaritons in polar dielectric heterostructures: erratum

Nikolai Christian Passler and Alexander Paarmann

This erratum (Passler and Paarmann, JOSA B 2019, **36**, 3246-3248 [**III**]) presents corrections to the originally published transfer matrix formalism [**II**] (reprinted on page 45), allowing for the correct calculation of the electric field distribution for birefringence, that is, for anisotropic media with non-zero off-diagonal elements of the dielectric permittivity tensor in the lab frame. All publications prior to this erratum investigate isotropic or anisotropic media with diagonal permittivity tensor, and thus are not affected by the error in the original formalism. The corrections are included in the online version of the open-source computer code programmed in Matlab [18] and Python [112].

Furthermore, revising the original work and correcting the equations triggered the development of an extended formalism, which is capable of calculating the layer-resolved absorption and transmittance in a multilayer system. This work has been published most recently [**VII**] and is reprinted on page 97.

Author contributions

N.C.P. and A.P. originated the concept. The manuscript was written by **N.C.P.** and A.P. **N.C.P.** and A.P. developed the corrections to the algorithm. The project management was provided by A.P.

go to list of publications

Research Article | Journal of the Optical Society of America B 1

Generalized 4 × 4 Matrix Formalism for Light Propagation in Anisotropic Stratified Media: Study of Surface Phonon Polaritons in Polar Dielectric Heterostructures: Erratum

NIKOLAI CHRISTIAN PASSLER[1,*] AND ALEXANDER PAARMANN[1]

[1] Fritz-Haber-Institut der Max-Planck-Gesellschaft, Faradayweg 4-6,14195 Berlin, Germany
[*] Corresponding author: passler@fhi-berlin.mpg.de

Compiled October 14, 2019

In our paper JOSA B 34, 2128 (2017) in section 2C, the calculation of the layer-dependent electric field distribution is only valid for media with permittivity tensors that are diagonal in the lab frame, i.e. non-birefringent media. This erratum corrects section 2C such that the electric field distribution in birefringent media is calculated correctly. Further, Eq. 20 and Eq. 33-36 are corrected. The associated MATLAB implementation has been updated.

OCIS codes:

http://dx.doi.org/10.1364/ao.XX.XXXXXX

2. A. 3. Transfer Matrix with Treatment of Singularities

The electric field vectors $\vec{\gamma}_{ij}$ of the four eigenmodes j in each layer i have been reported with an error in the components γ_{i13} and γ_{i33}. The correct components are [1]:

$$\gamma_{i13} = \begin{cases} -\frac{\mu_i\varepsilon_{i31}+\zeta q_{i1}}{\mu_i\varepsilon_{i33}-\zeta^2}, & q_{i1} = q_{i2} \\ -\frac{\mu_i\varepsilon_{i31}+\zeta q_{i1}}{\mu_i\varepsilon_{i33}-\zeta^2} - \frac{\mu_i\varepsilon_{i32}}{\mu_i\varepsilon_{i33}-\zeta^2}\gamma_{i12}, & q_{i1} \neq q_{i2} \end{cases}$$

$$\gamma_{i33} = \begin{cases} \frac{\mu_i\varepsilon_{i31}+\zeta q_{i3}}{\mu_i\varepsilon_{i33}-\zeta^2}, & q_{i3} = q_{i4} \\ \frac{\mu_i\varepsilon_{i31}+\zeta q_{i3}}{\mu_i\varepsilon_{i33}-\zeta^2} + \frac{\mu_i\varepsilon_{i32}}{\mu_i\varepsilon_{i33}-\zeta^2}\gamma_{i32}, & q_{i3} \neq q_{i4}. \end{cases} \quad \textbf{(20*)}$$

Furthermore, in order to ensure the correct calculation of the cross-polarization reflection and transmission coefficients for birefringent media, the eigenmode field vectors $\vec{\gamma}_{ij}$ have to be normalized:

$$\vec{\tilde{\gamma}}_{ij} = \frac{\vec{\gamma}_{ij}}{|\vec{\gamma}_{ij}|}, \quad \textbf{(E1)}$$

and $\vec{\tilde{\gamma}}_{ij}$ replaces $\vec{\gamma}_{ij}$ in the further formalism, specifically in Eq. 22 in Ref. [2].

2. B. Reflectance and Transmittance

In our original work [2], we had defined the transmission coefficients t_{ss}, t_{ps}, and t_{sp} with opposite sign compared to the original work by Yeh [3] for convenience of the previous electric field calculations. While this has no impact on the intensity enhancement $T_{kl} = |t_{kl}|^2$ (with $k, l = s, p$), the sign does matter for the corrected calculation of the electric fields (see following section). We therefore now employ the transmission coefficients following the sign convention of Yeh [3]:

$$t_{pp} = \frac{\Gamma^*_{33}}{\Gamma^*_{11}\Gamma^*_{33} - \Gamma^*_{13}\Gamma^*_{31}} \quad \textbf{(33)}$$

$$t_{ss} = \frac{\Gamma^*_{11}}{\Gamma^*_{11}\Gamma^*_{33} - \Gamma^*_{13}\Gamma^*_{31}} \quad \textbf{(34*)}$$

$$t_{ps} = \frac{-\Gamma^*_{31}}{\Gamma^*_{11}\Gamma^*_{33} - \Gamma^*_{13}\Gamma^*_{31}} \quad \textbf{(35*)}$$

$$t_{sp} = \frac{-\Gamma^*_{13}}{\Gamma^*_{11}\Gamma^*_{33} - \Gamma^*_{13}\Gamma^*_{31}}. \quad \textbf{(36*)}$$

2. C. Electric Field Distribution

In our paper [2], the four eigenmodes $j = 1 - 4$ in each layer i were assigned to be p-polarized ($j = 1, 3$) and s-polarized ($j = 2, 4$) modes (transmitted and reflected, respectively, where the plane of incidence is in the x-z-plane). This is true for any dielectric tensor that is diagonal in the lab frame (in the following referred to as non-birefringent), where for the p-polarized mode $E_y = 0$ and for the s-polarized mode $E_x = 0$. For birefringence, however, the eigenmodes are no longer p- and s-polarized, but can be distinguished as ordinary (o) and extraordinary (e) modes, both featuring $E_x \neq 0$ and $E_y \neq 0$. Therefore, in the case of a birefringent substrate, the transmission coefficients (Eq. 33-36 in

Passler, N.C., Paarmann, A.,
Generalized 4x4 matrix formalism for light propagation in anisotropic stratified media: study of surface phonon polaritons in polar dielectric heterostructures: erratum.
Journal of the Optical Society of America B 2019, 36, 11, 3246-3248. https://doi.org/10.1364/JOSAB.36.003246

[2]) must be labeled t_{po}, t_{se}, t_{pe}, t_{so} instead of t_{pp}, t_{ss}, t_{ps}, t_{sp}, and they describe the transmission into the ordinary/extraordinary mode for p- or s-polarized incident light, respectively. As a consequence, the electric field components E_x, E_y, and E_z cannot be calculated anymore directly from the transmission coefficients as shown in Eq. 39-41 in [2]. In the following, we present a generic solution for the calculation of the electric field vectors that is applicable to non-birefringent as well as arbitrarily birefringent media:

Using the interface and propagation matrices $\mathbf{L}_i$ and $\mathbf{P}_i$, respectively, the four-component electric field vector as defined in Eq. 23 in [2] can be projected to any point in the multilayer system. The four components describe the amplitudes of the p- and s-polarized modes in non-birefringent, and the amplitudes of the ordinary and extraordinary modes in birefringent media. Therefore, in the following we will refer to the four-component vector as the amplitude vector. Utilizing the corrected transmission coefficients given by Eq. 33-36*, the amplitudes of the modes, i.e. the amplitude vector $\vec{E}^+_{N+1}$, in the substrate at the interface with layer N (see Fig. 1(a) in [2]) can be calculated seperately for p- and for s-polarized incident light as follows:

$$\left(\vec{E}^+_{N+1}\right)_{p\text{ in}} = \begin{pmatrix} E^{p/o}_{\text{trans}} \\ E^{s/e}_{\text{trans}} \\ E^{p/o}_{\text{refl}} \\ E^{s/e}_{\text{refl}} \end{pmatrix} = \begin{pmatrix} t_{p(p/o)} \\ t_{p(s/e)} \\ 0 \\ 0 \end{pmatrix}$$
$$\left(\vec{E}^+_{N+1}\right)_{s\text{ in}} = \begin{pmatrix} E^{p/o}_{\text{trans}} \\ E^{s/e}_{\text{trans}} \\ E^{p/o}_{\text{refl}} \\ E^{s/e}_{\text{refl}} \end{pmatrix} = \begin{pmatrix} t_{s(p/o)} \\ t_{s(s/e)} \\ 0 \\ 0 \end{pmatrix}, \tag{37*}$$

where the reflected components are set to zero, since no light source is assumed to be on the substrate side of the multilayer system. Further note that we here conveniently go back to the field sorting according to Eq. 23 in [2], allowing to directly reuse any interface and propagation matrices that were calculated along the way to the full transfer matrix $\mathbf{\Gamma}_N$. As it is shown in Fig. 1(a) in [2], the amplitude vectors on both sides of an interface are connected by the interface matrix $\vec{E}^-_{i-1} = \mathbf{L}_i \vec{E}^+_i$. Furthermore, the propagation through layer i is given by the propagation matrix $\mathbf{P}_i$, which can be evaluated z-dependently:

$$\begin{aligned} \vec{E}_i(z) &= \mathbf{P}_i(z)\vec{E}^-_i \\ &= \begin{pmatrix} e^{-i\frac{\omega}{c}q_{i1}z} & 0 & 0 & 0 \\ 0 & e^{-i\frac{\omega}{c}q_{i2}z} & 0 & 0 \\ 0 & 0 & e^{-i\frac{\omega}{c}q_{i3}z} & 0 \\ 0 & 0 & 0 & e^{-i\frac{\omega}{c}q_{i4}z} \end{pmatrix} \vec{E}^-_i, \end{aligned} \tag{38}$$

with $0 < z < d_i$ being the relative z-position in layer i. As it is indicated by the black arrows in Fig. 1 in [2], starting from $\vec{E}^+_{N+1}$, interface matrices $\mathbf{L}_i$ and propagation matrices $\mathbf{P}_i$ are used to subsequently propagate the wave towards the incident medium. In the reverse direction, the inverse propagation matrix $\mathbf{P}^{-1}_{N+1}$ allows to calculate the $\vec{E}$-fields in the substrate. By this means, the four mode amplitudes $E^{p/o}_{\text{trans}}$, $E^{s/e}_{\text{trans}}$, $E^{p/o}_{\text{refl}}$, and $E^{s/e}_{\text{refl}}$ are obtained as a function of z within each layer. In contrast to the originally published paper, these calculations are performed seperately for p- and s-polarized incident light, ensuring that birefringence is treated correctly.

In order to obtain the three-component (x, y, z) electric field vectors for each of the four modes j, the four mode amplitudes are multiplied with their respective normalized eigenmode vector $\vec{\hat{\gamma}}_{ij}$ (Eq. 20 in [2] and Eq. E1). This yields the full electric fields of the four modes for p- and s-polarized incident light seperately, replacing Eq. 39-41 in [2]:

$$\begin{aligned} \left(\vec{E}^{p/o}_{\text{trans}}\right)_{p/s\text{ in}} &= \left(E^{p/o}_{\text{trans}}\right)_{p/s\text{ in}} \begin{pmatrix} \hat{\gamma}_{i11} \\ \hat{\gamma}_{i12} \\ \hat{\gamma}_{i13} \end{pmatrix} \\ \left(\vec{E}^{s/e}_{\text{trans}}\right)_{p/s\text{ in}} &= \left(E^{s/e}_{\text{trans}}\right)_{p/s\text{ in}} \begin{pmatrix} \hat{\gamma}_{i21} \\ \hat{\gamma}_{i22} \\ \hat{\gamma}_{i23} \end{pmatrix} \\ \left(\vec{E}^{p/o}_{\text{refl}}\right)_{p/s\text{ in}} &= \left(E^{p/o}_{\text{refl}}\right)_{p/s\text{ in}} \begin{pmatrix} \hat{\gamma}_{i31} \\ \hat{\gamma}_{i32} \\ \hat{\gamma}_{i33} \end{pmatrix} \\ \left(\vec{E}^{s/e}_{\text{refl}}\right)_{p/s\text{ in}} &= \left(E^{s/e}_{\text{refl}}\right)_{p/s\text{ in}} \begin{pmatrix} \hat{\gamma}_{i41} \\ \hat{\gamma}_{i42} \\ \hat{\gamma}_{i43} \end{pmatrix}, \end{aligned} \tag{E2}$$

for each layer i and as a function of z, where we have omitted the index i and the z dependence for the sake of readability.

Within each layer, there are only two possible shapes of the amplitudes of these eigenmodes: they either describe a (damped) sinusoidal propagating wave, or an exponentially decaying evanescent wave. In order to get the full electric field vectors present in the multilayer system, the electric field components of all four modes, the forward (transmitted) and backward (reflected), p/o and s/e, respectively, have to be summed up. Note that by utilizing the eigenmode vectors $\vec{\hat{\gamma}}_{ij}$, it is no longer necessary to consider phase flips upon reflection. Furthermore, all three components of the electric field vectors are calculated correctly even for birefringent media, and the fields are obtained seperately for p- and s-polarized incident light. The associated MATLAB code [4] has been updated, implementing the corrected formulas. Additionally, Jeannin implemented the formalism in Python [5].

Furthermore, in contrast to the reflection coefficients r which allow to directly calculate the reflectance $R = |r|^2$, the transmittance $\mathcal{T}$ cannot be calculated directly from the transmission coefficients, i.e. in general, $\mathcal{T} \neq |t|^2$ (only when the last material is vacuum the transmittance is $\mathcal{T} = |t|^2$). The correct calculation of the transmittance and absorption in a multilayer system of arbitrarily anisotropic media – including birefringence – will be treated elsewhere [6].

1. ACKNOWLEDGMENTS

The solution for the calculation of the electric field distribution in birefringent media presented in this erratum has been triggered by the feedback and discussion with various collegues in the community. For their contribution we therefore thank, in chronological order, Kevin Vynck (Institut d'Optique d'Aquitaine, Bordeaux), Ota Kunt (Technische Universität Dresden), Quianxiang

Ai (University of Kentucky), Lloyd Bumm (University of Oklahoma), Mathieu Jeannin (Ecole Normale Supérieure de Paris), Yujin Tong (Fritz Haber Institute, Berlin), and Kramer Campen (Fritz Haber Institute, Berlin).

REFERENCES

1. W. Xu, L. T. Wood, and T. D. Golding, "Optical degeneracies in anisotropic layered media: Treatment of singularities in a 4x4 matrix formalism," Physical Review B **61**, 1740–1743 (2000).
2. N. C. Passler, and A. Paarmann, "Generalized $\mathbf{4} \times \mathbf{4}$ Matrix Formalism for Light Propagation in Anisotropic Stratified Media: Study of Surface Phonon Polaritons in Polar Dielectric Heterostructures," JOSA B **34**, 2128 (2017).
3. P. Yeh, "Electromagnetic propagation in birefringent layered media," Journal of the Optical Society of America **69**, 742 (1979).
4. N. C. Passler and A. Paarmann, "Generalized 4x4 Matrix algorithm for light propagation in anisotropic stratified media (Matlab files)," https://doi.org/10.5281/zenodo.601496 (2019).
5. M. Jeannin, "Generalized 4x4 Matrix algorithm for light propagation in anisotropic stratified media (Python files)," https://doi.org/10.5281/zenodo.3417751 (2019).
6. N. C. Passler and A. Paarmann, "Layer-Resolved Transmittance and Absorption of Light Propagating in Arbitrarily Anisotropic Stratified Media," in preparation.

4.3 Strong Coupling of Epsilon-Near-Zero Phonon Polaritons in Polar Dielectric Heterostructures

Nikolai Christian Passler, Christopher R. Gubbin, Thomas Graeme Folland, Ilya Razdolski, D. Scott Katzer, David F. Storm, Martin Wolf, Simone De Liberato, Joshua D. Caldwell, and Alexander Paarmann

This publication (Passler *et al.*, Nano Letters 2018, **18**, 4285-4292 [**IV**]) reports on the first observation of the full hybridization of an ENZ thin-film polariton with a bulk SPhP. The experimental results were obtained employing the Otto type prism coupling setup (section 3.2), where varying the incident angle allows for reconstruction of the strongly coupled, anti-crossing polariton dispersions. The supporting information is reprinted in appendix A.2.

This work has been the first in the scope of this thesis in experimentally investigating polariton modes in stratified heterostructures, and was the trigger for the subsequent study of ENZ Berreman modes that are observable via free-space excitation in the same sample system [**V**] (reprinted on page 75). The transfer matrix formalism [**II**] (reprinted on page 45) is used as theoretical tool for the simulation of the measured optical response.

Author contributions

A.P. conceived the project. D.S.K. and D.F.S. performed the sample growth. **N.C.P.**, A.P. and I.R. conducted the experiment and analyzed the results. **N.C.P.** and A.P. wrote the manuscript, with all authors assisting in the proof-reading and preparation for final submission. C.G. and S.D.L. developed the analytical strong coupling model. Computations of the linear optical response in the Otto geometry were completed by A.P. and **N.C.P.** T.F. carried out the simulations of the near-field scattering at a nanoparticle. The project management was provided by J.D.C. and A.P.

go to list of publications

NANO LETTERS
Letter
Cite This: Nano Lett. 2018, 18, 4285−4292
pubs.acs.org/NanoLett

Strong Coupling of Epsilon-Near-Zero Phonon Polaritons in Polar Dielectric Heterostructures

Nikolai Christian Passler,*[,†] Christopher R. Gubbin,[‡] Thomas Graeme Folland,[§] Ilya Razdolski,[†] D. Scott Katzer,[∥] David F. Storm,[∥] Martin Wolf,[†] Simone De Liberato,[‡] Joshua D. Caldwell,[§,∥] and Alexander Paarmann*[,†]

[†]Fritz-Haber-Institut der Max-Planck-Gesellschaft, Faradayweg 4-6, 14195 Berlin, Germany
[‡]School of Physics and Astronomy, University of Southampton, Southampton SO17 1BJ, United Kingdom
[§]Vanderbilt Institute of Nanoscale Science and Engineering, 2301 Vanderbilt Place, PMB 350106, Nashville, Tennessee 37235-0106, United States
[∥]U.S. Naval Research Laboratory, 4555 Overlook Avenue SW, Washington, DC 20375, United States

Supporting Information

ABSTRACT: We report the first observation of epsilon-near-zero (ENZ) phonon polaritons in an ultrathin AlN film fully hybridized with surface phonon polaritons (SPhP) supported by the adjacent SiC substrate. Employing a strong coupling model for the analysis of the dispersion and electric field distribution in these hybridized modes, we show that they share the most prominent features of the two precursor modes. The novel ENZ-SPhP coupled polaritons with a highly propagative character and deeply subwavelength light confinement can be utilized as building blocks for future infrared and terahertz nanophotonic integration and communication devices.

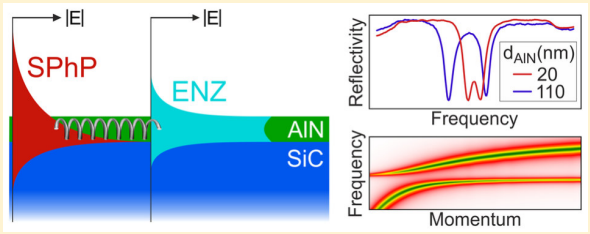

KEYWORDS: *Surface phonon polariton, epsilon-near-zero, infrared, nanophotonics, polar crystal, strong coupling, hybridization*

Integrated terahertz (THz) photonics relies on the development of artificially designed nanoscale metamaterials, where subwavelength structures in periodic patterns enable precise tuning of the material's optical response.[1−3] Truly extraordinary light propagation characteristics can be achieved in metamaterial-based epsilon-near-zero (ENZ) media,[4,5] that is, where the dielectric permittivity is vanishingly small. In particular, remarkable properties of the ENZ photonic modes include tunneling through narrow distorted channels,[6,7] enhanced nonlinear-optical conversion efficiency via enforced phase-matching,[8−10] high emission directionality,[11−13] and enable polaritonic waveguiding modes with broken time inversion symmetry and reduced scattering rate.[14,15]

An important challenge of future nanophotonics consists in enabling effective nanoscale communication and long-range information transfer. Both those objectives can be greatly facilitated by exploiting the unique properties of ENZ physics. In this regard, it is of key importance to find an appropriate class of systems where high-Q ENZ polaritons can be efficiently excited and coupled to other photonic excitations, while maintaining highly propagative character with reasonable group velocities. Commonly, bulk ENZ photonic modes excited in carefully designed metamaterials based on plasmonic nanostructures are considered, which are, however, characterized by high losses.[16,17] A complementary approach aims at utilizing the naturally occurring zero-crossing of the dielectric function in the spectral vicinity of intrinsic material vibrations, such as the transverse optical (TO) and longitudinal optical (LO) phonons in polar dielectric crystals.[18−20] Yet, employing freestanding films of polar dielectrics,[19] however, bears little practical importance, and the low dispersion results in a nonpropagative character of the ENZ polaritonic modes.[18]

In this work, we suggest a novel concept for ENZ excitations, which utilizes strong coupling between the ENZ and surface phonon polaritons (SPhPs) in the reststrahlen band of polar dielectrics (demarcated by the phonon frequencies ω_{TO} and ω_{LO}[21,22]). We demonstrate the hybridization of an ENZ polariton and a propagating low-loss SPhP at an adjacent interface in the strong coupling regime, thus adding a new pair of coupled nanophotonic excitations to an evergrowing suite.[23−27] We analyze the coupling of the ENZ and SPhP modes in an AlN/SiC bilayer, where the ENZ polariton in AlN occurs within the reststrahlen band of SiC. The novel coupled ENZ-SPhP modes inherit their properties from both ENZ and SPhP components, thus enabling highly efficient phase-matched excitation. Offering broad functionality, these ENZ-SPhP coupled modes feature a unique combination of deeply subwavelength confinement, large enhancements of the local electromagnetic fields, as well as

Received: March 29, 2018
Revised: May 30, 2018
Published: June 12, 2018

DOI: 10.1021/acs.nanolett.8b01273
Nano Lett. 2018, 18, 4285−4292

an intrinsically low-loss, propagative character with nonzero group velocity.

A SPhP mode supported at the interface of a polar dielectric in the Reststrahlen band is split into two branches upon reducing the film thickness d (Figure 1a), known as symmetric and antisymmetric modes.[18,19,28] Remarkably, in ultrathin films ($d/\lambda < 10^{-2}$ with λ being the free-space wavelength) the upper (symmetric) mode is pushed toward the LO phonon frequency,[18] where the real part of the dielectric permittivity approaches zero ($\varepsilon'(\omega = \omega_{LO}) = 0$). While this ultrathin film ENZ polariton loses its dispersive character, its ultralong wavelength leads to a strongly subwavelength mode confinement, enabling a gigantic enhancement of the electric field with minimal phase change over several times the free-space wavelength. The polariton dispersion curves in the bilayer with an ultrathin AlN film on top of a SiC substrate are exemplified in Figure 1b. Individually, the AlN film exhibits a nondispersive ENZ polariton mode (light blue) and the SiC a SPhP (dark blue), see Figure S1a of the Supporting Information. The combined bilayer structure (inset Figure 1b), however, reveals a strong interaction between the two modes, leading to two new dispersive branches featuring an avoided crossing (red).

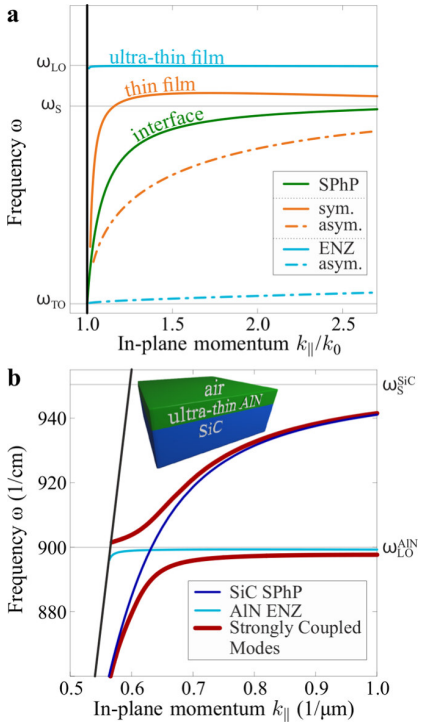

Figure 1. Interaction of a surface phonon polariton with an epsilon-near-zero mode. (a) A SPhP propagating at a single interface of air and a polar crystal has a dispersion relation (green curve) ranging from the transversal optical phonon frequency ω_{TO} up to a cutoff frequency ω_S, shown in green. For film thicknesses $d < \lambda/2$, where λ is the free-space wavelength, a symmetric and an antisymmetric branch appear (orange), splitting further apart with decreasing d. In the ultrathin limit of $d < \lambda/100$, the upper branch is pushed close to the longitudinal optical phonon frequency ω_{LO} (light blue), where the permittivity exhibits a natural zero-crossing. Therefore, the symmetric branch is termed an epsilon-near-zero mode. (b) When an ultrathin AlN film is placed on bulk SiC, the AlN epsilon-near-zero mode (light blue) intersects the SiC SPhP dispersion relation (dark blue). These modes strongly interact, inducing an avoided crossing and forming two new dispersion branches of the coupled system, drawn in red.

In the experiments, we realize phase-matched excitation of the coupled modes by employing the Otto prism geometry[29,30] with a schematic provided in Figure 2a. For total internal reflection inside the prism, the evanescent wave at the prism backside enables phase-matched excitation of the polariton modes in the sample. Spectroscopic reflectivity measurements with varied incidence angle allow for the mapping out of the polariton dispersion relation (for details on the experimental methods see Supporting Information Section 1). In our AlN/SiC structure, two polariton branches are present, and hence two resonance dips can be observed (Figure 2b), showing that the frequency splitting of the branches increases for thicker films. This trend is also evident in the experimental reflectivity maps and the transfer matrix calculations in Figure 3. Furthermore, our data reveal the anticipated avoided crossing in the dispersion of the interacting polariton modes, corroborating the strong coupling mechanism.

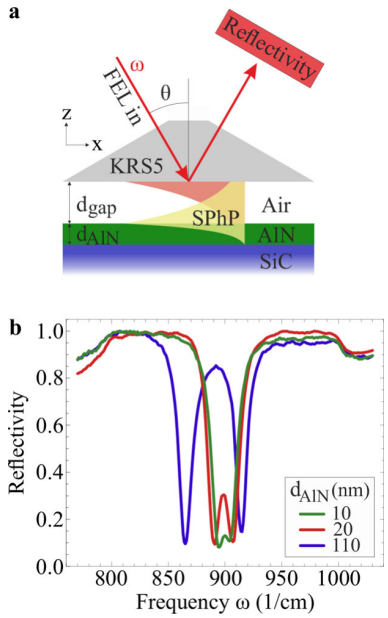

Figure 2. The variations of Rabi splitting for different AlN film thicknesses. (a) Prism coupling setup implementing the Otto configuration, where a highly refractive KRS5 prism ($n_{KRS5} \approx 2.4$) enables phase-matched excitation of phonon polaritons across a variable air gap. By tuning the incoming frequency ω and the incidence angle θ, polariton dispersion curves can be mapped out. (b) Reflectivity spectra for three different AlN film thicknesses d_{AlN} = 10, 20, 110 nm (θ = 29, 29, 30° and d_{gap} = 4.8, 4.5, 3.7 μm, respectively). The resonance dips represent the two strongly interacting polariton branches in the AlN/SiC heterostructure.

Analytically, the strong coupling can be described by a system of two coupled oscillators, modeling the ENZ and the SPhP modes, respectively. This allows us to calculate, in an analytically transparent way, the dispersion and the in-plane E-field distributions of the normal modes in the hybrid structure. The eigenfrequencies $\omega_q^{\pm}$ of the coupled system are then given by

DOI: 10.1021/acs.nanolett.8b01273
Nano Lett. 2018, 18, 4285−4292

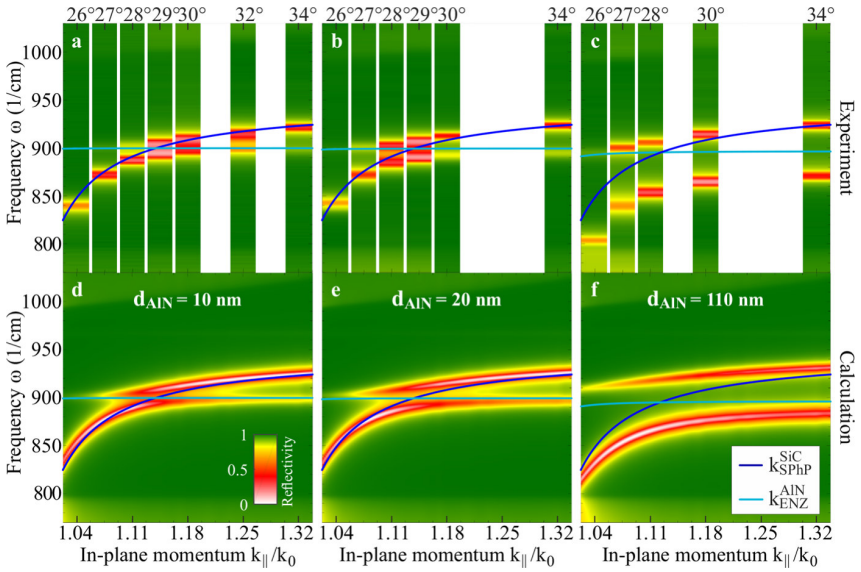

Figure 3. Mapping out the strongly coupled polariton dispersion. Experimental and calculated reflectivity maps for all three d_{AlN}, revealing the anticipated avoided crossing in the dispersion of the interacting polariton modes. The transfer matrix calculations (d–f) perfectly reproduce the experimental data (a–c). Clearly, the splitting of the modes is large for the thickest film and decreases for smaller thicknesses. The dark and light blue lines indicate the dispersion of the uncoupled SPhP and ENZ modes, respectively. The former is calculated in the limit of vanishing AlN thickness, while the latter is the dispersion of the ultrathin film polariton in a freestanding AlN film. We note that for the here shown film thicknesses, the dependence of the dispersion of the ultrathin film mode on d_{AlN} (compare to Figure 1a) is negligible.

$$\omega_q^{\pm} = \frac{\omega_q^e + \omega_q^s \pm \sqrt{(\omega_q^e - \omega_q^s)^2 + 4g_0^2}}{2} \quad (1)$$

where $\omega_q^{e,s}$ are the frequencies of the uncoupled ENZ and SPhP modes, respectively, and g_0 is the Rabi frequency, quantifying their mutual interaction. Although the eigenfrequencies in eq 1 can be derived using a classical coupled mode approach, as described in Methods, we decided to use instead the Hopfield model usually employed in solid-state cavity quantum electrodynamics,[31−34] which in our opinion allows us to gain a better insight into the hybrid nature of the resulting eigenmodes. We employ eq 1 to calculate the dispersion analytically (Figure 4a), finding excellent agreement of our strong coupling model with the numerical calculations and demonstrating that the description of the energetic hybridization of the modes in terms of strong coupling is correct.

Having established the strongly coupled oscillators model for the ultrathin AlN films on the SiC substrate, we now turn to its examination as a function of the AlN film thickness d_{AlN}. Two effects can be identified, which play an important role in the evolution of the strong coupling as d_{AlN} increases. First, because the SPhP is localized at the AlN/SiC interface and the ENZ mode in the entire AlN film, the spatial overlap of the two modes decreases, thus reducing the effective coupling strength. We can evaluate this through the distributions of the electric field calculated using the 4 × 4 transfer matrix formalism. These field distributions, exemplified for d_{AlN} = 110 nm in Figure S2c (see Supporting Information Section 4), indicate diminishing effective coupling strengths at $d_{AlN} \approx 50$ nm and beyond, while at smaller AlN thicknesses, this effect remains rather marginal, see Figure 4f. Second, because phonon polaritons are the collective excitations of atomic vibrations across individual bonds, increasing d_{AlN} in our model effectively results in a correspondingly larger oscillator strength f_{ENZ}. At these small thicknesses $d_{AlN} \ll \lambda$, the optical absorption scales almost linearly with thickness, leading to a concomitant linear increase of the oscillator strength. Within the strong coupling formalism, the Rabi frequency g_0 (determining half the distance between the two spectral peaks corresponding to the coupled modes) scales as $\sqrt{f_{ENZ}}$[35−37] and thus as $\sqrt{d_{AlN}}$. The Rabi frequency obtained from the fits of the calculated data using eq 1 follows this expected square root dependence with great accuracy, see Figure 4b. This behavior is further reproduced by the experimental coupling strengths also shown in Figure 4b, determined by half the frequency splitting in the respective reflectivity spectra (Figure 2b). Even though the Rabi frequency follows the $\sqrt{d_{AlN}}$ dependence up to $d_{AlN} \approx 500$ nm, the effective coupling strength is maximal for $d_{AlN} < 50$ nm due to the aforementioned loss of the spatial overlap of the two modes.

It is thus seen that the AlN/SiC bilayer can be tuned from the weak into the strong coupling regime by modifying the AlN layer thickness. In order to determine the lower limit of the d_{AlN} range of strong coupling, we employ the criterion which, quite intuitively, requires that the energy exchange rate between the two strongly coupled oscillators should exceed the loss rate, resulting in the appearance of two distinct frequencies in the spectrum.[38,39] A reliable and sufficient indication of the strong coupling is thus the avoided resonance crossing behavior (Figure 3) occurring if $2g_0/\gamma^* > 1$ is fulfilled, where $\gamma^* = (\gamma^e + \gamma^s)/2$ is the average of the loss rates of the two oscillators.

For our system, we obtain an estimate for the average loss rate of $\gamma^* = 5.8$. (While γ^s can be readily calculated using the transfer matrix method, determination of γ^e is not straightforward. As an estimation, we assume the proportionality of the loss rate γ to the imaginary part of the permittivity Im(ε) of the corresponding material where the mode is largely localized

DOI: 10.1021/acs.nanolett.8b01273
Nano Lett. 2018, 18, 4285−4292

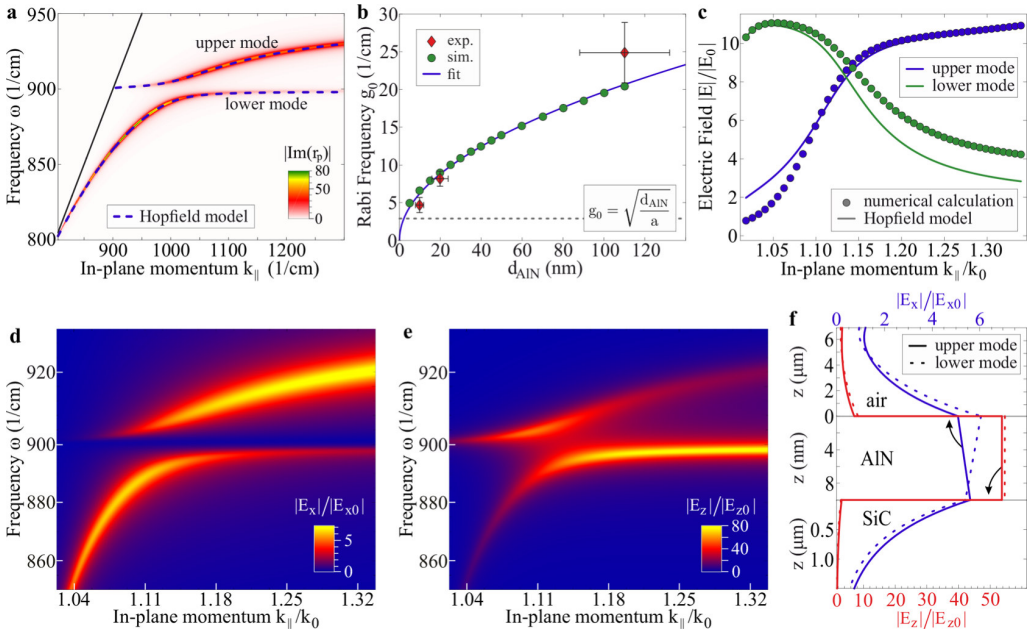

Figure 4. Coupling between the ENZ and SPhP modes. (a) Dispersion curves obtained by the analytical strong coupling model (dashed line) for an AlN film thickness of d_{AlN} = 10 nm on SiC on top of the numerically calculated dispersion curves obtained by computing the absolute imaginary part of the p-polarization reflection coefficient of the three layer system air/AlN/SiC. The analytical model features excellent agreement with the numerical calculations. (b) Rabi frequency g_0 as a function of d_{AlN} extracted from the analytical model (green circles) and experiments (red diamonds). As can be seen from the simple model fit (solid line, $a = 0.26 \times 10^{-13}$ m^3), the Rabi frequency follows a square root function characteristic for strong coupling. The dotted gray line indicates the threshold coupling strength for strong coupling according to the criterion discussed in the text. (c) Electric field strength obtained by the analytical model (solid line) and numerical calculations (circles) for the two strongly coupled modes, calculated at a probe point in air at the sample surface. At the avoided crossing, the two modes are completely hybridized, sharing equal field strength. At smaller in-plane momentum than at the avoided crossing, the lower branch has a larger field strength than the upper branch, and vice versa at larger momenta. The mode with larger field strength exhibits SPhP character because at the specific probe point the SPhP field dominates, whereas the ENZ polariton is localized inside the AlN film. (d,e) Normalized in-plane (E_x) and out-of-plane (E_z) field components along the entire dispersion. The SPhP has large in-plane and the ENZ polariton large out-of-plane fields, while the respective other component is small. This allows one to track the mode nature (SPhP or ENZ polariton) of both dispersion branches, which is exchanged at the avoided crossing, along the entire momentum range. (f) Normalized E_x and E_z fields of the upper and the lower mode at resonance ($k_\parallel/k_0$ = 1.13) across the air/AlN/SiC structure. The layer thicknesses are not to scale with respect to each other.

(AlN and SiC for the ENZ and SPhP modes, respectively). As such, at $\omega \approx 900$ cm^{-1} we get $\gamma^s \approx 8.7$ cm^{-1}, $\gamma^e \approx 3.0$ cm^{-1}, and thus $\gamma^* \approx 5.8$ cm^{-1}) The horizontal dotted line in Figure 4b illustrates the threshold coupling strength (2.9 cm^{-1}) corresponding to the onset of the strong coupling regime according to the aforementioned criterion. This value can be reached in AlN films with thicknesses of 2.2 nm. It is therefore seen that in the ultrathin AlN films on a SiC substrate discussed in this work, the ENZ and SPhP polaritons can indeed be strongly coupled for AlN film thicknesses 2.2 nm $\lesssim d_{AlN} \lesssim$ 50 nm.

Furthermore, our simple analytical model also correctly describes the electric field profiles. This is illustrated in Figure 4c, where we show the coinciding analytical and numerically calculated field intensities of both modes in front of the sample. We note that while a bare SiC substrate allows the SPhP component of the coupled modes to be quantified, the ENZ polariton component depends decisively on the substrate material and hence cannot be straightforwardly quantified. Therefore, we assumed the ENZ polariton to be fully confined in the AlN film, i.e., the field at the probe point is solely determined by the SPhP component of the coupled modes. This assumption is the reason for the discrepancy between the analytical and calculated field intensities at in-plane momenta where the respective mode features ENZ character ($k_\parallel/k_0 < 1.1$ and $k_\parallel/k_0 > 1.2$ in Figure 4c). However, despite its simplicity, our model reproduces the numerical field amplitudes extremely well, proving that the coupled modes can be described as a linear superposition of the ENZ and SPhP modes, weighted by the Hopfield coefficients. In consequence of this linear relationship, the strongly coupled modes at the avoided crossing share equal weights of SPhP and ENZ character, while the respective partitions change along the dispersion: the lower polariton starts as pure SPhP at small k and switches to ENZ beyond the avoided crossing, while the upper polariton shows the opposite behavior.

This switching of the mode nature can be illustrated by means of the in-plane (E_x) and out-of-plane (E_z) electric field components inside the AlN film, shown in Figure 4d,e, respectively. Note that the SPhP is characterized by a large in-plane field, whereas the ENZ polariton features pronounced out-of-plane field enhancement. The lower branch has strong in-plane fields at lower momentum (Figure 4d), illustrating that the mode is predominantly SPhP in nature. In contrast, the upper branch exhibits strong out-of-plane character at low $k_\parallel$ (Figure 4e). Across the strong coupling region, the modes interchange these characteristics with the upper branch exhibiting strong in-plane and the lower out-of-plane fields. At the avoided crossing, the fields of both modes are apparent and of equal weight, and even the spatial E_x and E_z field

DOI: 10.1021/acs.nanolett.8b01273
Nano Lett. 2018, 18, 4285−4292

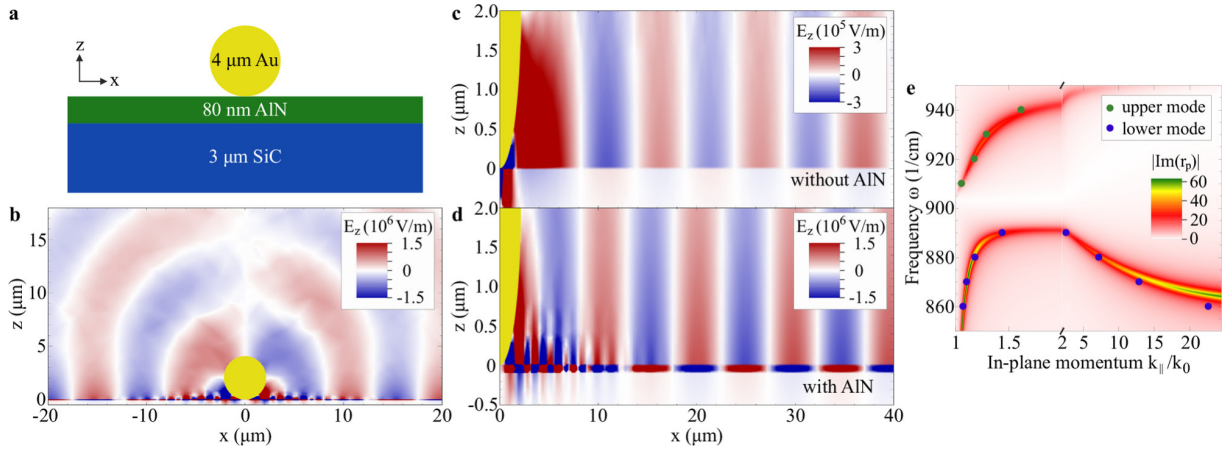

Figure 5. Numerical simulations of a high-k polariton with negative group velocity. (a) The simulation geometry, where plane waves are normally incident on a gold particle on the surface. Because of the large size of the particle, in (b) both surface waves and scattered free space waves are observed. (c,d) Surface electromagnetic field for a bare SiC substrate (c) and with an 80 nm AlN film on top (d). The field distributions in b–d were all calculated at an excitation frequency of 880 cm^{-1}. (e) Comparison between the dispersion relation calculated by a transfer matrix approach (background color map) and the values extracted from the simulations (circles). At large in-plane momentum ($k_{\parallel}/k_0 > 2$), the negative slope of the dispersion of the lower mode reveals its negative group velocity.

distributions of the modes across the multilayer structure show high agreement (Figure 4f). We have thus demonstrated the strong coupling and full hybridization of an ultrathin film ENZ phonon polariton with a SPhP in a polar dielectric heterostructure exemplified for AlN/SiC. However, we emphasize that strong coupling will emerge for a large number of hybrid systems that feature overlapping reststrahlen bands of the two constituents.[21,22] Furthermore, strong coupling can also be observed in the inverse structure of an ultrathin SiC film on AlN, occurring at the TO frequency of SiC (see Supporting Information Section 3).

Another important consideration which can be inferred from the distributions of the electric field is pertinent to the upper limit of the strong coupling. As mentioned above, for large thicknesses the spatial mismatch of the field distributions for the ENZ and SPhP modes (localized in the entire AlN film and at the AlN–SiC interface, respectively) becomes more and more important. For instance, in Supporting Information Section 4 the field distributions for the 110 nm thick AlN film are exemplified, clearly showing the lack of full hybridization of the ENZ and SPhP modes. Our calculations reveal that this effect becomes significant for thicknesses $d_{AlN} \gtrsim 50$ nm, thus reducing the effective coupling constant g_0. As such, we conclude that despite the fact that the mode splitting follows the $\sqrt{d_{AlN}}$ dependence up to $d_{AlN} \approx 500$ nm, ultrathin films with deeply subwavelength thicknesses of $d \sim \lambda/1000$ (11 nm for AlN) demonstrate the highest degree of strong coupling. In other words, within the strong coupling regime, thinner films provide higher quality ENZ wave characteristics, yet featuring full hybridization with the low-loss, highly confined SPhP, see Figure 4a–c. Within this regime, that is, for $d_{AlN} = 20$ nm, a propagation length of $L \approx 900$ μm with a group velocity of $v_g \approx 0.1$ c of the coupled modes is achieved. Thereby, the ENZ-SPhP modes offer a new promising approach for THz photonics on the nanoscale using traditional materials like III–V and II–VI semiconductors.[22] For instance, PbSe/PbS core–shell nanostructures[40] with wide tunability of the optical properties in the near-infrared additionally feature strongly coupled ENZ-SPhP modes in the THz range, allowing for a unique multispectral photonic integration.

To demonstrate that the general character of strong coupling is not restricted to the prism-based experiments, we complement our results with electromagnetic simulations of optical near-field scattering at nanoparticles. Motivated by previous results on scattering type scanning near field optical microscopy (s-SNOM) of Au nanostructures on SiC and boron nitride,[41,42] we consider here a Au cylinder on top of the AlN film on a SiC substrate, see Figure 5a. In the simulations, we monitor the spatial distribution of the electric field induced by normally incident plane waves at a series of frequencies. While an 80 nm AlN film was chosen in this simulation for a clear identification of the coupled polaritonic modes, similar results can be obtained for the AlN film thicknesses discussed earlier in this work.

Results for an 80 nm AlN film on top of a SiC substrate are presented in Figure 5b, showing the full electromagnetic field scattered from the Au cylinder at 880 cm^{-1}. To focus on the polaritons launched along the surface, in Figure 5c,d we consider the spatial distribution of the electric field along the surface in the two cases, namely, with and without the AlN layer. Without the AlN film (Figure 5c), the results of the simulations are indicative of a propagating SPhP wave launched across the surface with minimal confinement. In the presence of the AlN film, however, the simulations reveal two distinct modes with unequal wavelengths, see Figure 5d. The longer wavelength mode corresponds to that observed in our experiments, which is slightly compressed when compared with the wave propagating on the SiC surface. The short wavelength mode, however, was not observed in our measurements due to its large in-plane momentum. We attribute this mode to the breakdown of the thin film approximation for ENZ behavior which has been theoretically predicted at extremely large k.[18] One of the most striking features of this large-k mode is its negative group velocity, clearly visible from the dispersion in Figure 5e and confirmed by the time-dependent E-field distributions (Movie S1).

To better understand both the positive and negative group velocity modes observed in these simulations, we quantify the

DOI: 10.1021/acs.nanolett.8b01273
Nano Lett. 2018, 18, 4285–4292

polariton wavelength by Fourier transform (FT) of the simulated electromagnetic field. Here, we take the FT of the normal projection of the complex E_z field on the top surface of the AlN layer at a series of different excitation frequencies. The dispersion determined from the E_z Fourier spectra are plotted and compared against transfer matrix simulations of the polariton dispersion in Figure 5e. The excellent agreement between the numerically simulated frequencies and the calculated dispersion indicates that the key results of this paper regarding the spatial distribution of fields should be observable by the s-SNOM technique. Additionally, the latter should enable the observation of the high-k mode with negative dispersion, which is otherwise inaccessible in the prism-coupling experiments. We thus envisage rich perspectives of near-field microscopy in visualizing coupled phonon−polaritonic modes in hybrid or multilayer systems.

In conclusion, in this work we have demonstrated and characterized polaritonic modes in a strong coupling regime between an ENZ polariton and a bulk SiC SPhP in an ultrathin AlN/SiC structure. The full mode hybridization at the avoided crossing enables unique propagating ENZ polaritons. We have performed numerical simulations, revealing that the s-SNOM approach enables the observation of both the propagation length of the coupled ENZ-SPhP modes, and the properties of polaritons featuring negative group velocity. Our results illustrate the high suitability of near-field techniques like s-SNOM for the investigation of low-loss ENZ polaritons in polar dielectric heterostructures in order to further establish their potential for nanophotonic applications. We envision the generalization of employing polar dielectric ENZ heterostructures to open up a new platform of deeply subwavelength integrated THz photonics based on strongly coupled ENZ-SPhPs.

Methods. *Experimental Section.* The substrate of our samples is hexagonal 6H-SiC for the 110 nm AlN film, and 4H-SiC for the other two samples, all three with the extraordinary axis perpendicular to the sample surface (*c*-cut). The AlN layers were grown by RF-plasma assisted molecular beam epitaxy, and therefore also exhibit a *c*-cut, hexagonal crystal structure.

As an excitation source, we employ a mid-infrared free electron laser (FEL) with small bandwidth (~0.3%) and wide tunability of 3−50 μm, covering the spectral ranges of the SiC and AlN reststrahlen bands (details on the FEL have been reported elsewhere[43]). While the frequency is scanned by tuning the FEL, different in-plane momenta can be accessed via the incidence angle θ by rotating the entire Otto geometry (see Supporting Information Section 1 for more details), thus allowing for mapping out the complete dispersion curves experimentally.[30] In contrast to alternative approaches, the Otto geometry features experimental control over the excitation efficiency through tunability of the air gap width d_{gap}. At each incidence angle, spectra were taken at several d_{gap}. For the reconstruction of the dispersion curves (Figure 3), we selected the spectra at a gap size of critical coupling conditions d_{crit},[30] that is, where the polariton is excited the most efficiently (Supporting Information Section 2). Direct read-out of the gap width d_{gap} within a range of d = 1−50 μm is realized via whitelight interferometry, while the contrast of the interference spectrum grants parallel alignment of prism and sample.

Theoretical. Transfer Matrix. All calculations of the optical response and field distributions of Figures 1−4 were performed using a generalized 4 × 4 transfer matrix formalism.[44] In short, the formalism allows for the calculation of reflection and transmission coefficients in any number of stratified media with arbitrary dielectric tensor, which allows one to account for the anisotropy of our samples.

Three-Layer Dispersion. The dispersion curves in Figure 1 were obtained by numerical evaluation of the three-layer polariton dispersion formula[18,28,45]

$$1 + \frac{\varepsilon_1 k_{z3}}{\varepsilon_3 k_{z1}} = i \tan(k_{z2} d)\left(\frac{\varepsilon_2 k_{z3}}{\epsilon_3 k_{z2}} + \frac{\varepsilon_1 k_{z2}}{\varepsilon_2 k_{z1}}\right) \tag{2}$$

where the subscripts i = 1, 2, 3 correspond to the three stacked media, ε is the dielectric function, d is the film thickness of material 2, $k_{zi} = \sqrt{\frac{\omega}{c}\varepsilon_i - k_{||}}$ is the out-of-plane momentum, and $k_{||}$ is the in-plane momentum conserved in all layers.

Hopfield Model. In the rotating wave approximation, the two-oscillator Hopfield Hamiltonian for our system takes the form[31−34]

$$\mathcal{H} = \sum_q \hbar\omega_q^e \hat{a}_q^\dagger \hat{a}_q + \hbar\omega_q^s \hat{b}_q^\dagger \hat{b}_q + \hbar g_0 (\hat{a}_q^\dagger \hat{b}_q + \hat{a}_q \hat{b}_q^\dagger) \tag{3}$$

where $\hat{a}_q^\dagger$ ($\hat{a}_q$) and $\hat{b}_q^\dagger$ ($\hat{b}_q$) are the bosonic creation (annihilation) operators for the ENZ and SPhP modes. The Rabi frequency g_0 of the strong coupling model in eq 3 is introduced as a phenomenological coupling parameter and is equivalent to the overlap of the substrate SPhP and ENZ polariton in a classical electromagnetic approach. The eigenfrequencies (eq 1) of the coupled system are found by diagonalization of the Hopfield-Bogoliubov matrix H_q[33]

$$H_q = \begin{pmatrix} \omega_q^e & g_0 \\ g_0 & \omega_q^s \end{pmatrix} \tag{4}$$

for each in-plane wavevector q individually, where e and s stand for the ENZ polariton and the substrate SPhP, respectively. The eigenvalues of these matrices yield the eigenfrequencies $\omega_q^\pm$ shown in eq 1, and the respective normalized eigenvectors (X_q, Y_q) are built from the Hopfield coefficients X_q and Y_q, describing the weighting factors of the ENZ polariton and the substrate SPhP which compose the two hybridized modes along the avoided crossing. The analytic electric field strength shown in Figure 4c has been calculated by multiplying these Hopfield coefficients with the electric field of the substrate SPhP at the probe point in air at the sample surface. The bosonic annihilation operators $\hat{p}_q$ of the coupled modes are then given by

$$\begin{aligned} \hat{p}_q^+ &= X_q \hat{a}_q + Y_q \hat{b}_q \\ \hat{p}_q^- &= Y_q \hat{a}_q - X_q \hat{b}_q \end{aligned} \tag{5}$$

where the superscripts + and − denote the upper and the lower coupled polariton branch, respectively.

CST Simulations. Simulations for Figure 5 were performed in CST studio suite[46] using the frequency domain solver. To approximate the structure shown in Figure 5a within a finite 3D model, a unit cell with a size of 250 μm by 0.6 μm was chosen, which minimized nearest neighbor interactions. The optical constants of the respective materials were taken from literature.[47,48] Unit cell boundaries were used at the edges of the substrate, and a matched impedance layer was used to suppress substrate reflections. Fourier analysis was performed

DOI: 10.1021/acs.nanolett.8b01273
Nano Lett. 2018, 18, 4285−4292

using a one-dimensional field profile running along the top surface of the ENZ film down the center of the unit cell.

■ ASSOCIATED CONTENT

Supporting Information

The Supporting Information is available free of charge on the ACS Publications website at DOI: 10.1021/acs.nanolett.8b01273.

Experimental details (Section 1), critical coupling conditions of the strongly coupled modes (Section 2), strongly interacting modes in materials with overlapping reststrahlen bands (Section 3), deviation from strong coupling for larger film thicknesses (Section 4) (PDF)

Simulated time-dependent E-field distributions (Movie S1) (MPG)

■ AUTHOR INFORMATION

Corresponding Authors

*E-mail: passler@fhi-berlin.mpg.de.
*E-mail: alexander.paarmann@fhi-berlin.mpg.de.

ORCID

Nikolai Christian Passler: 0000-0002-7477-8611
Christopher R. Gubbin: 0000-0003-3988-028X
Joshua D. Caldwell: 0000-0003-0374-2168
Alexander Paarmann: 0000-0002-8271-2284

Notes

The authors declare no competing financial interest.

■ ACKNOWLEDGMENTS

We thank Wieland Schöllkopf and Sandy Gewinner for operating the FEL. D.S.K., D.F.S, and J.D.C. were supported by the Office of Naval Research through the U.S. Naval Research Laboratory and administered by the NRL Nanoscience Institute. The NRL team acknowledges the AlN characterization and processing contributions of Neeraj Nepal, Brian P. Downey, and Neil P. Green. S.D.L. is a Royal Society Research Fellow and he acknowledges support from the Innovation Fund of the EPSRC Programme EP/M009122/1.

■ REFERENCES

(1) Joannopoulos, J. D.; Johnson, S. G.; Winn, J. N.; Meade, R. D. *Photonic Crystals: Molding the Flow of Light*; Princeton University Press, 2008.
(2) Burgos, S. P.; De Waele, R.; Polman, A.; Atwater, H. A. *Nat. Mater.* **2010**, *9*, 407−412.
(3) Degl'Innocenti, R.; Kindness, S. J.; Beere, H. E.; Ritchie, D. A. *Nanophotonics* **2018**, *7*, 127−144.
(4) Li, Y.; Kita, S.; Muñoz, P.; Reshef, O.; Vulis, D. I.; Yin, M.; Lončar, M.; Mazur, E. *Nat. Photonics* **2015**, *9*, 738−742.
(5) Liberal, I.; Engheta, N. *Nat. Photonics* **2017**, *11*, 149−158.
(6) Silveirinha, M. G.; Engheta, N. *Phys. Rev. B: Condens. Matter Mater. Phys.* **2007**, *76*, 1−17.
(7) Edwards, B.; Al, A.; Silveirinha, M. G.; Engheta, N. *J. Appl. Phys.* **2009**, *105*, 044905.
(8) Argyropoulos, C.; Chen, P. Y.; D'Aguanno, G.; Engheta, N.; Alù, A. *Phys. Rev. B: Condens. Matter Mater. Phys.* **2012**, *85*, 1−5.
(9) Suchowski, H.; O'Brien, K.; Wong, Z. J.; Salandrino, A.; Yin, X.; Zhang, X. *Science* **2013**, *342*, 1223−1226.
(10) Mattiucci, N.; Bloemer, M. J.; D'Aguanno, G. *Opt. Express* **2014**, *22*, 6381.
(11) Enoch, S.; Tayeb, G.; Sabouroux, P.; Guérin, N.; Vincent, P. *Phys. Rev. Lett.* **2002**, *89*, 213902.
(12) Ziolkowski, R. W. *Physical Review E - Statistical, Nonlinear, and Soft Matter Physics* **2004**, *70*, 1−12.
(13) Kim, J.; Dutta, A.; Naik, G. V.; Giles, A. J.; Bezares, F. J.; Ellis, C. T.; Tischler, J. G.; Mahmoud, A. M.; Caglayan, H.; Glembocki, O. J.; et al. *Optica* **2016**, *3*, 339.
(14) Liu, R.; Roberts, C. M.; Zhong, Y.; Podolskiy, V. A.; Wasserman, D. *ACS Photonics* **2016**, *3*, 1045−1052.
(15) Engheta, N. *Science* **2007**, *317*, 1698−1702.
(16) Drachev, V. P.; Chettiar, U. K.; Kildishev, A. V.; Yuan, H.-K.; Cai, W.; Shalaev, V. M. *Opt. Express* **2008**, *16*, 1186−1195.
(17) Khurgin, J. B.; Boltasseva, A. *MRS Bull.* **2012**, *37*, 768−779.
(18) Campione, S.; Brener, I.; Marquier, F. *Phys. Rev. B: Condens. Matter Mater. Phys.* **2015**, *91*, 121408.
(19) Nordin, L.; Dominguez, O.; Roberts, C. M.; Streyer, W.; Feng, K.; Fang, Z. *Appl. Phys. Lett.* **2017**, *111*, 091105.
(20) Vassant, S.; Hugonin, J.-P.; Marquier, F.; Greffet, J.-J. *Opt. Express* **2012**, *20*, 23971.
(21) Caldwell, J. D.; Lindsay, L.; Giannini, V.; Vurgaftman, I.; Reinecke, T. L.; Maier, S. A.; Glembocki, O. J. *Nanophotonics* **2015**, *4*, 44−68.
(22) Feng, K.; Streyer, W.; Zhong, Y.; Hoffman, A.; Wasserman, D. *Opt. Express* **2015**, *23*, A1418.
(23) Caldwell, J. D.; Vurgaftman, I.; Tischler, J. G.; Glembocki, O. J.; Owrutsky, J. C.; Reinecke, T. L. *Nat. Nanotechnol.* **2016**, *11*, 9−15.
(24) Basov, D. N.; Fogler, M. M.; García De Abajo, F. J. *Science* **2016**, *354*, aag1992.
(25) Low, T.; Chaves, A.; Caldwell, J. D.; Kumar, A.; Fang, N. X.; Avouris, P.; Heinz, T. F.; Guinea, F.; Martin-Moreno, L.; Koppens, F. *Nat. Mater.* **2017**, *16*, 182−194.
(26) Simpkins, B. S.; Fears, K. P.; Dressick, W. J.; Spann, B. T.; Dunkelberger, A. D.; Owrutsky, J. C. *ACS Photonics* **2015**, *2*, 1460−1467.
(27) Dunkelberger, A. D.; Spann, B. T.; Fears, K. P.; Simpkins, B. S.; Owrutsky, J. C. *Nat. Commun.* **2016**, *7*, 13504.
(28) Burke, J. J.; Stegeman, G. I.; Tamir, T. *Phys. Rev. B: Condens. Matter Mater. Phys.* **1986**, *33*, 5186−5201.
(29) Otto, A. *Z. Phys. A: Hadrons Nucl.* **1968**, *216*, 398−410.
(30) Passler, N. C.; Razdolski, I.; Gewinner, S.; Schöllkopf, W.; Wolf, M.; Paarmann, A. *ACS Photonics* **2017**, *4*, 1048−1053.
(31) Hopfield, J. J. *Phys. Rev.* **1958**, *112*, 1555−1567.
(32) Savona, V.; Hradil, Z.; Quattropani, A.; Schwendimann, P. *Phys. Rev. B: Condens. Matter Mater. Phys.* **1994**, *49*, 8774−8779.
(33) Gubbin, C. R.; Martini, F.; Politi, A.; Maier, S. A.; De Liberato, S. *Phys. Rev. Lett.* **2016**, *116*, 1−6.
(34) Gubbin, C. R.; Maier, S. A.; De Liberato, S. *Phys. Rev. B: Condens. Matter Mater. Phys.* **2016**, *94*, 1−9.
(35) Lidzey, D. G.; Bradley, D. D. C.; Skolnick, M. S.; Virgili, T.; Walker, S.; Whittaker, D. M. *Nature* **1998**, *395*, 53−55.
(36) Cade, N. I.; Ritman-Meer, T.; Richards, D. *Phys. Rev. B: Condens. Matter Mater. Phys.* **2009**, *79*, 1−4.
(37) Baieva, S. V.; Hakala, T. K.; Toppari, J. J. *Nanoscale Res. Lett.* **2012**, *7*, 191.
(38) Auffèves, A.; Gerace, D.; Gérard, J. M.; Santos, M. F.; Andreani, L. C.; Poizat, J. P. *Phys. Rev. B: Condens. Matter Mater. Phys.* **2010**, *81*, 1−10.
(39) Rodriguez, S. R. K. *Eur. J. Phys.* **2016**, *37*, 025802.
(40) Lifshitz, E.; Brumer, M.; Kigel, A.; Sashchiuk, A.; Bashouti, M.; Sirota, M.; Galun, E.; Burshtein, Z.; Le Quang, A. Q.; Ledoux-Rak, I.; et al. *J. Phys. Chem. B* **2006**, *110*, 25356−25365.
(41) Huber, A. J.; Deutsch, B.; Novotny, L.; Hillenbrand, R. *Appl. Phys. Lett.* **2008**, *92*, 203104.
(42) Dai, S.; Ma, Q.; Yang, Y.; Rosenfeld, J.; Goldflam, M. D.; McLeod, A.; Sun, Z.; Andersen, T. I.; Fei, Z.; Liu, M.; et al. *Nano Lett.* **2017**, *17*, 5285−5290.
(43) Schöllkopf, W.; Gewinner, S.; Junkes, H.; Paarmann, A.; von Helden, G.; Bluem, H.; Todd, A. M. M. *Proc. SPIE* **2015**, *9512*, 95121L.
(44) Passler, N. C.; Paarmann, A. *J. Opt. Soc. Am. B* **2017**, *34*, 2128.

(45) Raether, H. *Surface Plasmons on Smooth and Rough Surfaces and on Gratings*; Tracts in Modern Physics; Springer, 1988; Vol. *111*.
(46) CST, CST Studio Suite. https://www.cst.com/products/csts2, (accessed May 07, 2018).
(47) Engelbrecht, F.; Helbig, R. *Phys. Rev. B: Condens. Matter Mater. Phys.* **1993**, *48*, 15698−15707.
(48) Moore, W. J.; Freitas, J. A.; Holm, R. T.; Kovalenkov, O.; Dmitriev, V. *Appl. Phys. Lett.* **2005**, *86*, 141912.

DOI: 10.1021/acs.nanolett.8b01273
Nano Lett. 2018, 18, 4285−4292

4.4 Second Harmonic Generation from Phononic Epsilon-Near-Zero Berreman Modes in Ultrathin Polar Crystal Films

Nikolai Christian Passler, Ilya Razdolski, D. Scott Katzer, D. F. Storm, Joshua D. Caldwell, Martin Wolf, and Alexander Paarmann

This publication (Passler *et al.*, ACS Photonics 2019, **6**, 1365-1371 [**V**]) reports on the first experimental observation of enhanced SHG arising from the Berreman mode in a subwavelength-thin AlN film, which can be excited at the AlN LO frequency where the dielectric function crosses zero. The origin of the high SHG yield is the immense field enhancement at ENZ frequencies in ultra-thin films, and the work provides a thorough analysis of the thickness dependence of the field enhancement. The supporting information is reprinted in appendix A.3.

The samples studied in this work comprise an ultra-thin AlN film on a SiC substrate, which are the same samples where the strong coupling of ENZ polaritons was observed [**IV**]. Complementary to the evanescent polariton modes that were investigated previously in the Otto geometry setup [**IV**], this work focuses on the optical response under free-space excitation, revealing the Berreman mode as a radiative virtual polaritonic mode. The theoretical calculations of the field enhancement were performed using the transfer matrix formalism that has been published previously [**II**] (reprinted on page 45).

Author contributions

A.P. originated the concept. D.S.K. and D.F.S. performed the sample growth. The manuscript was written by **N.C.P.** and I.R., with all authors assisting in the proof-reading and preparation for final submission. The SHG measurements were performed by **N.C.P.**, and the results were analyzed by **N.C.P.**, I.R. and A.P. Calculations of the optical response were completed by **N.C.P.** The experimental design and project management were provided by M.W., J.D.C. and A.P.

go to list of publications

ACS Photonics

Letter

Cite This: ACS Photonics 2019, 6, 1365−1371

pubs.acs.org/journal/apchd5

Second Harmonic Generation from Phononic Epsilon-Near-Zero Berreman Modes in Ultrathin Polar Crystal Films

Nikolai Christian Passler,*[,†] I. Razdolski,[†] D. Scott Katzer,[‡] D. F. Storm,[‡] Joshua D. Caldwell,[‡,§] Martin Wolf,[†] and Alexander Paarmann*[,†]

[†]Fritz-Haber-Institut der Max-Planck-Gesellschaft, Faradayweg 4-6, 14195 Berlin, Germany

[‡]U.S. Naval Research Laboratory, 4555 Overlook Avenue SW, Washington, D.C. 20375, United States

[§]Vanderbilt University, Institute of Nanoscale Science and Engineering, 2201 West End Avenue, PMB 350106, Nashville, Tennessee 37235-0106, United States

Supporting Information

ABSTRACT: Immense optical field enhancement was predicted to occur for the Berreman mode in ultrathin films at frequencies in the vicinity of epsilon-near-zero (ENZ). Here, we report the first experimental proof of this prediction in the mid-infrared by probing the resonantly enhanced second harmonic generation (SHG) at the longitudinal optic phonon frequency from a deeply subwavelength-thin aluminum nitride (AlN) film. Employing a transfer matrix formalism, we show that the field enhancement is completely localized inside the AlN layer, revealing that the observed SHG signal of the Berreman mode is solely generated in the AlN film. Our results demonstrate that ENZ Berreman modes in intrinsically low-loss polar dielectric crystals constitute a promising platform for nonlinear nanophotonic applications.

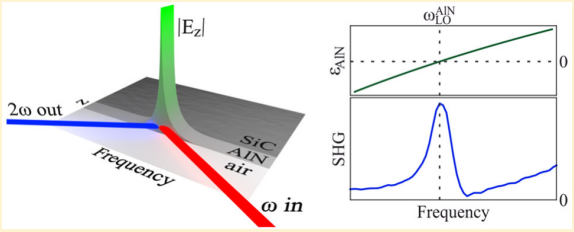

KEYWORDS: *Berreman mode, epsilon-near-zero, infrared, nanophotonics, second harmonic generation, field enhancement*

In nanophotonics, nonlinear optical phenomena are driven by the enhancement of local optical fields, which arises due to polaritonic resonances. These are traditionally observed as plasmon polaritons in metallic nanostructures or rough metal surfaces. Such strongly enhanced fields enable a variety of nanoscale applications,[1] such as all-optical switching,[2,3] low-loss frequency conversion,[4,5] and highly efficient sensing.[6,7] In the infrared (IR), an alternative to plasmonic resonances in metals are phonon polaritons supported in polar crystals,[8] as has been demonstrated in various seminal studies.[9−12] These phonon polaritons feature longer lifetimes than plasmon polaritons, leading to much larger quality factors and stronger field enhancements,[13−15] and thus, potentially enhanced efficiency of nonlinear optical effects.

One area in nanophotonics of distinct recent interest are investigations of polaritonic modes in plasmonic or polar dielectric subwavelength-thin films that emerge near zero permittivity. Over the past decades, the existence of such thin-film polaritonic modes has attracted broad attention.[16−26] Initially, radiation in a narrow spectral window at the plasma frequency of thin metal films was predicted[16] and later observed.[18−20] Its origin was associated with a collective surface plasma mode with polarization normal to the surface plane of the film.[18] At the same time, a similar effect was reported by Berreman in a thin polar dielectric film,[17] where absorption occurs at the longitudinal optic (LO) phonon frequency.

These absorption features in thin films were argued to originate in radiative virtual polaritonic modes,[21,22,24] naturally occurring at frequencies where the real part of the dielectric function crosses zero. This condition is met at the plasma frequency in a metal, and at the LO frequency of a polar crystal film. While these lossy polariton modes disperse on the low momentum side of the light line, it was discovered that a complementary evanescent polariton mode close to the LO frequency of a polar dielectric is also supported outside the light cone.[22] Just like the radiative modes, the evanescent polaritons naturally emerge in thin films at frequencies of vanishing dielectric function. Therefore, these modes offer an intriguing platform for exploiting the unique characteristics of waves propagating in so-called epsilon-near-zero (ENZ) materials.[27,28]

While most ENZ studies depend on carefully and intricately designed metamaterials,[29−32] thin metal or polar dielectric films stand out for their structural simplicity. Previous studies have reported promising applications employing these ENZ polariton modes, such as optoelectronic devices for the ultrafast control of absorption and emissivity,[33−35] directionally perfect absorption,[36,37] or long-range plasmon polaritons for the development of nanophotonic integrated technologies.[38,39]

Received: February 20, 2019
Published: June 3, 2019

DOI: 10.1021/acsphotonics.9b00290
ACS Photonics 2019, 6, 1365−1371

However, these previous studies mostly focused on the linear optical response, whereas only few reports of the nonlinear conversion efficiency of ultrathin films exist. This efficiency has been proposed to be strongly enhanced at ENZ frequencies,[40] but experimental verification is limited to a few studies of indium tin oxide (ITO) thin layers[41−43] excited at frequencies in the near-infrared spectral range. The nonlinear optical response of thin films of other materials with phonon resonances in the mid- to far-IR, in particular III−V or III-nitride polar semiconductor compounds, however, has to the best of our knowledge not yet been studied.

In this work, we investigate the linear and nonlinear optical response of ultrathin ($\lambda/1000$) AlN films on a SiC substrate in the radiative regime, where λ represents the free-space wavelength at the ENZ condition. We report strong SHG at the AlN LO phonon frequency arising from the Berreman mode in the ultrathin AlN film. The observed SHG yield provides experimental proof of the immense field enhancement inside the film and is attributed to the excitation of the Berreman resonance. Furthermore, we delineate several perspectives based on ENZ polaritons for the deployment of low-loss nonlinear nanophotonic applications.

A mode in a medium is defined as a solution of Maxwell's equations in the absence of an external perturbation. In a three-layer system, the dispersion of a polaritonic mode can be calculated by numerical evaluation of the following formula:[20,25,44]

$$1 + \frac{\varepsilon_1 k_{z3}}{\varepsilon_3 k_{z1}} = i \tan(k_{z2} d)\left(\frac{\varepsilon_2 k_{z3}}{\varepsilon_3 k_{z2}} + \frac{\varepsilon_1 k_{z2}}{\varepsilon_2 k_{z1}}\right) \quad (1)$$

where ε is the dielectric function, d is the film thickness of layer 2, $k_{zi} = \sqrt{\frac{\omega^2}{c^2}\varepsilon_i - k_x^2}$ is the out-of-plane momentum, k_x is the in-plane momentum conserved in all layers, and the subscripts i = 1, 2, and 3 refer to the three layered media. In principle, eq 1 can be solved either for a complex frequency ω and a real wavevector k_x, or for a complex k_x and a real ω. However, depending on the mode nature and the observables of interest, one of the representations is better suited than the other. We here choose the complex ω representation, following the rationales found in literature,[25,33,45,46] especially to account for the virtual nature of the Berreman mode[47] (for further details, see Supporting Information, Figure S1).

By solving eq 1 for an air/AlN/air system with varying thickness d_{AlN} of the AlN layer, the dispersion curves shown in Figure 1a are obtained. On the right-hand side of the light line, that is, in the region of evanescent surface-bound solutions, the symmetric (upper blue lines) and antisymmetric (lower blue lines) thin-film polaritons emerge. Spectrally, these modes are bound inside the AlN reststrahlen region between the TO and LO frequencies ω_{TO}^{AlN} and ω_{LO}^{AlN}, respectively. For thick films ($d_{AlN} > 1$), the two modes enclose the dispersion of a surface phonon polariton (SPhP) at the interface of a bulk AlN crystal (green line) and, for further increasing film thicknesses, eventually fall back onto this single green curve. On the other hand, for diminishing thicknesses, the two modes are pushed toward ω_{TO}^{AlN} and ω_{LO}^{AlN}. For d_{AlN} = 20 (solid line), the upper mode features a flat dispersion curve in the vicinity of ω_{LO}^{AlN}. At this frequency, the dielectric function approaches zero, and hence, the upper mode is an ENZ thin-film polariton.

The Berreman mode (red lines) arises as a continuation on the left-hand side of the light line, that is, in the region of

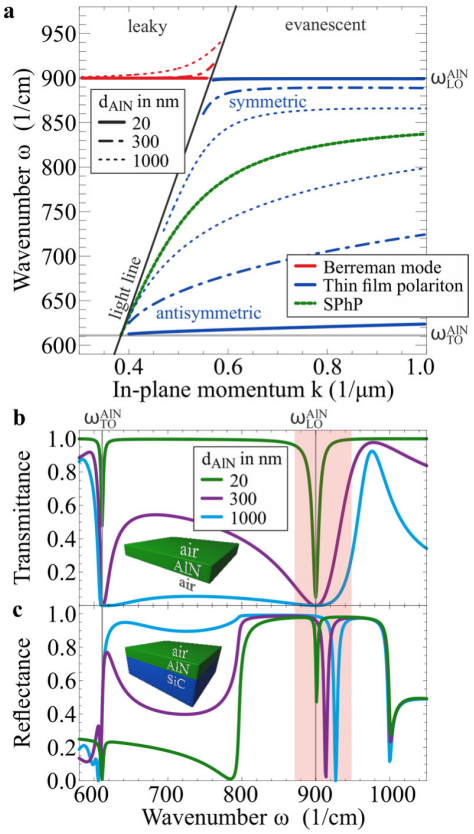

Figure 1. Berreman mode in a freestanding AlN film and on a SiC substrate. (a) Calculated dispersions of the Berreman mode and thin film polaritons in a freestanding AlN film, and that of a SPhP at the surface of a bulk AlN crystal. The Berreman mode is flat (red line) for ultrathin films ($d < \lambda/500$), while thicker films (dash dotted/dotted red lines) result in a dispersion bending upward in the vicinity of the light line in vacuum (black line). Analogous to the symmetric thin film polariton (blue line, upper branch), the dispersion of the Berreman mode lies close to the LO frequency where the real part of the dielectric function exhibits a zero-crossing. (b) Calculated transmittance of a freestanding AlN thin film for three different film thicknesses d_{AlN} at an incidence angle of 85°. The dip at the LO frequency for the thinnest film corresponds to the Berreman mode (red shade), which disappears with the buildup of the AlN reststrahlen band for increasing film thicknesses. (c) Calculated reflectance of an AlN thin film on a SiC substrate at an incidence angle of 85°. Here, the Berreman mode appears as a deep dip inside the reststrahlen band of SiC.

radiative solutions. Contrary to its evanescent counterpart, this leaky polariton mode undergoes a small upward bend close to the light line for larger film thicknesses. For d_{AlN} = 20 nm, however, the Berreman mode has a flat dispersion at ω_{LO} just like the evanescent polariton and, therefore, also exhibits ENZ character.

The feature in the transmittance spectrum of a thin film at the LO frequency originally reported by Berreman[17] is reproduced in the transmittance simulations shown in Figure 1b. The Berreman mode can only be excited by radiation with a nonzero out-of-plane electric field component, and hence p-polarized light at oblique incidence is required to observe the absorption peak. A visual explanation for the necessity of p-polarized excitation can be found in the spatial electric field

DOI: 10.1021/acsphotonics.9b00290
ACS Photonics 2019, 6, 1365−1371

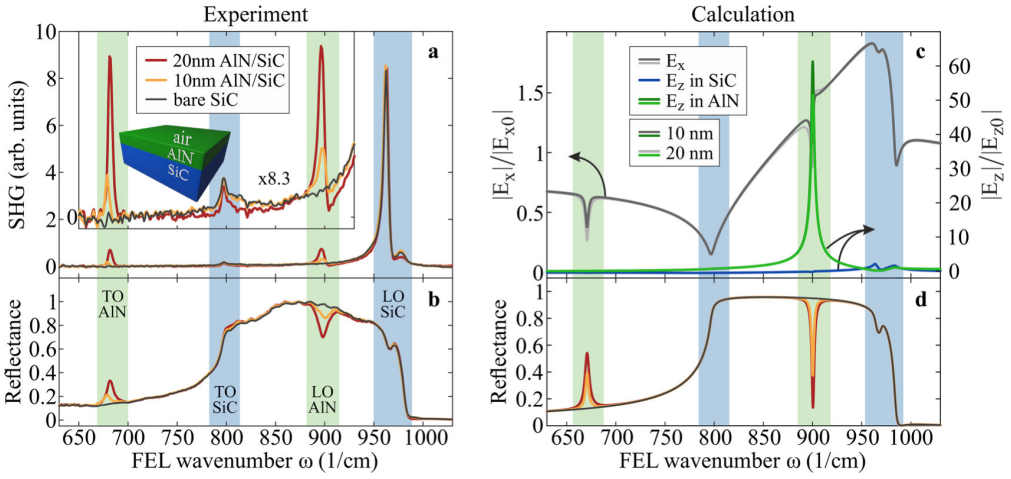

Figure 2. Strongly enhanced SHG from a Berreman mode in AlN. (a, b) Experimental SHG and reflectance spectra, respectively, taken for three samples consisting of (i) a 20 nm, (ii) a 10 nm thin AlN film on a 4H-SiC substrate, and (iii) a bare 4H-SiC crystal. Compared to the reference sample (iii), the AlN thin films only differ at the TO and LO frequencies of AlN, exhibiting small features in the reflectance and a strong SHG signal (enlarged by a factor of 8.3 in the inset in a). The origin of the strong SHG yield is illustrated in (c). While the in-plane E_x field enhancement is small at the AlN/SiC interface (gray lines, left y-axis), the out-of-plane E_z fields feature a strong enhancement of >60 at the AlN LO frequency (green lines, right y-axis). On the SiC side of the AlN/SiC interface, the E_z fields are small (blue line), revealing that the field enhancement is strictly confined inside the nanometric AlN layer. (d) Calculated reflectance curves of the investigated samples, being in excellent agreement with the experiment.

distribution of the Berreman mode (see Supporting Information and Figure 2a,b). Along the in-plane coordinate x, the field vectors perform a rotation in the x-z plane, that is, the plane of incidence, with z being the out-of-plane coordinate. In order to accentuate the Berreman absorption feature, the curves shown in Figure 1b and c were calculated at an incidence angle of 85°, leading to a strongly pronounced dip at $\omega_{LO}^{AlN} = 900$ for $d_{AlN} = 20$ nm.

The transition from an ultrathin AlN film with $d_{AlN} = 20$ nm to a thicker one with $d_{AlN} = 1000$ nm, is characterized by the buildup of the AlN reststrahlen band, featuring vanishing transmittance between the TO and LO frequencies, as shown in Figure 1b. Because of this buildup, already for $d_{AlN} = 300$ nm, the Berreman absorption dip is strongly broadened and its frequency position is not clearly defined. This is different in Figure 1c, were we show the reflectance curves for an air/AlN/SiC structure, resembling the experimentally investigated sample. Interestingly, the highly reflective reststrahlen band of the SiC substrate allows to observe the Berreman absorption feature in a reflectance measurement. In contrast to the freestanding film, a sharp and deep minimum is observed even for 1000 nm film thickness, indicating that the Berreman mode is still supported at the thick-film limit. In the Supporting Information, Figure S3b, the reflectance is shown for film thicknesses up to 5 μm. For $d_{AlN} > 1.5$ μm, the amplitude of the Berreman dip starts to diminish, approaching the optical response of a bulk AlN crystal that does not support a Berreman mode anymore.

In order to verify that the reflectance dips in Figure 1c originate in the Berreman mode, the theoretical dispersion for the air/AlN/SiC structure is calculated employing eq 1. While being quantitatively similar to the air/AlN/air Berreman mode dispersion, the SiC substrate leads to a smaller slope and a reduced frequency in proximity to the light line (see Supporting Information, Figure S3a). As is shown in Supporting Information, Figure S3b, the frequencies of the theoretical dispersion at 85° incidence angle and those of the numerical reflectance curves are in excellent agreement, corroborating that a reflectance measurement gives experimental access to the Berreman mode of the air/AlN/SiC structure.

We employ SHG spectroscopy[48] to probe the field enhancement associated with the excitation of the Berreman mode. The strongest field confinement occurs in ultrathin films leading to a strong field enhancement of the Berreman mode, which is a prerequisite for the observation of a significant SHG signal. We therefore focus on two samples with ultrathin AlN films of thickness $d_{AlN} = 10$ and 20 nm. The AlN films were grown by RF-plasma assisted molecular beam epitaxy onto a 4H-SiC substrate and, therefore, also feature a hexagonal crystal structure with the c-axis being perpendicular to the sample surface.

The reflectance and SHG spectroscopy measurements were performed in a noncollinear autocorrelator setup[48] at 30° and 60° incidence angle employing a tunable, narrow-band, p-polarized mid-IR free electron laser (FEL)[49] as an excitation source. Beforehand, intrinsic higher harmonics of the FEL are blocked by two dichroic 7 μm long-pass filters. The reflectance is recorded at 60° by a pyroelectric detector, whereas the two-pulse correlated SHG signal is generated at 45° between the reflected fundamental beams and is measured by a mercury–cadmium–telluride detector. For two p-polarized incident beams, the produced SHG signal is also p-polarized (PPP configuration). Because of the respective $\chi^{(2)}$ component for c-cut crystals being zero, there is no SPP contribution.[48,50] We note that the noncollinear excitation scheme is only applicable for ultrathin films where the shift of the Berreman resonance frequency with incidence angle is negligible (see Figure 1a), whereas for thicker films, a collinear setup would be necessary.[51]

The experimental SHG and reflectance spectra are plotted in Figure 2a and b, respectively. There, the yellow and red lines

DOI: 10.1021/acsphotonics.9b00290
ACS Photonics 2019, 6, 1365−1371

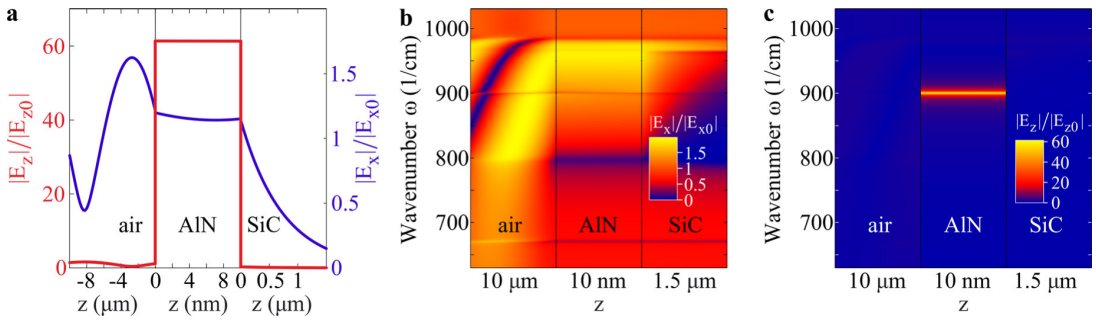

Figure 3. Field enhancement in a 10 nm thin AlN film. (a) In-plane and out-of-plane normalized fields E_x and E_z, respectively, along the z axis perpendicular to the interfaces and calculated at the Berreman resonance at 900 cm^{-1}. The large E_z field enhancement (red) is strongly localized inside the AlN. The E_x field (blue), on the other hand, does not feature any significant field enhancement. Note that in the air layer, the sum of the normalized incoming wave and the reflected wave is plotted, thus resulting in amplitudes larger than 1. (b, c) Spatio-spectral maps of E_x and E_z, respectively. The in-plane field E_x features a small enhancement at the SiC LO (965 cm^{-1}) and a minimum at the SiC TO (797 cm^{-1}). In between in the SiC reststrahlen band, the field decays evanescently into the SiC substrate. Interestingly, a local minimum in E_x can be observed at both the AlN TO (670 cm^{-1}) and the AlN LO (900 cm^{-1}). On the contrary, the out-of-plane field E_z in (c) features an immense and spectrally sharp field enhancement inside the AlN layer at the AlN LO frequency.

indicate the data for the 10 and 20 nm thick AlN films, respectively. Additionally, we show spectra for a bare SiC sample (black lines). As has been demonstrated previously,[48,50] the bulk SiC substrate produces SHG peaks at its TO and LO frequencies (blue shades), leading to the same response in all three samples in these regions ($\omega \sim 800$ and 970 cm^{-1}). In fact, the only deviations from the bulk reflectance and SHG spectra are seen at the AlN TO and LO frequencies (green shades), where we observe clear, strong peaks in the SHG signal scaling with the AlN film thickness (see inset in Figure 2a with enlarged vertical axis). The observation of such a sizable SHG yield at the LO frequency is astonishing, especially considering the exceptionally small effective volume of only a few nanometer AlN that is generating the signal.

The SHG intensity I_{SHG} is proportional to the tensor product of the field enhancement $\vec{E}(\omega)$ and the second-order susceptibility tensor $\chi^{(2)}$:[52]

$$I_{SHG} \propto \left|\chi^{(2)}(-2\omega;\, \omega,\, \omega)\vec{E}(\omega)\vec{E}(\omega)\right|^2 \tag{2}$$

It is clear that either a resonance peak in $\chi^{(2)}$ or $\vec{E}(\omega)$ will lead to an enhanced SHG yield and thus a peak in the SHG spectrum. However, at the LO frequency, the second-order susceptibility $\chi^{(2)}$ has no resonances.[48] As for the case of polaritons,[51] also here we do not need to introduce an additional resonance in the $\chi^{(2)}$ to reproduce the data. We therefore argue that the origin of the reported large SHG yield is the immense electric field enhancement in the AlN thin film. In order to get further insights into the electric field distributions, we employ a 4 × 4 transfer matrix formalism specifically designed to simultaneously handle media with fully anisotropic as well as isotropic dielectric tensors.[53] This allows us to account for the uniaxial anisotropy of both 4H-SiC and hexagonal AlN, leading to an accurate reproduction of the reflectance data with highly detailed qualitative accordance. For instance, even small features like the dip at the high-frequency reststrahlen edge of SiC originating from the SiC anisotropy are accurately reproduced, see Figure 2d. (Note that for Figure 1 the materials were taken to be isotropic, which is sufficient for the qualitative understanding of the Berreman mode.)

Quantitatively, the calculations feature a deeper and sharper Berreman dip in the reflectance than in the experiments, see Figure 2b. This discrepancy is mainly due to growth defects in the AlN layer and an unavoidable strain due to the lattice mismatch between SiC and AlN (1%),[54,55] leading to an effectively increased damping constant of AlN than assumed in the calculations (γ_{AlN} = 2.2 cm^{-1}).[56] Furthermore, an additional experimental broadening arises from the FEL line width (~4 cm^{-1}).

In Figure 2c, we show the in-plane (E_x) and out-of-plane (E_z) local electric field enhancements at the AlN/SiC interface in both media. Note that E_x and E_z are normalized to their respective incoming field amplitudes E_{x0} and E_{z0}. While E_x is conserved at the interface and is generally small (with a maximum value of ~1.9), the E_z field enhancement features a strong peak at ω_{LO}^{AlN} with a maximum of >60 for the 10 nm film.

Note that while the Berreman reflectance minimum deepens for larger film thicknesses, the E_z field enhancement is already 16% smaller in the 20 nm than in the 10 nm film. Thus, counterintuitively, thicker films that feature higher optical absorption, exhibit a smaller degree of field enhancement. In the observed SHG signal, this reduction is compensated by an increasing effective volume, leading to larger SHG yields. However, we emphasize that only ultrathin films (d_{AlN} < 50 nm) demonstrate such high field intensities, thus, opening new possibilities for deeply subwavelength nanophotonic applications in the IR.

The E_z field is fully confined inside the AlN layer, which is reflected in the flat frequency dependence and small magnitude of the E_z field enhancement in SiC (blue line in Figure 2c). This field localization is even better illustrated in Figure 3a, where we show the spatial distribution of the in-plane E_x and out-of-plane E_z field enhancements as a function of z, that is, along the surface normal, at ω = 900 cm^{-1}. The electric field has to obey Maxwell's boundary conditions, that is, continuity of the in-plane fields ($E_x^{air} = E_x^{AlN}$ and $E_y^{air} = E_y^{AlN}$) and of the out-of-plane displacement field $D_z = \varepsilon E_z$ is required:

$$\varepsilon_{air} E_z^{air} = \varepsilon_{AlN} E_z^{AlN} \tag{3}$$

Equation 3 is the physical reason for a field enhancement at ENZ conditions, since for vanishing ε_{AlN} adjacent to air with a finite ε_{air}, the electric field E_z^{AlN} strongly increases in order to

DOI: 10.1021/acsphotonics.9b00290
ACS Photonics 2019, 6, 1365−1371

fulfill the boundary condition. In a bulk crystal, the field enhancement at ENZ conditions typically reaches values on the order of 1−10 (e.g., in bare SiC[48] or in an AlN/SiC structure, see Supporting Information, Figure S4a).

However, in a bulk crystal the phase difference of the incoming and the reflected fields is close to zero, leading to a small total field at the air/AlN interface (E_z^{air}) due to destructive interference. As a consequence, following eq 3, the ENZ induced enhancement of the E_z^{AlN} field is strongly suppressed. In contrast, in the limit of an ultrathin AlN film ($d_{\mathrm{AlN}} \lesssim 100$ nm), the phase difference becomes sizable, thus, leading to the strong field enhancement as shown in Figure 2c and Figure 3a (for details, see Supporting Information, Figure S4b−g).

Figure 3b and c show spatio-spectral maps of the E_x and E_z fields each normalized to E_{x0} and E_{z0}, respectively. Interestingly, E_x features no considerable field enhancement, but exhibits small dips or peaks marking the TO and LO frequencies of both AlN and SiC. The spatio-spectral map of E_z in Figure 3c, on the other hand, clearly reveals the extreme, spectrally sharp and strongly confined field enhancement in the AlN layer at $\omega = 900$ cm^{-1}.

Finally, we turn to the TO frequency of AlN (670 cm^{-1}),[57] where the experimental data in Figure 2a exhibit a strong SHG signal of similar magnitude as at the LO frequency. Quite surprisingly, this AlN TO peak is even larger than the peak at the TO frequency of the SiC substrate. Partially, this can be attributed to a reduced field suppression at ω_{TO} for thin films compared to a bulk crystal[52] (see Supporting Information, Figure S5). Notably, the observed peak arises from a resonance in the second-order susceptibility $\chi^{(2)}$ at $\omega_{\mathrm{TO}}^{\mathrm{AlN}}$, and not from a field enhancement as for the LO peak. Therefore, to fully understand the SHG peak amplitudes at the TO frequencies, a quantitative model of the $\chi^{(2)}$ for AlN would be necessary.

In this work, we have observed an immense SHG signal arising from a Berreman mode in an ultrathin AlN film excited at ENZ frequencies in the mid-IR. Analogous to previous studies of ITO,[58] aluminum-doped ZnO,[59] and CdO,[60] the high optical nonlinearity at ENZ conditions in our system holds high promises for all-optical ultrafast control of polarization switching,[60] and even over the material's optical properties.[58,59] However, while all mentioned studies employ ultrathin films excited via free-space radiation, for which in our system the Berreman mode is accessible, dispersing inside the light cone in vacuum, a complementary polaritonic ENZ mode exists on the other side of the light line. The linear response of these ENZ polaritons has been studied recently,[61,62] but investigations of their nonlinear response are to the best of our knowledge still lacking. Analogous to the Berreman mode, a strong field enhancement also characterizes the ENZ thin film polariton due to its ENZ environment. We, therefore, highlight the nonlinear response of ENZ polaritons to be an intriguing subject, specifically in light of the development of polariton-based nonlinear nanophotonics.

Polar crystals such as AlN or SiC, where ENZ conditions are met at the LO phonon resonances in the mid-IR, feature several appealing properties that are unavailable in metals or ITO: (i) The imaginary part of the dielectric function ε_2 at ω_{LO} ($\varepsilon_{\mathrm{AlN}}(\omega = \omega_{\mathrm{LO}}) = 0 + 0.02i$) is significantly smaller than in metals,[63] and more than 1 order of magnitude smaller than for ITO ($\varepsilon_{\mathrm{ITO}}(\omega = \omega_{\mathrm{LO}}) = 0 + 0.5i$),[43] which strongly increases the field enhancement inside the thin layer and, hence, the SHG efficiency. (ii) Many polytypes of SiC as well as AlN exhibit a hexagonal crystal structure, resulting in a uniaxial anisotropy of the dielectric tensor. This anisotropy leads to a hyperbolic frequency region between the extraordinary and ordinary LO frequencies, that is, in the range of the ENZ polaritons, enabling a whole new range of phenomena yet to be explored. These phenomena include, as has been observed in different systems before, negative refraction,[64] negative phase velocity,[65] or subdiffraction imaging and focusing.[66,67] (iii) Compared to highly doped semiconductors, one drawback of polar crystals is the lack of tunability of the ENZ frequency, being fixed to the LO phonon. On the other hand, due to relatively short lifetimes of surface plasmon polaritons in metals or most highly doped semiconductors, plasmon-based nanophotonics exhibits intrinsic drawbacks due to inherently high losses, whereas SPhPs in polar crystals feature much longer polariton lifetimes due to long-lived phonon resonances.[8,68] Hence, the employment of the ENZ polariton at the LO frequency offers an appealing alternative for nanophotonic applications, where low-loss ENZ characteristics combine with ultrahigh field enhancements.

In conclusion, we have reported the first observation of a resonantly enhanced SHG yield from a phononic Berreman mode in a deeply subwavelength thin film, exemplified for AlN on a 4H-SiC substrate. The origin of this large SHG signal is the immense out-of-plane field enhancement arising due to the zero-crossing of the dielectric function at the thin film LO frequency, strongly confined to the ultrathin layer. Thanks to low phonon dampings in polar crystals such as AlN and SiC, nanophotonic systems based on such crystals offer an appealing alternative to plasmonics, featuring high-quality resonances with extreme field enhancements. As a possible pathway, we envision ultrathin-film Berreman modes featuring ENZ nature to provide new opportunities for ultrafast all-optical control by taking advantage of the high optical nonlinearity.

■ ASSOCIATED CONTENT

Supporting Information

The Supporting Information is available free of charge on the ACS Publications website at DOI: 10.1021/acsphotonics.9b00290.

Theoretical thin film polariton dispersions for either complex frequency or in-plane momentum (Figure S1); Electric field distribution of the Berreman mode in a 1 μm thick AlN slab (Figure S2); Comparsion of theoretically and numerically determined Berreman dispersion (Figure S3); Out-of-plane field enhancement E_z at the interfaces of the air/AlN/SiC system (Figure S4); Contributions to the SHG yield at the AlN TO frequency (Figure S5) (PDF)

■ AUTHOR INFORMATION

Corresponding Authors

*E-mail: passler@fhi-berlin.mpg.de.
*E-mail: alexander.paarmann@fhi-berlin.mpg.de.

ORCID

Nikolai Christian Passler: 0000-0002-7477-8611
Joshua D. Caldwell: 0000-0003-0374-2168
Alexander Paarmann: 0000-0002-8271-2284

Notes

The authors declare no competing financial interest.

DOI: 10.1021/acsphotonics.9b00290
ACS Photonics 2019, 6, 1365−1371

■ ACKNOWLEDGMENTS

We thank Wieland Schöllkopf and Sandy Gewinner for operating the FEL. D.S.K. and D.F.S. acknowledge funding support from the Office of Naval Research. J.D.C. acknowledges financial support from the Office of Naval Research under grant N00014-18-2107 and from Vanderbilt School of Engineering. We thank Christopher J. Winta for careful reading of the paper.

■ REFERENCES

(1) Kauranen, M.; Zayats, A. V. Nonlinear plasmonics. *Nat. Photonics* **2012**, *6*, 737−748.
(2) Lu, H.; Liu, X.; Wang, L.; Gong, Y.; Mao, D. Ultrafast all-optical switching in nanoplasmonic waveguide with Kerr nonlinear resonator. *Opt. Express* **2011**, *19*, 2910.
(3) Ren, M.; Jia, B.; Ou, J.-Y.; Plum, E.; Zhang, J.; MacDonald, K. F.; Nikolaenko, A. E.; Xu, J.; Gu, M.; Zheludev, N. I. Nanostructured Plasmonic Medium for Terahertz Bandwidth AllOptical Switching. *Adv. Mater.* **2011**, *23*, 5540−5544.
(4) Sederberg, S.; Elezzabi, A. Y. Coherent Visible-Light-Generation Enhancement in Silicon-Based Nanoplasmonic Waveguides via Third-Harmonic Conversion. *Phys. Rev. Lett.* **2015**, *114*, 227401.
(5) Shibanuma, T.; Grinblat, G.; Albella, P.; Maier, S. A. Efficient Third Harmonic Generation from MetalDielectric Hybrid Nanoantennas. *Nano Lett.* **2017**, *17*, 2647−2651.
(6) Nie, S.; Emory, S. R. Probing Single Molecules and Single Nanoparticles by Surface-Enhanced Raman Scattering. *Science* **1997**, *275*, 1102−1106.
(7) Kneipp, K.; Wang, Y.; Kneipp, H.; Perelman, L. T.; Itzkan, I.; Dasari, R. R.; Feld, M. S. Single Molecule Detection Using Surface-Enhanced Raman Scattering (SERS). *Phys. Rev. Lett.* **1997**, *78*, 1667−1670.
(8) Caldwell, J. D.; Lindsay, L.; Giannini, V.; Vurgaftman, I.; Reinecke, T. L.; Maier, S. A.; Glembocki, O. J. Low-loss, infrared and terahertz nanophotonics using surface phonon polaritons. *Nanophotonics* **2015**, *4*, 44−68.
(9) Hillenbrand, R.; Taubner, T.; Keilmann, F. Phonon-enhanced lightmatter interaction at the nanometre scale. *Nature* **2002**, *418*, 159−162.
(10) Wang, T.; Li, P.; Hauer, B.; Chigrin, D. N.; Taubner, T. Optical Properties of Single Infrared Resonant Circular Microcavities for Surface Phonon Polaritons. *Nano Lett.* **2013**, *13*, 5051−5055.
(11) Caldwell, J. D.; Glembocki, O. J.; Francescato, Y.; Sharac, N.; Giannini, V.; Bezares, F. J.; Long, J. P.; Owrutsky, J. C.; Vurgaftman, I.; Tischler, J. G.; et al. Low-Loss, Extreme Subdiffraction Photon Confinement via Silicon Carbide Localized Surface Phonon Polariton Resonators. *Nano Lett.* **2013**, *13*, 3690−3697.
(12) Autore, M.; Li, P.; Dolado, I.; AlfaroMozaz, F. J.; Esteban, R.; Atxabal, A.; Casanova, F.; Hueso, L. E.; Alonso-González, P.; Aizpurua, J.; et al. Boron nitride nanoresonators for phonon-enhanced molecular vibrational spectroscopy at the strong coupling limit. *Light: Sci. Appl.* **2018**, *7*, 17172.
(13) Chen, Y.; Francescato, Y.; Caldwell, J. D.; Giannini, V.; Maß, T. W. W.; Glembocki, O. J.; Bezares, F. J.; Taubner, T.; Kasica, R.; Hong, M.; et al. Spectral Tuning of Localized Surface Phonon Polariton Resonators for Low-Loss Mid-IR Applications. *ACS Photonics* **2014**, *1*, 718−724.
(14) Caldwell, J. D.; Kretinin, A. V.; Chen, Y.; Giannini, V.; Fogler, M. M.; Francescato, Y.; Ellis, C. T.; Tischler, J. G.; Woods, C. R.; Giles, A. J.; et al. Sub-diffractional volume-confined polaritons in the natural hyperbolic material hexagonal boron nitride. *Nat. Commun.* **2014**, *5*, 5221.
(15) Giles, A. J.; Dai, S.; Vurgaftman, I.; Hoffman, T.; Liu, S.; Lindsay, L.; Ellis, C. T.; Assefa, N.; Chatzakis, I.; Reinecke, T. L.; et al. Ultralow-loss polaritons in isotopically pure boron nitride. *Nat. Mater.* **2018**, *17*, 134−139.
(16) Ferrell, R. A. Predicted Radiation of Plasma Oscillations in Metal Films. *Phys. Rev.* **1958**, *111*, 1214−1222.
(17) Berreman, D. W. Infrared Absorption at Longitudinal Optic Frequency in Cubic Crystal Films. *Phys. Rev.* **1963**, *130*, 2193−2198.
(18) McAlister, A. J.; Stern, E. A. Plasma Resonance Absorption in Thin Metal Films. *Phys. Rev.* **1963**, *132*, 1599−1602.
(19) Bösenberg, J.; Raether, H. PlasmaResonance Emission of Potassium, Excited by Light. *Phys. Rev. Lett.* **1967**, *18*, 397−398.
(20) Burke, J. J.; Stegeman, G. I.; Tamir, T. Surface-polariton-like waves guided by thin, lossy metal films. *Phys. Rev. B: Condens. Matter Mater. Phys.* **1986**, *33*, 5186−5201.
(21) Bichri, A.; Lafait, J.; Welsch, H. Visible and infrared optical properties of Ag/SiO 2 multilayers: radiative virtual modes and coupling effects. *J. Phys.: Condens. Matter* **1993**, *5*, 7361−7374.
(22) Vassant, S.; Hugonin, J.-P.; Marquier, F.; Greffet, J.-J. Berreman mode and epsilon near zero mode. *Opt. Express* **2012**, *20*, 23971.
(23) Newman, W. D.; Cortes, C. L.; Atkinson, J.; Pramanik, S.; Decorby, R. G.; Jacob, Z. Ferrell-berreman modes in plasmonic epsilon-near-zero media. *ACS Photonics* **2015**, *2*, 2−7.
(24) Nordin, L.; Dominguez, O.; Roberts, C. M.; Streyer, W.; Feng, K.; Fang, Z.; Podolskiy, V. A.; Hoffman, A. J.; Wasserman, D. Mid-infrared epsilon-nearzero modes in ultra-thin phononic films. *Appl. Phys. Lett.* **2017**, *111*, No. 091105.
(25) Campione, S.; Brener, I.; Marquier, F. Theory of epsilon-near-zero modes in ultrathin films. *Phys. Rev. B: Condens. Matter Mater. Phys.* **2015**, *91*, 121408.
(26) Shaykhutdinov, T.; Furchner, A.; Rappich, J.; Hinrichs, K. Mid-infrared nanospectroscopy of Berreman mode and epsilon-near-zero local field confinement in thin films. *Opt. Mater. Express* **2017**, *7*, 3706.
(27) Li, Y.; Kita, S.; Muñoz, P.; Reshef, O.; Vulis, D. I.; Yin, M.; Lončar, M.; Mazur, E. On-chip zero-index metamaterials. *Nat. Photonics* **2015**, *9*, 738−742.
(28) Liberal, I.; Engheta, N. Near-zero refractive index photonics. *Nat. Photonics* **2017**, *11*, 149−158.
(29) Joannopoulos, J. D.; Johnson, S. G.; Winn, J. N.; Meade, R. D. *Photonic Crystals: Molding the Flow of Light*; Princeton University Press, 2008.
(30) Burgos, S. P.; de Waele, R.; Polman, A.; Atwater, H. A. A single-layer wide-angle negative-index metamaterial at visible frequencies. *Nat. Mater.* **2010**, *9*, 407−412.
(31) Sakoda, K. *Optical Properties of Photonic Crystals*; Springer Series in Optical Sciences; Springer-Verlag: Berlin/Heidelberg, 2005; Vol. *80*; p 258.
(32) Argyropoulos, C.; D'Aguanno, G.; Alù, A. Giant second-harmonic generation efficiency and ideal phase matching with a double ϵ-near-zero cross-slit metamaterial. *Phys. Rev. B: Condens. Matter Mater. Phys.* **2014**, *89*, 235401.
(33) Vassant, S.; Archambault, A.; Marquier, F.; Pardo, F.; Gennser, U.; Cavanna, A.; Pelouard, J. L.; Greffet, J. J. Epsilon-Near-Zero Mode for Active Optoelectronic Devices. *Phys. Rev. Lett.* **2012**, *109*, 237401.
(34) Vassant, S.; Moldovan Doyen, I.; Marquier, F.; Pardo, F.; Gennser, U.; Cavanna, A.; Pelouard, J. L.; Greffet, J. J. Electrical modulation of emissivity. *Appl. Phys. Lett.* **2013**, *102*, No. 081125.
(35) Vasudev, A. P.; Kang, J.-H.; Park, J.; Liu, X.; Brongersma, M. L. Electro-optical modulation of a silicon waveguide with an epsilon-near-zero material. *Opt. Express* **2013**, *21*, 26387.
(36) Luk, T. S.; Campione, S.; Kim, I.; Feng, S.; Jun, Y. C.; Liu, S.; Wright, J. B.; Brener, I.; Catrysse, P. B.; Fan, S.; et al. Directional perfect absorption using deep subwavelength low-permittivity films. *Phys. Rev. B: Condens. Matter Mater. Phys.* **2014**, *90*, No. 085411.
(37) Feng, S.; Halterman, K. Coherent perfect absorption in epsilon-near-zero metamaterials. *Phys. Rev. B: Condens. Matter Mater. Phys.* **2012**, *86*, 165103.
(38) Berini, P. Plasmon-polariton waves guided by thin lossy metal films of finite width: Bound modes of asymmetric structures. *Phys. Rev. B: Condens. Matter Mater. Phys.* **2001**, *63*, 125417.
(39) Berini, P. Long-range surface plasmon polaritons. *Adv. Opt. Photonics* **2009**, *1*, 484.
(40) Vincenti, M. A.; de Ceglia, D.; Ciattoni, A.; Scalora, M. Singularity-driven second- and third-harmonic generation at ϵ-near-

DOI: 10.1021/acsphotonics.9b00290
ACS Photonics 2019, 6, 1365−1371

zero crossing points. *Phys. Rev. A: At., Mol., Opt. Phys.* **2011**, *84*, No. 063826.
(41) Capretti, A.; Wang, Y.; Engheta, N.; Dal Negro, L. Comparative Study of SecondHarmonic Generation from Epsilon-NearZero Indium Tin Oxide and Titanium Nitride Nanolayers Excited in the NearInfrared Spectral Range. *ACS Photonics* **2015**, *2*, 1584−1591.
(42) Luk, T. S.; de Ceglia, D.; Liu, S.; Keeler, G. A.; Prasankumar, R. P.; Vincenti, M. A.; Scalora, M.; Sinclair, M. B.; Campione, S. Enhanced third harmonic generation from the epsilonnear-zero modes of ultrathin films. *Appl. Phys. Lett.* **2015**, *106*, 151103.
(43) Capretti, A.; Wang, Y.; Engheta, N.; Dal Negro, L. Enhanced third-harmonic generation in Si-compatible epsilon-near-zero indium tin oxide nanolayers. *Opt. Lett.* **2015**, *40*, 1500.
(44) Raether, H. *Surface Plasmons on Smooth and Rough Surfaces and on Gratings*; Springer Tracts in Modern Physics; Springer Berlin Heidelberg: Berlin, Heidelberg, 1988; Vol. *111*.
(45) Archambault, A.; Teperik, T. V.; Marquier, F.; Greffet, J. J. Surface plasmon Fourier optics. *Phys. Rev. B: Condens. Matter Mater. Phys.* **2009**, *79*, 195414.
(46) Alexander, R. W.; Kovener, G. S.; Bell, R. J. Dispersion Curves for Surface Electromagnetic Waves with Damping. *Phys. Rev. Lett.* **1974**, *32*, 154−157.
(47) Kliewer, K. L.; Fuchs, R. Optical Modes of Vibration in an Ionic Crystal Slab Including Retardation. II. Radiative Region. *Phys. Rev.* **1966**, *150*, 573−588.
(48) Paarmann, A.; Razdolski, I.; Melnikov, A.; Gewinner, S.; Schöllkopf, W.; Wolf, M. Second harmonic generation spectroscopy in the Reststrahl band of SiC using an infrared free-electron laser. *Appl. Phys. Lett.* **2015**, *107*, No. 081101.
(49) Schöllkopf, W.; Gewinner, S.; Junkes, H.; Paarmann, A.; von Helden, G.; Bluem, H.; Todd, A. M. M. The new IR and THz FEL facility at the Fritz Haber Institute in Berlin. *Proc. of SPIE*; SPIE, 2015; p 95121L. DOI: 10.1117/12.2182284
(50) Paarmann, A.; Razdolski, I.; Gewinner, S.; Schöllkopf, W.; Wolf, M. Effects of crystal anisotropy on optical phonon resonances in midinfrared second harmonic response of SiC. *Phys. Rev. B: Condens. Matter Mater. Phys.* **2016**, *94*, 134312.
(51) Passler, N. C.; Razdolski, I.; Gewinner, S.; Schöllkopf, W.; Wolf, M.; Paarmann, A. Second-Harmonic Generation from Critically Coupled Surface Phonon Polaritons. *ACS Photonics* **2017**, *4*, 1048−1053.
(52) Shen, Y. Optical Second Harmonic Generation At Interfaces. *Annu. Rev. Phys. Chem.* **1989**, *40*, 327−350.
(53) Passler, N. C.; Paarmann, A. Generalized 4 × 4 matrix formalism for light propagation in anisotropic stratified media: study of surface phonon polaritons in polar dielectric heterostructures. *J. Opt. Soc. Am. B* **2017**, *34*, 2128.
(54) Tairov, Y.; Tsvetkov, V. Progress in controlling the growth of polytypic crystals. *Prog. Cryst. Growth Charact.* **1983**, *7*, 111−162.
(55) Taylor, K. M.; Lenie, C. Some Properties of Aluminum Nitride. *J. Electrochem. Soc.* **1960**, *107*, 308.
(56) Moore, W. J.; Freitas, J. A.; Holm, R. T.; Kovalenkov, O.; Dmitriev, V. Infrared dielectric function of wurtzite aluminum nitride. *Appl. Phys. Lett.* **2005**, *86*, 141912.
(57) Davydov, V. Y.; Kitaev, Y. E.; Goncharuk, I. N.; Smirnov, A. N.; Graul, J.; Semchinova, O.; Uffmann, D.; Smirnov, M. B.; Mirgorodsky, A. P.; Evarestov, R. A. Phonon dispersion and Raman scattering in hexagonal GaN and AlN. *Phys. Rev. B: Condens. Matter Mater. Phys.* **1998**, *58*, 12899−12907.
(58) Alam, M. Z.; De Leon, I.; Boyd, R. W. Large optical nonlinearity of indium tin oxide in its epsilon-near-zero region. *Science* **2016**, *352*, 795−797.
(59) Kinsey, N.; DeVault, C.; Kim, J.; Ferrera, M.; Shalaev, V. M.; Boltasseva, A. Epsilon-near-zero Al-doped ZnO for ultrafast switching at telecom wavelengths. *Optica* **2015**, *2*, 616.
(60) Yang, Y.; Kelley, K.; Sachet, E.; Campione, S.; Luk, T. S.; Maria, J.-P.; Sinclair, M. B.; Brener, I. Femtosecond optical polarization switching using a cadmium oxide-based perfect absorber. *Nat. Photonics* **2017**, *11*, 390−395.
(61) Passler, N. C.; Gubbin, C. R.; Folland, T. G.; Razdolski, I.; Katzer, D. S.; Storm, D. F.; Wolf, M.; De Liberato, S.; Caldwell, J. D.; Paarmann, A. Strong Coupling of Epsilon-Near-Zero Phonon Polaritons in Polar Dielectric Heterostructures. *Nano Lett.* **2018**, *18*, 4285−4292.
(62) Runnerstrom, E. L.; Kelly, K. P.; Folland, T. G.; Engheta, N.; Caldwell, J. D.; Maria, J.-P. Polaritonic hybrid-epsilonnear-zero modes: engineering strong optoelectronic coupling and dispersion in doped cadmium oxide bilayers. *arXiv:1808.03847 [cond-mat.mes-hall]* **2019**, 7.
(63) Lynch, D. W.; Hunter, W. Comments on the Optical Constants of Metals and an Introduction to the Data for Several Metals. *Handbook of Optical Constants of Solids*; Academic Press, 1985; Vol. *1*, pp 275−367.
(64) Rodrigues da Silva, R.; Maĉedo da Silva, R.; Dumelow, T.; da Costa, J. A. P.; Honorato, S. B.; Ayala, A. P. Using Phonon Resonances as a Route to All-Angle Negative Refraction in the FarInfrared Region: The Case of Crystal Quartz. *Phys. Rev. Lett.* **2010**, *105*, 163903.
(65) Yoxall, E.; Schnell, M.; Nikitin, A. Y.; Txoperena, O.; Woessner, A.; Lundeberg, M. B.; Casanova, F.; Hueso, L. E.; Koppens, F. H. L.; Hillenbrand, R. Direct observation of ultraslow hyperbolic polariton propagation with negative phase velocity. *Nat. Photonics* **2015**, *9*, 674−678.
(66) Li, P.; Lewin, M.; Kretinin, A. V.; Caldwell, J. D.; Novoselov, K. S.; Taniguchi, T.; Watanabe, K.; Gaussmann, F.; Taubner, T. Hyperbolic phonon-polaritons in boron nitride for near-field optical imaging and focusing. *Nat. Commun.* **2015**, *6*, 7507.
(67) Dai, S.; Ma, Q.; Andersen, T.; Mcleod, A. S.; Fei, Z.; Liu, M. K.; Wagner, M.; Watanabe, K.; Taniguchi, T.; Thiemens, M.; et al. Subdiffractional focusing and guiding of polaritonic rays in a natural hyperbolic material. *Nat. Commun.* **2015**, *6*, 6963.
(68) Khurgin, J. B. How to deal with the loss in plasmonics and metamaterials. *Nat. Nanotechnol.* **2015**, *10*, 2−6.

DOI: 10.1021/acsphotonics.9b00290
ACS Photonics 2019, 6, 1365−1371

4.5 Surface Polariton-Like s-Polarized Waveguide Modes in Switchable Dielectric Thin Films on Polar Crystals

Nikolai Christian Passler, Andreas Heßler, Matthias Wuttig, Thomas Taubner, and Alexander Paarmann

This publication (Passler *et al.*, AOM 2020, **8**, 1901056 [**VI**]) presents a model system consisting of a PCM on a polar crystal substrate that supports simultaneously p-polarized SPhPs and s-polarized, polariton-like waveguide modes. By switching the crystal phase of the PCM, the work demonstrates volatile control over both modes with a switching contrast that far exceeds typical values in the field of modulated nanophotonics [113–116]. The concept is visualized in the cover picture of the special issue Polaritons in Nanomaterials reprinted on the following page [117]. The supporting information is reprinted in appendix A.4.

Most importantly, this work delineates a path to resolve two aspects of SPhPs that are disadvantageous for nanophotonic applications: Firstly, introducing s-polarized waveguide modes with polariton-like properties provides a way to circumvent the polarization bottleneck of polaritons [118], and secondly, employing a switchable PCM as waveguide core drastically improves the usually very limited tunability of surface polaritons [119]. As such, the here presented approach extends the versatility of surface polaritons, providing a complementary building block for actively tunable, omnipolarized nanophotonic applications.

The experimental results for this work were obtained using the Otto geometry implementing the white-light interferometry [**X**], and the theoretical calculations are based on the transfer matrix formalism [**II**] (reprinted on page 45), which are the key experimental and theoretical tools developed in the course of this thesis.

Author contributions

A.P. and T.T. originated the concept. A.H. performed the sample growth. The manuscript was written by **N.C.P.**, A.H. and A.P., with all authors assisting in the proof-reading and preparation for final submission. The measurements were performed by **N.C.P.**, and the results were analyzed by **N.C.P.** and A.P. The theoretical calculations were completed by **N.C.P.** The experimental design and project management were provided by T.T. and A.P.

go to list of publications

Vol. 8 • No. 5 • March 5 • 2020

www.advopticalmat.de

ADVANCED OPTICAL MATERIALS

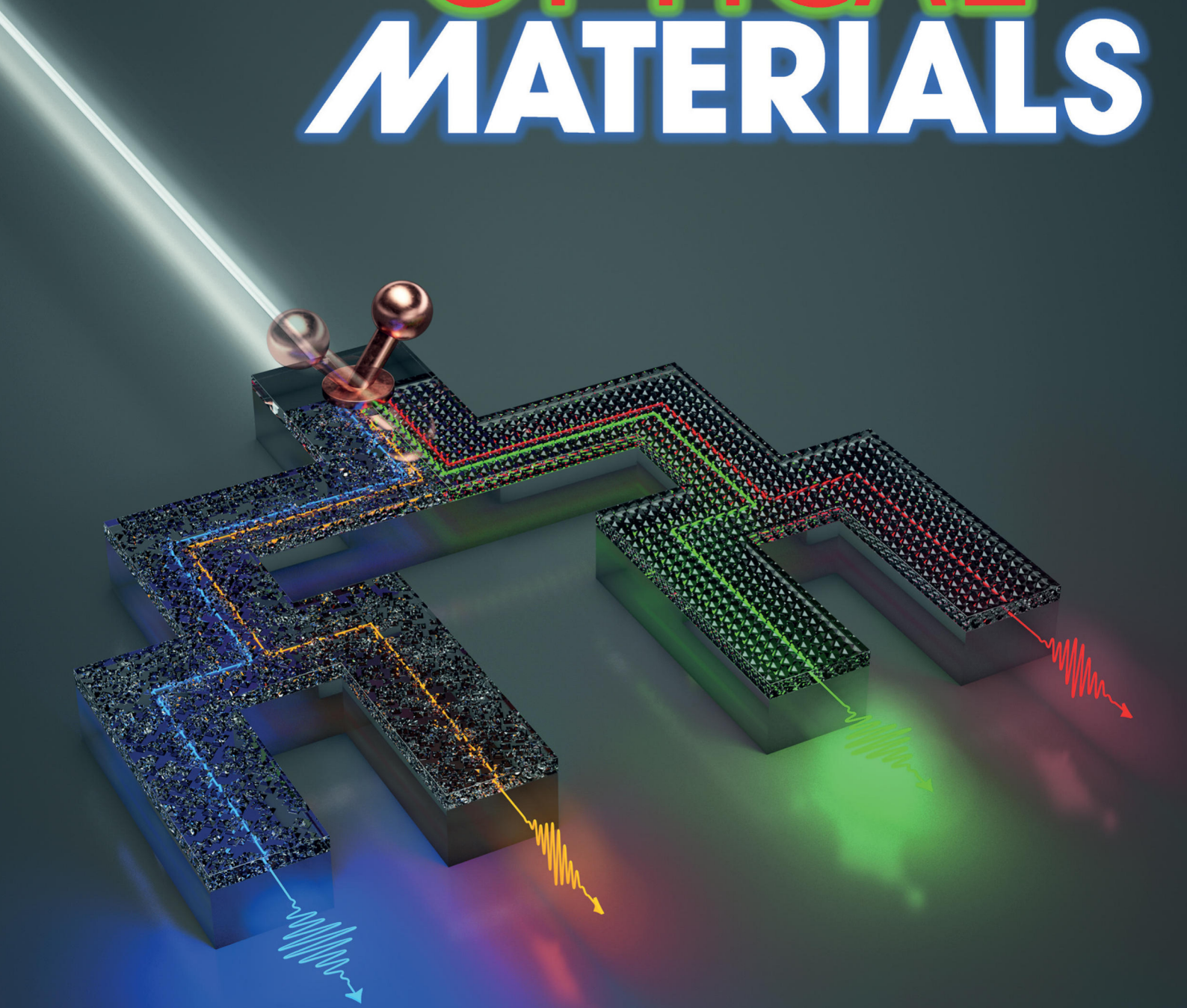

WILEY-VCH

Special Issue: Polaritons in Nanomaterials

Passler, N.C., Heßler, A., Wuttig, M., Taubner, T., Paarmann, A., Active Nanophotonics: Surface Polariton-Like s-Polarized Waveguide Modes in Switchable Dielectric Thin Films on Polar Crystals. Advanced Optical Materials 2020, 8, 5, 2070018, Cover Picture. https://doi.org/10.1002/adom.202070018

FULL PAPER

ADVANCED OPTICAL MATERIALS
www.advopticalmat.de

Surface Polariton-Like s-Polarized Waveguide Modes in Switchable Dielectric Thin Films on Polar Crystals

Nikolai Christian Passler, Andreas Heßler, Matthias Wuttig, Thomas Taubner, and Alexander Paarmann**

Surface phonon polaritons (SPhPs) and surface plasmon polaritons (SPPs), evanescent modes supported by media with negative permittivity, are a fundamental building block of nanophotonics. These modes are unmatched in terms of field enhancement and spatial confinement, and dynamical all-optical control can be achieved, e.g., by employing phase-change materials. However, the excitation of surface polaritons in planar structures is intrinsically limited to p-polarization. On the contrary, waveguide modes in high-permittivity films can couple to both p- and s-polarized light, and in thin films, their confinement can become comparable to surface polaritons. Here, it is demonstrated that the s-polarized waveguide mode in a thin $Ge_3Sb_2Te_6$ (GST) film features a similar dispersion, confinement, and electric field enhancement as the SPhP mode of the silicon carbide (SiC) substrate, while even expanding the allowed frequency range. Moreover, it is experimentally shown that switching the GST film grants nonvolatile control over the SPhP and the waveguide mode dispersions. An analytical model is provided for the description of the GST/SiC waveguide mode and it is shown that the concept is applicable to the broad variety of polar crystals throughout the infrared spectral range. As such, complementarily to the polarization-limited surface polaritons, the s-polarized waveguide mode constitutes a promising additional building block for nanophotonic applications.

1. Introduction

The field of nanophotonics pursues control over near-field optical phenomena that can be tailored in custom-designed nanoscale material systems. Key to achieve this control are surface-bound modes such as surface plasmon polaritons (SPPs) in metals[1] or surface phonon polaritons (SPhPs) in polar crystals,[2] which stand out by their unprecedented ability to confine and enhance the optical field in subwavelength structures.[3] In the past decades, the potential of these modes has been demonstrated by the large number of applications found in the fields of spectroscopy and sensing,[4–6] photonic circuitry,[7,8] lasers,[9,10] and nonlinear optical phenomena.[3,11,12]

SPPs and SPhPs are electromagnetic evanescent modes bound to the interface of two materials with permittivities Re(ε) of opposite sign. SPPs are supported in metals or doped semiconductors from infrared (IR) up to visible frequencies, where the negative Re(ε) arises from the Drude response of free electrons, whereas SPhPs arise in the mid to far IR range in the reststrahlen band of polar crystals between the transverse optical (TO) and longitudinal optical (LO) phonon frequencies. In comparison, SPhPs are valued for their longer lifetimes than SPPs due to the low losses of the driving phonon resonances.[2] Fundamentally, however, both modes consist of collective charge oscillations coupled to light, leading to shared properties such as subwavelength confinement, strong field enhancement, an asymptotic dispersion, and waveguiding characteristics, which are the reasons for the versatile usability of polaritonic modes.

However, SPPs and SPhPs in planar heterostructures intrinsically carry out-of-plane electric fields, and thus can only be excited by p-polarized light, while no s-polarized light can couple to them. This polarization restriction limits the versatility of polariton-based nanophotonics and potentially hinders the development of future technologies, such as emission control[13–15] or exploiting solar energy.[16,17] Very recently, omnipolarization waveguide modes in high-permittivity planar media were proposed to circumvent the polarization bottleneck of polaritons,[18] showing that in thin films, waveguide modes can reach comparable degrees of confinement as polaritons. However, while gaining a waveguide mode capable of coupling to s-polarized light, a high-permittivity thin film does not support a SPP or SPhP.

Another drawback of surface polaritons is their lack of active tunability when considered on a plain metal (polar crystal),

N. C. Passler, Dr. A. Paarmann
Fritz Haber Institute of the Max Planck Society
Faradayweg 4-6, 14195 Berlin, Germany
E-mail: passler@fhi-berlin.mpg.de;
alexander.paarmann@fhi-berlin.mpg.de
A. Heßler, Prof. M. Wuttig, Prof. T. Taubner
Institute of Physics (IA)
RWTH Aachen University
52056 Aachen, Germany
The ORCID identification number(s) for the author(s) of this article can be found under https://doi.org/10.1002/adom.201901056.

DOI: 10.1002/adom.201901056

ADVANCED SCIENCE NEWS
www.advancedsciencenews.com

ADVANCED OPTICAL MATERIALS
www.advopticalmat.de

because there the SPP (SPhP) dispersion is bounded by the fixed plasma frequency (optical phonon frequencies). For SPPs, this disadvantage can be overcome in doped semiconductors[19] or graphene,[20,21] where the photo or voltage-induced free charge carrier concentration enables tuning of the plasma frequency. A similar approach has been proposed for SPhPs,[22] but here, the tunability of the SPhPs gained by an additional photoinduced plasma contribution is limited.

A significantly larger and nonversatile switching contrast can be achieved by utilizing phase-change materials (PCMs)[23–25] such as the $Ge_3Sb_2Te_6$ compound (GST), which can be reversibly switched between its amorphous (a-) and crystalline (c-) phases by ultrafast electrical or optical pulses.[26–31] The high permittivity contrast between the two phases ($\varepsilon_{a\text{-}GST} \approx 13.8 + 0i$ and $\varepsilon_{c\text{-}GST} \approx 31.4 + 9i$; values are obtained from a global fitting procedure, see the Experimental Section for details) in the IR is sensed by SPhPs that evanescently penetrate the GST, leading to a significant shift of the SPhP mode frequency upon switching of the GST phase.[32] However, while systems utilizing PCMs have enabled active control over surface polaritons, the large potential of s-polarized waveguide modes in these systems remains, so far, unexploited.

2. Concept

In this work, we suggest a generic, actively tunable material system for the infrared spectral range that simultaneously supports p-polarized SPhPs and s-polarized waveguide modes. Intriguingly, the waveguide modes replicate the properties of the SPhP that define its suitability for nanophotonic applications, such as the enhancement of local electric fields and subwavelength confinement. We experimentally demonstrate active tuning of both excitations with exceptionally high tuning figures of merit[33,34] by means of a phase-change material, which, at the same time, constitutes the waveguide core. As a model system, we analyze the tuning of SPhP and waveguide modes in a GST/SiC structure, where the GST film can be switched between its amorphous and crystalline state. Offering broad functionality, such as polarization dependent polariton optics,[35,36] the proposed material system features a unique combination of active tunability of its guided modes and the lifting of the polarization bottleneck of conventional polaritonics.

An SPhP propagating along the surface of a polar crystal such as SiC exhibits an in-plane E_x field that peaks at the interface (**Figure 1**a). We define the x–z plane as the plane of incidence, and all waves propagate in x-direction. In Figure 1e (and zoomed into the reststrahlen region of SiC in Figure 1f), the dispersion of this SPhP is shown in black. By placing a 400 nm thin a-GST onto SiC, the SPhP dispersion is red-shifted (blue line in Figure 1e,f), while maintaining the shape of its in-plane electric field E_x (Figure 1b). Interestingly, here, the maximum field is encountered at the air/a-GST interface, and decays exponentially through the GST film into the SiC substrate (please note that for illustration purposes, the GST film thickness in Figure 1 a–d is not to scale with respect to the shown z-range of the adjacent air and the substrate).

A freestanding 400 nm thin a-GST film, on the other hand, supports an s-polarized waveguide mode owing to the high index contrast between a-GST and air.[37] The in-plane electric field E_y of this mode is shown in Figure 1d, and the corresponding dispersion is plotted in green in Figure 1e,f. Notably, this mode features a much larger penetration depth δ in positive and negative z-direction, with $E(z) = E(0)e^{-z/\delta}$, than the SPhP, hence it is much less confined within the a-GST film. The dispersion of this waveguide mode, however, is steeper and covers a much larger frequency range than the SPhP, which is restricted to the SiC reststrahlen band. Now, the combined system of a-GST/SiC supports not only the shifted p-polarized SPhP mode but simultaneously, at the

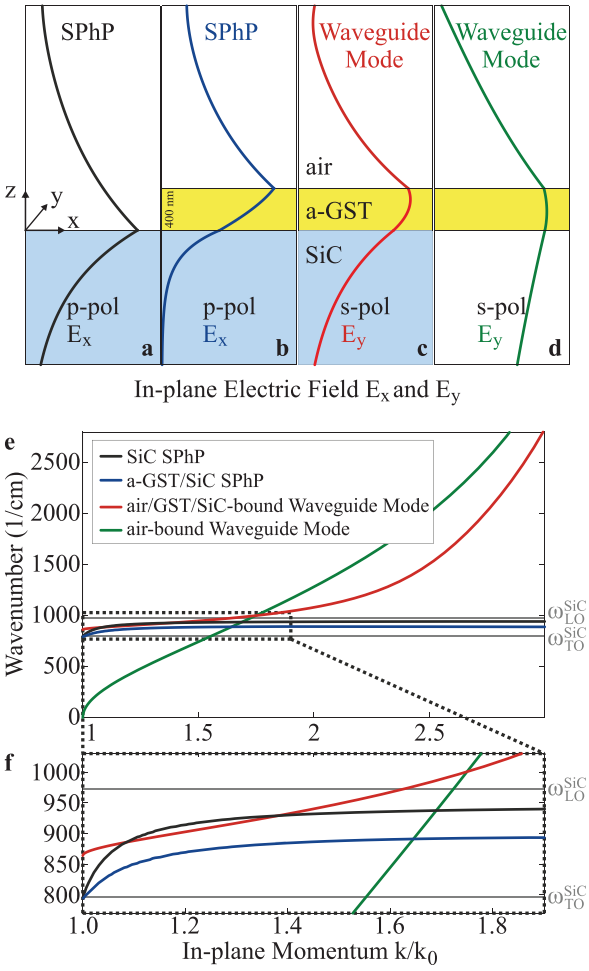

Figure 1. Guided modes in an a-GST film on an SiC substrate. a–d) Schematic in-plane electric field distributions of SPhPs and waveguide modes, excitable with p- and s-polarized light, respectively, supported a) on a bare SiC substrate, b,c) in a 400 nm thin a-GST film on SiC, and d) in a freestanding a-GST film. e,f) Dispersions of the four modes shown in (a)–(d), where (f) zooms into the SiC reststrahlen region between the TO and LO frequencies (ω_{TO} and ω_{LO}), marked by the dotted rectangle. The SiC substrate leads to a flattening of the waveguide mode (red line) compared to the air-bound mode (green line), leading to a comparable dispersion to the SPhP (black and blue lines) in the dispersion window shown in (f).

ADVANCED SCIENCE NEWS
www.advancedsciencenews.com

ADVANCED OPTICAL MATERIALS
www.advopticalmat.de

same frequency for smaller in-plane momenta, an s-polarized waveguide mode localized in the a-GST film. In Figure 1c, the in-plane electric field E_y of this air/GST/SiC-bound mode is shown, featuring a higher confinement than the air-bound waveguide mode due to the SiC substrate. Strikingly, the dispersion of the air/GST/SiC-bound waveguide mode (red line in Figure 1e,f), while approaching asymptotically the dispersion of the air-bound waveguide mode at large in-plane momenta k, experiences an upward bending for small k, becoming quite similar to the dispersion of the SPhP. Thus, the combined structure of a thin a-GST film on a SiC substrate not only supports both p-polarized SPhPs and s-polarized waveguide modes, but thanks to the reststrahlen characteristics[38] of the SiC substrate, the waveguide mode mimics the SPhP for small in-plane momenta k/k_0 in both field distribution and dispersion.

An a-GST film of ≈400 nm thickness, as discussed in Figure 1, yields optimal polariton-like characteristics of the waveguide mode, such as its field enhancement (see Figure 5 for details). However, the second aspect of our concept is the active tunability of the GST/SiC system via GST phase switching and the resulting tuning potential for both the SPhP and the waveguide mode. We find that the maximum frequency shift of the SPhP upon switching of the GST phase is obtained for an a-GST film thickness of ≈150 nm (see Figure S1 in the Supporting Information). Importantly, for this film thickness, the SPhP-like dispersion and a significant field enhancement of the waveguide mode are still conserved. Thus, experimentally, we choose to investigate a GST/SiC system with ≈150 nm thickness of the a-GST film.

3. Experiment

A 144 nm thin a-GST film was sputter-deposited onto a 4H-SiC substrate and placed into a home-build Otto-type prism coupling setup, sketched in **Figure 2**a (see the Experimental Section). In short, the incoming light impinges on the prism surface at an angle θ above the critical angle of total internal reflection (≈24.6° for KRS5). The generated evanescent wave in the air gap between prism and sample couples to the evanescent, bound modes in the sample, resulting in attenuated total reflection dips at the resonances in a reflectance spectrum. By taking several spectra at varying incident angle, dispersions can be mapped out.[39] As an excitation source for the reflectance spectroscopy measurements, we employed a mid-IR free electron laser (FEL) with tunable wavelength in the range of 3-60 µm and a spectral line width of ≈0.3%[40] (see the Experimental Section). In a first step, all experimental data were obtained for a-GST, and after crystallizing the a-GST on a heating plate (300 °C, 5 min), the measurements were repeated for the c-GST phase. Note that crystallization of a-GST is accompanied by a density reduction,[41,42] leading to a ≈8% thinner c-GST film of about 132 nm thickness.

In Figure 2b, reflectance spectra at an incident angle of 30° are shown for p-polarized and s-polarized incident light and for both GST phases, respectively. Clearly, each spectrum features a distinct resonance dip that corresponds to a p-polarized SPhP

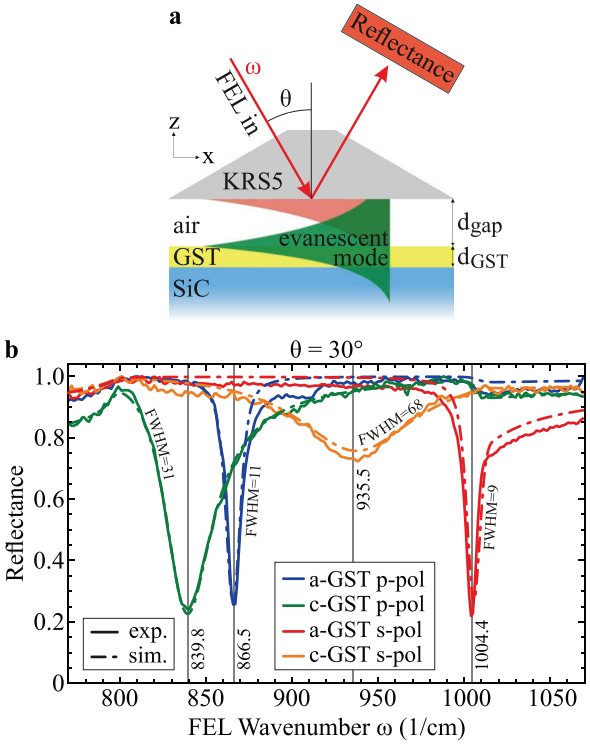

Figure 2. Tuning of the SPhP and the waveguide mode by switching the GST phase. a) Setup of the prism coupling experiments in the Otto geometry with variable air gap between the KRS5 (n_{KRS5} ≈ 2.4) prism and the sample, allowing for momentum-matched, critical coupling to evanescent modes supported by the sample such as SPhPs and waveguide modes. b) Reflectance spectra at $\theta = 30°$ for the crystalline and amorphous GST phases for s- and p-polarized incident light of a 144 nm (132 nm) thin a-GST (c-GST) film on SiC, demonstrating the tuning of both SPhP and waveguide mode upon switching the GST phase. A global fitting algorithm was used to fit simulated reflectances (dash-dotted lines) to the experimental spectra (solid lines).

(blue and green curves) or an s-polarized waveguide mode (red and orange curves). All data were fitted with a global fitting procedure (see the Experimental Section for details), and the resulting theoretical spectra calculated by means of a 4 × 4 transfer matrix formalism[43] are also shown in Figure 2b, nicely reproducing the experimental data. (The low amplitude of the waveguide mode in c-GST arises due to a prism coupling gap below the gap of critical coupling,[39] see the Experimental Section for details).

Furthermore, a Lorentzian line shape was fitted to the experimental reflectance dips in order to extract frequency positions μ and full width at half maxima (FWHM = 2σ) of the resonances. Interestingly, the measured quality factor ($Q = \mu$/FWHM) in a-GST of the waveguide mode (Q = 109) is even higher than that of the SPhP (Q = 82), whereas in c-GST, the waveguide mode has a broader resonance (Q = 14) than the SPhP (Q = 27). For the case of a-GST, these Q-factors easily lie in the range of the high-Q resonances arising from localized SPhPs in polar crystal nanostructures (45-360).[44–49] The generally lower Q-factors in c-GST, on the other hand, can be attributed to nonzero

ADVANCED SCIENCE NEWS
www.advancedsciencenews.com

ADVANCED OPTICAL MATERIALS
www.advopticalmat.de

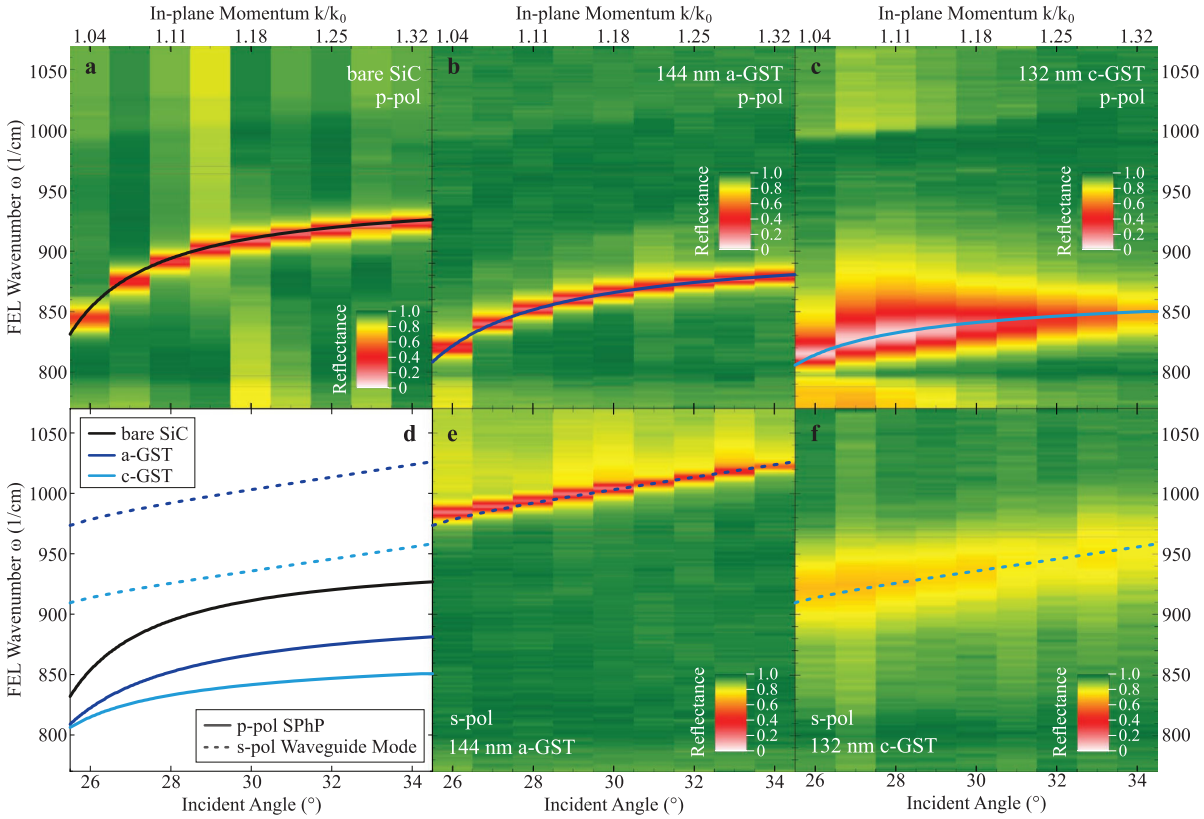

Figure 3. Experimental reflectance maps featuring the SPhP and waveguide mode dispersions. a–c) Reflectance maps for p-polarized incident light of bare SiC, a-GST/SiC, and c-GST/SiC, respectively, demonstrating the red-shift of the SPhP dispersion induced by the sensing of the increasing refractive index from air to c-GST. e,f) Reflectance maps for s-polarized incident light, showing the red-shift of the waveguide mode supported by the 144 nm (132 nm) thin a-GST (c-GST) film. d) Summary of all mode dispersions determined by the reflectance measurements, also plotted on top of the corresponding reflectance maps.

absorption (Im($\varepsilon_{c\text{-}GST}$) = 9) compared to a-GST. However, it is noteworthy that the waveguide mode features similar *Q*-factors as the SPhP in both GST phases, providing first evidence that the waveguide mode can indeed be seen as a polariton-like excitation with s-polarization.

Reflectance spectra were taken for incident angles of 26°–34° in steps of 1° resulting in reflectance maps that reproduce the dispersion of the corresponding mode. Maps for bare SiC, a-GST/SiC, and c-GST/SiC for p-polarized incident light are shown in **Figure 3**a–c, respectively, and maps for a-GST/SiC and c-GST/SiC for s-polarized incident light in Figure 3e,f. In Figure 3d, an overview over all modes is given, and the respective dispersion curves are additionally plotted on top of the individual reflectance maps. The theoretical dispersions were extracted from the imaginary part of the correspondingly polarized reflection coefficient obtained by transfer matrix calculations[43] using the parameters from the global fitting procedure. All experimental dispersions are well reproduced by the simulations.

For 144 nm thin a-GST and at $\theta = 30°$, the SPhP shifts by $\delta\omega = 27$ cm^{-1} upon switching the GST phase, and the waveguide mode by 69 cm^{-1}. This corresponds to a tuning figure of merit (TFOM) of TFOM = $\delta\omega$/FWHM = 2.5 for the SPhP and 7.7 for the waveguide mode, where we used the FWHM of the initial state (a-GST phase) according to literature.[33,34] These TFOM by far exceed other recently published results in the field of modulated nanophotonics with typical values of 0.5–1.4,[22,31,50–52] and, in the case of the waveguide mode with an exceptional TFOM of 7.7, even exceed the results on graphene, where values up to 5 have been reported.[53,54] In the experimental reflectance maps in Figure 3, this switching can be observed as a drastic red-shift of the corresponding dispersion curves. The GST film thickness was chosen such that the frequency shift is maximal for the SPhP. Notably, for the waveguide mode, a slightly larger frequency shift and thus also a larger TFOM is expected for GST films of ≈220 nm thickness (see Figure S1 in the Supporting Information). For even thicker films, the shift decreases, because all modes for both GST phases are pushed against the lower frequency limit given by ω_{TO}^{SiC} = 797 cm^{-1}.[55] For thinner films, on the other hand, the SPhP contrast decreases as well because of a reduced influence of the GST film, while the waveguide mode disappears completely. The film thickness dependence and the boundaries in which the waveguide mode is supported are discussed

ADVANCED SCIENCE NEWS
www.advancedsciencenews.com

ADVANCED OPTICAL MATERIALS
www.advopticalmat.de

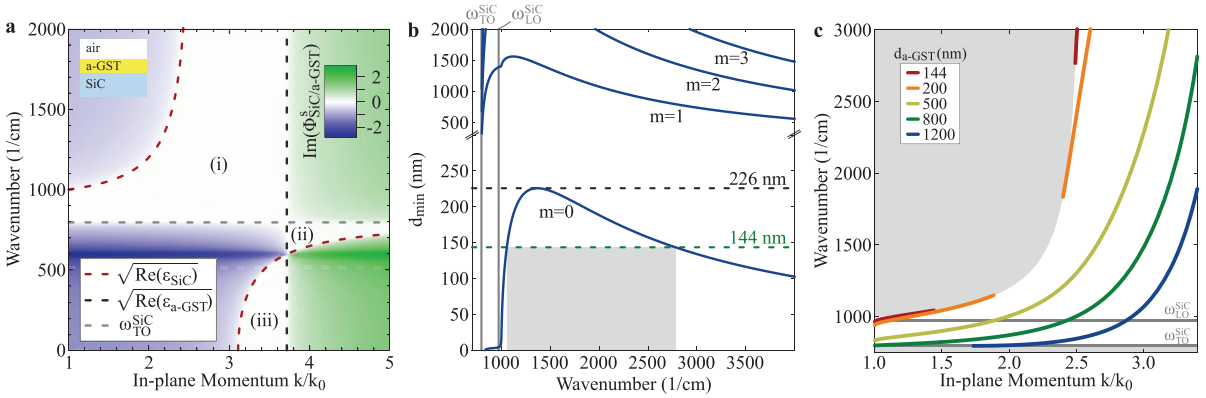

Figure 4. Theoretical dispersion of an s-polarized waveguide mode in an air/a-GST/SiC system. a) Imaginary part of the phase difference $\Phi^s_{SiC/GST}$ (Equation (2)) upon reflection of s-polarized light at the a-GST/SiC interface. White areas where $\mathrm{Im}(\Phi^s_{SiC/GST}) = 0$ indicate regions where the a-GST/SiC interface supports a waveguide mode. Dashed lines mark the respective boundaries given by material parameters. b) Minimum a-GST film thickness (Equation (4)) required to support an m-th order s-polarized waveguide mode. The $m = 0$ mode is supported at all frequencies for film thicknesses above 226 nm. For the a-GST film of 144 nm thickness employed in our experiments, the mode cannot exist in the frequency window of 1056–2769 cm^{-1} marked in gray. c) Theoretical dispersion (Equation (1)) of the s-polarized $m = 0$ air/GST/SiC-bound waveguide mode. The gray areas are the forbidden regions for the air/a-GST/SiC system given by $\mathrm{Im}(\Phi^s_{SiC/GST})$. The two thinnest films have forbidden frequency regions given by b) d_{min}, coinciding with the restriction given by $\mathrm{Im}(\Phi^s_{SiC/GST})$.

further below (**Figure 4**). For the exemplary film thickness of 144 nm, however, our experimental findings clearly demonstrate the tuning potential of both the p-polarized SPhP and the s-polarized waveguide mode supported in GST films on a SiC substrate via GST phase switching.

4. Waveguide Mode Theory

The theoretical description of waveguide modes in a slab waveguide structure is well known and has been given elsewhere.[37,56,57] Here, we follow the work by Tien and Ulrich[37] and apply the theoretical model to our air/GST/SiC system, in order to verify the waveguide nature of the s-polarized mode, as well as provide a thorough understanding of the dispersion of this mode and the boundaries in which it is supported. We will mainly focus our discussion on a-GST, which is the GST phase with lower losses, thus featuring better waveguide characteristics. We note, however, that the following theoretical description is equally valid for c-GST. In fact, except for a red-shift of the dispersion and a larger momentum range, the resulting dispersion for c-GST is qualitatively the same as for a-GST (except at the upper momentum boundary, see Figure S2 in the Supporting Information for details). The equation of waveguide modes is given by [37]

$$\frac{\omega}{c_0}\sqrt{\varepsilon_{GST}-\kappa^2}\,d - \Phi_{SiC/GST} - \Phi_{GST/air} = m\pi \tag{1}$$

where $\Phi_{SiC/GST}$ and $\Phi_{GST/air}$ are the phase differences upon reflection at the substrate/film (SiC/GST) and the film/incident medium (GST/air) interfaces, $\kappa \equiv k/k_0 = n_{air}\sin\theta$ is the in-plane momentum (with $k_0 = \omega/c_0$), d is the film thickness, ω is the frequency, and c_0 is the speed of light in vacuum. Please note that Equation (1) is valid for s- and p-polarized waveguide modes. In this work, however, we focus on the zero-order s-polarized waveguide mode and its comparability to the simultaneously supported SPhP mode (for the same frequency, the SPhP is found at larger in-plane momenta). The following discussion will therefore only consider the s-polarized waveguide solutions. The phase differences for s-polarization are given by[37]

$$\tan\left(\Phi^s_{SiC/GST}\right) = \sqrt{\frac{\kappa^2-\varepsilon_{SiC}}{\varepsilon_{GST}-\kappa^2}} \tag{2}$$

$$\tan\left(\Phi^s_{GST/air}\right) = \sqrt{\frac{\kappa^2-\varepsilon_{air}}{\varepsilon_{GST}-\kappa^2}} \tag{3}$$

In order to ensure total internal reflection inside the waveguide core (here GST), the phase differences Φ have to be real. As a consequence, the imaginary part of Φ allows to define those regions in the dispersion where a waveguide mode is supported, and those in which mode propagation is not possible. Figure 4a shows a map of $\Phi^s_{SiC/GST}$ for the air/a-GST/SiC system. The three white areas (i–iii) are the regions where the a-GST/SiC interface supports the s-polarized waveguide mode ($\mathrm{Im}(\Phi^s_{SiC/a\text{-}GST}) = 0$). However, for a mode to be supported in the film, the phase differences at both interfaces have to be real simultaneously. Therefore, region (ii) can be ruled out because for in-plane momenta $\kappa > \sqrt{\mathrm{Re}(\varepsilon_{a\text{-}GST})} \approx 3.7$ (black dashed line), the phase difference at the a-GST/air interface is complex, $\mathrm{Im}(\Phi^s_{a\text{-}GST/air}) > 0$ (see Figure S2 in the Supporting Information). For $\kappa < 3.7$, on the other hand, $\mathrm{Im}(\Phi^s_{a\text{-}GST/air}) = 0$ and thus regions (i) and (iii) can support waveguide modes, and their boundaries are solely governed by the a-GST/SiC interface. In fact, the lower boundary along the momentum axis is given by the SiC permittivity $\sqrt{\mathrm{Re}(\varepsilon_{SiC})}$ (red dashed line), which is a highly dispersive quantity and is the reason for the rich physics of waveguide modes bounded by polar crystal substrates. While in principle, region (iii) does support waveguide modes, we here only focus on region (i) due to its capacity of supporting the s-polarized

ADVANCED SCIENCE NEWS
www.advancedsciencenews.com

ADVANCED OPTICAL MATERIALS
www.advopticalmat.de

waveguide mode that features an upward bended, polariton-like dispersion in proximity to the SiC substrate SPhP mode (see Figure 1e,f). As for the SPhP, the lower boundary of region (i) along the frequency axis is defined by the TO phonon frequency of SiC, ω_{TO}^{SiC} (gray dashed line). Interestingly, the reason that ω_{TO}^{SiC} is a boundary is different for the two modes: The SPhP requires negative $\mathrm{Re}(\varepsilon_{SiC})$ to have an evanescently decaying electric field in z-direction. On the other hand, the waveguide mode requires $\mathrm{Re}(\varepsilon_{SiC}) < \mathrm{Re}(\varepsilon_{a\text{-}GST})$ to enable total internal reflection and thereby get evanescently decaying fields. For frequencies $\omega < \omega_{TO}^{SiC}$, both conditions are lost simultaneously.

Additional to the restrictions given by total internal reflection that are reflected in the phase differences Φ (Figure 4a), waveguide modes in asymmetric slab waveguides require a minimal film thickness d_{min} in order to be supported. Evaluation of Equation (1) at the lower and upper momentum boundaries leads to the following expression for d_{min} for s-polarized waveguide modes[37]

$$d_{min} = \frac{c_0}{\omega} \frac{m\pi + \arctan\left(\sqrt{\frac{\varepsilon_{SiC} - \varepsilon_{air}}{\varepsilon_{GST} - \varepsilon_{SiC}}}\right)}{\varepsilon_{GST} - \varepsilon_{SiC}} \quad (4)$$

Note that in asymmetric slab waveguides such as the air/GST/SiC system, the minimal film thickness for the zero-order s-polarized waveguide mode is smaller than for the zero-order p-polarized mode.[56] As a consequence, for the here studied film thickness range of 0–800 nm, only the s-polarized waveguide mode can be observed.

In Figure 4b, d_{min} of the air/a-GST/SiC system is plotted as a function of frequency for the first four orders m. Interestingly, in the SiC reststrahlen band, d_{min} of the $m = 0$ mode is almost zero, but features a rapid increase at larger frequencies with a maximum value of $d_{min} = 226$ nm. As a consequence, a-GST films of thicknesses $d_{a\text{-}GST} > 226$ nm support the $m = 0$ mode at any frequencies, while in thinner films, such as our sample with $d_{a\text{-}GST} = 144$ nm, the mode is forbidden in a broad frequency range (gray area in Figure 4b). Therefore, the $m = 0$ s-polarized waveguide mode we observe in our experiments is limited to a frequency range between 797 and 1056 cm^{-1}, which is very similar to the allowed frequency range of the SPhP defined by the SiC reststrahlen band (797–970 cm^{-1}).

The range in which the s-polarized air/a-GST/SiC waveguide mode can be observed is best illustrated in the dispersion plot we show in Figure 4c. Here, the gray areas indicate the forbidden regions given by $\mathrm{Im}(\Phi^{s}_{SiC/a\text{-}GST})$. For the two thinnest films of 144 and 200 nm (red and orange curves), d_{min} defines a frequency range where the $m = 0$ mode is forbidden, which is represented by the region in which the two dispersion curves are disrupted. The restriction given by d_{min} coincides exactly with the restriction given by $\mathrm{Im}(\Phi^{s}_{SiC/a\text{-}GST})$. For the three thicker films (light green, dark green, and blue curves), on the other hand, the mode dispersions are continuous, as there is no minimum film thickness required. However, these mode dispersions are pushed against the lower frequency boundary ω_{TO}^{SiC} with increasing film thickness, and the dispersion of the mode in the thickest film of 1200 nm even starts to disappear at this boundary. This behavior originates in the pole of the dielectric function of SiC at ω_{TO}^{SiC}, constituting the hard lower barrier of the frequency range in which waveguide modes can be supported. Notably, thanks to this boundary, the waveguide mode dispersion experiences the upward bending that leads to the resemblance of the SPhP mode dispersion. Finally, we note that the shifting of the dispersion with film thickness enables a straightforward way of tuning the mode resonance across the entire allowed frequency range.

5. Surface Polariton-Like Waveguide Modes for s-Polarized Nanophotonics

Equipped with this theoretical understanding, we now turn our focus on the comparability of the SPhP and the thin film s-polarized waveguide mode in terms of optical field enhancement and spatial confinement. **Figure 5**a–f shows z-profiles of the in-plane electric field enhancement (FE) of the SPhP (E_x) and the waveguide mode (E_y) at their corresponding resonance frequency for a set of different a-GST film thicknesses, calculated for excitation via a KRS5 coupling prism in the Otto geometry at an incident angle of $\theta = 30°$. Furthermore, the continuous behavior of the maximum field enhancement FE_{max} for the SPhP (blue curve) as a function of thin a-GST film thickness $d_{a\text{-}GST}$ is shown in Figure 5g, and Figure 5h shows the corresponding mode frequency ω_{mode} (FE_{max} and ω_{mode} for larger film thicknesses are shown in Figure S3, Supporting Information).

A bare SiC surface (Figure 5a) only supports an SPhP with a maximum field enhancement (FE_{max}) of ≈7, which is, however, reduced when an additional a-GST film of 144 nm is placed on top of SiC (Figure 5b). For increasing film thicknesses (Figure 5 c–e), the field enhancement of the SPhP drops even further and for the largest a-GST film of 800 nm thickness (Figure 5f), there is no enhancement observable at all, meaning that the structure does not support the air/SiC SPhP anymore. This transition toward a total loss of the SPhP for large film thicknesses stems, on the one hand, from the fact that the observed air/SiC SPhP originates in the dielectric contrast of the adjacent air and SiC, and for growing a-GST film thicknesses, there is no SiC/air interface anymore. On the other hand, the TO phonon is IR-active and therefore absorption in SiC increases drastically in the vicinity of ω_{TO}^{SiC}, contributing to the observed loss of field enhancement. Finally, we cannot observe the emergence of any other SPhP for thicker films, because the air/a-GST interface does not feature permittivities of opposite sign, while a potential a-GST/SiC SPhP cannot be excited via prism coupling with a KRS5 prism, because the required momenta are too large ($n_{KRS5} < n_{a\text{-}GST}$).

The s-polarized waveguide mode, on the other hand, features a maximum field enhancement of ≈8 in a 250–400 nm thin a-GST film, which decreases for both thinner and thicker films (Figure 5g, red curve). In order to explain this behavior, we recall that for small in-plane momenta ($1 < \kappa < 2$), the waveguide mode is restricted to a frequency range between $\omega_{TO}^{SiC} = 797$ and 1000–1200 cm^{-1}, where the upper boundary depends on κ (Figure 4c). With increasing film thickness, the dispersion red-shifts through the allowed frequency region and eventually is pushed against ω_{TO}^{SiC}, as can be observed in Figure 5h (red curve). Here, analogous to the SPhP, the high absorption in SiC close to ω_{TO}^{SiC} leads to the observed loss of field enhancement. At the upper frequency boundary, on the other

ADVANCED SCIENCE NEWS
www.advancedsciencenews.com

ADVANCED OPTICAL MATERIALS
www.advopticalmat.de

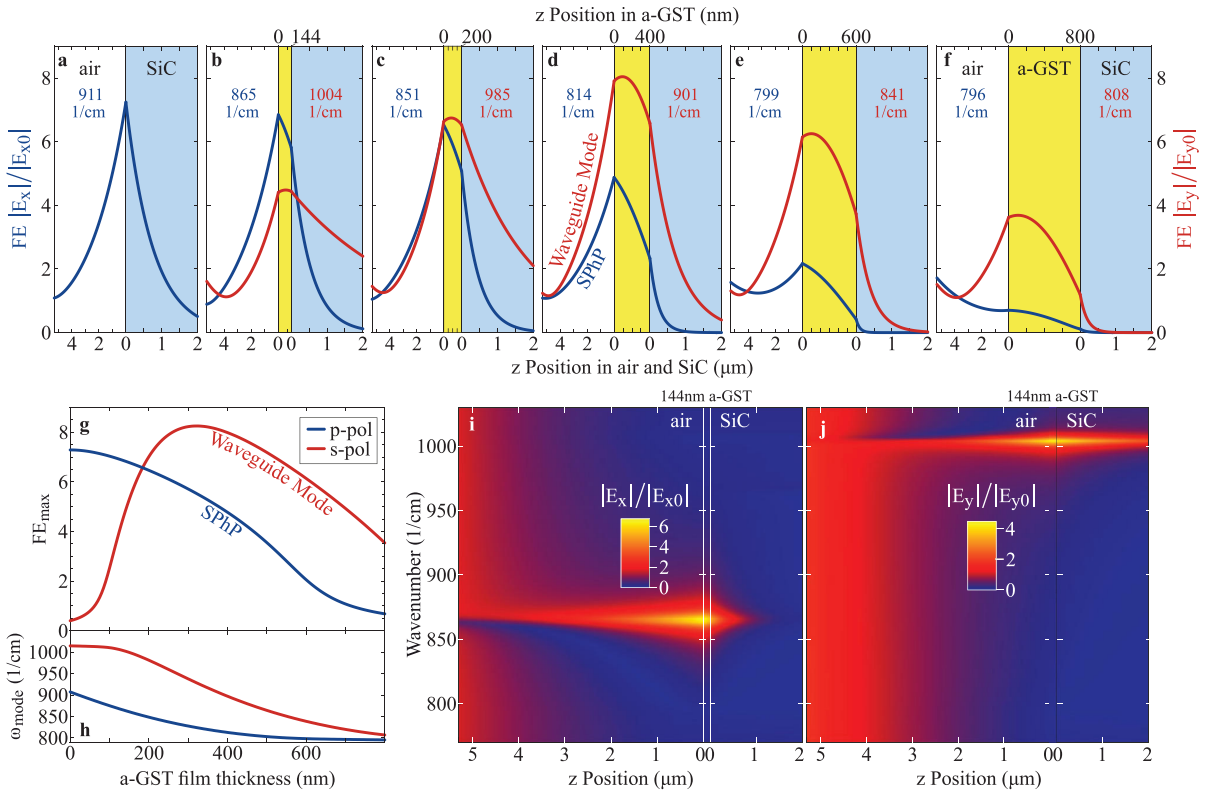

Figure 5. Electric field enhancement of an SPhP and a waveguide mode in an a-GST film. a–f) In-plane electric field profiles along the *z*-axis perpendicular to the air/a-GST/SiC interfaces of the SPhP (blue lines, E_x due to p-polarization) and the waveguide mode (red lines, E_y due to s-polarization) for a series of a-GST film thicknesses. The field enhancements (FEs) are calculated within the Otto geometry for an in-plane momentum of $k/k_0 = 1.18$ and at the respective resonance frequency (specified in each graph). Note the different scales of the *z*-axis for air and SiC (bottom scale) and the GST film (top scale), which are used to cover all relevant length scales. g) Maximum field enhancement FE_{max} inside the a-GST film as a function of a-GST film thickness for s- (red curve) and p-polarization (blue curve) calculated at h) the respective mode frequencies. i,j) Spatio-spectral maps of the in-plane electric field enhancements of the p-polarized SPhP and the s-polarized waveguide mode, respectively, showing their different resonance frequencies while featuring comparable *Q*-factors. The maps are also calculated for an in-plane momentum of $k/k_0 = 1.18$. In contrast to (a)–(f), we here plot with a single scale of the *z*-axis in order to better visualize the evanescent depth of the modes along the *z*-direction. The *z*-positions are labeled relative to the respective interface with a-GST.

hand, the permittivity of SiC is close to 1, resulting in a less confined mode in SiC compared to modes at frequencies further into the reststrahlen band (compare the penetration depth into SiC of the waveguide mode in Figure 5b,d), thus leading to smaller field enhancements.

The penetration depth into the SiC substrate δ, and thus the spatial confinement of the modes, is solely a function of the SiC permittivity tensor. Close to ω_{TO}^{SiC}, both the SPhP and the waveguide mode are strongly confined (with a penetration depth of $\delta \approx 100$ nm at 800 cm^{-1}), whereas at higher frequencies, the confinement decreases and the modes leak further into the SiC substrate ($\delta \approx 1.5$ μm at 950 cm^{-1}, see Figure S3 in the Supporting Information for details). This frequency dependence of the spatial confinement can also be seen in Figure 5i,j, where we show spatio-spectral maps of the SPhP and the waveguide mode, respectively, for a 144 nm thin a-GST film, resembling the experimentally studied sample. Clearly, the waveguide mode leaks further into SiC, whereas the SPhP is stronger confined because the frequency of the latter is much closer to ω_{TO}^{SiC} than that of the former. The opposite behavior can be observed when the waveguide mode frequency is close to ω_{TO}^{SiC} (Figure 5f) and the SPhP mode sits at higher frequencies (for example Figure 5a,b).

As we have shown exemplarily for a SiC substrate, a thin overlying GST film enables an s-polarized waveguide mode with features such as its dispersion, field enhancement, and spatial confinement being comparable to those of the simultaneously supported SPhP. Strikingly, this concept can be easily transferred to any polar crystal substrate. In **Figure 6**, we compare SiC to aluminum nitride (AlN), gallium nitride (GaN), and zinc oxide (ZnO), all featuring a single reststrahlen band, and the multimode material α-quartz (α-SiO_2). For each material, the dispersions of the supported SPhPs (blue and green circles) and s-polarized waveguide modes (red and orange circles) are plotted for a 144 nm thin a-GST and a 132 nm c-GST film, respectively. The vertical gray bars correspond to the FWHM of the mode resonances extracted from calculated spectra of the imaginary part of the corresponding reflection coefficient,

ADVANCED SCIENCE NEWS
www.advancedsciencenews.com

ADVANCED OPTICAL MATERIALS
www.advopticalmat.de

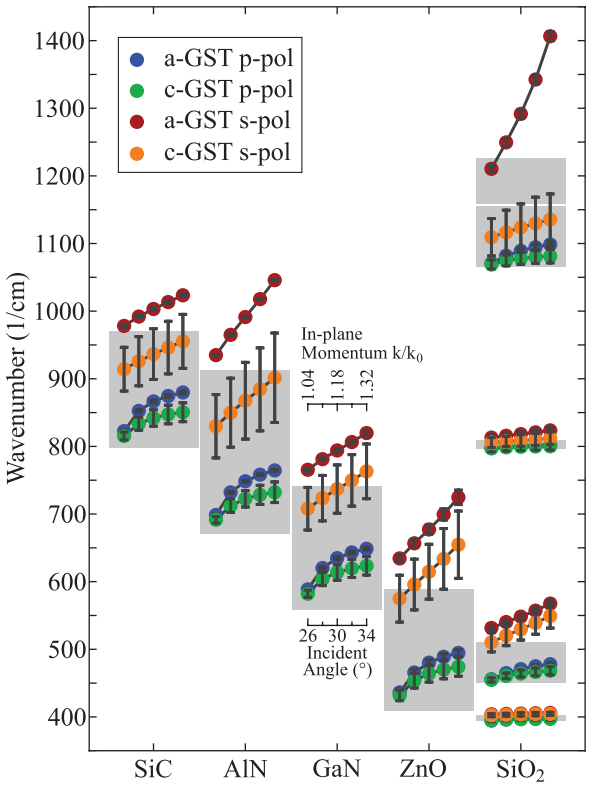

Figure 6. Comparison of GST on different polar crystal substrates for supporting s- and p-polarized modes. SiC, AlN, GaN, and ZnO have a single reststrahlen band (gray areas) and thus support one SPhP (blue, green) and one waveguide mode (red, orange) for each GST phase. The multimode material α-SiO_2, on the other hand, features four reststrahlen bands and thus four different sets of guided modes. The a-GST (c-GST) film thickness is that of the experimentally studied sample of 144 nm (132 nm). Resonance positions were extracted from maxima in the imaginary part of the correspondingly polarized reflection coefficient $\mathrm{Im}(r^{p,s})$ at the in-plane momenta shown for GaN. The peaks were fitted with a Lorentzian function. The obtained FWHMs are plotted as vertical gray bars on top of each resonance point.

$\mathrm{Im}(r^{p,s})$. The dispersions are visibly shifted by more than the modes' FWHM between the two GST phases (blue-green and red-orange), clearly demonstrating the good switching contrast achievable in any of the five substrate materials. The gray areas mark the respective reststrahlen bands of SiC, AlN, GaN, and ZnO, and the four bands of α-SiO_2. In each reststrahlen band, a SPhP within the reststrahlen band and a waveguide mode dispersing above or at the upper edge of the reststrahlen band are supported, highlighting the generality of our concept for the broad IR frequency range of 400–1400 cm^{-1}.

6. Conclusion

In conclusion, we have presented a generic material system comprising a subwavelength thin PCM film on a polar crystal substrate that simultaneously supports a p-polarized SPhP and an s-polarized waveguide mode. Our experimental data of the exemplary GST/SiC system demonstrate that high-contrast active tuning of both modes can be realized via switching of the GST phase, achieving an exceptional tuning figure of merit of up to 7.7. We have presented a simple theoretical model for the waveguide mode, revealing the similarity of the SPhP and waveguide mode dispersions in the reststrahlen region of the substrate material. Furthermore, by analyzing the electric field distributions across the system interfaces, we have shown that the waveguide mode can feature spatial confinement and field enhancement factors comparable to those of an SPhP, while expanding the allowed frequency range beyond the reststrahlen band. Thus, in addition to the polarization-limited surface polaritons, polariton-like waveguide modes supported by phase-change materials on polar crystal substrates provide a promising complementary building block for actively tunable, low-loss, and omnipolarized nanophotonic applications, such as in-plane metasurfaces or polariton lenses.[35,36]

7. Experimental Section

Experimental: The 144 nm thick film of the phase-change material $Ge_3Sb_2Te_6$ was deposited onto the SiC substrate by direct current magnetron sputtering with a background pressure of about 2×10^{-6} mbar and 20 sccm Ar flow in constant power mode (20 W) using stoichiometric targets of 99.99% purity.

The experimental setup is illustrated in Figure 2a and has been described before.[39,58] In short, the Otto geometry was implemented employing three motorized actuators (Newport TRA12PPD) to control the relative position of the coupling prism (KRS5, 25 mm high, 25 mm wide, angles of 30°, 30°, and 120°, with the 120° edge cut-off, Korth Kristalle GmbH) with respect to the sample. The motors pushed the prism against springs away from the sample and thus enabled continuous tuning of the air gap width d_{gap}. The 120° prism edge was cut-off parallel to the backside in order to quantify d_{gap} via whitelight interferometry.[59] The smallest gap width achieved was of ≈3 µm. In principle, gap widths below 3 µm can be measured, but were not feasible for the GST/SiC sample probably due to a not perfectly flat sample surface.

For each incident angle and polarization, the air gap of critical mode coupling d_{crit}[39] was determined by optimizing the mode resonance depth in the reflectance signal, and all spectra were taken at d_{crit}. However, d_{crit} scales with the resonance quality, because large losses into the sample require equally large radiative losses that are provided by the proximate coupling prism, thus leading to very small d_{crit}. This can lead to d_{crit} being smaller than the experimentally achieved minimum gap of 3 µm, resulting in low resonance depths due to undercoupling.[59] This is, indeed, the reason why the waveguide mode resonance in the lossy c-GST maximally dropped by 30% in the experiments (see Figures 2a and 3), whereas all other resonances achieved 80%.

Furthermore, it is noted that the in-plane electric field distributions of SPhPs and waveguide modes in Figure 1 a–d, analogous to Figure 5a–f, were calculated for excitation via a KRS5 coupling prism in the Otto geometry at an incident angle of $\theta = 30°$. For all four systems, the coupling gap was fixed to the critical coupling gap of the SPhP on bare SiC ($d_{crit} = 5.3$ µm). This asymmetric excitation scheme is the reason for the asymmetric field distribution of the air-bound waveguide mode in Figure 1d.

The mid-infrared FEL employed as excitation source was operated at an electron energy of 31 MeV, yielding a tuning range of the FEL output wavelength between ≈7 and 18 µm (≈1400–550 cm^{-1}, covering the spectral range of the SiC reststrahlen band) by moving the motorized undulator gap. The micropulse repetition rate was set 1 GHz, and the macropulse had a duration of 10 µs at a repetition rate of 10 Hz, yielding picosecond-pulses with a typical FWHM <5 cm^{-1} (≈0.3%). The macropulse and micropulse energies were ≈30 mJ and 10 µJ,

ADVANCED SCIENCE NEWS
www.advancedsciencenews.com

ADVANCED OPTICAL MATERIALS
www.advopticalmat.de

respectively. However, the incident FEL beam was attenuated by −18 dB in order to avoid irreversible damage of the GST film and unintentional crystallization. Further details on the FEL are given elsewhere.[40]

The reflectance signal was detected with a pyroelectric sensor (Eltec 420M7). A second sensor measured the power reflected off a thin KBr plate placed prior to the setup in the beam. This reference signal was used to normalize all reflectance signals and was measured on a single shot basis in order to minimize the impact of shot-to-shot fluctuations of the FEL. The spectral response function of the setup was determined by taking a reflectance spectrum at large gap widths $d_{gap} \approx 40$ µm, where the beam was totally reflected at the prism backside across the full spectral range. References were measured for each incident angle and polarization individually, and all reflectance spectra were normalized to their respective response function.

Global Fitting Procedure: The spectra in Figure 2b, the dispersion curves in Figures 1e,f, 3, and 6, and the electric field distributions in Figure 5 were all calculated with a 4 × 4 transfer matrix formalism[43] that accounts for the anisotropy of the c-cut hexagonal 4H-SiC substrate. For the calculations, most of the material parameters and system variables were set to values from literature or in advance determined values (including the phonon frequencies $\omega_{TO,o}^{SiC} = 797$ cm^{-1}, $\omega_{TO,e}^{SiC} = 788$ cm^{-1}, $\omega_{LO,o}^{SiC} = 970$ cm^{-1}, $\omega_{LO,e}^{SiC} = 964$ cm^{-1} where o stands for ordinary and e for the extraordinary crystal direction,[55] the damping $\gamma_{SiC} = 3.75$ cm^{-1}, $\varepsilon_{inf}^{SiC} = 6.5$,[60] the spectral width of the FEL $\Delta\omega = 5.56$ cm^{-1}, the angular width of the excitation beam $\Delta\theta = 0.24°$, and all nine incident angles $\theta = 26°$–$34°$). The remaining parameters, on the other hand, were extracted from a global fitting procedure and comprised the a-GST film thickness $d_{a\text{-}GST} = 144$ nm (the c-GST film thickness was calculated by a constant factor, $d_{c\text{-}GST} = 0.92\, d_{a\text{-}GST} = 132$ nm[41,42]), the real and imaginary part of the permittivity of c-GST ($\varepsilon_{c\text{-}GST} = 31.4 + 9i$), the real permittivity of a-GST ($\varepsilon_{a\text{-}GST} = 13.8 + 0i$), the gap widths d_{gap}, and a multiplication factor a to account for slow FEL power drifts ($0.96 < a < 1$). The data sets of all four system configurations (p-polarization and s-polarization for a-GST and c-GST, respectively), each containing nine spectra at different incident angles, were fitted globally, where $d_{a\text{-}GST}$, $\varepsilon_{a\text{-}GST}$, and $\varepsilon_{c\text{-}GST}$ were global fitting parameters, while the factors a and the gap widths d_{gap} were adjusted individually for each spectrum.

Supporting Information

Supporting Information is available from the Wiley Online Library or from the author.

Acknowledgements

The authors thank Wieland Schöllkopf and Sandy Gewinner for operating the FEL, and Martin Wolf and the Max Planck Society for supporting this work. They also thank Jialiang Gao for sputtering the GST film. This work was supported by the German Federal Ministry of Education and Research within the funding program Photonics Research Germany (contract number 13N14151) and the DFG (German Science Foundation) within the collaborative research center SFB 917 Nanoswitches.

Conflict of Interest

The authors declare no conflict of interest.

Keywords

active nanophotonics, highly confined waveguide modes, infrared spectral range, phase-change materials, surface phonon polaritons

Received: June 25, 2019
Revised: September 10, 2019
Published online:

[1] S. A. Maier, *Plasmonics: Fundamentals and Applications*, Springer US, New York **2007**.
[2] J. D. Caldwell, L. Lindsay, V. Giannini, I. Vurgaftman, T. L. Reinecke, S. A. Maier, O. J. Glembocki, *Nanophotonics* **2015**, *4*, 44.
[3] M. Kauranen, A. V. Zayats, *Nat. Photonics* **2012**, *6*, 737.
[4] J. Homola, S. S. Yee, G. Gauglitz, *Sens. Actuators, B* **1999**, *54*, 3.
[5] E. C. Le Ru, P. G. Etchegoin, *Annu. Rev. Phys. Chem.* **2012**, *63*, 65.
[6] R. Berte, C. R. Gubbin, V. D. Wheeler, A. J. Giles, V. Giannini, S. A. Maier, S. De Liberato, J. D. Caldwell, *ACS Photonics* **2018**, *5*, 2807.
[7] N. Engheta, *Science* **2007**, *317*, 1698.
[8] R. Degl'Innocenti, S. J. Kindness, H. E. Beere, D. A. Ritchie, *Nanophotonics* **2018**, *7*, 127.
[9] D. J. Bergman, M. I. Stockman, *Phys. Rev. Lett.* **2003**, *90*, 027402.
[10] P. Berini, I. De Leon, *Nat. Photonics* **2012**, *6*, 16.
[11] R. Hillenbrand, T. Taubner, F. Keilmann, *Nature* **2002**, *418*, 159.
[12] N. C. Passler, I. Razdolski, D. S. Katzer, D. F. Storm, J. D. Caldwell, M. Wolf, A. Paarmann, *ACS Photonics* **2019**, *6*, 1365.
[13] Y. C. Jun, K. C. Huang, M. L. Brongersma, *Nat. Commun.* **2011**, *2*, 283.
[14] K. Ito, T. Matsui, H. Iizuka, *Appl. Phys. Lett.* **2014**, *104*, 051127.
[15] T. Nakamura, *Phys. Rev. Appl.* **2016**, *6*, 044009.
[16] K. R. Catchpole, A. Polman, *Opt. Express* **2008**, *16*, 21793.
[17] V. E. Ferry, M. A. Verschuuren, H. B. T. Li, E. Verhagen, R. J. Walters, R. E. I. Schropp, H. A. Atwater, A. Polman, *Opt. Express* **2010**, *18*, A237.
[18] G. T. Papadakis, A. Davoyan, P. Yeh, H. A. Atwater, *Phys. Rev. Mater.* **2019**, *3*, 015202.
[19] E. L. Runnerstrom, K. P. Kelley, T. G. Folland, J. R. Nolen, N. Engheta, J. D. Caldwell, J.-P. Maria, *Nano Lett.* **2019**, *19*, 948.
[20] G. X. Ni, L. Wang, M. D. Goldflam, M. Wagner, Z. Fei, A. S. McLeod, M. K. Liu, F. Keilmann, B. Özyilmaz, A. H. Castro Neto, J. Hone, M. M. Fogler, D. N. Basov, *Nat. Photonics* **2016**, *10*, 244.
[21] Z. Fei, A. S. Rodin, G. O. Andreev, W. Bao, A. S. McLeod, M. Wagner, L. M. Zhang, Z. Zhao, M. Thiemens, G. Dominguez, M. M. Fogler, A. H. Castro Neto, C. N. Lau, F. Keilmann, D. N. Basov, *Nature* **2012**, *487*, 82.
[22] A. D. Dunkelberger, C. T. Ellis, D. C. Ratchford, A. J. Giles, M. Kim, C. S. Kim, B. T. Spann, I. Vurgaftman, J. G. Tischler, J. P. Long, O. J. Glembocki, J. C. Owrutsky, J. D. Caldwell, *Nat. Photonics* **2018**, *12*, 50.
[23] M. Wuttig, *Nat. Mater.* **2008**, *4*, 265.
[24] M. Wuttig, V. L. Deringer, X. Gonze, C. Bichara, J.-Y. Raty, *Adv. Mater.* **2018**, *30*, 1803777.
[25] J. Raty, M. Schumacher, P. Golub, V. L. Deringer, C. Gatti, M. Wuttig, *Adv. Mater.* **2019**, *31*, 1806280.
[26] M. Wuttig, N. Yamada, *Nat. Mater.* **2007**, *6*, 824.
[27] G. Bruns, P. Merkelbach, C. Schlockermann, M. Salinga, M. Wuttig, T. D. Happ, J. B. Philipp, M. Kund, *Appl. Phys. Lett.* **2009**, *95*, 043108.
[28] B. Gholipour, J. Zhang, K. F. MacDonald, D. W. Hewak, N. I. Zheludev, *Adv. Mater.* **2013**, *25*, 3050.
[29] L. Waldecker, T. A. Miller, M. Rudé, R. Bertoni, J. Osmond, V. Pruneri, R. E. Simpson, R. Ernstorfer, S. Wall, *Nat. Mater.* **2015**, *14*, 991.
[30] Q. Wang, E. T. F. Rogers, B. Gholipour, C.-M. Wang, G. Yuan, J. Teng, N. I. Zheludev, *Nat. Photonics* **2016**, *10*, 60.
[31] A.-K. U. Michel, A. Heßler, S. Meyer, J. Pries, Y. Yu, T. Kalix, M. Lewin, J. Hanss, A. De Rose, T. W. W. Maß, M. Wuttig, D. N. Chigrin, T. Taubner, *Adv. Mater.* **2019**, *31*, 1901033.
[32] P. Li, X. Yang, T. W. W. Maß, J. Hanss, M. Lewin, A.-K. U. Michel, M. Wuttig, T. Taubner, *Nat. Mater.* **2016**, *15*, 870.
[33] I. M. Pryce, K. Aydin, Y. A. Kelaita, R. M. Briggs, H. A. Atwater, *Nano Lett.* **2010**, *10*, 4222.
[34] A.-K. U. Michel, D. N. Chigrin, T. W. W. Maß, K. Schönauer, M. Salinga, M. Wuttig, T. Taubner, *Nano Lett.* **2013**, *13*, 3470.

ADVANCED SCIENCE NEWS
www.advancedsciencenews.com

ADVANCED OPTICAL MATERIALS
www.advopticalmat.de

[35] T. G. Folland, A. Fali, S. T. White, J. R. Matson, S. Liu, N. A. Aghamiri, J. H. Edgar, R. F. Haglund, Y. Abate, J. D. Caldwell, *Nat. Commun.* **2018**, *9*, 4371.
[36] K. Chaudhary, M. Tamagnone, X. Yin, C. M. Spägele, S. L. Oscurato, J. Li, C. Persch, R. Li, N. A. Rubin, L. A. Jauregui, K. Watanabe, T. Taniguchi, P. Kim, M. Wuttig, J. H. Edgar, A. Ambrosio, F. Capasso, **2019**, arXiv:1905.01277.
[37] P. K. Tien, R. Ulrich, *J. Opt. Soc. Am.* **1970**, *60*, 1325.
[38] A. Paarmann, I. Razdolski, A. Melnikov, S. Gewinner, W. Schöllkopf, M. Wolf, *Appl. Phys. Lett.* **2015**, *107*, 081101.
[39] N. C. Passler, I. Razdolski, S. Gewinner, W. Schöllkopf, M. Wolf, A. Paarmann, *ACS Photonics* **2017**, *4*, 1048.
[40] W. Schöllkopf, S. Gewinner, H. Junkes, A. Paarmann, G. von Helden, H. Bluem, A. M. M. Todd, *Proc. SPIE* **2015**, *9512*, 95121L.
[41] W. K. Njoroge, H.-w. Wöltgens, M. Wuttig, *J. Vac. Sci. Technol., A* **2002**, *20*, 230.
[42] A.-K. U. Michel, *Ph.D. Thesis*, RWTH Aachen University **2016**.
[43] N. C. Passler, A. Paarmann, *J. Opt. Soc. Am. B* **2017**, *34*, 2128.
[44] T. Wang, P. Li, B. Hauer, D. N. Chigrin, T. Taubner, *Nano Lett.* **2013**, *13*, 5051.
[45] J. D. Caldwell, O. J. Glembocki, Y. Francescato, N. Sharac, V. Giannini, F. J. Bezares, J. P. Long, J. C. Owrutsky, I. Vurgaftman, J. G. Tischler, V. D. Wheeler, N. D. Bassim, L. M. Shirey, R. Kasica, S. A. Maier, *Nano Lett.* **2013**, *13*, 3690.
[46] H. Sumikura, T. Wang, P. Li, A.-K. U. Michel, A. Heßler, L. Jung, M. Lewin, M. Wuttig, D. N. Chigrin, T. Taubner, *Nano Lett.* **2019**, *19*, 2549.
[47] J. D. Caldwell, A. V. Kretinin, Y. Chen, V. Giannini, M. M. Fogler, Y. Francescato, C. T. Ellis, J. G. Tischler, C. R. Woods, A. J. Giles, M. Hong, K. Watanabe, T. Taniguchi, S. A. Maier, K. S. Novoselov, *Nat. Commun.* **2014**, *5*, 5221.
[48] Y. Chen, Y. Francescato, J. D. Caldwell, V. Giannini, T. W. W. Maß, O. J. Glembocki, F. J. Bezares, T. Taubner, R. Kasica, M. Hong, S. A. Maier, *ACS Photonics* **2014**, *1*, 718.
[49] M. Tamagnone, K. Chaudhary, A. Zhu, M. Meretska, J. Li, J. H. Edgar, A. Ambrosio, F. Capasso, **2019**, arXiv:1905.02177.
[50] Y. Yao, M. A. Kats, P. Genevet, N. Yu, Y. Song, J. Kong, F. Capasso, *Nano Lett.* **2013**, *13*, 1257.
[51] G. Si, E. S. P. Leong, X. Jiang, J. Lv, J. Lin, H. Dai, Y. J. Liu, *Phys. Chem. Chem. Phys.* **2015**, *17*, 13223.
[52] S. Dai, J. Zhang, Q. Ma, S. Kittiwatanakul, A. McLeod, X. Chen, S. G. Corder, K. Watanabe, T. Taniguchi, J. Lu, Q. Dai, P. Jarillo-Herrero, M. Liu, D. N. Basov, *Adv. Mater.* **2019**, *31*, 1900251.
[53] Z. Fang, S. Thongrattanasiri, A. Schlather, Z. Liu, L. Ma, Y. Wang, P. M. Ajayan, P. Nordlander, N. J. Halas, F. J. García de Abajo, *ACS Nano* **2013**, *7*, 2388.
[54] W. Gao, G. Shi, Z. Jin, J. Shu, Q. Zhang, R. Vajtai, P. M. Ajayan, J. Kono, Q. Xu, *Nano Lett.* **2013**, *13*, 3698.
[55] F. Engelbrecht, R. Helbig, *Phys. Rev. B* **1993**, *48*, 15698.
[56] S. O. Kasap, *Optoelectronics & Photonics: Principles & Practices*, 2nd ed., Pearson, London **2013**, p. 544.
[57] H. Kogelnik, in *Integrated Optics* (Ed: T. Tamir), Springer, Berlin **1975**, Ch. 2, pp. 13–81.
[58] N. C. Passler, C. R. Gubbin, T. G. Folland, I. Razdolski, D. S. Katzer, D. F. Storm, M. Wolf, S. De Liberato, J. D. Caldwell, A. Paarmann, *Nano Lett.* **2018**, *18*, 4285.
[59] K. Pufahl, N. C. Passler, N. B. Grosse, M. Wolf, U. Woggon, A. Paarmann, *Appl. Phys. Lett.* **2018**, *113*, 161103.
[60] B. Neuner III, D. Korobkin, C. Fietz, D. Carole, G. Ferro, G. Shvets, *Opt. Lett.* **2009**, *34*, 2667.

4.6 Layer-Resolved Absorption of Light in Arbitrarily Anisotropic Heterostructures

Nikolai Christian Passler, Mathieu Jeannin, and Alexander Paarmann

This publication (Passler *et al.*, PRB 2020, **101**, 165425 [**VII**]) presents a formalism to describe the layer-resolved transmittance and absorption in layered heterostructures of arbitrarily anisotropic, birefringent, and absorbing media, capable of treating light of any polarization at oblique incidence onto any number of layers. An online version of the computer code programmed in Matlab [19] and Python [120] has been published as open source.

The idea of this work emerged during the development of the erratum to the transfer matrix formalism [**III**] (reprinted on page 59). The resulting algorithm describes any linear light-matter interaction in layered anisotropic media, and thus aims at a broad readership covering numerous research areas in nanophotonics and optics. The examples that are discussed in this publication are selected from three different research fields in order to highlight the generality of the formalism.

Author contributions

A.P. originated the concept. The manuscript was written by **N.C.P.** and M.J., with all authors assisting in the proof-reading and preparation for final submission. **N.C.P.** devised the fundamental framework of the formalism, and **N.C.P.** and A.P. developed the final algorithm. Design and computations of the nanophotonic device structures were completed by **N.C.P.**, M.J. and A.P. The project management was provided by A.P.

go to list of publications

PHYSICAL REVIEW B **101**, 165425 (2020)

Layer-resolved absorption of light in arbitrarily anisotropic heterostructures

Nikolai Christian Passler [1,*] Mathieu Jeannin [2] and Alexander Paarmann [1,†]

[1] *Fritz-Haber-Institut der Max-Planck-Gesellschaft, Faradayweg 4-6, 14195 Berlin, Germany*

[2] *Laboratoire de Physique de l'École Normale Supérieure, ENS, Paris Sciences Lettres, CNRS, Université de Paris, 24 Rue Lhomond, 75005 Paris, France*

(Received 11 February 2020; revised manuscript received 31 March 2020; accepted 1 April 2020; published 23 April 2020)

We present a generalized formalism to describe the optical energy flow and spatially resolved absorption in arbitrarily anisotropic layered structures. The algorithm is capable of treating any number of layers of arbitrarily anisotropic, birefringent, and absorbing media and is implemented in an open-access computer program. We derive explicit expressions for the transmitted and absorbed power at any point in the multilayer structure, using the electric field distribution from a 4×4 transfer matrix formalism. As a test ground, we study three nanophotonic device structures featuring unique layer-resolved absorption characteristics, making use of (i) in-plane hyperbolic phonon polaritons, (ii) layer-selective, cavity-enhanced exciton absorption in transition-metal dichalcogenide monolayers, and (iii) intersubband-cavity polaritons in quantum wells. Covering such a broad spectral range from the far infrared to the visible, the case studies demonstrate the generality and wide applicability of our approach.

DOI: 10.1103/PhysRevB.101.165425

I. INTRODUCTION

The absorption of light in thin layers of strongly anisotropic materials has received enormous attention since the dawn of two-dimensional (2D) materials and their heterostructures [1]. Tremendous progress has been reported using 2D materials for numerous nanophotonic applications such as hybrid graphene-based photodetectors [2,3], optoelectronic [4,5] and photovoltaic [6,7] devices employing transition-metal dichalcogenide (TMDC) monolayers, enhanced light-matter interaction using photonic integration with optical cavities [8,9], approaches toward TMDC-based nanolasers [10,11], hyperlensing [12,13] based on hyperbolic polaritons [14], biosensing [15], and thermoelectric applications using black phosphorus (BP) monolayers [16,17]. In light of these thriving developments and the great potential entailed in nanophotonic technology, a robust and consistent theoretical framework for the description of light-matter interaction in layered heterostructures of anisotropic materials is of central importance.

In order to understand, analyze, and predict the optical response of multilayer structures, the transfer matrix formalism has proven to be of great utility [18–20]. In isotropic layered media, a 2×2 transfer matrix fully describes any light-matter interaction, and with knowledge of the local electric and magnetic fields, the optical power flow can be described by the Pointing vector $\mathcal{S}$ [21,22]. However, what already proves intricate in isotropic multilayers becomes even more cumbersome when the materials are uniaxial or even biaxial, requiring a 4×4 transfer matrix formalism [23–25], as is the case for many state-of-the-art nanophotonic materials like hexagonal boron nitride (hBN) [26], molybdenum trioxide (MoO_3) [27], or BP [28]. In consequence, to the best of our knowledge, previous approaches aiming at the analytical computation of light absorption in anisotropic multilayers are restricted to special cases [29–32], whereas a fully generalized formalism applicable to any number of layers of media with arbitrary permittivity has not been proposed so far.

In this work, we derive explicit expressions for the layer-resolved transmittance and absorption in stratified heterostructures of arbitrarily anisotropic, birefringent, and absorbing media, using the electric field distribution provided by our previous transfer matrix formalism [25,33]. Our algorithm is numerically stable, yields continuous solutions, and is implemented in an open-access computer program [34,35], enabling a robust and consistent framework that is capable of treating light of any polarization impinging at any incident angle onto any number of arbitrarily anisotropic, birefringent, and absorbing layers. To demonstrate the capabilities of our algorithm, we present and discuss simulation results for three nanophotonic device structures, featuring several phenomena such as azimuth-dependent hyperbolic phonon polaritons in a MoO_3 / aluminum nitride (AlN) / silicon carbide (SiC) heterostructure, layer-selective exciton absorption of molybdenum disulfide (MoS_2) monolayers in a Fabry-Pérot cavity, and strong light-matter coupling between a cavity mode and an epsilon-near-zero (ENZ) mode in a doped gallium nitride (GaN) multi-quantum-well system. Section II summarizes the

*passler@fhi-berlin.mpg.de

†alexander.paarmann@fhi-berlin.mpg.de

transfer matrix framework that is used to calculate the electric field distribution and the momenta of the eigenmodes in an anisotropic multilayer system. Based on this theory, Sec. III introduces the calculation of the layer-resolved transmittance and absorption. In Sec. IV, the simulation results are presented.

II. TRANFER MATRIX FRAMEWORK

The 4×4 transfer matrix formalism comprising the calculation and sorting of the eigenmodes and the treatment of singularities (Sec. II A), the calculation of reflection and transmission coefficients (Sec. II B), and of the electric fields (Sec. II C) is based on our previous work [25], and therefore is here only briefly summarized in order to provide the necessary framework for the calculation of the layer-resolved absorption (Sec. III).

A. Matrix formalism

The incident medium is taken to be nonabsorptive with isotropic (relative) permittivity ε_{inc}, while all other media can feature absorption and fully anisotropic (relative) permittivity tensors $\bar{\varepsilon}$. Each permittivity tensor $\bar{\varepsilon}_i$ of medium i with principle relative permittivities in the crystal frame ε_x, ε_y, and ε_z can be rotated into the laboratory frame using a three-dimensional coordinate rotation matrix [24] (Eq. (2) in Ref. [25]). In the following, media with a diagonal permittivity tensor in the laboratory frame are referred to as nonbirefringent, while media with a permittivity tensor that features nonzero off-diagonal elements is called birefringent. Furthermore, all media are assumed to have an isotropic magnetic permeability μ.

The coordinate system in the laboratory frame is defined such that the multilayer interfaces are parallel to the x-y plane, while the z direction points from the incident medium toward the substrate and has its origin at the first interface between incident medium and layer $i = 1$. The layers are indexed from $i = 1$ to $i = N$, and the thickness of each layer is d_i. Furthermore, $i = 0$ refers to the incident medium and $i = N + 1$ to the substrate. The plane of incidence is the x-z plane, yielding the following wave vector $\vec{k}_i$ in layer i:

$$\vec{k}_i = \frac{\omega}{c}(\xi, 0, q_i), \tag{1}$$

where ω is the circular frequency of the incident light, c is the speed of light in vacuum, $\xi = \sqrt{\varepsilon_{\text{inc}}}\,\sin(\theta)$ is the in-plane x component of the wave vector which is conserved throughout the entire multilayer system, θ is the incident angle, and q_i is the dimensionless z component of the wave vector in layer i.

In any medium, the propagation of an electromagnetic wave is described by exactly four eigenmodes $j = 1, 2, 3, 4$ with different z components q_{ij} of the wave vector. These four q_{ij} can be obtained for each medium i individually by solving the eigenvalue problem of a characteristic matrix $\mathbf{\Delta}$ (Eq. (11) in Ref. [25]), as has been derived originally by Berreman [23]. However, for media with highly dispersive permittivities, the four obtained eigenvalues q_{ij} and their related eigenmodes can switch their order as a function of frequency, and thus have to be identified in an unambiguous manner. Following Li *et al.* [36], the modes are separated into forward- and backward-propagating waves according to the sign of q_{ij} (Eq. (12) in Ref. [25]). We assign the forward-propagating (transmitted) waves to be described by q_{i1} and q_{i2}, and the backward propagating (reflected) waves by q_{i3} and q_{i4}. Furthermore, each pair is sorted by the polarization of the corresponding mode, utilizing the electric fields given by the eigenvectors Ψ_{ij} (Eq. (13) in Ref. [25]). In nonbirefringent media, the two modes are separated into p-polarized (q_{i1} and q_{i3}) and s-polarized (q_{i2} and q_{i4}) waves by analyzing the x component of their electric fields. For birefringent media, on the other hand, the sorting is realized by analyzing the x component of the Poynting vector $\vec{S}_{ij} = \vec{E}_{ij} \times \vec{H}_{ij}$, and the modes are separated into ordinary (q_{i1} and q_{i3}) and extraordinary (q_{i2} and q_{i4}) waves [25].

In the case of nonbirefringent media, the four solutions q_{ij} become degenerate, leading to singularities in the formalisms of previous works [23,24,37]. To resolve this problem, we follow the solution presented by Xu *et al.* [38]. Using the appropriately sorted q_{ij}, obtained as described above, the eigenvectors $\vec{\gamma}_{ij}$ of the four eigenmodes in each layer i are

$$\vec{\gamma}_{ij} = \begin{pmatrix} \gamma_{ij1} \\ \gamma_{ij2} \\ \gamma_{ij3} \end{pmatrix}, \tag{2}$$

with the values of γ_{ijk} given by Xu *et al.* [38] (Eq. (20) in Ref. [25]), and $k = 1, 2, 3$ being the x, y, and z components of $\vec{\gamma}_{ij}$. Furthermore, $\vec{\gamma}_{ij}$ has to be normalized:

$$\tilde{\gamma}_{ij} = \frac{\vec{\gamma}_{ij}}{|\vec{\gamma}_{ij}|}. \tag{3}$$

We note that this normalization is essential to ensure a correct calculation of the cross-polarization components of the transfer matrix. The normalized electric field eigenvectors $\tilde{\gamma}_{ij}$, being free from singularities, replace the eigenvectors Ψ_{ij} for all further calculations in the formalism.

At each interface, the boundary conditions for electric and magnetic fields allow to connect the fields of the two adjacent layers $i - 1$ and i. Formulated for all four modes simultaneously, the boundary conditions are

$$\mathbf{A}_{i-1}\vec{E}_{i-1} = \mathbf{A}_i\vec{E}_i, \tag{4}$$

where $\mathbf{A}_i$ is a 4×4 matrix calculated from the eigenvectors γ_{ijk} [38] (Eq. (22) in Ref. [25]), and $\vec{E}_i$ is a dimensionless four-component electric field vector containing the amplitudes of the resulting electric fields of all four modes. In the following, we refer to $\vec{E}_i$ as the amplitude vector, and its components are sorted as follows:

$$\vec{E} \equiv \begin{pmatrix} E^{p/o}_{\Rightarrow} \\ E^{s/e}_{\Rightarrow} \\ E^{p/o}_{\Leftarrow} \\ E^{s/e}_{\Leftarrow} \end{pmatrix}, \tag{5}$$

where $\Rightarrow$ ($\Leftarrow$) stands for the forward-propagating, transmitted (backward-propagating, reflected) modes, and p, s refer to the p- and s-polarized modes in nonbirefringent media, while o, e indicate the ordinary and extraordinary modes in birefringent media. By multiplying ${\mathbf{A}_{i-1}}^{-1}$ on both sides of Eq. (4), we find the implicit definition of the interface matrix $\mathbf{L}_i$, which

projects the amplitude vector in medium i onto the amplitude vector in medium $i-1$:

$$\vec{E}_{i-1} = {\mathbf{A}_{i-1}}^{-1}\mathbf{A}_i\vec{E}_i \equiv \mathbf{L}_i\vec{E}_i. \tag{6}$$

For the transition between two birefringent or between two nonbirefringent media, the projection of a wave of one particular polarization in layer i only yields a finite amplitude in layer $i-1$ of the mode of same polarization, i.e., $s/e \leftrightarrow s/e$ and $p/o \leftrightarrow p/o$. For the transition between a birefringent and a nonbirefringent medium, on the other hand, the interface matrix $\mathbf{L}_i$ projects a mode of one particular polarization in layer i onto both polarization states in layer $i-1$. This cross-polarized projection occurs because in birefringent media, the in-plane directions of the ordinary and extraordinary eigenmodes are rotated ($\neq n\pi$, $n \in \mathbb{N}_0$) with respect to the directions of the p- and s-polarized eigenmodes in the nonbirefringent medium.

The propagation of all four eigenmodes through layer i is described by the propagation matrix $\mathbf{P}_i$ [24]:

$$\mathbf{P}_i = \begin{pmatrix} e^{-i\frac{\omega}{c}q_{i1}d_i} & 0 & 0 & 0 \\ 0 & e^{-i\frac{\omega}{c}q_{i2}d_i} & 0 & 0 \\ 0 & 0 & e^{-i\frac{\omega}{c}q_{i3}d_i} & 0 \\ 0 & 0 & 0 & e^{-i\frac{\omega}{c}q_{i4}d_i} \end{pmatrix}, \tag{7}$$

where the rotation of polarization in birefringent media arises due to a phase difference that is accumulated during propagation through the medium, because of different propagation speeds of the ordinary and extraordinary modes ($q_{i1} \neq q_{i2}$ and $q_{i3} \neq q_{i4}$).

The transfer matrix $\mathbf{T}_i$ of a single layer i is defined as

$$\mathbf{T}_i = \mathbf{A}_i\mathbf{P}_i{\mathbf{A}_i}^{-1}, \tag{8}$$

and the full transfer matrix $\mathbf{\Gamma}$ of all N layers is

$$\mathbf{\Gamma} = {\mathbf{A}_0}^{-1}\left(\prod_{i=1}^{N}\mathbf{T}_i\right)\mathbf{A}_{N+1}, \tag{9}$$

where ${\mathbf{A}_0}^{-1}$ ($\mathbf{A}_{N+1}$) ensures the correct mode projection between the multilayer system and the incident medium (substrate).

B. Reflection and transmission coefficients

The full transfer matrix $\mathbf{\Gamma}$ projects the amplitude vector in the substrate $\vec{E}^+_{N+1}$ onto the amplitude vector in the incident medium $\vec{E}^-_0$:

$$\vec{E}^-_0 = \mathbf{\Gamma}\vec{E}^+_{N+1}, \tag{10}$$

where $\vec{E}^-_{i-1}$ and $\vec{E}^+_i$ denote the fields on both sides of the interface between layer $i-1$ and i, respectively. Following the equations presented by Yeh [24], the transmission (t) and reflection (r) coefficients for incident p- or s-polarization can be calculated in terms of the matrix elements of $\mathbf{\Gamma}$ as follows:

$$r_{pp} = \frac{\Gamma_{31}\Gamma_{22} - \Gamma_{32}\Gamma_{21}}{\Gamma_{11}\Gamma_{22} - \Gamma_{12}\Gamma_{21}}, \quad t_{p(p/o)} = \frac{\Gamma_{22}}{\Gamma_{11}\Gamma_{22} - \Gamma_{12}\Gamma_{21}}, \tag{11}$$

$$r_{ss} = \frac{\Gamma_{11}\Gamma_{42} - \Gamma_{41}\Gamma_{12}}{\Gamma_{11}\Gamma_{22} - \Gamma_{12}\Gamma_{21}}, \quad t_{s(s/e)} = \frac{\Gamma_{11}}{\Gamma_{11}\Gamma_{22} - \Gamma_{12}\Gamma_{21}}, \tag{12}$$

$$r_{ps} = \frac{\Gamma_{41}\Gamma_{22} - \Gamma_{42}\Gamma_{21}}{\Gamma_{11}\Gamma_{22} - \Gamma_{12}\Gamma_{21}}, \quad t_{p(s/e)} = \frac{-\Gamma_{21}}{\Gamma_{11}\Gamma_{22} - \Gamma_{12}\Gamma_{21}}, \tag{13}$$

$$r_{sp} = \frac{\Gamma_{11}\Gamma_{32} - \Gamma_{31}\Gamma_{12}}{\Gamma_{11}\Gamma_{22} - \Gamma_{12}\Gamma_{21}}, \quad t_{s(p/o)} = \frac{-\Gamma_{12}}{\Gamma_{11}\Gamma_{22} - \Gamma_{12}\Gamma_{21}}, \tag{14}$$

where the subscripts refer to the incoming and outgoing polarization states, respectively. The transmission coefficients describe the transmitted electric field amplitude into p- and s-polarized states in the case of a nonbirefringent substrate and into the ordinary and extraordinary eigenstates in the case of a birefringent substrate. We note that the indices of $\mathbf{\Gamma}$ differ from the equations reported by Yeh [24] in order to account for a different order of the eigenmodes in the amplitude vector [Eq. (5)].

C. Electric field distribution

Employing the interface and propagation matrices $\mathbf{L}_i$ and $\mathbf{P}_i$, respectively, an amplitude vector can be projected to any z point in the multilayer system (please note the published erratum that corrects the calculation of the electric field distribution in our original work [33]). However, due to the rotation of polarization in birefringent media and thus the mixing of polarization states, in general, the cases of incident p and s polarization have to be treated separately. As a starting point, the transmission coefficients can be utilized to formulate the amplitude vector $\vec{E}^+_{N+1}$ for either p- or s-polarized incident light in the substrate at the interface with layer N as follows:

$$(\vec{E}^+_{N+1})_{p\text{ in}} = \begin{pmatrix} E^{p/o}_{\Rightarrow} \\ E^{s/e}_{\Rightarrow} \\ E^{p/o}_{\Leftarrow} \\ E^{s/e}_{\Leftarrow} \end{pmatrix} = \begin{pmatrix} t_{p(p/o)} \\ t_{p(s/e)} \\ 0 \\ 0 \end{pmatrix},$$
$$(\vec{E}^+_{N+1})_{s\text{ in}} = \begin{pmatrix} E^{p/o}_{\Rightarrow} \\ E^{s/e}_{\Rightarrow} \\ E^{p/o}_{\Leftarrow} \\ E^{s/e}_{\Leftarrow} \end{pmatrix} = \begin{pmatrix} t_{s(p/o)} \\ t_{s(s/e)} \\ 0 \\ 0 \end{pmatrix}, \tag{15}$$

where the reflected ($\Leftarrow$) components are set to zero, since no light source is assumed to be on the substrate side of the multilayer system. Furthermore, in order to obtain the electric field amplitudes as a function of z, the propagation through layer i is calculated by means of the propagation matrix $\mathbf{P}_i$:

$$\vec{E}_i(z) = \mathbf{P}_i(z)\vec{E}^-_i = \begin{pmatrix} e^{-i\frac{\omega}{c}q_{i1}z} & 0 & 0 & 0 \\ 0 & e^{-i\frac{\omega}{c}q_{i2}z} & 0 & 0 \\ 0 & 0 & e^{-i\frac{\omega}{c}q_{i3}z} & 0 \\ 0 & 0 & 0 & e^{-i\frac{\omega}{c}q_{i4}z} \end{pmatrix}\vec{E}^-_i, \tag{16}$$

with $0 < z < d_i$ being the relative z position in layer i. Starting from $\vec{E}^+_{N+1}$, the interface matrices $\mathbf{L}_i$ and propagation matrices $\mathbf{P}_i$ subsequently propagate the amplitude vector toward the incident medium. In the reverse direction, the inverse propagation matrix ${\mathbf{P}_{N+1}}^{-1}$ allows us to calculate the $\vec{E}$ fields in the substrate. As a result, the four mode amplitudes $E^{p/o}_{\Rightarrow}$, $E^{s/e}_{\Rightarrow}$, $E^{p/o}_{\Leftarrow}$, and $E^{s/e}_{\Leftarrow}$ are obtained as a function of z within each layer.

In order to obtain the three components $\mathcal{E}_x$, $\mathcal{E}_y$, and $\mathcal{E}_z$ of the electric field for each of the four modes j, the

four mode amplitudes have to be multiplied with their respective eigenmode vector $\vec{\gamma}_{ij}$ [Eq. (3)]. This yields for the electric fields $\vec{\mathcal{E}}$ of the four modes for each layer i, as a function of z, and for either p- or s-polarized incident light:

$$
\begin{aligned}
(\vec{\mathcal{E}}^{p/o}_{\Rightarrow})_{p/s\,\mathrm{in}} &= (E^{p/o}_{\Rightarrow})_{p/s\,\mathrm{in}} \begin{pmatrix} \hat{\gamma}_{i11} \\ \hat{\gamma}_{i12} \\ \hat{\gamma}_{i13} \end{pmatrix}, \quad j = 1, \\
(\vec{\mathcal{E}}^{s/e}_{\Rightarrow})_{p/s\,\mathrm{in}} &= (E^{s/e}_{\Rightarrow})_{p/s\,\mathrm{in}} \begin{pmatrix} \hat{\gamma}_{i21} \\ \hat{\gamma}_{i22} \\ \hat{\gamma}_{i23} \end{pmatrix}, \quad j = 2, \\
(\vec{\mathcal{E}}^{p/o}_{\Leftarrow})_{p/s\,\mathrm{in}} &= (E^{p/o}_{\Leftarrow})_{p/s\,\mathrm{in}} \begin{pmatrix} \hat{\gamma}_{i31} \\ \hat{\gamma}_{i32} \\ \hat{\gamma}_{i33} \end{pmatrix}, \quad j = 3, \\
(\vec{\mathcal{E}}^{s/e}_{\Leftarrow})_{p/s\,\mathrm{in}} &= (E^{s/e}_{\Leftarrow})_{p/s\,\mathrm{in}} \begin{pmatrix} \hat{\gamma}_{i41} \\ \hat{\gamma}_{i42} \\ \hat{\gamma}_{i43} \end{pmatrix}, \quad j = 4, \qquad (17)
\end{aligned}
$$

where we have omitted the index i and the z dependence for the sake of readability. The full electric field $\vec{\mathcal{E}}_i(z)$ for either p- or s-polarized incident light in layer i at point z is given by the sum of all four electric field vectors:

$$
\vec{\mathcal{E}}_i(z) = \vec{\mathcal{E}}^{p/o}_{\Rightarrow,i}(z) + \vec{\mathcal{E}}^{s/e}_{\Rightarrow,i}(z) + \vec{\mathcal{E}}^{p/o}_{\Leftarrow,i}(z) + \vec{\mathcal{E}}^{s/e}_{\Leftarrow,i}(z). \qquad (18)
$$

The in-plane components of the sum, $\mathcal{E}_x$ and $\mathcal{E}_y$, are continuous throughout the entire multilayer structure, as it is required by Maxwell's boundary conditions.

III. LAYER-RESOLVED TRANSMITTANCE AND ABSORPTION

The total reflectance $\mathcal{R}$ of the multilayer system for a given ingoing and outgoing polarization a and b, respectively, can be readily calculated from the corresponding reflection coefficient [Eqs. (11)–(14)]:

$$
\mathcal{R}^{ab} = |r_{ab}|^2, \quad a, b = p, s. \qquad (19)
$$

The transmittance $\mathcal{T}$, which is the transmitted power into the substrate, on the other hand, in general is not given by the electric field intensity $\mathcal{T} \neq |t|^2$ (except for the special case if the substrate is vacuum, $\varepsilon = 1$). Instead, $\mathcal{T}$ can be calculated from the time-averaged Poynting vector $\vec{\mathcal{S}}$ [39–41], which describes the direction and magnitude of the energy flux of an electromagnetic wave at any point z in the structure:

$$
\vec{\mathcal{S}}_i(z) = \frac{1}{2}\mathrm{Re}[\vec{\mathcal{E}}_i(z) \times \vec{\mathcal{H}}_i^*(z)]. \qquad (20)
$$

The full electric field $\vec{\mathcal{E}}$ (for incident polarization a) as a function of z in each layer i was calculated in the previous section [Eq. (18)], and the full magnetic field $\vec{\mathcal{H}}$ is obtained as follows using Maxwell's equations:

$$
\begin{aligned}
\vec{\mathcal{H}}_i(z) = \frac{1}{\omega\mu_i}\big[&\vec{k}_{i1} \times \vec{\mathcal{E}}^{p/o}_{\Rightarrow,i}(z) + \vec{k}_{i2} \times \vec{\mathcal{E}}^{s/e}_{\Rightarrow,i}(z) \\
&+ \vec{k}_{i3} \times \vec{\mathcal{E}}^{p/o}_{\Leftarrow,i}(z) + \vec{k}_{i4} \times \vec{\mathcal{E}}^{s/e}_{\Leftarrow,i}(z)\big], \qquad (21)
\end{aligned}
$$

where $\vec{k}_{ij}$ are the wave vectors in layer i of the four modes j; see Eq. (1). Because $\vec{\mathcal{E}}$ and $\vec{\mathcal{H}}$ are known in each layer i and as a function of z from the transfer matrix formalism, the Poynting vector can be evaluated likewise, yielding $\vec{\mathcal{S}}_i(z)$, which will be used in the following to calculate the transmittance and absorption at any point z in the multilayer system.

It is important to note that while $\vec{\mathcal{E}}$ and $\vec{\mathcal{H}}$ can be calculated for each of the four modes j individually, this mode separation in general—specifically, in the case of birefringent media—is not possible for the Poynting vector $\vec{\mathcal{S}}$. In other words, in birefringent media, the sum of the Poynting vectors of the four modes is not equal to the Poynting vector calculated from the total fields $\vec{\mathcal{E}}$ [Eq. (18)] and $\vec{\mathcal{H}}$ [Eq. (21)]. The difference arises because in birefringent media, $\vec{\mathcal{E}} \not\perp \vec{\mathcal{H}}$. Therefore, the cross products $\vec{\mathcal{E}} \times \vec{\mathcal{H}}$ between different modes j are no longer zero. For the correct calculation of the Poynting vector in birefringent media, it is thus necessary to calculate the cross product of the total fields $\vec{\mathcal{E}}$ and $\vec{\mathcal{H}}$, as shown in Eq. (20). Interestingly, this means that the energy flux in birefringent media cannot be split up into the ordinary and extraordinary eigenmodes but has to be considered as a single quantity. In the following, we therefore discuss the transmittance and absorption for s- or p-polarized incident light without differentiating between the eigenmodes anymore.

An exception is the incident medium, which is set to be isotropic. Here, the Poynting vector can be calculated for each mode individually, and for the purpose of normalizing the transmitted power, we calculate the Poynting vector of the incident light $\vec{\mathcal{S}}_{\mathrm{inc}}$ (in layer $i = 0$ at position $z = 0$) for either p or s polarization as follows:

$$
\begin{aligned}
\vec{\mathcal{S}}^{p}_{\mathrm{inc}} &= \tfrac{1}{2}\mathrm{Re}\big[\vec{\mathcal{E}}^{p}_{\Rightarrow,0}(0) \times \big(\vec{k}_{01} \times \vec{\mathcal{E}}^{p}_{\Rightarrow,0}(0)\big)^*\big], \\
\vec{\mathcal{S}}^{s}_{\mathrm{inc}} &= \tfrac{1}{2}\mathrm{Re}\big[\vec{\mathcal{E}}^{s}_{\Rightarrow,0}(0) \times \big(\vec{k}_{02} \times \vec{\mathcal{E}}^{s}_{\Rightarrow,0}(0)\big)^*\big]. \qquad (22)
\end{aligned}
$$

In a stratified multilayer system, the transmitted energy is given by the z component of the Poynting vector. Thus, we note that alternatively to Eq. (19), the reflectance $\mathcal{R}$ can be calculated from the Poynting vector:

$$
\mathcal{R}^{ab} = \frac{-\mathcal{S}^{b}_{\mathrm{refl},z}}{\mathcal{S}^{a}_{\mathrm{inc},z}}, \qquad (23)
$$

where the minus sign accounts for the negative z direction of the reflected light. $\mathcal{S}^{b}_{\mathrm{refl},z}$ is the z component of the Poynting vector of the reflected light of polarization $b = p, s$ (in layer $i = 0$ at position $z = 0$) given by

$$
\begin{aligned}
\vec{\mathcal{S}}^{p}_{\mathrm{refl}} &= \tfrac{1}{2}\mathrm{Re}\big[\vec{\mathcal{E}}^{p}_{\Leftarrow,0}(0) \times \big(\vec{k}_{03} \times \vec{\mathcal{E}}^{p}_{\Leftarrow,0}(0)\big)^*\big], \\
\vec{\mathcal{S}}^{s}_{\mathrm{refl}} &= \tfrac{1}{2}\mathrm{Re}\big[\vec{\mathcal{E}}^{s}_{\Leftarrow,0}(0) \times \big(\vec{k}_{04} \times \vec{\mathcal{E}}^{s}_{\Leftarrow,0}(0)\big)^*\big]. \qquad (24)
\end{aligned}
$$

As discussed above, for anisotropic media, a separation of the energy flow into the different eigenmodes of polarization b is not generally possible. Therefore, all following equations calculate the total transmittance or absorption for the respective incident polarization a.

The transmittance $\mathcal{T}$ into the substrate $i = N + 1$ at the interface with layer N for incident light of polarization a is given by

$$
\mathcal{T}^{a} = \frac{\mathcal{S}^{a}_{N+1,z}(D)}{\mathcal{S}^{a}_{\mathrm{inc},z}}, \qquad (25)
$$

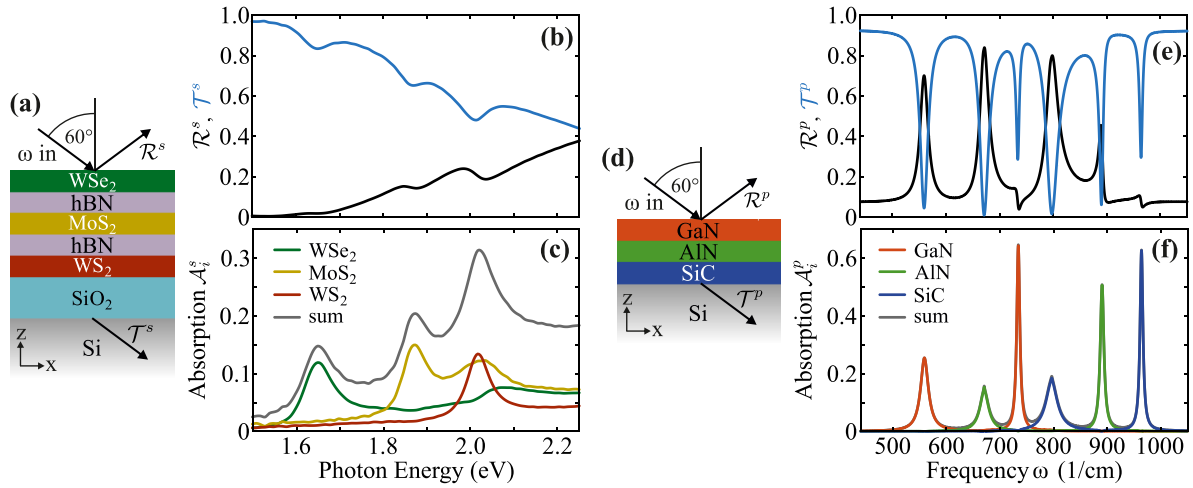

FIG. 1. Layer-resolved absorption calculations of two simple test structures. (a) Sketch of the TMDC heterostructure comprising monolayers of WSe_2, MoS_2, and WS_2 [42] separated by hBN monolayers on a 140-nm-thick SiO_2 film on a Si substrate. (b) Reflectance (black line) and transmittance (blue line) spectra of the system at visible wavelengths and at an incident angle of 60° for *s*-polarized incident light. (c) Layer-resolved absorption spectra of the TMDC monolayers (colored lines), revealing their respective contribution to the overall absorption spectrum (gray line). (d) Sketch of the polar dielectric heterostructure comprising 100-nm-thin GaN, AlN, and SiC films on a Si substrate. (e) Reflectance and transmittance spectra and (f) layer-resolved absorption spectra of the second system, enabling identification of the absorbing layer for each of the six absorption lines.

where $D = \sum_{i=1}^{N} d_i$ is the thickness of the multilayer system. The full z dependence of the transmittance can be evaluated by using the z component of the Poynting vector $\mathcal{S}_{i,z}(z)$ at a certain z position in layer i:

$$\mathcal{T}_i^a(z) = \frac{\mathcal{S}_{i,z}^a(z)}{\mathcal{S}_{\mathrm{inc},z}^a}. \tag{26}$$

With this, the absorption $\mathcal{A}$ of the entire multilayer system, that is, up to the last interface between layer N and the substrate, is given by

$$\mathcal{A}^a = 1 - \mathcal{R}^a - \mathcal{T}^a, \tag{27}$$

and the z-resolved absorption $\mathcal{A}_i(z)$ in each layer i is

$$\mathcal{A}_i^a(z) = 1 - \mathcal{R}^a - \mathcal{T}_i^a(z), \tag{28}$$

where $\mathcal{R}^a = \mathcal{R}^{ap} + \mathcal{R}^{as}$ is the total reflectance. Note that Eq. (28) describes the total absorption starting from $z = 0$ at the first interface up to the specified position z in layer i. The layer-i-resolved absorption, on the other hand, is given by

$$\begin{aligned} \mathcal{A}_i^a &= \mathcal{T}_i^a(d_{1\ldots i-1}) - \mathcal{T}_i^a(d_{1\ldots i-1} + d_i) \\ &= \mathcal{A}_i^a(d_{1\ldots i-1} + d_i) - \mathcal{A}_i^a(d_{1\ldots i-1}), \end{aligned} \tag{29}$$

where $d_{1\ldots i-1} = \sum_{i=1}^{i-1} d_i$ is the thickness of all layers through which the incident light has propagated before reaching the layer i.

Before we study three nanophotonic device structures in the following section, we calculate the layer-resolved absorption for two simple test structures in Fig. 1. The first is a typical TMDC heterostructure, comprising monolayers of tungsten diselenide (WSe_2), MoS_2, and tungsten disulfide (WS_2) sandwiched between hBN monolayers [sketched in Fig. 1(a)], where each TMDC monolayer features individual exciton absorption lines. In Fig. 1(b), the reflection and transmittance of the entire structure is plotted, and Fig. 1(c) shows the absorption spectra of each TMDC monolayer. The total absorption [gray line in Fig. 1(c)] obtained from the reflectance and transmittance spectra [Eq. (27)] exhibits three indistinguishable absorption features, whereas the layer-resolved absorption calculations unravel the absorption spectrum, allowing us to identify the contribution of each TMDC monolayer.

In Figs. 1(d)–1(f), we show the absorption in a polar dielectric heterostructure of SiC, AlN, and GaN thin films on a Si substrate probed at infrared (IR) frequencies. Polar dielectric crystals feature an IR-active transverse optical (TO) phonon mode, where light is predominantly absorbed, whereas the longitudinal optical (LO) phonon mode is not IR active and thus featureless in a bulk crystal. Thin films, on the other hand, support the so-called Berreman mode in proximity to the LO frequency, leading to a strong absorption feature for *p*-polarization at oblique incidence [43–46]. Thus, the reflectance and transmittance spectra [Fig. 1(e)] of the polar dielectric heterostructure are of complicated shape, exhibiting six different features arising from the three different polar crystal thin films. The layer-resolved absorption calculations split these features into three spectra with two absorption peaks each [Fig. 1(f)], allowing us to identify the respective polar crystal thin film that leads to the absorption at its respective TO and LO frequencies.

IV. SIMULATIONS OF NANOPHOTONIC DEVICES

The transfer matrix formalism and the calculation of the layer-resolved absorption and transmittance presented in the previous section can be applied for any wavelength and any number of layers, consisting of birefringent or nonbirefringent media described by an arbitrary permittivity tensor $\bar{\varepsilon}_i$. As case studies, in this section we describe three selected

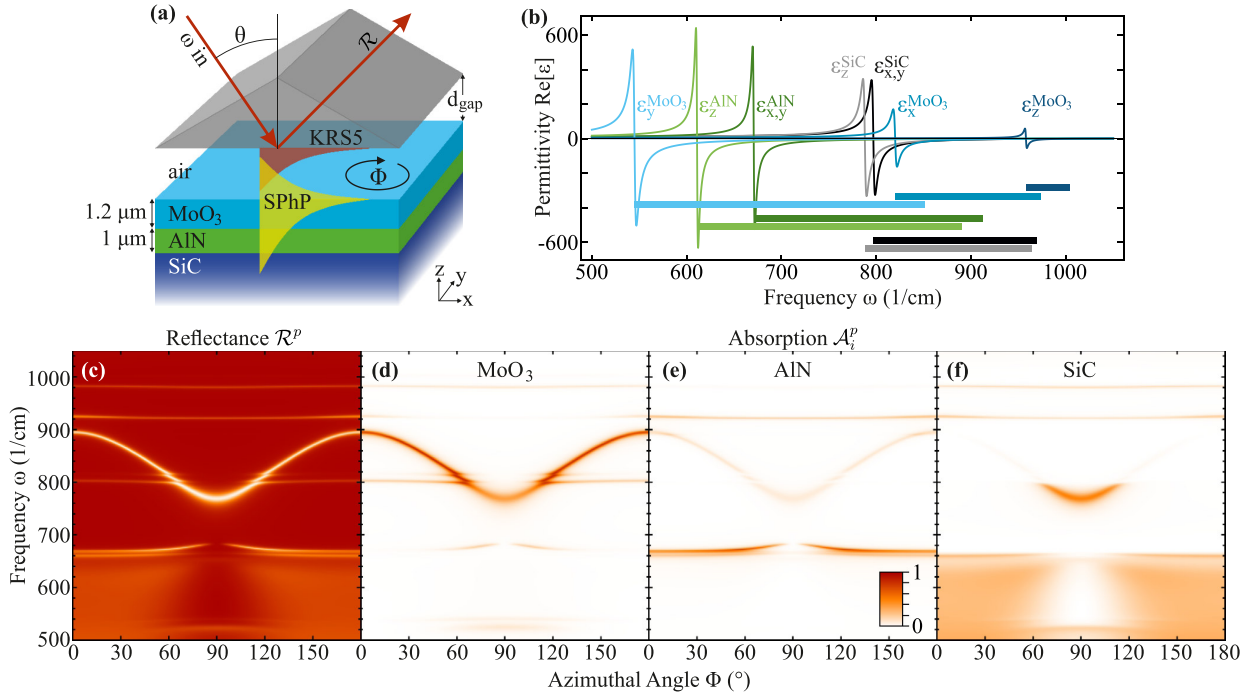

FIG. 2. Azimuthal dependence of the layer-resolved absorption in a MoO_3/AlN/SiC heterostructure. (a) Prism coupling setup in the Otto geometry for the evanescent excitation of phonon polaritons in a 1200-nm MoO_3 / 1000-nm AlN / SiC substrate multilayer sample with p-polarized incident light. The incident angle is fixed to $\theta = 28°$ and the air gap to $d_{gap} = 8\,\mu$m. (b) Real value of the principle relative permittivities ε_x, ε_y, and ε_z of uniaxial SiC and AlN and biaxial MoO_3. Their respective reststrahlen bands located between the corresponding TO and LO phonon frequencies are indicated by the horizontal color bars. (c) Reflectance $\mathcal{R}^p$ of the entire system as a function of incident frequency ω and azimuthal angle of the sample Φ. [(d)–(f)] Absorptions $\mathcal{A}_i^p$ [Eq. (29)] of the MoO_3, AlN, and SiC layers as a function of ω and Φ.

nanophotonic device structures. The first example discusses the hyperbolic phonon polaritons arising in a MoO_3/AlN/SiC system excited evanescently at far-IR wavelengths, highlighting the potential of the formalism for nanophotonic studies in stratified media. The second example describes the free-space response in the visible of a van der Waals heterostructure of monolayers of MoS_2 embedded in a hBN matrix, featuring layer-selective absorption of the MoS_2 excitons. Finally, the third example calculates the mid-IR absorption of strongly coupled modes formed from intersuband plasmons in multi-quantum wells embedded in an optical cavity.

A. Hyperbolic phonon polaritons in MoO_3/AlN/SiC

Polar crystals such as MoO_3, AlN, and SiC support surface phonon polaritons (SPhP) at frequencies inside their reststrahlen region between the TO and LO phonon frequencies [48]. On smooth surfaces, SPhPs can be excited via prism coupling in the Otto geometry [49,50] as illustrated in Fig. 2(a), where the air gap width d_{gap} governs the excitation efficiency and the incident angle θ defines the in-plane momentum of the launched SPhP [51]. The system we investigate here is a multilayer heterostructure comprising an MoO_3 and AlN film on a SiC substrate. Employing the presented transfer matrix formalism, the layer-resolved absorption $\mathcal{A}_i$ of such a structure can be calculated as a function of incident angle θ, incident frequency ω, layer thicknesses d_i, and azimuthal angle Φ of the sample.

The absorption in the MoO_3, AlN, and SiC layers as a function of ω and Φ and for fixed θ and d_i is shown in Figs. 2(d)–2(f). The reflectance of the entire system is plotted in Fig. 2(c). As required by energy conservation, the sum of the absorbed power in the three polar crystals equals the attenuated power visible as absorption dips in the reflectance. However, while the reflectance only yields the total absorption, the layer-resolved calculations allow us to identify the exact position of a power drain in a multilayer system.

In particular, the MoO_3/AlN/SiC heterostructure features several sharp absorption lines at 660, 800, 920, and 980 cm^{-1} that are mostly independent of Φ, and one prominent absorption line that strongly varies with Φ, indicating that the latter depends on in-plane anisotropy ($\varepsilon_x \neq \varepsilon_y$) while the former do not. In the multilayer sample, only the MoO_3 layer exhibits in-plane anisotropy, while AlN and SiC are c-cut uniaxial crystals [principle relative permittivities ε_x, ε_y, and ε_z are shown in Fig. 2(b)]. Indeed, the Φ-dependent feature is mostly absorbed in the MoO_3 layer. This feature is the hyperbolic phonon polariton (hPhP) supported in the MoO_3 thin film arising in the in-plane reststrahlen bands of MoO_3. Its tunability in frequency arises from the large in-plane anisotropy of MoO_3, which leads to a Φ-dependent effective permittivity sensed by the hPhP upon azimuthal rotation.

Notably, below the SiC TO frequencies ($\approx$800 cm^{-1}), a significant part of the hPhP leaks into the SiC substrate, while above $\omega_{\mathrm{TO}}^{\mathrm{SiC}}$ the mode is mostly confined to the MoO_3 layer. The high confinement above $\omega_{\mathrm{TO}}^{\mathrm{SiC}}$ occurs because of the negative permittivity in the SiC reststrahlen band, while below $\omega_{\mathrm{TO}}^{\mathrm{SiC}}$, the mode can penetrate the substrate. Interestingly, this mode penetration happens across the AlN layer, where only a small part of the mode is absorbed. Since AlN features its reststrahlen bands across the entire frequency range of the hPhP supported by the MoO_3, and thus evanescently attenuates all modes, the hPhP appears to tunnel through the AlN layer to be absorbed by the SiC substrate.

The multilayer system presented here only scratches the surface of various possible material configurations and compositions that can potentially be employed for tailoring surface and interface polariton resonances [20,52–57]. In particular, the emerging field of volume-confined hyperbolic polaritons [14,20,58,59], enabled by the anisotropic permittivity of the supporting media, holds great potential for future nanophotonic applications, such as subdiffraction imaging and hyperlensing [12,13]. Providing the full layer-resolved absorption, our algorithm paves the way to predict and study hyperbolic polariton modes in any anisotropic stratified heterostructure.

B. Layer-selective absorption of MoS_2 excitons in a Fabry-Pérot cavity

TMDC monolayers such as MoS_2 feature strong exciton resonances at visible frequencies [42,47]. By inserting these monolayers into van der Waals heterostructures forming a Fabry-Pérot cavity, the light-matter interaction enabled by the TMDC exciton can be strongly enhanced [60]. Here, we embed two MoS_2 monolayers into a $d_c = 1.9$–2.4-μm-thick hBN cavity with a SiO_2 back-reflector on a Si substrate [61], as sketched in Fig. 3(a). Employing the presented formalism, the absorption $\mathcal{A}_i$ in the two MoS_2 monolayers as a function of photon energy and cavity thickness d_c can be calculated.

In the photon energy range of 1.7–2.2 eV, MoS_2 features two excitons (A and B) at $\approx$1.9 and $\approx$2.1 eV. These excitons are apparent as resonance peaks in the isotropic relative permittivity plotted in Fig. 3(b) and resulting in peaks in an absorption spectrum. However, the Fabry-Pérot cavity creates a static modulation of the electric field enhancement with peaks and nodes as a function of the z position, and thus the resulting absorption in a MoS_2 monolayer not only depends on the photon energy, but also sensitively depends on the z position of the MoS_2 monolayer in the cavity. Taking advantage of this field modulation, we place one MoS_2 monolayer (layer 4) at the center of the cavity where the cavity modes alternate between node and peak with maximal amplitude, and the other MoS_2 monolayer (layer 2) in close proximity where the cavity features a node when there is a peak in the center, and vice versa.

The cavity modes yield the periodic modulation in photon energy and cavity thickness d_c that can be seen in the reflectance (transmittance) maps shown in Figs. 3(f) and 3(g) [Figs. 3(l) and 3(m)], for incoming s- and p-polarized light, respectively. The different modulation contrast for $\mathcal{R}^s$ and $\mathcal{R}^p$ ($\mathcal{T}^s$ and $\mathcal{T}^p$) arises from the large incident angle of $\theta = 70°$, which was chosen to optimize the absorption $\mathcal{A}^s$ in the MoS_2 monolayers for s-polarized incident light. For smaller incident angles, the differences for s- and p-polarization decrease, but with a reduction in the absorption $\mathcal{A}^s$.

In Figs. 3(h) and 3(i) [Figs. 3(j) and 3(k)], the absorption for s- and p-polarized incident light in the first MoS_2 monolayer, $\mathcal{A}_2^{s,p}$ (second MoS_2 monolayer, $\mathcal{A}_4^{s,p}$), is shown. Due to the choice of the z positions of the two MoS_2 monolayers, each film is sensitive to only every second cavity mode, where layer 2 (first MoS_2 monolayer) absorbs those modes that are not absorbed by layer 4 (second MoS_2 monolayer). In addition to the absorption modulation imposed by the cavity, the A and B excitons of MoS_2 yield two absorption features at their respective energies, marked by dotted vertical lines in Figs. 3(h)–3(k). For the optimized case of s-polarized incident light, the MoS_2 monolayers reach cavity-enhanced absorption values of up to 20% at both exciton energies. At a cavity thickness of $d_c = 2.15\,\mu$m for s polarization, layer 2 only absorbs at the energy of exciton A, while in layer 4, absorption only occurs at the energy of exciton B. This layer-selective absorption is further illustrated in the absorption spectra (solid lines) for a fixed cavity thickness of $d_c = 2.15\,\mu$m shown in Figs. 3(d) and 3(e) for s- and p-polarized light, respectively. For both polarizations, a high contrast between the two layers at each exciton absorption line is achieved, yielding efficient layer selectivity.

Finally, we compare these results obtained for an isotropic permittivity model [42] with the same calculations performed for an anisotropic model of MoS_2 [47]. In Fig. 3(c), the in-plane ($\varepsilon_{x,y}$) and out-of-plane (ε_z) permittivity values taken from Funke *et al.* [47] are plotted. While $\varepsilon_{x,y}$ are qualitatively the same as the values from Jung *et al.* [42] [Fig. 3(b)], ε_z differs strongly, taking the almost constant value of $\varepsilon_z = 1 + 0\,i$. Even though the difference in ε_z is substantial, the absorption spectra shown in Figs. 3(d) and 3(e) (dashed lines) are qualitatively identical to the spectra calculated from an isotropic permittivity model (solid lines). This confirms that spectroscopic measurements of TMDC monolayers are mostly insensitive to their out-of-plane permittivity [42], with the exception of cases where ε_z features a zero crossing, the so-called epsilon-near-zero frequency, giving rise to drastic optical responses such as enhanced higher harmonic generation [45,62,63]. However, this is not the case for MoS_2, and therefore the spectra are almost identical.

In this example, the layer-resolved absorption calculations from our algorithm provide the essential information for simulating the layer-selective exciton absorption and optimizing the system parameters. In the thriving field of 2D nanophotonics featuring TMDC van der Waals heterostructures, where structures are optimized for maximal light harvesting [6,7], optoelectronic devices [4,5], or nanolasers [10,11], such layer-resolved absorption calculations promise to be of essential importance. Because of the generality of the presented algorithm, the light-matter interaction in any 2D heterostructure can be readily investigated, highlighting the broad applicability of our approach.

C. Strong coupling in a multi-quantum-well–cavity system

Doped semiconductor quantum wells (QWs) support transitions between consecutive quantum-confined electronic

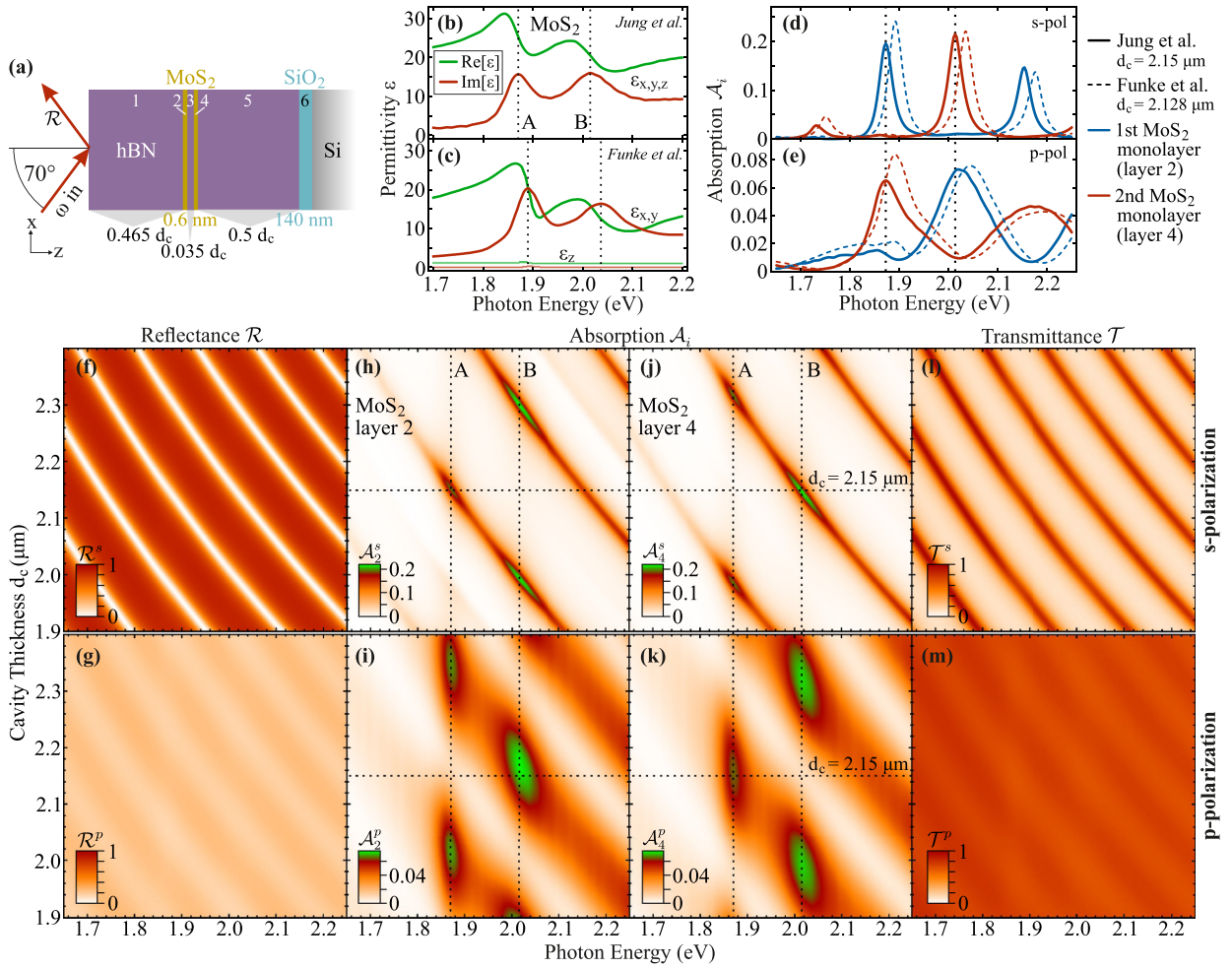

FIG. 3. Cavity-enhanced exciton absorption in MoS_2 monolayers. (a) Structure of the Fabry-Pérot cavity. A 140-nm-thin SiO_2 film on the Si substrate serves as a back-reflector, while the cavity with variable thickness $d_c = 1.9$–$2.4\,\mu$m is made of three layers of hBN of relative thicknesses 0.465 d_c, 0.035 d_c, and 0.5 d_c, separated by two 0.6-nm-thin MoS_2 monolayers. (b) Real and imaginary values of the isotropic relative permittivity of MoS_2 [42]. All calculations are based on this permittivity, except the dashed lines in subfigures (d) and (e). (c) Anisotropic relative permittivity of MoS_2 [47]. (d) Absorption spectra of the two MoS_2 monolayers for *s*-polarized incident light, for a cavity thickness of $d_c = 2.15\,\mu$m ($d_c = 2.128\,\mu$m) optimized for layer-selective absorption of the two MoS_2 excitons, calculated with the MoS_2 permittivities of Jung *et al.* (Funke *et al.*). (e) Analogous calculations as in subfigure (d) but for *p*-polarized incident light. [(f), (g)] Reflectance $\mathcal{R}^s$ and $\mathcal{R}^p$ for *s*- and *p*-polarized incident light, respectively. Subfigures [(h), (i)] and [(j), (k)] show absorption $\mathcal{A}_i^s$ and $\mathcal{A}_i^p$ of the two MoS_2 monolayers, respectively. [(l), (m)] Transmitted power $\mathcal{T}^s$ and $\mathcal{T}^p$ into the Si substrate, respectively. The maps of $\mathcal{R}$, $\mathcal{A}$, and $\mathcal{T}$ are all plotted as a function of the incident photon energy and the cavity thickness d_c.

levels, called intraband or intersubband (ISB) transitions. Contrary to interband transitions, ISB transitions do not only depend on the band-gap properties of the semiconductor but also on the electronic confinement inside the QWs, and thus offer a great frequency tunability by changing the width and the doping level inside the QW. They play a major role in semiconductor optic devices operating in the IR where semiconducting materials with a suitable band gap are lacking, and are the building block of quantum well IR photodetectors [64] and quantum cascade lasers [65]. They also offer a practical platform to study the optical properties of dense confined electron gases [66], which notably led to the demonstration of the strong [67,68] and ultrastrong light-matter coupling regimes [69,70]. It is remarkable that such fundamental electrodynamical phenomena are directly observable on semiconductor devices [71–73]. One peculiar aspect of these ISB transitions is that they only couple to the component of the electric field along the confinement direction of the QW structure. Hence, the optical properties of a doped QW can be described by an effective permittivity tensor with different in-plane ($\varepsilon_{x,y}$) and out-of-plane (ε_z) values, which has been realized by several permittivity models [74–77]. The description of light propagation in stratified anisotropic media containing such QWs requires a complex formalism, such as the transfer matrix method the here-presented algorithm builds on Ref. [25].

We focus here on an existent experimental configuration to further demonstrate the potential of our formalism for the case of strong light-matter coupling between a cavity mode

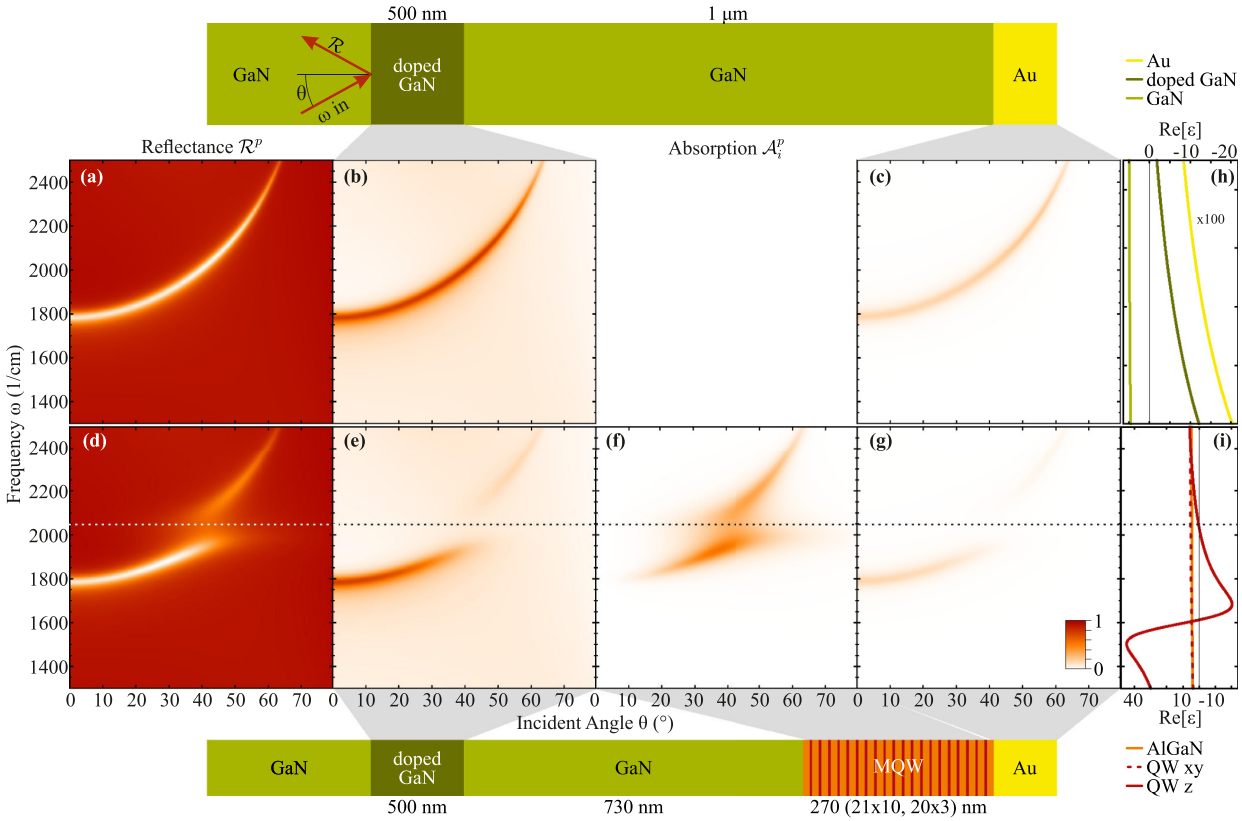

FIG. 4. Strong coupling between an ENZ mode in a MQW superlattice and a cavity mode. A 1-μm-thick GaN cavity is formed between an Au mirror and a 500-nm-thick doped GaN slab on a GaN substrate (top sketch). The doped GaN slab acts as a low-index mirror. (a) Simulated reflectance $\mathcal{R}^p$ of the cavity mode showing its dispersion relation as a function of the angle of incidence θ inside the GaN substrate. [(b), (c)] Layer-resolved absorption $\mathcal{A}^p$ inside the doped GaN slab and in the Au mirror, respectively. (d) Calculated reflectance $\mathcal{R}^p$ of the 1-μm-thick cavity partially filled with a doped GaN/AlGaN MQW superlattice (see bottom sketch), featuring an electronic excitation at $\approx$2030 cm^{-1} (white dotted line). The strong light-matter coupling between the cavity mode and QW resonance leads to an avoided crossing and the emergence of two polariton branches. [(e)–(g)] Layer-resolved absorption $\mathcal{A}^p$ inside the doped GaN mirror, the superlattice, and the Au mirror, respectively. (h) Real part of the permittivity of the isotropic layers forming the cavity. (i) Real part of the different components of the permittivity tensor of the doped GaN QW and of the AlGaN barrier, showing the ENZ mode frequency of the QW at $\approx$2030 cm^{-1}.

and a collective intersubband excitation in a multi-quantum well (MQW) superlattice. The system is composed of a GaN cavity formed by a 500-nm-thick, Si-doped GaN slab and a Au mirror, as sketched at the top of Fig. 4. The doped GaN layer is modeled using the Drude model and acts as a low-index mirror. The two mirrors are separated by a 1-μm-thick GaN spacer, forming an empty cavity. The system sustains a guided transverse magnetic (TM) mode, where the electric field is confined mostly between the two mirrors and its out-of-plane component is maximal near the Au mirror. This guided mode can be probed in a reflectance experiment, as discussed in the following. In order to probe large internal angles of incidence experimentally, the sample has to be prepared in a prism shape, for example, by cleaving the incident GaN layer facets. The calculated p-polarized reflectance $\mathcal{R}^p$ is shown in Fig. 4(a), evidencing the dispersion relation of the cavity mode with varying incidence angles inside the GaN substrate. The layer-resolved absorption spectra as a function of the angle of incidence for this system are reported in Figs. 4(b) and 4(c) and reveal that absorption occurs mostly in the doped GaN mirror. Notably, for an internal incidence angle of 48° at the guided mode frequency, all the light is dissipated in the mirrors, leading to a minimum of zero reflectance in Fig. 4(a).

We now turn to the system's response when the cavity is partially filled with a MQW structure [Figs. 4(d)–4(g)]. The superlattice is composed of 20 repetitions of a 3-nm-thick GaN QW, Si-doped with a concentration of 2×10^{13} cm^{-2} and 21 lossless 10-nm-thick $Al_{0.26}Ga_{0.74}N$ barriers. Since the guided mode is a TM mode, it naturally provides a component of the electric field along the z direction for nonzero angles of incidence, which fulfills the ISB transition selection rule. In order to maximize the coupling between the ISB transition in the MQW and the cavity mode, the superlattice is placed where the z component of the electric field is the largest, that is just below the Au mirror, as shown at the bottom of Fig. 4. The QW dielectric tensor is modeled using a semiclassical approach [75]. We selected the QW dimension and doping level in a way that it sustains a strong, collective electronic excitation known as an intersubband plasmon [66]. The components of the real part of the dielectric permittivity

tensor of all the layers are presented in Figs. 4(h) and 4(i). Note that while the ISB transition in the quantum well has a resonance frequency of $\approx$1600 cm^{-1}, the Coulomb interaction between the QW electrons results in an ENZ mode at $\approx$2030 cm^{-1}, marked by the dotted line in Fig. 4(i). The ENZ mode dominates the optical response of the QWs.

We show in Fig. 4(d) the calculated reflectance $\mathcal{R}^p$ of the cavity containing the MQW. The white dotted line shows the ENZ frequency. A clear anticrossing can be seen between the cavity mode and the ENZ resonance, which is characteristic of the strong light-matter coupling regime, resulting in two polariton branches. The minimal separation between the two branches amounts to a vacuum Rabi splitting $2\Omega_R =$ 200 cm^{-1}. The layer-resolved absorption spectra as a function of the angle of incidence are shown in Figs. 4(e)–4(g) for the GaN mirror, the MQW superlattice, and the Au mirror, respectively. When the cavity mode is far detuned from the ENZ frequency, the absorption occurs mostly in the two mirrors, and especially in the GaN mirror, as for the empty cavity case. The situation changes dramatically when the cavity mode is tuned near the ENZ frequency. The absorption then mostly occurs in the MQW. It is, however, important to note that the absorption is maximal at the frequencies of the two polaritons and not at the ENZ frequency, as it would occur in the case of a weak coupling between the cavity mode and the QW resonance. For an internal incidence angle of 48°, the maximum absorption inside the MQW stack is now 0.5 at each of the frequencies of the two polaritons.

The algorithm presented here thus allows us to directly calculate the light absorption in the complex case of a doped MQW superlattice strongly coupled to a cavity mode. In addition to the known features, such as the avoided crossing in the angle-dependent reflectance spectrum, we can directly calculate the absorption inside the MQW active region, which can be usefully linked to the detected photocurrent in the perspective of using such structures in photodetector devices [67,71,73].

V. DISCUSSION

We have presented three nanophotonic devices based on anisotropic multilayer structures made from metals, polar dielectrics, and TMDC monolayers, covering incident wavelengths from the far-IR up to the visible. Our formalism allows us to calculate the transmittance and absorption in any layer, giving unprecedented insight into the physics of light propagation in anisotropic, and even birefringent, stratified systems.

In recent years, the field of nanophotonics has intensely investigated the optical response of two-dimensional (2D) heterostructures. A particularly thriving subject has been polaritonic excitations, which can be supported by a broad variety of systems including slabs of metals, doped semiconductors, polar dielectrics, 2D materials such as TMDC monolayers, and their stratified heterostructures [17,54,78]. Key features of polaritons for nanophotonic technologies are their high spatial confinement and field enhancement, which are driven by the particular design of the multilayer materials, stacking order, and layer thicknesses. Potential applications of such systems range from sensing [79,80] and solar cells [81], over optoelectronic devices [3] and beam manipulation via metamaterials [82], to waveguiding [56,83], and ultrafast optical components [45,84]. However, due to the lack of a general formalism, the optical response of these polaritonic multilayer systems is often either approximated by effective, isotropic permittivity models [85–87] or described by specifically derived formulas [29–32]. Our generalized formalism allows for a precise, layer-resolved study that includes any isotropic, anisotropic, or even birefringent response of any number of layers, and thus holds great potential for the prediction and analysis of polariton modes in stratified heterostructures.

This is especially relevant for systems where one or more materials feature anisotropic permittivity with spectral regions of hyperbolicity where the principle real permittivities have opposite signs, such as hBN or MoO_3. Recently, these hyperbolic materials have attracted increasing interest [14,20,58,59] due to the existence of hyperbolic polaritons, featuring novel properties for nanophotonic applications such as subdiffraction imaging and hyperlensing [12,13]. Because of the strong anisotropy of these systems, an effective permittivity approach is not purposeful. Here, our formalism provides the essential theoretical framework that is necessary to model, predict, and analyze the optical response of such hyperbolic heterostructures, as we have discussed using a MoO_3/AlN/SiC system as an example (Fig. 2). Providing the full layer-resolved information about the field distribution and power flow of the excited polaritons, our method allows us to readily and concisely model and study hyperbolic polariton modes in any anisotropic stratified heterostructure.

Furthermore, the layer-resolved absorption formalism provides a description for designing optoelectronic devices such as detectors, for which the photoresponse is linked to the light absorption solely in the active region of the device. In the case of the MQW system, optimizing the overall light absorption by minimizing both the reflectance and transmittance of the system would not be sufficient to model the performances of a photodetector in the strong light-matter coupling regime [71,73]. Unfortunately, these are the only quantities that can be probed in a reflectance experiment. Calculating the layer-resolved absorption in the structure allows us to optimize the cavity and MQW design, aiming at minimizing the light absorption in the cavity mirrors while maximizing the absorption in the MQW. This is well shown in Figs. 4(e) and 4(f), where we can see that the light is preferably dissipated in either the doped GaN mirror or the MQW superlattice depending on the detuning between the cavity mode and the QW resonance. This behavior cannot be deduced only from the reflectance measurement simulated in Fig. 4(d). Fitting experimental reflectance data using our formalism [25] would allow us to retrieve the amount of light dissipated inside the active region only from the experimentally observable quantities and to estimate figures of merit such as the quantum efficiency of the device. The present method thus provides a convenient way to model and optimize complex, optically anisotropic heterostructures for optoelectronic devices.

VI. CONCLUSION

In this work, we have derived explicit expressions for the calculation of the layer-resolved transmittance and

absorption of light propagating in arbitrarily anisotropic, birefringent, and absorbing multilayer media. The algorithm relies on the electric field distribution computed from a 4×4 transfer matrix formalism [25,33], yielding a robust and consistent framework for light-matter interaction in stratified systems of arbitrary permittivity, which is implemented in an open-access computer program [34,35]. As case studies, we applied the algorithm to simulations of three nanophotonic device structures featuring hyperbolic phonon polaritons in a polar dielectric heterostructure, MoS_2 excitons in a Fabry-Pérot cavity, and ENZ resonances in a cavity-coupled multi-quantum well, where we observed azimuth-dependent hyperbolic polariton tunneling, layer-selective exciton absorption, and strong coupling between ENZ and cavity modes. Allowing for a detailed analysis of the layer-resolved electric field distribution, transmittance, and absorption of light in any multilayer system, our algorithm holds great potential for the prediction of nanophotonic light-matter interactions in arbitrarily anisotropic stratified heterostructures.

ACKNOWLEDGMENTS

We thank M. Wolf, S. Wasserroth, and R. Ernstorfer (FHI Berlin) for careful reading of the manuscript and M. Wolf and the Max Planck Society for supporting this work.

[1] A. K. Geim and I. V. Grigorieva, Nature (London) **499**, 419 (2013).
[2] N. M. Gabor, J. C. W. Song, Q. Ma, N. L. Nair, T. Taychatanapat, K. Watanabe, T. Taniguchi, L. S. Levitov, and P. Jarillo-Herrero, Science **334**, 648 (2011).
[3] M. Freitag, T. Low, W. Zhu, H. Yan, F. Xia, and P. Avouris, Nat. Commun. **4**, 1951 (2013).
[4] K. He, C. Poole, K. F. Mak, and J. Shan, Nano Lett. **13**, 2931 (2013).
[5] J. S. Ross, P. Klement, A. M. Jones, N. J. Ghimire, J. Yan, D. G. Mandrus, T. Taniguchi, K. Watanabe, K. Kitamura, W. Yao, D. H. Cobden, and X. Xu, Nat. Nanotechnol. **9**, 268 (2014).
[6] E. Fortin and W. Sears, J. Phys. Chem. Solids **43**, 881 (1982).
[7] W. J. Yu, Y. Liu, H. Zhou, A. Yin, Z. Li, Y. Huang, and X. Duan, Nat. Nanotechnol. **8**, 952 (2013).
[8] M. Liu, X. Yin, E. Ulin-Avila, B. Geng, T. Zentgraf, L. Ju, F. Wang, and X. Zhang, Nature (London) **474**, 64 (2011).
[9] M. Furchi, A. Urich, A. Pospischil, G. Lilley, K. Unterrainer, H. Detz, P. Klang, A. M. Andrews, W. Schrenk, G. Strasser, and T. Mueller, Nano Lett. **12**, 2773 (2012).
[10] X. Gan, Y. Gao, K. Fai Mak, X. Yao, R.-J. Shiue, A. van der Zande, M. E. Trusheim, F. Hatami, T. F. Heinz, J. Hone, and D. Englund, Appl. Phys. Lett. **103**, 181119 (2013).
[11] A. Sobhani, A. Lauchner, S. Najmaei, C. Ayala-Orozco, F. Wen, J. Lou, and N. J. Halas, Appl. Phys. Lett. **104**, 031112 (2014).
[12] S. Dai, Q. Ma, T. Andersen, A. S. Mcleod, Z. Fei, M. K. Liu, M. Wagner, K. Watanabe, T. Taniguchi, M. Thiemens, F. Keilmann, P. Jarillo-Herrero, M. M. Fogler, and D. N. Basov, Nat. Commun. **6**, 6963 (2015).
[13] L. Ferrari, C. Wu, D. Lepage, X. Zhang, and Z. Liu, Prog. Quantum Electron. **40**, 1 (2015).
[14] W. Ma, P. Alonso-González, S. Li, A. Y. Nikitin, J. Yuan, J. Martín-Sánchez, J. Taboada-Gutiérrez, I. Amenabar, P. Li, S. Vélez, C. Tollan, Z. Dai, Y. Zhang, S. Sriram, K. Kalantar-Zadeh, S.-T. Lee, R. Hillenbrand, and Q. Bao, Nature (London) **562**, 557 (2018).
[15] D. Rodrigo, O. Limaj, D. Janner, D. Etezadi, F. J. Garcia de Abajo, V. Pruneri, and H. Altug, Science **349**, 165 (2015).
[16] R. Fei, A. Faghaninia, R. Soklaski, J. A. Yan, C. Lo, and L. Yang, Nano Lett. **14**, 6393 (2014).
[17] F. Xia, H. Wang, D. Xiao, M. Dubey, and A. Ramasubramaniam, Nat. Photon. **8**, 899 (2014).
[18] C. Scarlat, K. M. Mok, S. Zhou, M. Vinnichenko, M. Lorenz, M. Grundmann, M. Helm, M. Schubert, and H. Schmidt, Phys. Status Solidi C **7**, 334 (2010).
[19] D. Mounier, M. Kouyaté, P. Thomas, G. Vaudel, P. Ruello, P. Picart, J.-m. Breteau, and V. Gusev, Chin. J. Phys. **49**, 191 (2011).
[20] D. C. Ratchford, C. J. Winta, I. Chatzakis, C. T. Ellis, N. C. Passler, J. Winterstein, P. Dev, I. Razdolski, J. R. Matson, J. R. Nolen, J. G. Tischler, I. Vurgaftman, M. B. Katz, N. Nepal, M. T. Hardy, J. A. Hachtel, J. C. Idrobo, T. L. Reinecke, A. J. Giles, D. S. Katzer, N. D. Bassim, R. M. Stroud, M. Wolf, A. Paarmann, and J. D. Caldwell, ACS Nano **13**, 6730 (2019).
[21] J. Chilwell and I. Hodgkinson, J. Opt. Soc. Am. A **1**, 742 (1984).
[22] O. Deparis, Opt. Lett. **36**, 3960 (2011).
[23] D. W. Berreman, J. Opt. Soc. Am. **62**, 502 (1972).
[24] P. Yeh, J. Opt. Soc. Am. **69**, 742 (1979).
[25] N. C. Passler and A. Paarmann, J. Opt. Soc. Am. B **34**, 2128 (2017).
[26] R. Geick, C. H. Perry, and G. Rupprecht, Phys. Rev. **146**, 543 (1966).
[27] L. Lajaunie, F. Boucher, R. Dessapt, and P. Moreau, Phys. Rev. B **88**, 115141 (2013).
[28] X. Liu, C. R. Ryder, S. A. Wells, and M. C. Hersam, Small Methods **1**, 1700143 (2017).
[29] E. Collett, Am. J. Phys. **39**, 517 (1971).
[30] D. P. Gia Russo and J. H. Harris, J. Opt. Soc. Am. **63**, 138 (1973).
[31] O. Schwelb, J. Opt. Soc. Am. A **3**, 188 (1986).
[32] M. Ciumac, D.-M. Baboiu, and D. Mihalache, Opt. Commun. **111**, 548 (1994).
[33] N. C. Passler and A. Paarmann, J. Opt. Soc. Am. B **36**, 3246 (2019).
[34] N. C. Passler and A. Paarmann, Layer-resolved absorption of light in arbitrarily anisotropic heterostructures (MATLAB files), doi: https://doi.org/10.5281/zenodo.3648041.
[35] M. Jeannin, Layer-resolved absorption of light in arbitrarily anisotropic heterostructures (PYTHON files), doi: https://doi.org/10.5281/zenodo.3724503.
[36] Z.-M. Li, B. T. Sullivan, and R. R. Parsons, Appl. Opt. **27**, 1334 (1988).
[37] P. J. Lin-Chung and S. Teitler, J. Opt. Soc. Am. A **1**, 703 (1984).

[38] W. Xu, L. T. Wood, and T. D. Golding, Phys. Rev. B **61**, 1740 (2000).
[39] A. Yariv and P. Yeh, *Optical Waves in Crystals: Propagation and Control of Laser Radiation*, 1st ed. (John Wiley & Sons, New York, 1984), p. 604.
[40] C. Alberdi, S. Alfonso, M. Berrogui, J. M. Diñeiro, C. Sáenz, and B. Hernández, J. Mod. Opt. **49**, 1553 (2002).
[41] H. Weber, J. Mod. Opt. **61**, 1219 (2014).
[42] G.-H. Jung, S. Yoo, and Q.-H. Park, Nanophotonics **8**, 263 (2019).
[43] D. W. Berreman, Phys. Rev. **130**, 2193 (1963).
[44] S. Vassant, J.-P. Hugonin, F. Marquier, and J.-J. Greffet, Opt. Express **20**, 23971 (2012).
[45] N. C. Passler, I. Razdolski, D. S. Katzer, D. F. Storm, J. D. Caldwell, M. Wolf, and A. Paarmann, ACS Photon. **6**, 1365 (2019).
[46] A. D. Dunkelberger, D. C. Ratchford, A. B. Grafton, V. M. Breslin, E. S. Ryland, D. S. Katzer, K. P. Fears, R. J. Weiblen, I. Vurgaftman, A. J. Giles, C. T. Ellis, J. G. Tischler, J. D. Caldwell, and J. C. Owrutsky, ACS Photon. **7**, 279 (2020).
[47] S. Funke, B. Miller, E. Parzinger, P. Thiesen, A. W. Holleitner, and U. Wurstbauer, J. Phys.: Condens. Matter **28**, 385301 (2016).
[48] J. D. Caldwell, L. Lindsay, V. Giannini, I. Vurgaftman, T. L. Reinecke, S. A. Maier, and O. J. Glembocki, Nanophotonics **4**, 44 (2015).
[49] A. Otto, Z. Phys. A **216**, 398 (1968).
[50] B. Neuner III, D. Korobkin, C. Fietz, D. Carole, G. Ferro, and G. Shvets, Opt. Lett. **34**, 2667 (2009).
[51] N. C. Passler, I. Razdolski, S. Gewinner, W. Schöllkopf, M. Wolf, and A. Paarmann, ACS Photon. **4**, 1048 (2017).
[52] Y. Jia, H. Zhao, Q. Guo, X. Wang, H. Wang, and F. Xia, ACS Photon. **2**, 907 (2015).
[53] S. Dufferwiel, S. Schwarz, F. Withers, A. A. P. Trichet, F. Li, M. Sich, O. Del Pozo-Zamudio, C. Clark, A. Nalitov, D. D. Solnyshkov, G. Malpuech, K. S. Novoselov, J. M. Smith, M. S. Skolnick, D. N. Krizhanovskii, and A. I. Tartakovskii, Nat. Commun. **6**, 8579 (2015).
[54] T. Low, A. Chaves, J. D. Caldwell, A. Kumar, N. X. Fang, P. Avouris, T. F. Heinz, F. Guinea, L. Martin-Moreno, and F. Koppens, Nat. Mater. **16**, 182 (2017).
[55] D. Wintz, K. Chaudhary, K. Wang, L. A. Jauregui, A. Ambrosio, M. Tamagnone, A. Y. Zhu, R. C. Devlin, J. D. Crossno, K. Pistunova, K. Watanabe, T. Taniguchi, P. Kim, and F. Capasso, ACS Photon. **5**, 1196 (2018).
[56] N. C. Passler, A. Heßler, M. Wuttig, T. Taubner, and A. Paarmann, Adv. Opt. Mater. **8**, 1901056 (2020).
[57] Q. Zhang, Z. Zhen, C. Liu, D. Jariwala, and X. Cui, Opt. Express **27**, 18628 (2019).
[58] P. Li, M. Lewin, A. V. Kretinin, J. D. Caldwell, K. S. Novoselov, T. Taniguchi, K. Watanabe, F. Gaussmann, and T. Taubner, Nat. Commun. **6**, 7507 (2015).
[59] S. Dai, M. Tymchenko, Y. Yang, Q. Ma, M. Pita-Vidal, K. Watanabe, T. Taniguchi, P. Jarillo-Herrero, M. M. Fogler, A. Alù, and D. N. Basov, Adv. Mater. **30**, 1706358 (2018).
[60] C. Schneider, M. M. Glazov, T. Korn, S. Höfling, and B. Urbaszek, Nat. Commun. **9**, 2695 (2018).
[61] M. M. Benameur, B. Radisavljevic, J. S. Héron, S. Sahoo, H. Berger, and A. Kis, Nanotechnology **22**, 125706 (2011).
[62] M. A. Vincenti, D. de Ceglia, A. Ciattoni, and M. Scalora, Phys. Rev. A **84**, 063826 (2011).
[63] A. Capretti, Y. Wang, N. Engheta, and L. Dal Negro, Opt. Lett. **40**, 1500 (2015).
[64] B. F. Levine, K. K. Choi, C. G. Bethea, J. Walker, and R. J. Malik, Appl. Phys. Lett. **50**, 1092 (1987).
[65] J. Faist, F. Capasso, D. L. Sivco, C. Sirtori, A. L. Hutchinson, and A. Y. Cho, Science **264**, 553 (1994).
[66] A. Vasanelli, Y. Todorov, and C. Sirtori, C. R. Phys. **17**, 861 (2016).
[67] A. Liu, Phys. Rev. B **55**, 7101 (1997).
[68] D. Dini, R. Köhler, A. Tredicucci, G. Biasiol, and L. Sorba, Phys. Rev. Lett. **90**, 116401 (2003).
[69] C. Ciuti, G. Bastard, and I. Carusotto, Phys. Rev. B **72**, 115303 (2005).
[70] Y. Todorov, A. M. Andrews, R. Colombelli, S. De Liberato, C. Ciuti, P. Klang, G. Strasser, and C. Sirtori, Phys. Rev. Lett. **105**, 196402 (2010).
[71] E. Dupont, H. C. Liu, A. J. Spring Thorpe, W. Lai, and M. Extavour, Phys. Rev. B **68**, 245320 (2003).
[72] P. Jouy, A. Vasanelli, Y. Todorov, L. Sapienza, R. Colombelli, U. Gennser, and C. Sirtori, Phys. Rev. B **82**, 045322 (2010).
[73] P.-B. Vigneron, S. Pirotta, I. Carusotto, N.-L. Tran, G. Biasiol, J.-M. Manceau, A. Bousseksou, and R. Colombelli, Appl. Phys. Lett. **114**, 131104 (2019).
[74] T. Ando, A. B. Fowler, and F. Stern, Rev. Mod. Phys. **54**, 437 (1982).
[75] M. Załużny and C. Nalewajko, Phys. Rev. B **59**, 13043 (1999).
[76] F. Alpeggiani and L. C. Andreani, Phys. Rev. B **90**, 115311 (2014).
[77] G. Pegolotti, A. Vasanelli, Y. Todorov, and C. Sirtori, Phys. Rev. B **90**, 035305 (2014).
[78] J. D. Caldwell and K. S. Novoselov, Nat. Mater. **14**, 364 (2015).
[79] B. Neuner, D. Korobkin, C. Fietz, D. Carole, G. Ferro, and G. Shvets, J. Phys. Chem. C **114**, 7489 (2010).
[80] R. Berte, C. R. Gubbin, V. D. Wheeler, A. J. Giles, V. Giannini, S. A. Maier, S. De Liberato, and J. D. Caldwell, ACS Photon. **5**, 2807 (2018).
[81] T. S. Luk, N. T. Fofang, J. L. Cruz-Campa, I. Frank, and S. Campione, Opt. Express **22**, A1372 (2014).
[82] J. Zeng, X. Wang, J. Sun, A. Pandey, A. N. Cartwright, and N. M. Litchinitser, Sci. Rep. **3**, 2826 (2013).
[83] T. C. H. Liew, A. V. Kavokin, T. Ostatnický, M. Kaliteevski, I. A. Shelykh, and R. A. Abram, Phys. Rev. B **82**, 033302 (2010).
[84] G. X. Ni, L. Wang, M. D. Goldflam, M. Wagner, Z. Fei, A. S. McLeod, M. K. Liu, F. Keilmann, B. Özyilmaz, A. H. Castro Neto, J. Hone, M. M. Fogler, and D. N. Basov, Nat. Photon. **10**, 244 (2016).
[85] H.-L. Liu, C.-C. Shen, S.-H. Su, C.-L. Hsu, M.-Y. Li, and L.-J. Li, Appl. Phys. Lett. **105**, 201905 (2014).
[86] Y. Li, A. Chernikov, X. Zhang, A. Rigosi, H. M. Hill, A. M. van der Zande, D. A. Chenet, E.-M. Shih, J. Hone, and T. F. Heinz, Phys. Rev. B **90**, 205422 (2014).
[87] M. A. Huber, F. Mooshammer, M. Plankl, L. Viti, F. Sandner, L. Z. Kastner, T. Frank, J. Fabian, M. S. Vitiello, T. L. Cocker, and R. Huber, Nat. Nanotechnol. **12**, 207 (2017).

CHAPTER 5

Perspectives

In recent years, the growing research interest in polaritons in nanostructures has triggered numerous advances in the field of nanophotonics, including single-molecule sensing with SERS [7], plasmon-driven ultra-short electron point sources [91], highly directional thermal emission [121], or femtosecond optical polarization switching with an ENZ-based perfect absorber [122]. Within these developments, phonon polaritons have emerged as a low-loss, versatile platform for nanophotonic applications in the IR [14], enabling novel devices such as hyper-lenses based on hyperbolic materials [16, 68], phonon polariton-enhanced electroluminescence for efficient electronic cooling [123], and electrically pumped phonon-polariton lasers [124].

As has been demonstrated in the previous chapter, the investigations performed in this thesis form part of these recent prosperous advances in nanophotonics, contributing to the development of modern devices based on phonon polaritons in heterostructures of arbitrarily anisotropic materials. Based on the presented advances, this chapter discusses the perspectives of the implemented techniques by outlining several possible pathways for future developments in polariton-driven nanophotonics.

Hyperbolic materials have recently shifted into the spotlight of scientific interest. These materials feature a hyperbolic isofrequency surface, enabling a huge photonic density of states with arbitrarily large in-plane momenta [125]. These unusual properties lead to a variety of unique phenomena, such as sub-wavelength imaging [16, 46, 47] or slow light [126–128]. However, natural hyperbolic materials such as SiO_2 or hBN only feature hyperbolicity in narrow spectral windows that are fixed by the intrinsic material parameters [129]. Alternatively, hyperbolic metamaterials (HMMs) composed of alternating ultra-thin layers of different materials offer a platform for engineering materials with a user-defined hyperbolic optical response [130], such as the XHs discussed in section 2.2.2 and in publication [**IX**].

On a different note, doped semiconductors such as cadmium oxide (CdO) featuring plasmon polaritons have recently been discussed in parallel with polar crystals supporting phonon polaritons. Doped CdO thin-films support low-loss plasmonic modes in a broad spectral range in the IR, providing a complementary polaritonic excitation at phonon polariton frequencies. In particular, Runnerstrom *et al.* have demonstrated the strong coupling of a SPP to a plasmonic ENZ mode in a doped CdO thin film [131], complementary to the strong coupling of a bulk SPhP to a thin-film ENZ phonon polariton as discussed in the publication reprinted on page 65 [**V**]. By strongly coupling to an ENZ mode, the resulting CdO plasmon polaritons combine long propagation distances with high spatial confinement, while featuring broad frequency tunability by controlling the electron concentration via photo-injection.

Doped semiconductors such as CdO also offer new routes in the field of HMMs. Composed of alternating doped and undoped semiconductors, such semiconductor HMMs are, complementary to XHs,

promising candiates for hyperbolic nanophotonic applications [62–64]. These metallic/dielectric multilayer HMMs support so-called volume plasmon polaritons (VPPs), arising as a collective excitation composed of coupled SPPs supported in each metallic thin-film [132–136]. Very recently, VPPs in doped semiconductor HMMs have been shown to feature high quality factors across a large frequency range in the IR [63], providing a potential platform for low-loss, IR optoelectronic devices.

The excitation of VPPs in doped semiconductor HMMs is typically realized via grating coupling [63, 64]. So far, however, these systems have only been investigated in the linear optical regime. Experiments investigating the non-linear optical response are currently in the planning stage and will be performed in the near future, providing new insights for the thorough understanding of VPPs in HMMs and their potential for nanophotonic applications.

While HMMs offer more structural flexibility than natural hyperbolic materials, the extraordinary axis in layered HMMs lies by design along the surface normal, while in-plane anisotropy cannot be achieved. Biaxial single crystals, on the other hand, feature three distinct dielectric permittivities along the principal crystal axes, and thus can provide in-plane anisotropy with hyperbolic frequency bands for any crystal cut. An example of such a natural in-plane hyperbolic material is molybdenum trioxide (MoO_3). This material supports azimuth-dependent, hyperbolic phonon polaritons with novel polaritonic properties, as has been highlighted in the publication reprinted on page 97 [**VII**].

One step beyond biaxial crystals, another intriguing material class are monoclinic crystals, which are currently on the verge of attracting broad attention in the nanophotonics community. In search of new materials for next-generation semiconductor power devices, β-gallium oxide (β-Ga_2O_3) has been discovered as a promising candidate, enabling applications as transparent electrodes [137] and high-performance power devices [138]. Only recently, the complicated dielectric permittivity tensor of monoclinic β-Ga_2O_3 has been described by Schubert *et al.*, containing non-zero off-diagonal elements that do not vanish under orientation along the crystal axes [139]. In a subsequent study, coupling between the various LO phonon modes and free charge carriers in doped β-Ga_2O_3 was reported, forming so-called longitudinal phonon plasmon coupled modes with non-trivial directionality [140].

The phonon polariton modes supported by a monoclinic crystal such as β-Ga_2O_3, however, have not yet been investigated[1]. The constructed Otto geometry setup enables such a study, and the experiments on β-Ga_2O_3 are already programmed for the near future. Additionally, in order to access the dependence of the phonon polariton modes on azimuthal rotation, the Otto geometry setup has been equipped with the possibility to rotate the sample while being mounted. Considering the rich optical response from IR spectroscopic ellipsometry [140], the planned pilot investigations on phonon polaritons in β-Ga_2O_3 bear great potential for the development of future nanophotonic devices based on monoclinic crystals, such as non-trivial azimuth dependency of the polariton dispersion, or direction-dependent coupling to polaritons in adjacent media.

As has been demonstrated in the research conducted in this thesis, employing the developed transfer matrix formalism for the theoretical computation of the linear optical response, the electric field distribution, and the layer-resolved absorption and transmittance enables thorough insight into the optical properties of the experimentally investigated sample. The above mentioned experimental perspectives employ layered systems of anisotropic materials, and therefore can be analogously corroborated by theoretical calculations. By scanning various parameters such as film thicknesses,

[1] to the best of my knowledge

incident angle, azimuthal angle, and frequency, the optical response of the system can be systematically analyzed, allowing to optimize the sample structure for the experiments, as well as predict the observable polariton modes and the associated nanophotonic phenomena.

In general, the transfer matrix formalism allows to study all dielectric resonances – evanescent or radiative – ranging from electronic intersubband-transitions and IR-active phonons, over excitons and plasma resonances, up to interband transitions and core level excitations, covering any multilayer system of materials with arbitrarily anisotropic permittivity. Therefore, going one step beyond corroborating experimental data, the transfer matrix formalism resembles the ideal theoretical tool for predictive studies of yet undiscovered nanophotonic materials and devices, as has been exemplarily demonstrated in the most recent publication (reprinted on page 97 [**VII**]).

Another intriguing field of research explores surface magnon polaritons (SMPs) in anisotropic antiferromagnets, where applying an external magnetic field provides straight-forward, active control over the supported magnon polaritons [141, 142]. Furthermore, hybrid plasmon-magnon polaritons in graphene-antiferromagnet heterostructures have been demonstrated, opening new possibilities for nanophotonic applications by combining the realms of photons, magnons, and plasmons [143]. The optical response of magnetic resonances is dictated by the magnetic permeability $\bar{\mu}$, and for anisotropic antiferromagnets at terahertz frequencies, $\bar{\mu}$ is a 3×3 tensor with non-zero off-diagonal elements (analogous to the dielectric permittivity tensor, see Eq. 2.1.2). However, the transfer matrix formalism as it is derived in this work only handles materials with isotropic permeability μ. Therefore, incorporating the possibility to include media of fully anisotropic permeability would considerably amplify the application spectrum of the formalism, allowing to investigate SMPs in antiferromagnets as well as their interaction with SPPs and SPhPs in yet unexplored anisotropic heterostructures of magnetic, polar dielectric, and plasmonic material layers.

In the last three years in the course of this thesis, the combination of the Otto geometry and the transfer matrix formalism has proven fruitful for the investigation of polaritons in anisotropic layered heterostructures. As the above selection of perspectives demonstrates, this developed experimental-theoretical tool box bears great potential for future investigations in modern polariton-based nanophotonics that is far from being exhausted.

CHAPTER 6

Conclusion

This thesis provides an extensive, detailed experimental and theoretical study of phonon polaritons in layered heterostructures of arbitrarily anisotropic media. The findings of various new fundamental phenomena of phonon polaritons as well as the developed versatile experimental and theoretical tools constitute a significant contribution to the scientific field, advancing the development of novel polariton-based nanophotonic technologies.

As concept, this work promotes multilayer systems of various different materials as a platform for designable polaritonic materials with user-defined characteristics and functionalities. This concept is demonstrated on the basis of various heterostructures composed of SiC, AlN, GaN, GST, MoO_3, molybdenum disulfide (MoS_2), Au, and hBN, revealing numerous novel phenomena such as propagating ENZ modes, strongly coupled phonon polaritons, polariton-like s-polarized waveguide modes, and azimuth-dependent hyperbolic phonon polaritons.

Experimentally, these systems were investigated by means of reflectance and SHG spectroscopy in the home-built Otto geometry setup, using the FHI FEL as excitation source. The findings include the first SHG measurements of propagating SPhPs on a bulk SiC crystal, the first experimental proof of the immense optical field enhancement of the Berreman mode in ultra-thin AlN films, and the demonstration of the exceptional tuning capabilities of polaritons in a switchable GST/SiC heterostructure.

On the theoretical side, this work has developed a 4×4 transfer matrix formalism for the description of light-matter interaction in multilayer systems of arbitrarily anisotropic media, producing a versatile, robust framework that is implemented in an open-access computer program. The capabilities of the formalism are demonstrated by the accurate description of the experimental data as well as by various predictive theoretical studies, promoting yet unexplored nanophotonic device structures with novel functionalities such as azimuth-dependent hyperbolic polariton tunneling or layer-selective exciton absorption.

As a summary, this work constitutes a comprehensive study of the physics of phonon polaritons excited with light in polar dielectric heterostructures. By implementing a new experimental and theoretical methodology, novel phenomena of phonon polaritons in heterostructures and their unique interaction nature were discovered, boosting the development of polariton-based technologies. Furthermore, this thesis lays out perspectives on how to use the developed experimental and theoretical methods for a number of future studies, bearing great potential to further advance the field of infrared nanophotonics.

List of Publications

[I] N. C. Passler, I. Razdolski, S. Gewinner, W. Schöllkopf, M. Wolf, and A. Paarmann, "Second-Harmonic Generation from Critically Coupled Surface Phonon Polaritons", ACS Photonics **4**, 1048–1053 (2017).

[II] N. C. Passler and A. Paarmann, "Generalized 4 x 4 matrix formalism for light propagation in anisotropic stratified media: study of surface phonon polaritons in polar dielectric heterostructures", Journal of the Optical Society of America B **34**, 2128 (2017).

[III] N. C. Passler and A. Paarmann, "Generalized 4 x 4 matrix formalism for light propagation in anisotropic stratified media: study of surface phonon polaritons in polar dielectric heterostructures: erratum", Journal of the Optical Society of America B **36**, 3246 (2019).

[IV] N. C. Passler, C. R. Gubbin, T. G. Folland, I. Razdolski, D. S. Katzer, D. F. Storm, M. Wolf, S. De Liberato, J. D. Caldwell, and A. Paarmann, "Strong Coupling of Epsilon-Near-Zero Phonon Polaritons in Polar Dielectric Heterostructures", Nano Letters **18**, 4285–4292 (2018).

[V] N. C. Passler, I. Razdolski, D. S. Katzer, D. F. Storm, J. D. Caldwell, M. Wolf, and A. Paarmann, "Second Harmonic Generation from Phononic Epsilon-Near-Zero Berreman Modes in Ultrathin Polar Crystal Films", ACS Photonics **6**, 1365–1371 (2019).

[VI] N. C. Passler, A. Heßler, M. Wuttig, T. Taubner, and A. Paarmann, "Surface Polariton-Like s-Polarized Waveguide Modes in Switchable Dielectric Thin Films on Polar Crystals", Advanced Optical Materials **8**, 1901056 (2020).

[VII] N. C. Passler, M. Jeannin, and A. Paarmann, "Layer-resolved absorption of light in arbitrarily anisotropic heterostructures", Physical Review B **101**, 165425 (2020).

[VIII] I. Razdolski, N. C. Passler, C. R. Gubbin, C. J. Winta, R. Cernansky, F. Martini, A. Politi, S. A. Maier, M. Wolf, A. Paarmann, and S. De Liberato, "Second harmonic generation from strongly coupled localized and propagating phonon-polariton modes", Physical Review B **98**, 125425 (2018).

[IX] D. C. Ratchford, C. J. Winta, I. Chatzakis, C. T. Ellis, N. C. Passler, J. Winterstein, P. Dev, I. Razdolski, J. R. Matson, J. R. Nolen, J. G. Tischler, I. Vurgaftman, M. B. Katz, N. Nepal, M. T. Hardy, J. A. Hachtel, J. C. Idrobo, T. L. Reinecke, A. J. Giles, D. S. Katzer, N. D. Bassim, R. M. Stroud, M. Wolf, A. Paarmann, and J. D. Caldwell, "Controlling the Infrared Dielectric Function through Atomic-Scale Heterostructures", ACS Nano **13**, 6730–6741 (2019).

[X] K. Pufahl, N. C. Passler, N. B. Grosse, M. Wolf, U. Woggon, and A. Paarmann, "Controlling nanoscale air-gaps for critically coupled surface polaritons by means of non-invasive white-light interferometry", Applied Physics Letters **113**, 161103 (2018).

Bibliography

[1] E. Abbe, "Beiträge zur Theorie des Mikroskops und der mikroskopischen Wahrnehmung", Archiv für Mikroskopische Anatomie **9**, 413–468 (1873).

[2] R. F. Oulton, V. J. Sorger, D. A. Genov, D. F. P. Pile, and X. Zhang, "A hybrid plasmonic waveguide for subwavelength confinement and long-range propagation", Nature Photonics **2**, 496–500 (2008).

[3] J. D. Caldwell, O. J. Glembocki, Y. Francescato, N. Sharac, V. Giannini, F. J. Bezares, J. P. Long, J. C. Owrutsky, I. Vurgaftman, J. G. Tischler, V. D. Wheeler, N. D. Bassim, L. M. Shirey, R. Kasica, and S. a. Maier, "Low-Loss, Extreme Subdiffraction Photon Confinement via Silicon Carbide Localized Surface Phonon Polariton Resonators", Nano Letters **13**, 3690–3697 (2013).

[4] P. Li, X. Yang, T. W. W. Maß, J. Hanss, M. Lewin, A.-K. U. Michel, M. Wuttig, and T. Taubner, "Reversible optical switching of highly confined phonon–polaritons with an ultrathin phase-change material", Nature Materials **15**, 870–875 (2016).

[5] T. S. Luk, N. T. Fofang, J. L. Cruz-Campa, I. Frank, and S. Campione, "Surface plasmon polariton enhanced ultrathin nano-structured CdTe solar cell", Optics Express **22**, A1372 (2014).

[6] M. Ren, B. Jia, J.-Y. Ou, E. Plum, J. Zhang, K. F. MacDonald, A. E. Nikolaenko, J. Xu, M. Gu, and N. I. Zheludev, "Nanostructured Plasmonic Medium for Terahertz Bandwidth All-Optical Switching", Advanced Materials **23**, 5540–5544 (2011).

[7] K. Kneipp, Y. Wang, H. Kneipp, L. T. Perelman, I. Itzkan, R. R. Dasari, and M. S. Feld, "Single Molecule Detection Using Surface-Enhanced Raman Scattering (SERS)", Physical Review Letters **78**, 1667–1670 (1997).

[8] S. Assefa, F. Xia, and Y. A. Vlasov, "Reinventing germanium avalanche photodetector for nanophotonic on-chip optical interconnects", Nature **464**, 80–84 (2010).

[9] T. P. H. Sidiropoulos, R. Röder, S. Geburt, O. Hess, S. A. Maier, C. Ronning, and R. F. Oulton, "Ultrafast plasmonic nanowire lasers near the surface plasmon frequency", Nature Physics **10**, 870–876 (2014).

[10] M. Fleischmann, P. Hendra, and A. McQuillan, "Raman spectra of pyridine adsorbed at a silver electrode", Chemical Physics Letters **26**, 163–166 (1974).

[11] J.-F. Li, C.-Y. Li, and R. F. Aroca, "Plasmon-enhanced fluorescence spectroscopy", Chemical Society Reviews **46**, 3962–3979 (2017).

[12] D. E. Chang, A. S. Sørensen, E. A. Demler, and M. D. Lukin, "A single-photon transistor using nanoscale surface plasmons", Nature Physics **3**, 807–812 (2007).

[13] D. J. Bergman and M. I. Stockman, "Surface Plasmon Amplification by Stimulated Emission of Radiation: Quantum Generation of Coherent Surface Plasmons in Nanosystems", Physical Review Letters **90**, 027402 (2003).

[14] J. D. Caldwell, L. Lindsay, V. Giannini, I. Vurgaftman, T. L. Reinecke, S. A. Maier, and O. J. Glembocki, "Low-loss, infrared and terahertz nanophotonics using surface phonon polaritons", Nanophotonics **4**, 44–68 (2015).

[15] Z. Jacob, "Hyperbolic phonon–polaritons", Nature Materials **13**, 1081–1083 (2014).

[16] P. Li, M. Lewin, A. V. Kretinin, J. D. Caldwell, K. S. Novoselov, T. Taniguchi, K. Watanabe, F. Gaussmann, and T. Taubner, "Hyperbolic phonon-polaritons in boron nitride for near-field optical imaging and focusing", Nature Communications **6**, 7507 (2015).

[17] A. Paarmann, I. Razdolski, A. Melnikov, S. Gewinner, W. Schöllkopf, and M. Wolf, "Second harmonic generation spectroscopy in the Reststrahl band of SiC using an infrared free-electron laser", Applied Physics Letters **107**, 10.1063/1.4929358 (2015).

[18] N. C. Passler and A. Paarmann, *Generalized 4x4 Matrix algorithm for light propagation in anisotropic stratified media (Matlab files)*, *https://doi.org/10.5281/zenodo.601496*, 2017.

[19] N. C. Passler and A. Paarmann, *Layer-Resolved Absorption of Light in Arbitrarily Anisotropic Heterostructures (Matlab files)*, *https://doi.org/10.5281/zenodo.3648040*, 2020.

[20] K. B. Tolpygo, "Physical Properties of a Rock Salt Lattice Made Up of Deformable Ions", Ukranian Journal of Physics **20**, 497–509 (1950).

[21] S. I. Pekar, "Theory of electromagnetic waves in a crystal with excitons", Journal of Physics and Chemistry of Solids **5**, 11–22 (1958).

[22] G. Pegolotti, A. Vasanelli, Y. Todorov, and C. Sirtori, "Quantum model of coupled intersubband plasmons", Physical Review B **90**, 35305 (2014).

[23] A. Otto, "Excitation of nonradiative surface plasma waves in silver by the method of frustrated total reflection", Zeitschrift für Physik A Hadrons and nuclei **216**, 398–410 (1968).

[24] Ö. O. Soykal and M. E. Flatté, "Strong Field Interactions between a Nanomagnet and a Photonic Cavity", Physical Review Letters **104**, 77202 (2010).

[25] D. N. Basov, M. M. Fogler, and F. J. Garcia de Abajo, "Polaritons in van der Waals materials", Science **354**, 195 (2016).

[26] W. Nolting, *THEORETICAL PHYSICS 3* (Springer International Publishing, Cham, 2016), p. 659.

[27] M. Fox, "QUANTUM OPTICS - AN INTRODUCTION", in (Oxford University Press, Oxford, 2006).

[28] S. I. Bozhevolnyi, L. Martin-Moreno, and F. Garcia-Vidal, *QUANTUM PLASMONICS*, Vol. 185, Springer Series in Solid-State Sciences (Springer International Publishing, Cham, 2017).

[29] H. G. Tompkins and E. A. Irene, *HANDBOOK OF ELLIPSOMETRY*, Vol. 15 (Springer, Heidelberg, Feb. 2005), pp. 1–870.

[30] P. Drude, "Zur Elektronentheorie der Metalle", Annalen der Physik **306**, 566–613 (1900).

[31] H. Ibach and H. Lüth, *FESTKÖRPERPHYSIK*, 7th ed., Springer-Lehrbuch (Springer Berlin Heidelberg, Berlin, Heidelberg, 2009).

[32] M. Waldman and R. G. Gordon, "Generalized electron gas–Drude model theory of intermolecular forces", The Journal of Chemical Physics **71**, 1340–1352 (1979).

[33] Chin-Yi Tsai, Chin-Yao Tsai, Chih-Hsiung Chen, Tien-Li Sung, Tsu-Yin Wu, and Fang-Ping Shih, "Theoretical model for intravalley and intervalley free-carrier absorption in semiconductor lasers: beyond the classical Drude model", IEEE Journal of Quantum Electronics **34**, 552–559 (1998).

[34] A. Vial, A.-S. Grimault, D. Macías, D. Barchiesi, and M. L. de la Chapelle, "Improved analytical fit of gold dispersion: Application to the modeling of extinction spectra with a finite-difference time-domain method", Physical Review B **71**, 85416 (2005).

[35] E. M. Chudnovsky, "Theory of Spin Hall Effect: Extension of the Drude Model", Physical Review Letters **99**, 206601 (2007).

[36]N. Sharma, A. Joy, A. K. Mishra, and R. K. Verma, "Fuchs Sondheimer–Drude Lorentz model and Drude model in the study of SPR based optical sensors: A theoretical study", Optics Communications **357**, 120–126 (2015).

[37]W. S. M. Werner, K. Glantschnig, and C. Ambrosch-Draxl, "Optical Constants and Inelastic Electron-Scattering Data for 17 Elemental Metals", Journal of Physical and Chemical Reference Data **38**, 1013–1092 (2009).

[38]M. van Exter and D. Grischkowsky, "Carrier dynamics of electrons and holes in moderately doped silicon", Physical Review B **41**, 12140–12149 (1990).

[39]P. J. Burke, I. B. Spielman, J. P. Eisenstein, L. N. Pfeiffer, and K. W. West, "High frequency conductivity of the high-mobility two-dimensional electron gas", Applied Physics Letters **76**, 745–747 (2000).

[40]M. Scheffler, M. Dressel, M. Jourdan, and H. Adrian, "Extremely slow Drude relaxation of correlated electrons", Nature **438**, 1135–1137 (2005).

[41]P. Y. Yu and M. Cardona, *FUNDAMENTALS OF SEMICONDUCTORS: PHYSICS AND MATERIALS PROPERTIES*, 4th (Springer, Heidelberg, 2010).

[42]N. C. Passler, "Excitation of Surface Phonon Polaritons with an Infrared Free Electron Laser", (2016).

[43]F. Engelbrecht and R. Helbig, "Effect of crystal anisotropy on the infrared reflectivity of 6H-SiC", Physical Review B **48**, 15698–15707 (1993).

[44]V. Y. Davydov, Y. E. Kitaev, I. N. Goncharuk, A. N. Smirnov, J. Graul, O. Semchinova, D. Uffmann, M. B. Smirnov, A. P. Mirgorodsky, and R. A. Evarestov, "Phonon dispersion and Raman scattering in hexagonal GaN and AlN", Physical Review B **58**, 12899–12907 (1998).

[45]A. S. Barker, "Direct Optical Coupling to Surface Excitations", Physical Review Letters **28**, 892–895 (1972).

[46]T. Taubner, D. Korobkin, Y. Urzhumov, G. Shvets, and R. Hillenbrand, "Near-Field Microscopy Through a SiC Superlens", Science **313**, 1595 (2006).

[47]S. Dai, Q. Ma, T. Andersen, A. S. McLeod, Z. Fei, M. K. Liu, M. Wagner, K. Watanabe, T. Taniguchi, M. Thiemens, F. Keilmann, P. Jarillo-Herrero, M. M. Fogler, and D. N. Basov, "Subdiffractional focusing and guiding of polaritonic rays in a natural hyperbolic material", Nature Communications **6**, 1–7 (2015).

[48]M. Autore, P. Li, I. Dolado, F. J. Alfaro-Mozaz, R. Esteban, A. Atxabal, F. Casanova, L. E. Hueso, P. Alonso-González, J. Aizpurua, A. Y. Nikitin, S. Vélez, and R. Hillenbrand, "Boron nitride nanoresonators for phonon-enhanced molecular vibrational spectroscopy at the strong coupling limit", Light: Science and Applications **7**, 17172 (2018).

[49]C. Argyropoulos, P.-Y. Chen, G. D'Aguanno, N. Engheta, and A. Alù, "Boosting optical nonlinearities in ε-near-zero plasmonic channels", Physical Review B **85**, 045129 (2012).

[50]H. Suchowski, K. O'Brien, Z. J. Wong, A. Salandrino, X. Yin, and X. Zhang, "Phase Mismatch-Free Nonlinear Propagation in Optical Zero-Index Materials", Science **342**, 1223–1226 (2013).

[51]N. Mattiucci, M. J. Bloemer, and G. D'Aguanno, "Phase-matched second harmonic generation at the Dirac point of a 2-D photonic crystal", Optics Express **22**, 6381 (2014).

[52]S. Kim, J. Jin, Y.-J. Kim, I.-Y. Park, Y. Kim, and S.-W. Kim, "High-harmonic generation by resonant plasmon field enhancement", Nature **453**, 757–760 (2008).

[53]C. Ciraci, R. T. Hill, J. J. Mock, Y. Urzhumov, A. I. Fernandez-Dominguez, S. A. Maier, J. B. Pendry, A. Chilkoti, and D. R. Smith, "Probing the Ultimate Limits of Plasmonic Enhancement", Science **337**, 1072–1074 (2012).

[54]D. Ji, A. Cheney, N. Zhang, H. Song, J. Gao, X. Zeng, H. Hu, S. Jiang, Z. Yu, and Q. Gan, "Efficient Mid-Infrared Light Confinement within Sub-5-nm Gaps for Extreme Field Enhancement", Advanced Optical Materials **5**, 1700223 (2017).

[55]J. J. Burke, G. I. Stegeman, and T. Tamir, "Surface-polariton-like waves guided by thin, lossy metal films", Physical Review B **33**, 5186–5201 (1986).

[56]H. Raether, *SURFACE PLASMONS ON SMOOTH AND ROUGH SURFACES AND ON GRATINGS*, Vol. 111, Springer Tracts in Modern Physics (Springer Berlin Heidelberg, Berlin, Heidelberg, 1988).

[57]S. Campione, I. Brener, and F. Marquier, "Theory of epsilon-near-zero modes in ultrathin films", Physical Review B **91**, 121408 (2015).

[58]I. Balin, N. Dahan, V. Kleiner, and E. Hasman, "Slow surface phonon polaritons for sensing in the midinfrared spectrum", Applied Physics Letters **94**, 111112 (2009).

[59]C. H. Gan and P. Lalanne, "Well-confined surface plasmon polaritons for sensing applications in the near-infrared", Optics Letters **35**, 610 (2010).

[60]S. E. Swiontek, D. P. Pulsifer, and A. Lakhtakia, "Optical sensing of analytes in aqueous solutions with a multiple surface-plasmon-polariton-wave platform", Scientific Reports **3**, 1409 (2013).

[61]P. K. Tien and R. Ulrich, "Theory of Prism–Film Coupler and Thin-Film Light Guides", Journal of the Optical Society of America **60**, 1325 (1970).

[62]D. Wei, C. Harris, and S. Law, "Volume plasmon polaritons in semiconductor hyperbolic metamaterials", Optical Materials Express **7**, 2672 (2017).

[63]P. Sohr, D. Wei, S. Tomasulo, M. K. Yakes, and S. Law, "Simultaneous Large Mode Index and High Quality Factor in Infrared Hyperbolic Metamaterials", ACS Photonics **5**, 4003–4008 (2018).

[64]P. Sohr, C. I. Ip, and S. Law, "Far-field thermal emission from a semiconductor hyperbolic metamaterial", Optics Letters **44**, 1138 (2019).

[65]J. D. Caldwell, I. Vurgaftman, J. G. Tischler, O. J. Glembocki, J. C. Owrutsky, and T. L. Reinecke, "Atomic-scale photonic hybrids for mid-infrared and terahertz nanophotonics", Nature Nanotechnology **11**, 9–15 (2016).

[66]S. Dai, M. Tymchenko, Y. Yang, Q. Ma, M. Pita-Vidal, K. Watanabe, T. Taniguchi, P. Jarillo-Herrero, M. M. Fogler, A. Alù, and D. N. Basov, "Manipulation and Steering of Hyperbolic Surface Polaritons in Hexagonal Boron Nitride", Advanced Materials **30**, 1706358 (2018).

[67]A. J. Giles, S. Dai, I. Vurgaftman, T. Hoffman, S. Liu, L. Lindsay, C. T. Ellis, N. Assefa, I. Chatzakis, T. L. Reinecke, J. G. Tischler, M. M. Fogler, J. H. Edgar, D. N. Basov, and J. D. Caldwell, "Ultralow-loss polaritons in isotopically pure boron nitride", Nature Materials **17**, 134–139 (2018).

[68]S. Dai, Z. Fei, Q. Ma, A. S. Rodin, M. Wagner, A. S. McLeod, M. K. Liu, W. Gannett, W. Regan, K. Watanabe, T. Taniguchi, M. Thiemens, G. Dominguez, A. H. C. Neto, A. Zettl, F. Keilmann, P. Jarillo-Herrero, M. M. Fogler, and D. N. Basov, "Tunable Phonon Polaritons in Atomically Thin van der Waals Crystals of Boron Nitride", Science **343**, 1125–1129 (2014).

[69]Y. R. Shen, *THE PRINCIPLES OF NONLINEAR OPTICS* (Wiley-Interscience, California, 2003).

[70]A. Paarmann, I. Razdolski, S. Gewinner, W. Schöllkopf, and M. Wolf, "Effects of crystal anisotropy on optical phonon resonances in midinfrared second harmonic response of SiC", Physical Review B **94**, 134312 (2016).

[71]J. Bluet, K. Chourou, M. Anikin, and R. Madar, "Weak phonon modes observation using infrared reflectivity for 4H, 6H and 15R polytypes", Materials Science and Engineering: B **61-62**, 212–216 (1999).

[72]Y. V. G. S. Murti and C. Vijayan, *ESSENTIALS OF NONLINEAR OPTICS* (Wiley, Chichester, 2014).

[73]T. F. Heinz, C. K. Chen, D. Ricard, and Y. R. Shen, "Spectroscopy of Molecular Monolayers by Resonant Second-Harmonic Generation", Physical Review Letters **48**, 478–481 (1982).

[74]Y. R. Shen, "Surface Second Harmonic Generation: A New Technique for Surface Studies", Annual Review of Materials Science **16**, 69–86 (1986).

[75]Y. Shen, "Optical Second Harmonic Generation At Interfaces", Annual Review of Physical Chemistry **40**, 327–350 (1989).

[76]V. Pellegrini, R. Colombelli, I. Carusotto, F. Beltram, S. Rubini, R. Lantier, A. Franciosi, C. Vinegoni, and L. Pavesi, "Resonant second harmonic generation in ZnSe bulk microcavity", Applied Physics Letters **74**, 1945–1947 (1999).

[77]S. N. Rashkeev, S. Limpijumnong, and W. R. L. Lambrecht, "Second-harmonic generation and birefringence of some ternary pnictide semiconductors", Physical Review B **59**, 2737–2748 (1999).

[78]H.-t. Bian, R.-r. Feng, Y.-y. Xu, Y. Guo, and H.-f. Wang, "Increased interfacial thickness of the NaF, NaCl and NaBr salt aqueous solutions probed with non-resonant surface second harmonic generation (SHG)", Physical Chemistry Chemical Physics **10**, 4920 (2008).

[79]H. Hoshi, T. Yamada, K. Ishikawa, H. Takezoe, and A. Fukuda, "Second-harmonic generation in centrosymmetric molecular films: Analysis under anisotropic conditions", Physical Review B **52**, 12355–12365 (1995).

[80]R. Kiessling, Y. Tong, A. J. Giles, S. Gewinner, W. Schöllkopf, J. D. Caldwell, M. Wolf, and A. Paarmann, "Surface Phonon Polariton Resonance Imaging Using Long-Wave Infrared-Visible Sum-Frequency Generation Microscopy", ACS Photonics **6**, 3017–3023 (2019).

[81]S. Nie and S. R. Emory, "Probing Single Molecules and Single Nanoparticles by Surface-Enhanced Raman Scattering", Science **275**, 1102–1106 (1997).

[82]H. Lu, X. Liu, L. Wang, Y. Gong, and D. Mao, "Ultrafast all-optical switching in nanoplasmonic waveguide with Kerr nonlinear resonator", Optics Express **19**, 2910 (2011).

[83]S. Sederberg and A. Y. Elezzabi, "Coherent Visible-Light-Generation Enhancement in Silicon-Based Nanoplasmonic Waveguides via Third-Harmonic Conversion", Physical Review Letters **114**, 227401 (2015).

[84]T. Shibanuma, G. Grinblat, P. Albella, and S. A. Maier, "Efficient Third Harmonic Generation from Metal-Dielectric Hybrid Nanoantennas", Nano Letters **17**, 2647–2651 (2017).

[85]Y. Chen, Y. Francescato, J. D. Caldwell, V. Giannini, T. W. W. Maß, O. J. Glembocki, F. J. Bezares, T. Taubner, R. Kasica, M. Hong, and S. A. Maier, "Spectral Tuning of Localized Surface Phonon Polariton Resonators for Low-Loss Mid-IR Applications", ACS Photonics **1**, 718–724 (2014).

[86]I. Razdolski, Y. Chen, A. J. Giles, S. Gewinner, W. Schöllkopf, M. Hong, M. Wolf, V. Giannini, J. D. Caldwell, S. A. Maier, and A. Paarmann, "Resonant Enhancement of Second-Harmonic Generation in the Mid-Infrared Using Localized Surface Phonon Polaritons in Subdiffractional Nanostructures", Nano Letters **16**, 6954–6959 (2016).

[87]C. R. Gubbin, F. Martini, A. Politi, S. A. Maier, and S. De Liberato, "Strong and Coherent Coupling between Localized and Propagating Phonon Polaritons", Physical Review Letters **116**, 246402 (2016).

[88]D. Beaglehole, "Coherent and incoherent radiation from optically excited surface plasmons on a metal grating", Physical Review Letters **22**, 708–711 (1969).

[89]J. C. Quail and H. J. Simon, "Second-harmonic generation from a silver grating with surface plasmons", Journal of the Optical Society of America B **5**, 325 (1988).

[90]C. Ropers, C. C. Neacsu, T. Elsaesser, M. Albrecht, M. B. Raschke, and C. Lienau, "Grating-Coupling of Surface Plasmons onto Metallic Tips: A Nanoconfined Light Source", Nano Letters **7**, 2784–2788 (2007).

[91] M. Müller, V. Kravtsov, A. Paarmann, M. B. Raschke, and R. Ernstorfer, "Nanofocused Plasmon-Driven Sub-10 fs Electron Point Source", ACS Photonics **3**, 611–619 (2016).

[92] A. K. Hafeli, E. Rephaeli, S. Fan, D. G. Cahill, and T. E. Tiwald, "Temperature dependence of surface phonon polaritons from a quartz grating", Journal of Applied Physics **110**, 10.1063/1.3624603 (2011).

[93] V. M. Agranovich and A. Maradudin, *SURFACE POLARITONS* (North-Holland Publishing Company, Amsterdam, 1982).

[94] E. Kretschmann, "Die Bestimmung optischer Konstanten von Metallen durch Anregung von Oberflächenplasmaschwingungen", Zeitschrift für Physik **241**, 313–324 (1971).

[95] A. Hatta, Y. Chiba, and W. Suëtaka, "Infrared absorption study of adsorbed species at metal/water interface by use of the Kretschmann configuration", Surface Science **158**, 616–623 (1985).

[96] Y. Suzuki, M. Osawa, A. Hatta, and W. Suëtaka, "Mechanism of absorption enhancement in infrared ATR spectra observed in the Kretschmann configuration", Applied Surface Science **33-34**, 875–881 (1988).

[97] R. Naraoka, H. Okawa, K. Hashimoto, and K. Kajikawa, "Surface plasmon resonance enhanced second-harmonic generation in Kretschmann configuration", Optics Communications **248**, 249–256 (2005).

[98] I. Razdolski, D. Makarov, O. G. Schmidt, A. Kirilyuk, T. Rasing, and V. V. Temnov, "Nonlinear Surface Magnetoplasmonics in Kretschmann Multilayers", ACS Photonics **3**, 179–183 (2016).

[99] F. Keilmann and R. Hillenbrand, "Near-field microscopy by elastic light scattering from a tip", Philosophical Transactions of the Royal Society of London. Series A: Mathematical, Physical and Engineering Sciences **362**, edited by D. Richards and A. Zayats, 787–805 (2004).

[100] F. Keilmann, "Scattering-type near-field optical microscopy", Journal of Electron Microscopy **53**, 187–192 (2004).

[101] L. Novotny and S. J. Stranick, "Near-Field Optical Microscopy and Spectroscopy with Pointed Probes", Annual Review of Physical Chemistry **57**, 303–331 (2006).

[102] R. Hillenbrand, T. Taubner, and F. Keilmann, "Phonon-enhanced light–matter interaction at the nanometre scale", Nature **418**, 159–162 (2002).

[103] A. J. Huber, A. Ziegler, T. Köck, and R. Hillenbrand, "Infrared nanoscopy of strained semiconductors", Nature Nanotechnology **4**, 153–157 (2009).

[104] B. Lahiri, G. Holland, V. Aksyuk, and A. Centrone, "Nanoscale Imaging of Plasmonic Hot Spots and Dark Modes with the Photothermal-Induced Resonance Technique", Nano Letters **13**, 3218–3224 (2013).

[105] A. Centrone, "Infrared Imaging and Spectroscopy Beyond the Diffraction Limit", Annual Review of Analytical Chemistry **8**, 101–126 (2015).

[106] W. Schöllkopf, S. Gewinner, W. Erlebach, H. Junkes, A. Liedke, G. Meijer, A. Paarmann, G. von Helden, H. Bluem, D. Dowell, R. Lange, J. Rathke, A. M. M. Todd, L. M. Young, U. Lehnert, P. Michel, W. Seidel, R. Wünsch, and S. C. Gottschalk, "The New IR FEL Facility at the Fritz-Haber-Institut in Berlin", Proceedings of FEL 2014, 629–634 (2014).

[107] D. W. Berreman, "Optics in Stratified and Anisotropic Media: 4x4-Matrix Formulation", Journal of the Optical Society of America **62**, 502 (1972).

[108] P. Yeh, "Electromagnetic propagation in birefringent layered media", Journal of the Optical Society of America **69**, 742 (1979).

[109] P. J. Lin-Chung and S. Teitler, "4 x 4 Matrix formalisms for optics in stratified anisotropic media", Journal of the Optical Society of America A **1**, 703 (1984).

[110] Z.-M. Li, B. T. Sullivan, and R. R. Parsons, "Use of the 4 x 4 matrix method in the optics of multilayer magnetooptic recording media", Applied Optics **27**, 1334 (1988).

[111] W. Xu, L. T. Wood, and T. D. Golding, "Optical degeneracies in anisotropic layered media: Treatment of singularities in a 4x4 matrix formalism", Physical Review B **61**, 1740–1743 (2000).

[112] M. Jeannin, *Generalized 4x4 matrix algorithm for light propagation in anisotropic stratified media (Python files), https://zenodo.org/record/3470876*, 2019.

[113] Y. Yao, M. A. Kats, P. Genevet, N. Yu, Y. Song, J. Kong, and F. Capasso, "Broad Electrical Tuning of Graphene-Loaded Plasmonic Antennas", Nano Letters **13**, 1257–1264 (2013).

[114] Z. Fang, S. Thongrattanasiri, A. Schlather, Z. Liu, L. Ma, Y. Wang, P. M. Ajayan, P. Nordlander, N. J. Halas, and F. J. García de Abajo, "Gated Tunability and Hybridization of Localized Plasmons in Nanostructured Graphene", ACS Nano **7**, 2388–2395 (2013).

[115] G. Si, E. S. Leong, X. Jiang, J. Lv, J. Lin, H. Dai, and Y. J. Liu, "All-optical, polarization-insensitive light tuning properties in silver nanorod arrays covered with photoresponsive liquid crystals", Physical Chemistry Chemical Physics **17**, 13223–13227 (2015).

[116] S. Dai, J. Zhang, Q. Ma, S. Kittiwatanakul, A. McLeod, X. Chen, S. G. Corder, K. Watanabe, T. Taniguchi, J. Lu, Q. Dai, P. Jarillo-Herrero, M. Liu, and D. N. Basov, "Phase-Change Hyperbolic Heterostructures for Nanopolaritonics: A Case Study of hBN/VO_2", Advanced Materials **31**, 1900251 (2019).

[117] N. C. Passler, A. Heßler, M. Wuttig, T. Taubner, and A. Paarmann, "Active Nanophotonics: Surface Polariton-Like s-Polarized Waveguide Modes in Switchable Dielectric Thin Films on Polar Crystals (Advanced Optical Materials 5/2020)", Advanced Optical Materials **8**, 2070018 (2020).

[118] G. T. Papadakis, A. Davoyan, P. Yeh, and H. A. Atwater, "Mimicking surface polaritons for unpolarized light with high-permittivity materials", Physical Review Materials **3**, 015202 (2019).

[119] A. D. Dunkelberger, C. T. Ellis, D. C. Ratchford, A. J. Giles, M. Kim, C. S. Kim, B. T. Spann, I. Vurgaftman, J. G. Tischler, J. P. Long, O. J. Glembocki, J. C. Owrutsky, and J. D. Caldwell, "Active tuning of surface phonon polariton resonances via carrier photoinjection", Nature Photonics **12**, 50–56 (2018).

[120] M. Jeannin, *Layer-Resolved Absorption in Arbitrarily Anisotropic Heterostructures (Python files), doi.org/10.5281/zenodo.3724504*, 2020.

[121] T. Ribaudo, D. W. Peters, A. R. Ellis, P. S. Davids, and E. A. Shaner, "Highly directional thermal emission from two-dimensional silicon structures", Optics Express **21**, 6837 (2013).

[122] Y. Yang, K. Kelley, E. Sachet, S. Campione, T. S. Luk, J.-P. Maria, M. B. Sinclair, and I. Brener, "Femtosecond optical polarization switching using a cadmium oxide-based perfect absorber", Nature Photonics **11**, 390–395 (2017).

[123] E. Baudin, C. Voisin, and B. Plaçais, "Hyperbolic Phonon Polariton Electroluminescence as an Electronic Cooling Pathway", Advanced Functional Materials **30**, 1904783 (2020).

[124] K. Ohtani, B. Meng, M. Franckié, L. Bosco, C. Ndebeka-Bandou, M. Beck, and J. Faist, "An electrically pumped phonon-polariton laser", Science Advances **5**, eaau1632 (2019).

[125] Z. Jacob, J.-Y. Kim, G. V. Naik, A. Boltasseva, E. E. Narimanov, and V. M. Shalaev, "Engineering photonic density of states using metamaterials", Applied Physics B **100**, 215–218 (2010).

[126] H. Hu, D. Ji, X. Zeng, K. Liu, and Q. Gan, "Rainbow Trapping in Hyperbolic Metamaterial Waveguide", Scientific Reports **3**, 1249 (2013).

[127] A. A. Sayem, M. R. C. Mahdy, D. N. Hasan, and M. A. Matin, "Tunable slow light with graphene based hyperbolic metamaterial", in 8th international conference on electrical and computer engineering (2014), pp. 230–233.

[128] A. W. Zeng and B. Guo, "Characteristics of slow light in a magnetized plasma hyperbolic metamaterial waveguide", Optical and Quantum Electronics **49**, 200 (2017).

[129] K. Korzeb, M. Gajc, and D. A. Pawlak, "Compendium of natural hyperbolic materials", Optics Express **23**, 25406 (2015).

[130] A. Poddubny, I. Iorsh, P. Belov, and Y. Kivshar, "Hyperbolic metamaterials", Nature Photonics **7**, 948–957 (2013).

[131] E. L. Runnerstrom, K. P. Kelley, T. G. Folland, J. R. Nolen, N. Engheta, J. D. Caldwell, and J.-P. Maria, "Polaritonic Hybrid-Epsilon-near-Zero Modes: Beating the Plasmonic Confinement vs Propagation-Length Trade-Off with Doped Cadmium Oxide Bilayers", Nano Letters **19**, 948–957 (2019).

[132] S. V. Zhukovsky, O. Kidwai, and J. E. Sipe, "Physical nature of volume plasmon polaritons in hyperbolic metamaterials", Optics Express **21**, 14982 (2013).

[133] S. V. Zhukovsky, A. Andryieuski, J. E. Sipe, and A. V. Lavrinenko, "From surface to volume plasmons in hyperbolic metamaterials: General existence conditions for bulk high-k waves in metal-dielectric and graphene-dielectric multilayers", Physical Review B **90**, 155429 (2014).

[134] S. V. Zhukovsky, A. A. Orlov, V. E. Babicheva, A. V. Lavrinenko, and J. E. Sipe, "Photonic-band-gap engineering for volume plasmon polaritons in multiscale multilayer hyperbolic metamaterials", Physical Review A **90**, 13801 (2014).

[135] K. V. Sreekanth, A. De Luca, and G. Strangi, "Excitation of volume plasmon polaritons in metal-dielectric metamaterials using 1D and 2D diffraction gratings", Journal of Optics **16**, 105103 (2014).

[136] L. Sun, X. Yang, and J. Gao, "Analysis of nonlocal effective permittivity and permeability in symmetric metal–dielectric multilayer metamaterials", Journal of Optics **18**, 65101 (2016).

[137] Z. Galazka, "β-Ga_2O_3 for wide-bandgap electronics and optoelectronics", Semiconductor Science and Technology **33**, 113001 (2018).

[138] M. Higashiwaki and G. H. Jessen, "Guest Editorial: The dawn of gallium oxide microelectronics", Applied Physics Letters **112**, 60401 (2018).

[139] M. Schubert, R. Korlacki, S. Knight, T. Hofmann, S. Schöche, V. Darakchieva, E. Janzén, B. Monemar, D. Gogova, Q.-T. Thieu, R. Togashi, H. Murakami, Y. Kumagai, K. Goto, A. Kuramata, S. Yamakoshi, and M. Higashiwaki, "Anisotropy, phonon modes, and free charge carrier parameters in monoclinic β-gallium oxide single crystals", Physical Review B **93**, 125209 (2016).

[140] M. Schubert, A. Mock, S. Korlacki Rafałand Knight, Z. Galazka, G. Wagner, V. Wheeler, M. Tadjer, K. Goto, and V. Darakchieva, "Longitudinal phonon plasmon mode coupling in β-Ga_2O_3", Applied Physics Letters **114**, 102102 (2019).

[141] R. Macêdo, T. Dumelow, and R. L. Stamps, "Tunable Focusing in Natural Hyperbolic Magnetic Media", ACS Photonics **3**, 1670–1677 (2016).

[142] R. Macêdo and R. E. Camley, "Engineering terahertz surface magnon-polaritons in hyperbolic antiferromagnets", Physical Review B **99**, 14437 (2019).

[143] Y. V. Bludov, J. N. Gomes, G. A. Farias, J. Fernández-Rossier, M. I. Vasilevskiy, and N. M. R. Peres, "Hybrid plasmon-magnon polaritons in graphene-antiferromagnet heterostructures", 2D Materials **6**, 45003 (2019).

Appendices

APPENDIX A

Supporting Information to Publications

A.1 Supporting Information: Second Harmonic Generation from Critically Coupled Surface Phonon Polaritons

Nikolai Christian Passler, Ilya Razdolski, Sandy Gewinner, Wieland Schöllkopf, Martin Wolf, and Alexander Paarmann

Supporting Information Second-Harmonic Generation from Critcally Coupled Surface Phonon Polaritons

Nikolai Christian Passler, Ilya Razdolski, Sandy Gewinner, Wieland Schöllkopf, Martin Wolf, and Alexander Paarmann*

Fritz-Haber-Institut der Max-Planck-Gesellschaft, Faradayweg 4-6, 14195 Berlin, Germany

E-mail: alexander.paarmann@fhi-berlin.mpg.de

S1 Experimental

The experimental setup was schematically shown in Fig. 1 (a) of the main text. The Otto-type prism coupling is realized by placing a triangular prism (KRS5, 25mm high, 25mm wide, angles of 30°, 30°, and 120°, Korth Kristalle GmbH) on a motorized mount in front of the sample. Details on the implemtation are shown in Fig. S1. Three motorized actuators (Newport TRA12PPD) are used to push (against springs) the prism away from the sample, which is mounted on a plate (25mm diameter) equipped with three mN force sensors (Honeywell FSS1500SSB). Each force sensor indicates the point of contact, allowing for parallel alignment of the sample and the prism back surface. The motorized actuators allow for continuous tuning of the air gap width d.

We note that macroscopic protrusions and non-flatness of the sample can lead to strain between sample and prism, resulting in a lower limit of air gap width (typically ~ 1.5 μm) and slight nonlinearities of the actual air gap width and the actuator readback values, specifically at close approach. Therefore, we fitted the values of d from the reflectivity data, using the procedure described in Sec. S3, the results of which are in qualitative (but not quantitative) agreement with the actuator readback values. Gap width scans of the signals are typically performed by starting at closest achievable approach, followed by defined steps (identical for all three actuators) away from the sample.

Given the large refractive index of KRS5 of $n_{KRS5} \approx 2.4$, external angles differ respectively when going away from $\theta_{\text{ext}} = 30°$, i.e., the internal angle θ inside the prism is $\theta = 30° + \arcsin(\sin(\theta_{\text{ext}} - 30°)/n_{KRS5})$. This arrangement allows for internal angles from below the total internal reflection cutoff at $\theta_{\text{cutoff}} \approx 25°$ to about $\theta = 52°$, covering the majority of the SPhP dispersion. We note that using more convenient semi-cylindrical prisms results in strong horizontal focusing, increasing angular spread of the beam and thereby much degraded momentum resolution. Additionally, this horizontal focusing distorts the beam to an elliptical shape making it harder to focus onto small detectors.

We use an infrared FEL[1] as tunable, narrowband, and p-polarized excitation source. We focus the beam mildly ($f \approx 60$ cm, Edmund Optics) onto the sample surface to minimize angular spread of the beam. Details on the IR-FEL are given elsewhere.[1] In short, the electron gun is operated at a micropulse repetition rate of 1 GHz with an electron macropulse duration of 10 μs and a macropulse repetition rate of 10 Hz. The electron energy is set to 31 MeV, allowing to tune the FEL output wavelength between $\sim 7 - 18$ μm ($\sim 1400 - 550$ cm^{-1}) using the motorized undulator gap, providing ps-pulses with typical full-width-at-half-maximum

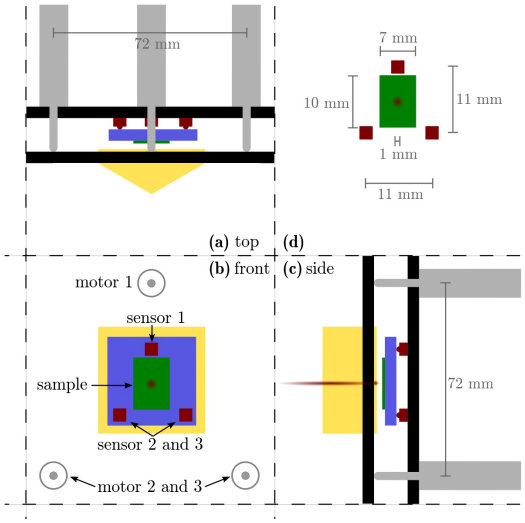

Figure S1: Practical implementation of the Otto-type prism coupling to surface polaritons. Three motorized actuators push (against springs) the prism mount away from the sample. When pulled back, the point of contact is detected using three mN force sensors, allowing for parallel alignment of the prism and sample surfaces and continuous scanning of the gap width d.

(FWHM) of < 5 cm^{-1}.

Reflected fundamental and SHG beams are split using a 7 μm long-pass filter (LOT). The reflectivity is detected with a home-built pyro-electric sensor (Eltec 420M7). The SHG signal is detected with a liquid nitrogen cooled mercury cadmium telluride/indium antimony sandwich detector (Infrared Associates), after blocking the fundamental light using 5 mm of MgF_2 and a 7 μm short-pass filter (LOT). Additionally, intrinsic harmonics in the FEL beam are blocked prior to the setup using a 7 μm and a 9 μm long-pass filter (both LOT). We also measure reference power on a single shot basis to minimize the impact of shot-to-shot fluctuations of the FEL using the reflection off a thin KBr plate placed in the beam prior to the setup. This reference signal is also detected by a pyro-electric detector, and we normalize all signals to this reference signal on a single-shot basis, i.e. for each macropulse. The spectral response function of the setup is determined by measuring the reflectivity for very large gap width $d \approx 40$ μm, i.e. in total reflection across the full spectral range, for each incidence angle. All spectra are normalized for these reference data. Finally, we note that changing the incidence angle requires detection realignment, giving rise to an experimental uncertainty for the signal magnitudes of 10-20% between different incidence angles. This has no influence on the reflectivity, since the reflectivity reference is acquired for each incidence angle. However, no such reference is available for the SHG, such that confident interpretation of the absolute SHG intensities between different incidence angles is not given.

S2 Transfer Matrix Approach

For all calculations of reflectivity, local fields, and transmittance, a 4×4 - matrix formalism was developed capable of treating any number of layers, each described by a dielectric tensor $\hat{\epsilon}$. In contrast to other approaches,[2–4] our formalism is numerically stable and handles isotropic and anisotropic materials simultaneously, including the substrate.

The multilayer surfaces are chosen to extend perpendicular to z and the incident wave impinges in the xz-plane with wavevector $\vec{k}_i = \frac{\omega}{c}(\xi, 0, q_i)$ in layer i. The x-component $\xi = \sqrt{\epsilon_{inc}}\sin(\theta)$ is conserved throughout the complete multilayer system, and q_i is the unit-free, layer-dependent z-component. In any medium, Maxwell's equations yield four independent plane-wave solutions characterized by q_{ij} ($j = 1..4$), which are determined as shown by Berreman.[2] In order to avoid instability and discontinuities, the four solutions have to be ordered unambiguously, which is done based on the work of Li *et al.*.[5]

In continuation, the treatment of singularities of Xu *et al.*[6] is employed in order to generalize the formalism to any isotropic or anisotropic medium, yielding the electric field components $\vec{E}_{ij} = (\gamma_{ij1}, \gamma_{ij2}, \gamma_{ij3})$ of the four eigenmodes j in layer i. With these components, a matrix $\mathbf{A}_i$ is formulated (see equation 24 in ref.[6]), rep-

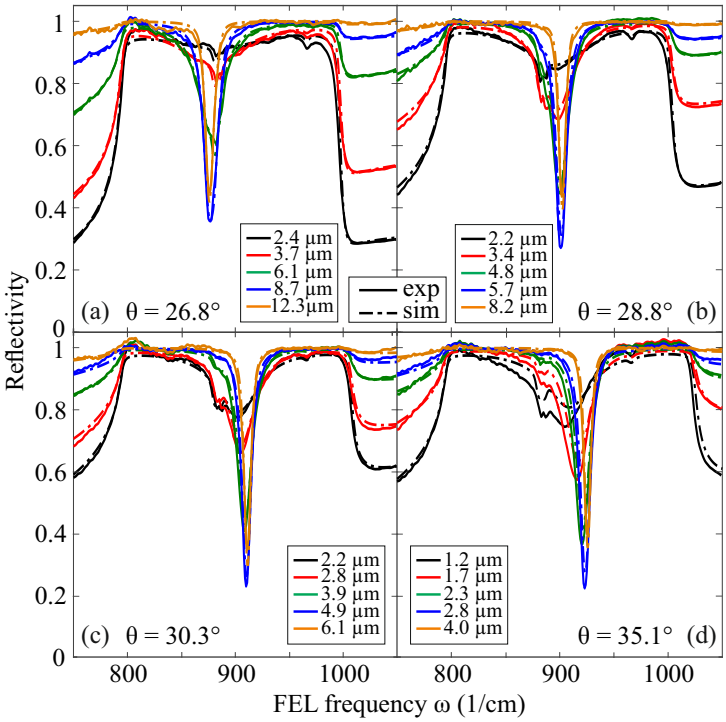

Figure S2: Experimental (solid lines) and calculated (dot-dashed lines) reflectivity spectra of 6H-SiC in the Otto configuration, shown for four different incidence angles θ (a,b,c,d), each with a set of five selected air gap widths d (see legends).

resenting Maxwell's boundary conditions at the interface $i-1$, i. The $\vec{E}$-fields are then connected by the interface matrix $\mathbf{L}_i$ as follows:

$$\vec{E}_{i-1} = \mathbf{A}_{i-1}^{-1}\mathbf{A}_i\vec{E}_i \equiv \mathbf{L}_i\vec{E}_i. \qquad \text{(S1)}$$

The propagation through layer i is described by a diagonal matrix $\mathbf{P}_i$ with elements $e^{-i\frac{\omega}{c}q_{ij}d_i}$, where $j = 1..4$ is the nth diagonal element. The transfer matrix $\mathbf{\Gamma}_N$ of the complete multilayer system reads

$$\mathbf{\Gamma}_N = \mathbf{L}_1\mathbf{P}_1\mathbf{L}_2\mathbf{P}_2...\mathbf{L}_N\mathbf{P}_N\mathbf{L}_{N+1}. \qquad \text{(S2)}$$

Finally, reflection and transmission coefficients for p-polarization are calculated in terms of $\mathbf{\Gamma}_N$ components as shown by Yeh.[3]

S3 Fitting Procedure

The reflectivity data were fitted employing the matrix formalism, and convolving the results to account for finite broadening of the incidence angle and FEL frequency, $\Delta\theta = 0.2°$ and $\Delta\omega = 4.4$ cm^{-1}, respectively. For each incidence angle, the data were normalized by a reference spectrum taken at large gap width d (≈ 40 μm). This accounts for the spectral response function of the setup, while additionally slow FEL power drifts are accounted for in the fitting procedure by a multiplication factor a for every individual spectrum ($0.98 < a < 1.04$).

The data sets of all four incidence angles θ were fitted globally, where θ, $\Delta\theta$, $\Delta\omega$, and the 6H-SiC parameters such as TO and LO frequencies and damping were global fitting parameters, while gap widths d and factors a were adjusted individually. Thereby, $\Delta\theta$ was fitted only for the two smaller angles, and $\Delta\omega$ for the other two. This is justified due to the shape of the SPhP dispersion, being more sensitive to the incidence angle but less to the frequency at smaller θ, and vice versa for larger angles.

By fitting all four data sets in several iterations, the global parameters converged common values. In a final run, all data sets were fitted

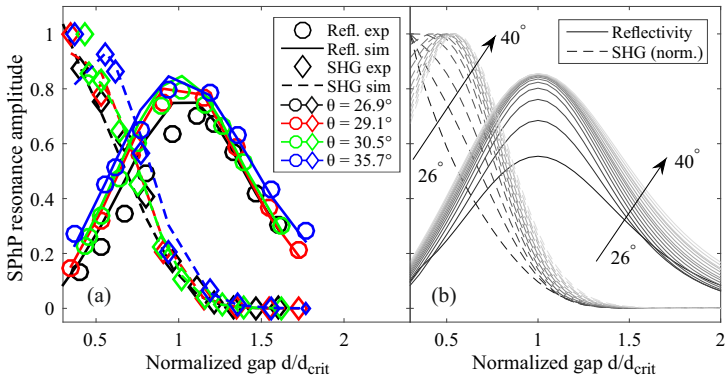

Figure S3: (a) Experimental (symbols) and simulated (lines) SPhP resonance amplitudes in the reflectivity (circles, solid lines) and SHG (diamonds, dashed lines) as a function of the gap width d normalized to the critical gap width d_{crit} of the respective incidence angle, and (b) simulated curves for a larger set of incidence angles.

again using averages of the global parameters, yielding the curves and parameters shown in fig. S2.

S4 Normalization to Critical Gap Width

The amplitude of the SPhP resonance (see Fig. 3 (a,b) of the main text) depends on both the incidence angle θ and gap width d. We have numerically determined the critical gap width d_{crit} as a function of θ, allowing for renormalization of the gap width d to d_{crit} at corresponding incidence angle. This is illustrated in Fig. S3 (a) where we plot the experimental and simulated amplitudes of the SPhP resonance in the reflectivity and SHG, respectively, against the normalized gap. For better clarity of the trends, we also show the simulated data for a larger set of incidence angles in (b). All spectra fall back onto a unversial curve; the reflectivity SPhP amplitude peaks at critical coupling conditions, while the SHG intensity drops to $< 20\%$ at d_{crit} as compared to close gap due to inefficient SHG out-coupling in the Otto geometry. The trend in the SHG resonance amplitudes for increasing incidence angle is a result of multiple competing effects: angular and spectral dispersion of the out-coupling efficiency, see section S5, spectral dispersion of the nonlinear suseptibility,[7] as well as increasing field enhancements (see Fig. 4 of the main text), as we move along in the SPhP dispersion with larger incidence angles.

S5 Calculation of the Second-Harmonic Intensity

The calculations of the second-harmonic intensity are largely based on previous work of SHG spectroscopy using free space excitation.[7] In order to correctly describe the multilayer (KRS5/air/SiC) system, we needed to replace the Fresnel transmission coefficients with appropriate expressions derived from the transfer matrix approach. Particular care is needed for the transmission of the outgoing SHG, as will be discussed below.

We first calculate the nonlinear polarization $\vec{P}^{NL}$ at 2ω generated in SiC, before projecting it onto the appropriate mode at 2ω responsible for the out-coupling of the SHG into the far field. Therefore, we rewrite Eq. 2 of the main text as:

$$I(2\omega) \propto |(T_b \vec{E}_{SiC}(2\omega)) \cdot \vec{P}^{NL}(2\omega)/\Delta k|^2 \quad \text{(S3)}$$

with

$$\vec{P}^{NL}(2\omega) \propto (\chi^{(2)}(-2\omega;\omega,\omega)\vec{E}^2_{SiC}(\omega))|^2. \quad \text{(S4)}$$

We use the dispersion of the nonlinear susceptibility tensor $\chi^{(2)}(-2\omega;\omega,\omega)$ of 6H-SiC as ex-

tracted in our previous work.[7,8] The local fields $\vec{E}^2_{SiC}(\omega)$ on the SiC side of the air–SiC interface are calculated as follows.

First, we evaluate the transfer matrix $\mathbf{\Gamma}$ for a specific configuration of incidence angle, frequency and air gap width, employing the algorithm presented in Sec. S2. Then, the in-plane field component $E_{x,SiC}$ can be directly calculated from the transfer matrix $\mathbf{\Gamma}$ as the transmission coefficient for p-polarized light:[3]

$$E_{x,SiC} = \frac{\mathbf{\Gamma}[3,3]}{\mathbf{\Gamma}[1,1]\mathbf{\Gamma}[3,3] - \mathbf{\Gamma}[1,3]\mathbf{\Gamma}[3,1]} \quad \text{(S5)}$$

where $\mathbf{\Gamma}[i,j]$ denote the (i,j) components of the 4×4 matrix (Eq. S2). The out-of-plane component is determined using Maxwell's equation $\bigtriangledown \times H = \epsilon \frac{dE}{dt}$:

$$E_{z,SiC} = -\frac{q_x \epsilon_x}{q_z \epsilon_z} E_{x,SiC}, \quad \text{(S6)}$$

with $q_{x(z)}$ and $\epsilon_{x(z)}$ the in-plane (out-of-plane) components of the wave vector and diagonal dielectric tensor of SiC, respectively. With this information, Eq. S4 can now be evaluated.

The out-coupling of the SHG is accounted for as follows. First, we calculate the transfer matrix $\mathbf{\Gamma}$ at 2ω and, importantly, also $2k_{\parallel}$. Then, we invert $\mathbf{\Gamma}(2\omega)$ to describe the backward propagation. Finally we project $\vec{P}^{NL}$ onto the respective mode propagating from SiC back into the prism, and calculate the SHG intensity:

$$\begin{aligned} I(2\omega) &= \frac{1}{|\Delta k|^2} \Big| \left(\vec{E}_{SiC}(2\omega) \cdot \vec{P}^{NL}(2\omega) \right) \times \\ &\quad \times \frac{|E_{prism}(2\omega)|}{|E_{SiC}(2\omega)|} \Big|^2, \end{aligned} \quad \text{(S7)}$$

where $E_{x,SiC}(2\omega) \equiv 1$ and $E_{z,SiC}(2\omega)$ is calculated using the expression analogous to Eq. S6. The last factor represents the transmission coefficient T_b for the second-harmonic field across the air gap. $E_{x,prism}(2\omega)$ is evaluated analogous to Eq. S5, however, employing $[\mathbf{\Gamma}(2\omega)]^{-1}$ as the transfer matrix, and $E_{z,prism}(2\omega)$ is again calculated using Eq. S6.

References

(1) Schöllkopf, W.; Gewinner, S.; Junkes, H.; Paarmann, A.; von Helden, G.; Bluem, H.; Todd, A. M. M. The new IR and THz FEL facility at the Fritz Haber Institute in Berlin. Proc. SPIE **2015**, 9512, 95121L

(2) Berreman, D. W. Optics in Stratified and Anisotropic Media: 4x4-Matrix Formulation. Journal of the Optical Society of America **1972**, 62, 502

(3) Yeh, P. Electromagnetic propagation in birefringent layered media. Journal of the Optical Society of America **1979**, 69, 742

(4) Lin-Chung, P. J.; Teitler, S. 4x4 Matrix formalisms for optics in stratified anisotropic media. Journal of the Optical Society of America A **1984**, 1, 703

(5) Li, Z.-M.; Sullivan, B. T.; Parsons, R. R. Use of the 4x4 matrix method in the optics of multilayer magnetooptic recording media. Applied Optics **1988**, 27, 1334

(6) Xu, W.; Wood, L. T.; Golding, T. D. Optical degeneracies in anisotropic layered media: Treatment of singularities in a 4x4 matrix formalism. Physical Review B **2000**, 61, 1740–1743

(7) Paarmann, A.; Razdolski, I.; Gewinner, S.; Schöllkopf, W.; Wolf, M. Effects of crystal anisotropy on optical phonon resonances in midinfrared second harmonic response of SiC. Physical Review B **2016**, 94, 134312

(8) Paarmann, A.; Razdolski, I.; Melnikov, A.; Gewinner, S.; Schöllkopf, W.; Wolf, M. Second harmonic generation spectroscopy in the Reststrahl band of SiC using an infrared free-electron laser. Applied Physics Letters **2015**, 107, 081101

A.2 Supporting Information: Strong Coupling of Epsilon-Near-Zero Phonon Polaritons in Polar Dielectric Heterostructures

Nikolai Christian Passler, Christopher R. Gubbin, Thomas Graeme Folland, Ilya Razdolski, D. Scott Katzer, David F. Storm, Martin Wolf, Simone De Liberato, Joshua D. Caldwell, and Alexander Paarmann

Supporting Information: Strong Coupling of Epsilon-Near-Zero Phonon Polaritons in Polar Dielectric Heterostructures

Nikolai Christian Passler,[1, a)] Christopher R. Gubbin,[2] Thomas Graeme Folland,[3] Ilya Razdolski,[1] D. Scott Katzer,[4] David F. Storm,[4] Martin Wolf,[1] Simone De Liberato,[2] Joshua D. Caldwell,[3,4] and Alexander Paarmann[1, b)]

[1)] *Fritz-Haber-Institut der Max-Planck-Gesellschaft, Faradayweg 4-6,14195 Berlin, Germany*

[2)] *School of Physics and Astronomy, University of Southampton, Southampton SO17 1BJ, United Kingdom*

[3)] *Vanderbilt Institute of Nanoscale Science and Engineering, 2301 Vanderbilt Place, PMB 350106, Nashville, TN 37235-0106*

[4)] *US Naval Research Laboratory, 4555 Overlook Avenue SW, Washington DC 20375, USA*

(Dated: May 29, 2018)

S1. EXPERIMENTAL

The experimental setup is sketched in Fig. 2a of the main text. The Otto geometry is implemented using three motorized actuators (Newport TRA12PPD) to control the position of the triangular coupling prism (KRS5, 25mm high, 25mm wide, angles of 30°, 30°, and 120°, with the 120° edge cut-off, Korth Kristalle GmbH) relative to the sample. The motors push the prism against springs away from the sample and allow for continuous tuning of the air gap d_{gap}. The 120° prism edge is cut-off parallel to the backside in order to perpendicularly couple in the collimated light from a stabilized broadband tungsten-halogen light source (Thorlabs SLS201L). The back-reflected spectrum (registered with Ocean Optics, NIRQuest512) carries interferometric information about the air gap, allowing to quantify d_{gap} by means of the modulation period, and to achieve parallel alignment of prism and sample by optimizing the contrast of the spectral modulations. The absolute read-out of d_{gap} is limited to maximally ~ 60 μm due to the resolution of the spectrometer, while gap sizes below 1 μm could be measured in principle, but are typically not feasible because of macroscopic protrusions and non-flatness of the sample.

At external incidence angles θ_{ext} away from 30°, the high refractive index of KRS5 ($n_{KRS5} \approx 2.4$) leads to strong refraction, resulting in an internal incidence angle θ inside the prism of $\theta = 30° + \arcsin\left(\sin\left(\theta_{ext} - 30°\right)/n_{KRS5}\right)$. In this configuration, angles from below the critical angle of total internal reflection ($\theta_{crit} \approx 25°$) up to about 52° are accessible, covering in-plane momenta across and far beyond the anti-crossing of the strongly coupled modes (52° corresponds to $k_{\parallel}/k_0 = 1.86$). Different in-plane momenta can be accessed via the incidence angle θ by rotating the entire Otto geometry, thus allowing for mapping out the complete dispersion curves experimentally.

As excitation source we employ a mid-infrared free electron laser (FEL) as tunable, narrowband, and p-polarized excitation source. Details on the FEL are given elsewhere[1]. In short, the electron gun is operated at a micropulse repetition rate of 1 GHz with a macropulse duration of 10 μs and a repetition rate of 10 Hz. The electron energy is set to 31 MeV, allowing to tune the FEL output wavelength between $\sim 7 - 18$ μm ($\sim 1400 - 550$ cm^{-1}, covering the spectral ranges of the SiC and AlN reststrahlen bands) using the motorized undulator gap, providing ps-pulses with typical full-width-at-half-maximum (FWHM) of < 5 cm^{-1}. The macropulse and micropulse energies are ~ 30 mJ and ~ 10 μJ, respectively.

The reflectivity signal is detected with a pyroelectric sensor (Eltec 420M7). A second sensor is employed to measure the power reflected off a thin KBr plate placed prior to the setup in the beam. This signal is used as reference for normalization of all reflectivity signals, and is measured on a single shot basis in order to minimize the impact of shot-to-shot fluctuations of the FEL. The spectral response function of the setup is determined by measuring the reflectivity at large gap widths $d_{gap} \approx 40$ μm, where the prism features total internal reflection across the full spectral range. This is done for each incidence angle individually, and all spectra are normalized to their respective response function.

S2. CRITICAL COUPLING CONDITIONS OF THE STRONGLY COUPLED MODES

The Otto geometry grants experimental control over the excitation efficiency by means of the tunability of the air gap width d_{gap}. At a certain critical gap d_{crit}, the excitation efficiency is optimal[2], and we emphasize that d_{crit} is significantly different for the two modes considered ($d_{crit}^{ENZ} < d_{crit}^{SPhP}$). Therefore, in a single spec-

[a)] Electronic mail: passler@fhi-berlin.mpg.de
[b)] Electronic mail: alexander.paarmann@fhi-berlin.mpg.de

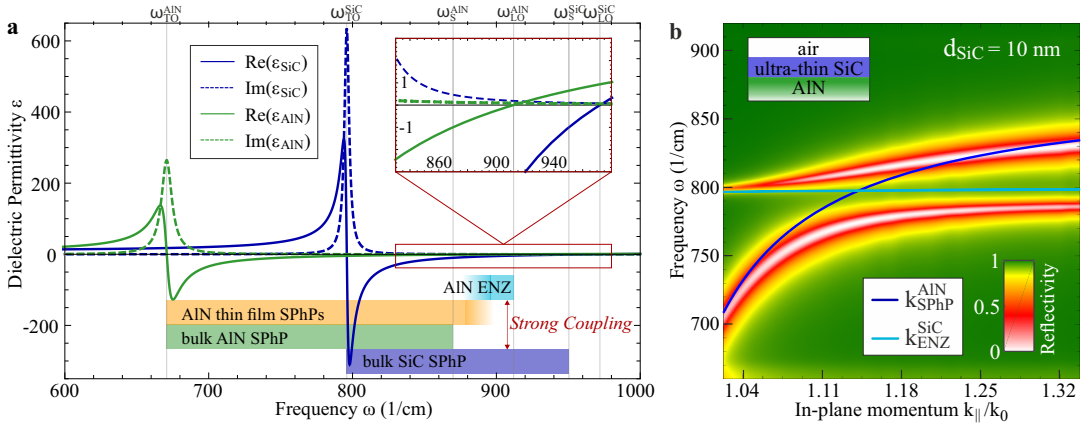

Figure S1. **Frequency ranges of phonon polaritons in AlN and SiC. a** The real (solid line) and imaginary (dashed line) part of the dielectric function ε of SiC (blue) and AlN (green) are shown. At the respective optically active TO phonon frequency ω_{TO}, they feature a strong resonance, while at the LO frequencies ω_{LO}, the real part of ε crosses zero, as illustrated in the inset. In a bulk material, a single SPhP is supported in the frequency range between ω_{TO} and the cut-off frequency ω_S (blue and green color bars). In a thin AlN film ($d_{AlN} < \lambda/2$), two thin film polaritons emerge with the asymmetric mode having a dispersion at frequencies above ω_S (orange color bar), see main text. In the ultra-thin limit of an AlN film ($d_{AlN} < \lambda/50$), the asymmetric mode disperses close to ω_{LO}^{AlN} where $Re(\varepsilon_{AlN}) \approx 0$, hence being an ENZ mode. The strong coupling demonstrated in the main text arises between the SiC substrate SPhP and the AlN ENZ mode. **b** Reflectivity map of the inverse structure of an ultrathin SiC film on top of an AlN substrate at frequencies around the TO frequency of SiC $\omega_{TO}^{SiC} \approx 796$ cm^{-1}. The theoretical dispersions of the asymmetric SiC ENZ mode (light blue line) and the substrate AlN SPhP (dark blue line) are plotted on top, exhibiting a crossing point analogous to the structure discussed in the main text. Interestingly, the dispersion in the combined structure also splits up into two branches, featuring an avoided crossing.

trum with fixed gap width, the two modes cannot be excited equally efficiently, resulting in drastically different resonance dip depths. The data shown in Fig. 2b of the main text, however, were taken at in-plane momentum corresponding to the strong coupling conditions. Note that the two reflectivity dips in each spectrum are of equal depth, evidencing the hybrid nature of the two modes. The tunability and reproducibility of the gap in our setup is therefore a substantial tool for the measurement of polariton resonances, revealing information about their coupling efficiency.

S3. STRONGLY INTERACTING MODES IN MATERIALS WITH OVERLAPPING RESTSTRAHLEN BANDS

In Fig. S1a, the dielectric functions ε of AlN and SiC are shown. They feature a strong resonance at the respective TO frequency ω_{TO} due to its infrared activity, while at the non-IR-active LO frequency ω_{LO}, the real part of ε crosses zero. For the strong coupling to arise, it is necessary that the reststrahlen bands of the two materials overlap, i.e. in the case of an AlN film on SiC, that the ω_{LO} frequency of AlN is located inside the reststrahlen band of SiC. Only then, the ENZ mode supported by the ultra-thin AlN film lies at frequencies where the SiC substrate supports a SPhP, allowing the modes to strongly interact, as demonstrated in the main text.

A similar scenario is obtained for the inverse structure not discussed in the main text, i.e. an ultra-thin SiC film on top of AlN. The SiC film, as shown in Fig. 1a of the main text, supports not only the symmetric thin film mode close to ω_{LO}, but additionally an asymmetric thin film mode lying close to the TO frequency ω_{TO}. In the inverse structure, this lower mode disperses at frequencies where the AlN substrate supports a SPhP, and these two modes can also strongly interact. In Fig. S1b, we show a calculated reflectivity map covering the dispersion range of the substrate AlN SPhP (theoretical curve plotted in dark blue) and the SiC asymmetric thin film mode close to $\omega_{TO}^{SiC} = 796$ cm^{-1} (light blue). In the coupled system, these two modes strongly interact and form an avoided crossing, resulting in two new dispersion branches.

We note that two distinctions have to be made comparing this system with the structure discussed in the main text. First, the dielectric function of SiC close to ω_{TO} is highly dispersive, and therefore only slightly away from ω_{TO} the mode loses its ENZ character. Secondly, the material is strongly absorptive at ω_{TO} and hence the thin-film mode is very likely lossy, hence limiting its practicability. However, such strong coupling in the presence of significant losses is out of the scope of this work.

S4. DEVIATION FROM STRONG COUPLING FOR LARGER FILM THICKNESSES

As stated in the main text, for film thicknesses exceeding $d \gtrsim 50$ nm, the interaction of the modes is not well-

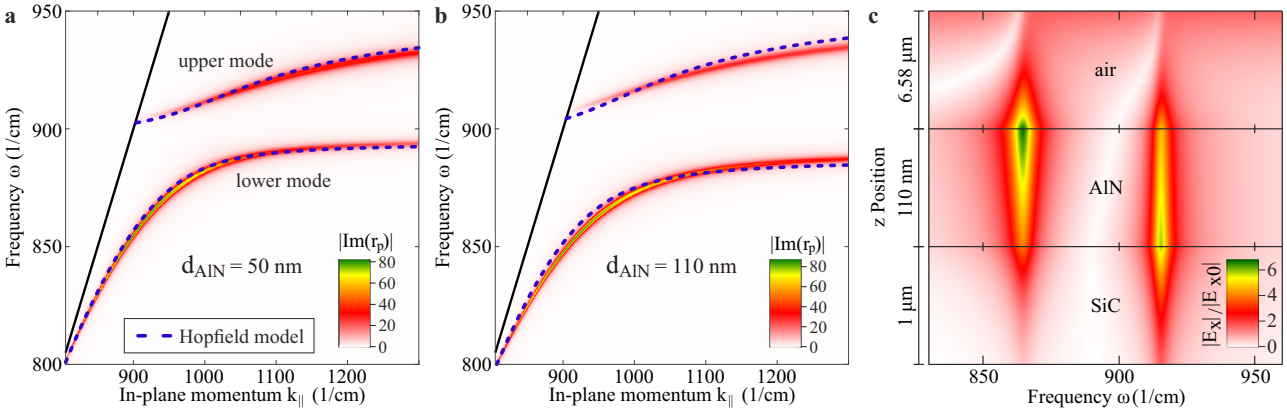

Figure S2. **Deviation from strong coupling for larger film thicknesses. a,b** Reflectivity maps of the AlN/SiC structure from the main text in the Otto geometry for $d_{AlN} = 50, 110$ nm, respectively, featuring the two dispersion branches of the interacting modes with avoided crossing. On top, the dispersion curves extracted from the strong coupling Hopfield model are plotted (blue dashed lines), exhibiting increasing deviation from the numerical calculations for larger film thicknesses. **c** In-plane (x) field enhancement E_x as a function of frequency and z-position plotted at the avoided crossing and for an AlN film thickness of $d_{AlN} = 110$ nm, where the layer thicknesses are not to scale with respect to each other. The prism lies adjacent to air at the top, but is not shown here. At the corresponding resonance frequency of the two modes, strong field enhancements can be observed, which peak at the air/AlN and the AlN/SiC interface, demonstrating that the two modes are not hybridized anymore.

described by our strong coupling model anymore. This can be seen both in the mode dispersion predicted by Eq. 2 of the main text and in the field profiles. However, while the latter originates from the approximation of the ENZ mode dispersion, the former provides a physical limit of strong coupling.

The dispersion curves for $d = 50, 110$ nm are shown in Fig. S2a and b, respectively, plotted on top of numerically calculated reflectivity maps demonstrating a good agreement. However, the increasing deviation of the theoretically predicted dispersion (blue dashed lines) for larger film thicknesses is evident. The reason for that is that in our model, the ENZ mode dispersion is assumed to be constant (900 cm^{-1}), which is sufficiently accurate for $d_{AlN} \lesssim 50$ nm. However, for increasing film thickness the dispersion of the ENZ mode evolves into a thin film mode, see Fig. 1a of the main text. The deviation of the predicted mode dispersion for larger film thicknesses is thus given by the limitation of our model.

Nonetheless, for increasing film thicknesses, a bare AlN SPhP evolves from the lower mode, which is already largely decoupled from the substrate SiC SPhP at $d \approx 110$ nm. The upper mode, on the other hand, develops towards a pure SiC/AlN interface phonon polariton (IPhP), spectrally confined by the ω_{LO}^{AlN} frequency and the SiC cut-off frequency ω_S^{SiC}.

In order to show this disintegration into two distinct modes and thus the breakdown of strong coupling for $d_{AlN} \gtrsim 50$ nm, we analyze the electric field distributions at film thickness $d_{AlN} = 110$ nm. In Fig. S2c, the normalized in-plane (x) electric field amplitude is plotted as a function of frequency and z-position (perpendicular to the interfaces) along the three media (air, AlN, and SiC). Clearly, the two modes appear as strong peaks in the field enhancement at their corresponding resonance frequency. But even though the incidence angle was chosen such that the modes are excited at the avoided crossing ($\theta = 28.5°$, $k_\parallel/k_0 = 1.13$), the field distributions of the two modes differ strongly. The lower mode (~ 865 cm^{-1}) features the strongest E_x at the air/AlN interface, while the upper mode (~ 915 cm^{-1}) exhibits its maximum field enhancement at the SiC/AlN interface, clearly demonstrating that the hybridization of the strong coupling is lost. This can be attributed to the fact that the losses of AlN grow linearly and thus faster than $g_0 \propto \sqrt{d}$ with increasing film thickness d. Furthermore, the localization of the modes at the two different interfaces stays the same on both sides of the avoided crossing (not shown), emphasizing their respective bare AlN SPhP and SiC/AlN IPhP nature across the entire dispersion. In fact, both modes feature a similar in-plane field enhancement while the extreme out-of-plane field enhancement is strongly reduced (not shown), meaning that the ENZ characteristics observed in an ultrathin film ($d < 50$ nm) are not present anymore.

REFERENCES

[1] W. Schöllkopf, S. Gewinner, H. Junkes, A. Paarmann, G. von Helden, H. Bluem, and A. M. M. Todd, **9512**, 95121L (2015).
[2] N. C. Passler, I. Razdolski, S. Gewinner, W. Schöllkopf, M. Wolf, and A. Paarmann, ACS Photonics **4**, 1048 (2017).

A.3 Supporting Information: Second Harmonic Generation from Phononic Epsilon-Near-Zero Berreman Modes in Ultrathin Polar Crystal Films

Nikolai Christian Passler, Ilya Razdolski, D. Scott Katzer, D. F. Storm, Joshua D. Caldwell, Martin Wolf, and Alexander Paarmann

Supporting Information:

Second Harmonic Generation from Phononic Epsilon-Near-Zero Berreman Modes in Ultrathin Polar Crystal Films

Nikolai Christian Passler,[1, a)] I. Razdolski,[1] D. Scott Katzer,[2] D. F. Storm,[2] Joshua D. Caldwell,[2, 3] Martin Wolf,[1] and Alexander Paarmann[1, b)]

[1)] *Fritz-Haber-Institut der Max-Planck-Gesellschaft, Faradayweg 4-6,14195 Berlin, Germany*

[2)] *US Naval Research Laboratory, 4555 Overlook Avenue SW, Washington DC 20375, USA*

[3)] *Vanderbilt University, Institute of Nanoscale Science and Engineering, 2201 West End Ave, PMB 350106, Nashville, TN 37235-0106, USA*

(Dated: 24 April 2019)

[a)] Electronic mail: passler@fhi-berlin.mpg.de

[b)] Electronic mail: alexander.paarmann@fhi-berlin.mpg.de

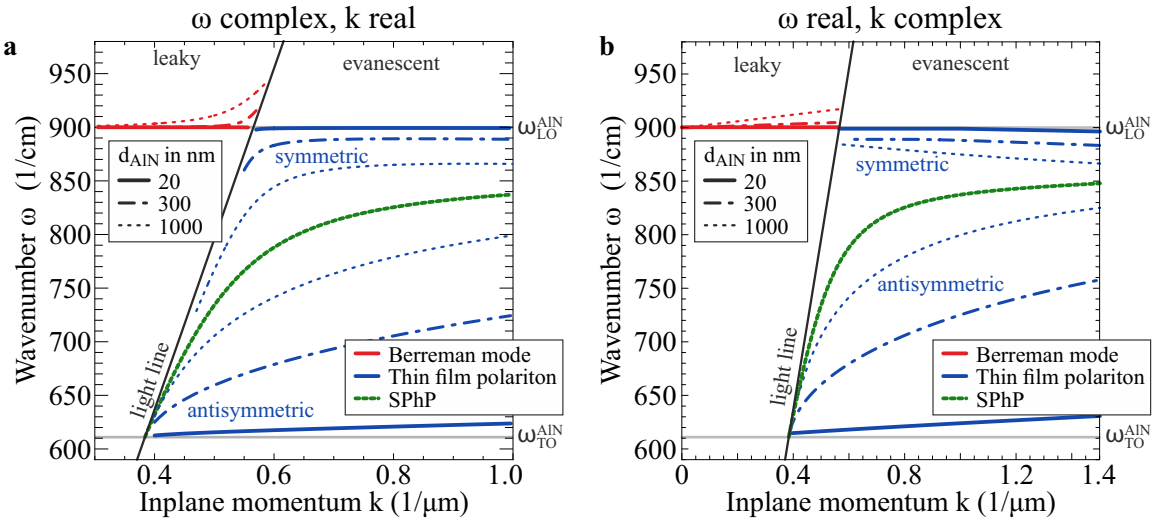

FIG. S1. **Theoretical thin film polariton dispersions for either complex frequency or in-plane momentum.** Solving Eq. 1 of the main text for a complex frequency ω and real in-plane momentum k_x leads to the dispersions shown in **a**, while a real ω and complex k_x yields the curves in **b**. Depending on the chosen observable, one representation is better suited than the other[1]. For instance, the complex frequencies representation is recommended for short pulse excitations, while the complex wavevector representation should be used to analyze the local density of states of a system[2]. For the here investigated air/AlN/SiC system, the complex ω representation (**a**) is the adequate choice: Firstly, solving the system without damping and thus for real ω and real k_x, qualitatively, the same dispersion curves as shown in **a** are obtained[3]. Secondly, the leaky Berreman mode resembles a virtual polariton mode, i.e. its fields are related to an energy flow out of the system, which decreases with time[4]. As has been discussed by Kliewer and Fuchs[4], the correct choice for a standard virtual-mode treatment is the complex ω representation.

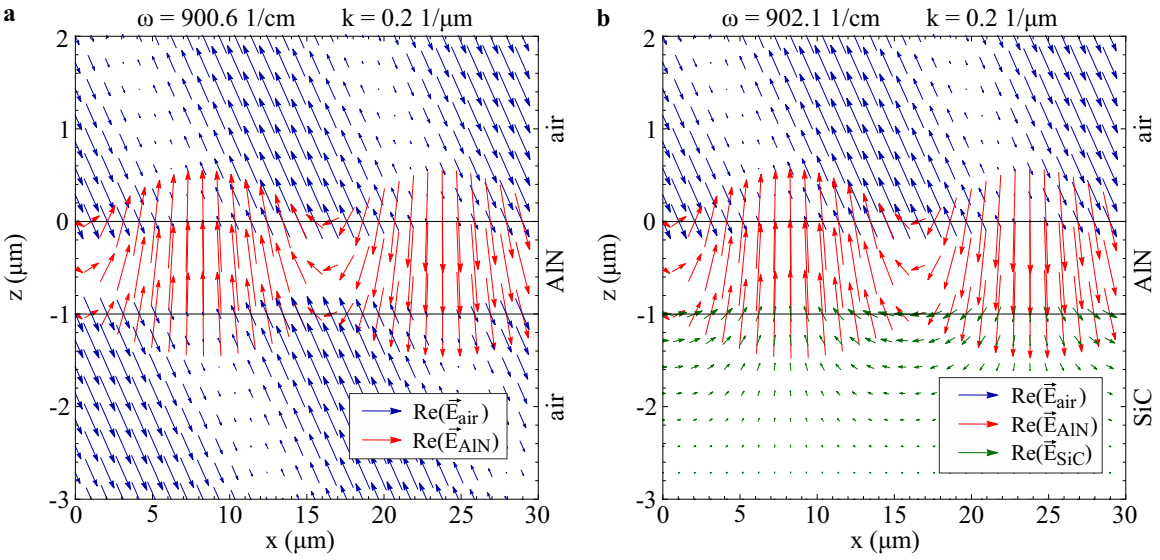

FIG. S2. **Electric field distribution of the Berreman mode in a 1 µm thick AlN slab. a (b)** Vector plots of the electric field distribution in an air/AlN/air (air/AlN/SiC) system of the Berreman mode at an incidence angle of 21° (corresponding to an in-plane momentum of $k = 0.2\,\mu\text{m}^{-1}$ at $\omega = 900.6\,\text{cm}^{-1}$ ($\omega = 902.1\,\text{cm}^{-1}$), lying on the respective Berreman dispersion). The fields of the Berreman mode (red arrows) perform a counterclockwise rotation in positive x-direction characteristic for polaritonic modes. Please note that the real part is plotted in order to capture the propagation characteristics. The imaginary part features the same behavior with a phase difference of $\pi/2$. The absolute in-plane fields are conserved at the interfaces as required by Maxwells boundary conditions, while the absolute out-of-plane fields experience a strong enhancement in the AlN film. The film thickness was chosen to be 1 µm for illustration purposes. In thinner films, the fields qualitatively exhibit the same distribution, but feature much more pronounced out-of-plane field amplitudes. Interestingly, the substrate material (air in a, SiC in b) has no notable effect on the field distribution of the Berreman mode in the AlN film.

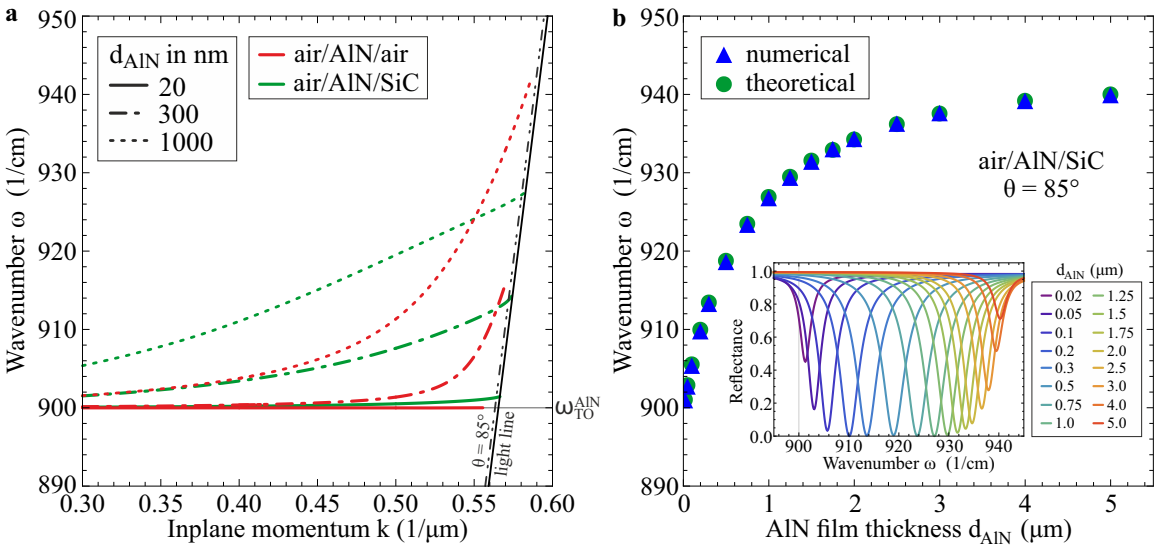

FIG. S3. **Comparison of theoretically and numerically determined Berreman dispersion.** **a** Berreman dispersions for three different AlN film thicknesses d_{AlN} supported in an air/AlN/air (red curves) and an air/AlN/SiC (green curves) system calculated with Eq. 1 from the main text. The dispersion in a freestanding AlN is flatter for smaller in-plane momenta than for the AlN on a SiC substrate, but exhibits a steeper upwards bending close to the light line. **b** Plot of the frequencies of the Berreman dispersion as a function of d_{AlN} in the air/AlN/SiC system at an incidence angle of 85°, calculated numerically with the transfer-matrix method (blue triangles) and theoretically as shown in subfigure a (green circles), showing perfect agreement. The inset shows the Berreman reflectance dip as a function of d_{AlN}. The frequencies of the minima were extracted to obtain the numerical data (blue triangles).

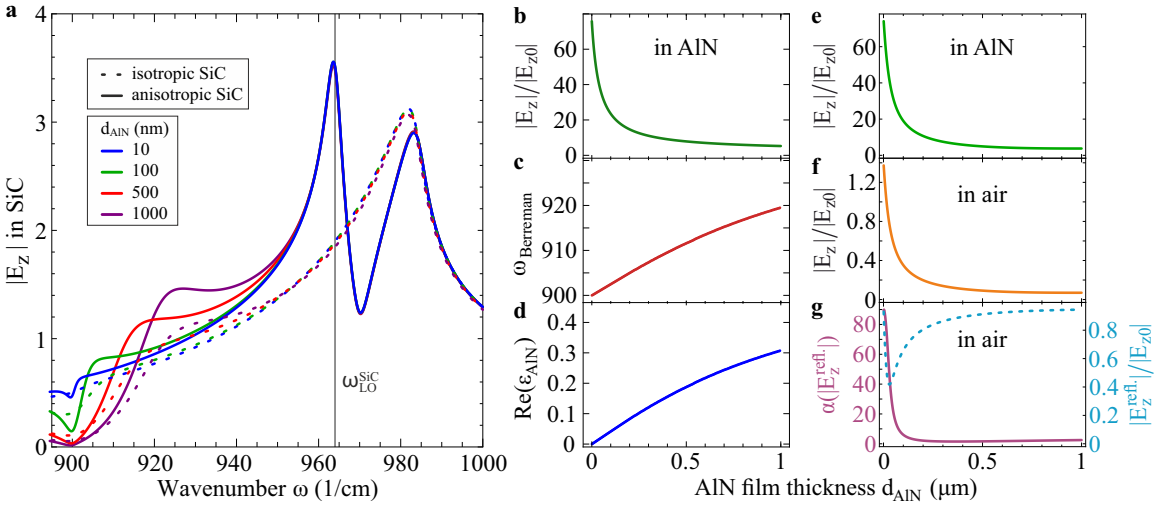

FIG. S4. **Out-of-plane field enhancement E_z at the interfaces of the air/AlN/SiC system.** **a** E_z field enhancement as a function of frequency in isotropic (dashed lines) and anisotropic (solid lines) SiC for four different AlN film thicknesses d_{AlN} at an incidence angle of 60°. At the LO frequency of anisotropic SiC ω_{LO}^{SiC}, the field enhancement reaches a maximum of ~ 3.5 due to the zero-crossing of the SiC dielectric function, while the peak at higher frequency arises from a resonance condition in the Fresnel transmission coefficient (also observed in isotropic SiC)[5]. Both features are mainly independent of d_{AlN} because AlN is transparent in this frequency range. The E_z peaks give rise to the SHG signals reported in Fig. 2a of the main text (compare also with[5]). **b-d** show the E_z field enhancement of the Berreman mode at resonance frequency, the corresponding resonance frequency ω_{Berreman}, and the real part of the dielectric function of AlN at ω_{Berreman}, respectively, as a function of AlN film thickness d_{AlN} and at an incidence angle of 60°. Clearly, the E_z field enhancement (b) experiences a strong increase in the limit of ultrathin films ($d_{AlN} < 200\,\text{nm}$), which can be attributed to the proximity of the Berreman resonance frequency (c) to the ALN LO frequency at $900\,\text{cm}^{-1}$, where the dielectric function (d) crosses zero. For thicker films, on the other hand, the Berreman mode disperses at frequencies where $\text{Re}(\varepsilon_{AlN}) > 0$, yielding a much weaker field enhancement. It is thus seen that only for ultrathin films the Berreman mode, due to its ENZ nature, exhibits the reported strong field enhancement. **e-g** show the E_z field enhancement at the air/AlN interface in AlN and air, and the reflected wave together with its phase, respectively, as a function of AlN film thickness d_{AlN} at fixed frequency $\omega = 900\,\text{cm}^{-1}$ and at an incidence angle of 60°. Surprisingly, also at fixed ENZ frequency, the field enhancement in AlN (e) decreases with increasing film thickness, which, following Eq. 3 of the main text, happens because of a decreasing E_z field in air (f). The latter behavior arises due to the following reasons. The total field in air is the difference of the incident and the reflected field, $E_z = E_z^{\text{inc.}} - E_z^{\text{refl.}}$, where $E_z^{\text{inc.}} \equiv 1$ and its phase $\alpha(E_z^{\text{inc.}}) = 0$. The reflected field $E_z^{\text{refl.}}$ has a minimum value of ~ 0.4 at $d_{AlN} = 30\,\text{nm}$ due to the Berreman resonance. Its phase, however, approaches 90° in the limit of a vanishing AlN film, but drops rapidly to values close to 0° for increasing film thickness. As a consequence, for a phase difference of 0°, the reflected field and the incoming field interfere destructively at the air/AlN interface, leading to a small total field amplitude for increasing film thickness both in air and in AlN. In the ultrathin film limit, on the other hand, the significant phase difference of incoming and reflected wave leads to a sizable total field in air, and thus, in combination with the ENZ condition (see Eq. 3 of the main text), to the strong E_z field enhancement inside the AlN film.

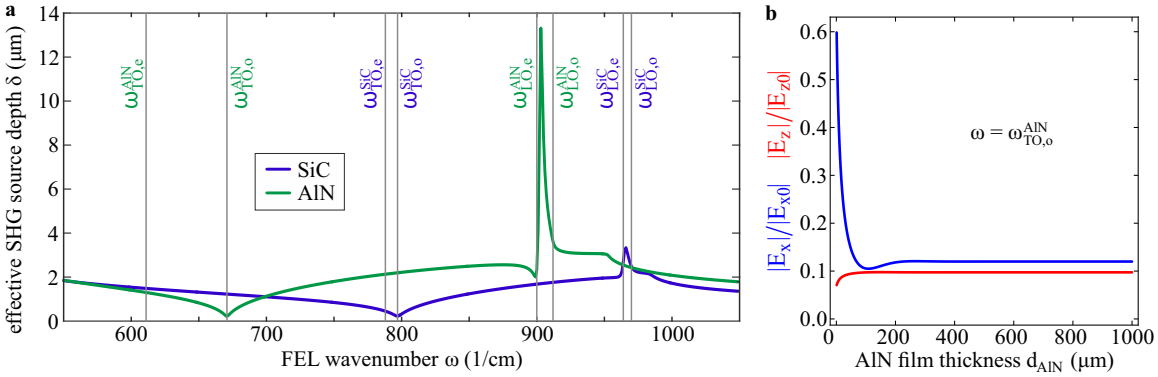

FIG. S5. **Contributions to the SHG yield at the AlN TO frequency.** **a** Effective SHG source depth $\delta = 1/\Delta k$ for bulk SiC and bulk AlN calculated by means of the wavevector mismatch $\Delta k^2 = \left|\vec{k}_{\mathrm{SHG}} - \vec{k}_{1,\mathrm{in}} - \vec{k}_{2,\mathrm{in}}\right|^2$.[6] At the ordinary TO frequency, δ features a minimum of $\sim 200\,\mathrm{nm}$ whereas in the range of the LO frequencies, δ reaches maximum values of a couple of micrometer. Thus, in a bulk sample, a lot more volume contributes to the SHG signal at the LO than at the TO, whereas in a very thin film ($d < 200\,\mathrm{nm}$), the effective source depth is equal at both frequencies and given by the film thickness. Therefore, in an ultrathin AlN film, the TO SHG signal is stronger compared to the LO signal than for a bulk crystal. **b** In-plane E_x and out-of-plane E_z fields at the ordinary AlN TO frequency ($670.8\,\mathrm{cm}^{-1}$) as a function of AlN film thickness. As stated in the main text, in a bulk crystal the field enhancement is strongly suppressed at the TO frequency[6], leading to a suppressed SHG yield despite the strong $\chi^{(2)}$ resonance. In an ultrathin film, however, this suppression is reduced, as can be seen by the sharp increase of the E_x field for $d_{AlN} < 100\,\mathrm{nm}$.

REFERENCES

[1]R. W. Alexander, G. S. Kovener, and R. J. Bell, "Dispersion Curves for Surface Electromagnetic Waves with Damping," Physical Review Letters **32**, 154–157 (1974).

[2]A. Archambault, T. V. Teperik, F. Marquier, and J. J. Greffet, "Surface plasmon Fourier optics," Physical Review B **79**, 195414 (2009).

[3]K. L. Kliewer and R. Fuchs, "Optical Modes of Vibration in an Ionic Crystal Slab Including Retardation. I. Nonradiative Region," Physical Review **144**, 495–503 (1966).

[4]K. L. Kliewer and R. Fuchs, "Optical Modes of Vibration in an Ionic Crystal Slab Including Retardation. II. Radiative Region," Physical Review **150**, 573–588 (1966).

[5]A. Paarmann, I. Razdolski, A. Melnikov, S. Gewinner, W. Schöllkopf, and M. Wolf, "Second harmonic generation spectroscopy in the Reststrahl band of SiC using an infrared free-electron laser," Applied Physics Letters **107**, 081101 (2015).

[6]A. Paarmann, I. Razdolski, S. Gewinner, W. Schöllkopf, and M. Wolf, "Effects of crystal anisotropy on optical phonon resonances in midinfrared second harmonic response of SiC," Physical Review B **94**, 134312 (2016).

A.4 Supporting Information: Surface Polariton-Like s-Polarized Waveguide Modes in Switchable Dielectric Thin Films on Polar Crystals

Nikolai Christian Passler, Andreas Heßler, Matthias Wuttig, Thomas Taubner, and Alexander Paarmann

ADVANCED OPTICAL MATERIALS

Supporting Information

for *Adv. Optical Mater.*, DOI: 10.1002/adom.201901056

Surface Polariton-Like s-Polarized Waveguide Modes in Switchable Dielectric Thin Films on Polar Crystals

Nikolai Christian Passler, Andreas Heßler, Matthias Wuttig, Thomas Taubner, and Alexander Paarmann**

Supporting Information:

Surface Polariton-Like s-Polarized Waveguide Modes in Switchable Dielectric Thin-Films on Polar Crystals

Nikolai Christian Passler,[1, a)] Andreas Heßler,[2] Matthias Wuttig,[2] Thomas Taubner,[2] and Alexander Paarmann[1, b)]

[1)] *Fritz Haber Institute of the Max Planck Society, Faradayweg 4-6, 14195 Berlin, Germany*

[2)] *Institute of Physics (IA), RWTH Aachen University, 52056 Aachen, Germany*

(Dated: 21 August 2019)

[a)] Electronic mail: passler@fhi-berlin.mpg.de

[b)] Electronic mail: alexander.paarmann@fhi-berlin.mpg.de

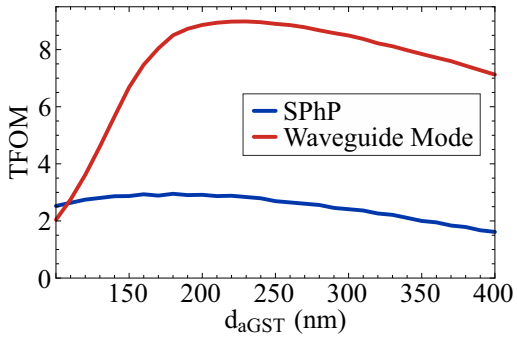

FIG. S1. **Tuning figure of merit (TFOM) of the SPhP and the waveguide mode in air/GST/SiC.** TFOM $= \delta\omega/\mathrm{FWHM}$ as a function of GST film thickness d_{aGST} calculated from reflectance simulations of the air/GST/SiC system in Otto geometry (with KRS5 prism as incident medium) at an incident angle of 30° with the parameters given in the Methods section of the main text. For $d_{\mathrm{aGST}} \approx 150 - 170\,\mathrm{nm}$, the SPhP features a maximal TFOM, while the waveguide mode reaches a maximal predicted TFOM of ~ 9 at $d_{\mathrm{aGST}} \approx 210 - 230\,\mathrm{nm}$. For both modes, the change in the TFOM as a function of d_{aGST} primarily arises from the frequency shift $\delta\omega$ (compare Figure S3 c and f), which varies strongly as the modes shift to lower frequencies towards $\omega_{TO}^{\mathrm{SiC}}$.

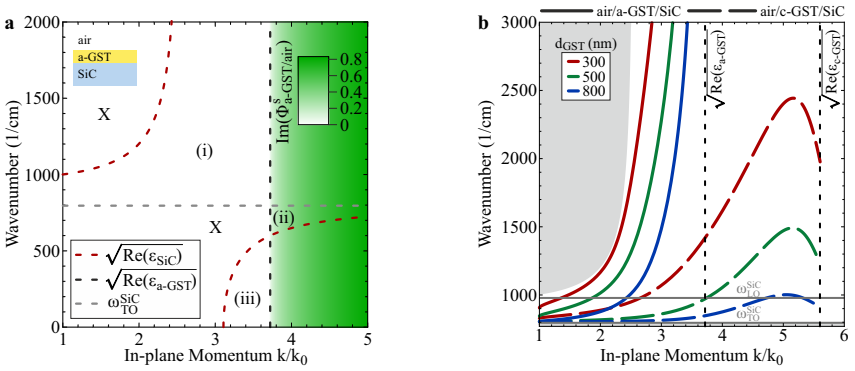

FIG. S2. **Theoretical dispersion of the m=0 order s-polarized waveguide mode in a-GST and c-GST on SiC. a** Imaginary part of the phase difference $\mathrm{Im}(\Phi^s_{\text{a-GST/air}})$ upon reflection at the a-GST/air interface calculated with Eq. 3 from the main text[1]. Where $\mathrm{Im}(\Phi^s_{\text{a-GST/air}}) > 0$, no waveguide modes can be supported, which is the case for $k/k_0 > \sqrt{\mathrm{Re}(\varepsilon_{\text{a-GST}})}$. Therefore, region (ii) is ruled out, even though the SiC/a-GST interface would allow a waveguide mode ($\mathrm{Im}(\Phi^s_{\text{SiC/a-GST}}) = 0$), see Fig. 4a of the main text. Regions marked with an X are excluded because there, $\mathrm{Im}(\Phi^s_{\text{SiC/a-GST}}) > 0$. Thus, the air/a-GST/SiC system only supports waveguide modes in regions (i) and (iii). **b** Comparison of the dispersion of an m=0 s-polarized waveguide mode in an air/a-GST/SiC (solid lines) and an air/c-GST/SiC system (dashed lines) for three different GST film thicknesses. The upper momentum boundary of the dispersions for both systems is given by the refractive index ($n = \sqrt{\varepsilon}$) of the respective GST phase (dashed black lines). The dispersions in a-GST, which has neglectable absorption in the shown frequency range ($\mathrm{Im}(\varepsilon_{\text{a-GST}}) = 0$), approach the upper momentum boundary asymtotically, whereas the dispersions in c-GST experience a red-shift in proximity to the upper momentum boundary due to significant absorption ($\mathrm{Im}(\varepsilon_{\text{c-GST}}) = 9$). For small in-plane momenta ($1 < k/k_0 < 2$), however, which is the range studied in this work, the dispersions in the two GST phases are qualitatively the same, where in c-GST the modes are red-shifted compared to a-GST.

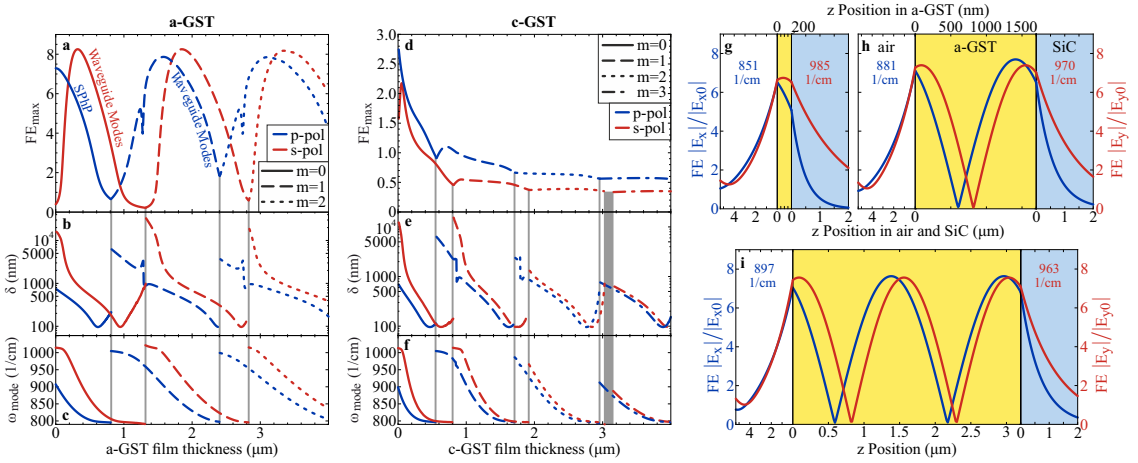

FIG. S3. **Higher-order waveguide modes in a-GST and c-GST on SiC. a,d** Maximum field enhancement $\mathrm{FE}_{\mathrm{max}}$ for p- (blue curves) and s-polarization (red curves) as a function of a-GST and c-GST film thickness d_{GST}, respectively, at $\theta = 30°$. The respective penetration depths δ into SiC are plotted in **b,e**, and **c,f** shows the corresponding mode frequencies ω_{mode}. Above certain d_{GST} (marked by gray lines where the mode frequencies jump), however, the first-order s- and p-polarized waveguide modes start being supported, appearing at the upper frequency boundary. Noteworthily, the SPhP mode propagating at a single boundary smoothly fits into the waveguide mode picture that dominates at larger d_{GST}, and could even be seen as a continuation of the p-polarized waveguide mode in the limit of vanishing film thicknesses. However, while all higher-order p-polarized ($m \geq 1$) and all s-polarized waveguide modes are also supported in thin films on dielectric materials, the SPhP requires the negative permittivity of the SiC substrate. In summary, the reasons for a structure to support a SPhP or a waveguide mode are different, but otherwise SPhPs and waveguide modes can be treated very similarly. The penetration depth δ is a function of the SiC substrate permittivity, and is large for $\varepsilon > 0$ (above $\omega_{LO}^{\mathrm{SiC}} = 970\,\mathrm{cm}^{-1}$) while reaching a minimum of $\delta = 100\,\mathrm{nm}$ for mode frequencies close to $\omega_{TO}^{\mathrm{SiC}} = 797\,\mathrm{cm}^{-1}$ (where $\varepsilon \ll 0$). For p-polarization, the field enhancement and the penetration depth experience a small, sharp feature where the mode crosses the region between the LO ordinary (o) and extraordinary (e) phonon frequencies $\omega_{LO,\mathrm{o}}^{\mathrm{SiC}} = 970\,\mathrm{cm}^{-1}$ and $\omega_{LO,\mathrm{e}}^{\mathrm{SiC}} = 964\,\mathrm{cm}^{-1}$, being an effect of the SiC c-cut uniaxial crystal anisotropy[2]. In comparison to a-GST, the high absorption of c-GST leads to a significantly reduced field enhancement especially for the higher-order modes. Due to larger internal losses, the critical coupling gap of c-GST (1.5 µm) where the modes are excited optimally in the Otto geometry is smaller than for a-GST (3.7 µm). **g-i** Electric field profiles for p- and s-polarized incident light across an air/a-GST/SiC system for a-GST films of 200, 1700, and 3200 nm film thickness, respectively, excited in the Otto geometry. For $d_{\text{a-GST}} = 1700\,\mathrm{nm}$ (h), the $m = 1$ waveguide modes for both polarizations are supported, featuring a node inside the a-GST film, where for $d_{\text{a-GST}} = 3200\,\mathrm{nm}$ (i), the $m = 2$ waveguide modes with two nodes inside the a-GST film can be observed.

REFERENCES

[1]P. K. Tien and R. Ulrich, "Theory of Prism-Film Coupler and Thin-Film Light Guides," Journal of the Optical Society of America **60**, 1325 (1970).

[2]I. Razdolski, Y. Chen, A. J. Giles, S. Gewinner, W. Schöllkopf, M. Hong, M. Wolf, V. Giannini, J. D. Caldwell, S. A. Maier, and A. Paarmann, "Resonant Enhancement of Second-Harmonic Generation in the Mid-Infrared Using Localized Surface Phonon Polaritons in Subdiffractional Nanostructures," Nano Letters **16**, 6954–6959 (2016).

List of Figures

List of Tables

List of Acronyms

2D two-dimensional
3D three-dimensional

AFM atomic force microscope
AlN aluminium nitride
AOM Advanced Optical Materials
APL Applied Physics Letters
Au gold

β-$\mathbf{Ga_2O_3}$ β-gallium oxide
BPhP bulk phonon polariton

CdO cadmium oxide

ENZ epsilon-near-zero

FEL free electron laser
FHI Fritz Haber Insitute

GaN gallium nitride
GST $Ge_3Sb_2Te_6$

hBN hexagonal boron nitride
HMM hyperbolic metamaterial
hPhP hyperbolic phonon polariton

IR infrared

JOSA B Journal of the Optical Society of America

KRS-5 thallium bromo-iodide

LO longitudinal optical
LSPhR localized surface phonon resonance

MIR mid-infrared
MoO_3 molybdenum trioxide
MoS_2 molybdenum disulfide

n-shifted refractive index-shifted
N.C.P. the author of this thesis
NIR near-infrared

PCM phase-change material
PRB Physical Review B
PTIR photothermal-induced resonance

s-SNOM scattering-type scanning near-field optical microscopy
SERS surface-enhanced raman scattering
SFG sum frequency generation
SH second harmonic
SHG second harmonic generation
SiC silicon carbide
SiO_2 quartz
SMP surface magnon polariton
SPhP surface phonon polariton
SPP surface plasmon polariton

TFP thin-film polariton
TO transverse optical

VPP volume plasmon polariton

WM waveguide mode

XH crystalline hybrid

Acknowledgements

I want to thank everybody involved in the development of this thesis. First of all, I thank Martin Wolf and Paul Fumagalli for supervising this work. As head of the PC Department at the FHI, Martin Wolf has been very supportive and encouraging, and I thank him for nurturing a pleasant and fruitful work environment.

My special gratitude goes to Alexander Paarmann for being a particularly supportive mentor, who triggered the ideas for this doctoral thesis, never hesitating to assist and encourage the ongoing process. I thank him deeply for cultivating the exceptionally cordial and positive working atmosphere and coherence in our Lattice Dynamics Group. To him goes a special thanks for attentively reading the thesis and suggesting fruitful corrections.

I furthermore thank the Lattice Dynamics Group for the pleasant office ambience, for the helpful discussions and for the generally cheerful mood sprinkled with jokes and laughs. I highly appreciate the sound mixture of responsibility and jollity, combining high productivity with interludes of refining our frisbee skills in the late afternoon sun.

Another thanks goes to the Fritz Haber Institute for making this work possible in the first place, and for being such a marvelous place of work where I found a warm welcome and quickly felt at home. I also want to thank Wieland Schöllkopf and Sandy Gewinner for enabling the usage of the Free Electron Laser, enduringly accompanying the numerous beamtimes until the early hours.

Moreover, I am very glad to have been part of the IMPRS Functional Interfaces in Physics and Chemistry, and I want to thank everybody involved in running the school and organizing the stimulating meetings and lectures. I furthermore want to express my thanks to the IMPRS and the PC Department for facilitating my attendance at various inspiring conferences in Germany and abroad.

Furthermore, I want to deeply thank my parents and my sister for staying close and supportive, always believing in me and my choice to pursue a doctorate. Finally, my most profound gratitude goes to my beloved wife Gabriela, for being the most beautiful and lovable life companion imaginable. This work would not have been possible without her, granting me the privilege of her unfailing encouragement, inspiring soulfulness and unlimited love.

Abstract

The field of nanophotonics aims at understanding and harnessing light-matter interaction in structures of dimensions far below the wavelength. By squeezing light into nanostructures, the local electric fields can be immensely enhanced, boosting the efficiency of applications such as solar cells or molecular sensing. Furthermore, nanophotonics facilitates the miniaturization of optical devices, pushing forward the development of modern communication technologies and all-optical integrated circuitry.

The fundamental excitation driving nanophotonics is the surface polariton, arising in different types depending on the supporting material. A promising candidate for applications at infrared frequencies is the surface phonon polariton (SPhP) supported by polar crystals. However, a SPhP on a single polar crystal possesses several limitations that hinder the application in nanophotonic technologies.

This work implements layered heterostructures built from various different materials as a versatile platform for phonon polariton nanophotonics, overcoming the limitations of a conventional SPhP. By studying a variety of different polar crystal heterostructures, novel polariton modes with intriguing characteristics are discovered, such as ultra-thin film modes with immense field enhancements, strongly coupled polaritons at epsilon-near-zero frequencies, and waveguide modes with polariton-like properties.

Furthermore, a new experimental and theoretical methodology is developed, enabling the systematic, extensive study of phonon polaritons in layered heterostructures of arbitrarily anisotropic media. In the conducted experiments, the phonon polaritons are excited via prism coupling in a home-built Otto geometry, featuring full control over the excitation conditions with direct read-out of the characteristic air gap size between prism and sample. This unique setup allows to characterize a polariton dispersion at critical coupling conditions, yielding the discovery of new phonon polariton modes.

As an excitation source, the free electron laser at the Fritz Haber Institute is employed, allowing for non-linear optical spectroscopy measurements at infrared phonon-polariton frequencies. The results include the first observation of second harmonic generation from propagating SPhPs and from the ultra-thin film Berreman polariton, enabling experimental access to the field enhancement of the excited polariton mode.

The theoretical advances of this work comprise a transfer matrix formalism for the calculation of light-matter interaction in arbitrarily anisotropic layered heterostructures. The developed versatile and robust framework enables the simulation, analysis and prediction of polaritons and their properties in any multilayer system, constituting a significant contribution to the field of polaritonic nanophotonics. The formalism is implemented in an open-access computer program, facilitating future studies towards phonon polariton-based technologies.

By discovering various new phenomena and implementing a new experimental and theoretical methodology with great potential for future investigations, this work constitutes a comprehensive study of phonon polaritons in polar dielectric heterostructures. Furthermore, this thesis lays out perspectives on how to use the developed experimental and theoretical methods for a number of future studies, bearing great potential to further advance the field of infrared nanophotonics.

Kurzfassung

Das Gebiet der Nanophotonik zielt darauf ab, die Wechselwirkung zwischen Licht und Materie in Strukturen mit Größenskalen weit unterhalb der Wellenlänge zu verstehen und zu nutzen. Durch das Einbringen von Licht in Nanostrukturen können die lokalen elektrischen Felder immens überhöht werden, was die Effizienz von Anwendungen wie Solarzellen oder molekularer Sensorik verbessert. Darüber hinaus ermöglicht die Nanophotonik die Miniaturisierung optischer Bauelemente und treibt so die Entwicklung moderner Kommunikationstechnologien und rein optischer integrierter Schaltkreise voran.

Die grundlegende Anregung, die die Nanophotonik vorantreibt, ist das Oberflächenpolariton, das je nach Trägermaterial in verschiedenen Typen auftritt. Ein vielversprechender Kandidat für Anwendungen bei Infrarotfrequenzen ist das auf polaren Kristallen existierende Oberflächenphononenpolariton (OPhP). Ein OPhP auf einem einzelnen polaren Kristall weist jedoch mehrere Einschränkungen auf, die die Anwendung in nanophotonischen Technologien behindern.

Diese Arbeit implementiert geschichtete Heterostrukturen aus verschiedenen Materialien als vielseitige Plattform für die Phononenpolaritonen-Nanophotonik und überwindet so die Einschränkungen eines herkömmlichen OPhP. Durch die Untersuchung einer Vielzahl verschiedener polarer Kristallheterostrukturen werden neue Polaritonenmoden mit interessanten Eigenschaften entdeckt, wie etwa Moden in ultradünnen Filmen mit immensen Feldverstärkungen, stark gekoppelte Polaritonen bei Epsilon-nahe-Null-Frequenzen und Wellenleitermoden mit polaritonenähnlichen Eigenschaften.

Darüber hinaus wird eine neue experimentelle und theoretische Methodik entwickelt, die die systematische und umfassende Untersuchung von Phononenpolaritonen in geschichteten Heterostrukturen beliebig anisotroper Medien ermöglicht. In den durchgeführten Experimenten werden die Phononenpolaritonen durch Prismenkopplung in einer selbstgebauten Otto-Geometrie angeregt, wobei die Anregungsbedingungen vollständig gesteuert werden können und die charakteristische Luftspaltgröße zwischen Prisma und Probe direkt ausgelesen wird. Dieser einzigartige Aufbau ermöglicht die Charakterisierung einer Polaritondispersion bei kritischen Kopplungsbedingungen, wodurch neue Phononenpolaritonenmoden entdeckt werden können.

Als Anregungsquelle wird der Freie-Elektronen-Laser am Fritz-Haber-Institut eingesetzt, der nichtlineare optische Spektroskopiemessungen bei infraroten Phonon-Polariton-Frequenzen ermöglicht. Die Ergebnisse umfassen die erste Beobachtung der Erzeugung der zweiten Harmonischen von propagierenden OPhP und von dem Berreman-Polariton in ultradünnen Filmen, wodurch die experimentelle Einsicht in die Feldverstärkung der angeregten Polaritonenmode ermöglicht wird.

Die theoretischen Fortschritte dieser Arbeit umfassen einen Transfermatrix-Formalismus zur Berechnung der Wechselwirkung zwischen Licht und Materie in beliebig anisotropen geschichteten Heterostrukturen. Der entwickelte vielseitige und robuste Formalismus ermöglicht die Simulation, Analyse und Vorhersage von Polaritonen und ihren Eigenschaften in jedem beliebigen Mehrschichtsystem, was einen wesentlichen Beitrag auf dem Gebiet der polaritonischen Nanophotonik darstellt. Der Formalismus ist in einem Open-Access-Computerprogramm implementiert, was zukünftige Studien in Richtung Phonon-Polariton-basierten Technologien erleichtert.

Durch die Entdeckung verschiedener neuer Phänomene und die Implementierung einer neuen experimentellen und theoretischen Methodik mit großem Potenzial für zukünftige Studien stellt diese Arbeit ein gründliches Werk über Phononenpolaritonen in polaren dielektrischen Heterostrukturen dar. Darüber hinaus skizziert diese Arbeit Perspektiven für die Verwendung der entwickelten experimentellen und theoretischen Methoden für eine Reihe zukünftiger Studien, die ein großes Potenzial für die Weiterentwicklung des Bereichs der Infrarot-Nanophotonik bieten.